

STRENGTHENING OF EXISTING
REINFORCED CONCRETE STRUCTURES
USING ULTRA HIGH PERFORMANCE
FIBER REINFORCED CONCRETE

SPYRIDON A. PASCHALIS

PHD 2017

Abstract

Most of the new Reinforced Concrete (RC) structures which are built nowadays have a high safety level. Nevertheless, we cannot claim the same for structures built in the past. Many of these were designed without any regulations, or are based on those which have proved to be inadequate. Additionally, it seems that many old structures have reached the end of their service life and, in many cases, were designed to carry loads significantly lower than the current needs specify. Therefore, the structural evaluation and intervention are considered necessary, so they can meet the same requirements as the structures which are built today. Existing techniques for the strengthening and retrofitting of RC structures present crucial disadvantages which are mainly related to the ease of application, the high cost, the time it takes to be applied, the relocation of the tenants during the application of the technique and the poor performance. Research is now focused on new techniques which combine strength, cost effectiveness and ease of application. The superior mechanical properties of Ultra High Performance Fiber Reinforced Concrete (UHPFRC) compared to conventional concrete, together with the ease of preparation and application of the material, make the application of UHPFRC in the field of strengthening of RC structures attractive.

The present research aims to investigate the effectiveness of UHPFRC as a strengthening material, and to examine if the material is able to increase the load carrying capacity of existing RC elements. This has been achieved through an extensive experimental and numerical investigation. The first part of the present research is focused on the experimental investigation of the properties of the material which are missing from the literature and the development of a mixture design which can be used for strengthening applications. The second part is focused on the realistic application of the material for the strengthening of existing RC elements using different strengthening configurations. Finally, in the last part, certain significant parameters of the examined technique, which are mainly related to the design of the technique, are investigated numerically.

From the experimental and numerical investigation of the present research it was clear that UHPFRC is a material with enhanced properties and the strengthening with UHPFRC is a well promising technique. Therefore, in all the examined cases, the performance of the strengthened elements was improved. Finally, an important finding of the present research was that the bonding between UHPFRC and concrete is effective with low values of slip at the interface.

Table of Contents

Abstract	I
List of Tables	VIII
List of Figures	IX
List of Symbols	XIX
Acknowledgements	XXIII
Declaration	XXIV
1. INTRODUCTION.....	1
1.1 Research significance.....	1
1.2 Methodology and structure of the present research	4
1.2.1 Methodology.....	4
1.2.2 Structure of the present thesis.....	5
2. LITERATURE REVIEW	6
2.1 Introduction.....	6
2.2 Existing methods for the strengthening and retrofitting of reinforced concrete structures	6
2.3 Development of cementitious materials.....	10
2.4 Existing knowledge and applications of UHPFRC.....	11
2.5 Knowledge gaps.....	20
3. EXPERIMENTAL INVESTIGATION OF THE PROPERTIES OF ULTRA HIGH PERFORMANCE FIBER REINFORCED CONCRETE (UHPFRC).....	22
3.1 Introduction.....	22
3.2 Investigation of different mixture designs	24
3.2.1 Examined mixture designs	24
3.2.2 Preparation of specimens.....	25
3.2.3 Experimental setup	26
3.2.4 Experimental results	27

3.3 The effect of cement type on the performance of UHPFRC	31
3.4 The effect of the curing time and curing regime on the performance of UHPFRC.....	33
3.4.1 Experimental investigation	33
3.4.2 Experimental results	35
3.5 Investigation of different types of fibers.....	48
3.6 The effect of fiber content on the performance of UHPFRC.....	52
3.6.1 Experimental investigation	52
3.6.2 Preparation of the material	53
3.6.3 Measurement of the workability for the different fiber contents	54
3.6.4 Testing of the UHPFRC for the different fiber contents	56
3.6.5 Modelling of the stress-strain and the stress-crack opening behavior of UHPFR in tension for the different fiber contents	62
3.6.6 The effect of fiber content on the fracture energy of UHPFRC	66
3.7 Measurement of shrinkage of UHPFRC	68
3.8 Investigation of the ‘size effect’ of UHPFRC.....	70
3.8.1 Specimens and Materials	71
3.8.2 Testing Setup and Experimental Results	72
3.8.3 Flexural Tests of Prisms	73
3.8.4 Proposed Equation for the ‘size effect’	76
3.9 UHPFRC under Cyclic Loading	77
3.9.1 Experimental Investigation.....	78
3.9.2 Experimental Setup	78
3.9.3 Experimental results and discussion.....	79
3.9.4 Analytical investigation	83
3.9.5 Validation of the proposed constitutive model.....	88
3.9.6 UHPFRC under cyclic loading for different fiber contents.....	89
3.10 Conclusions	90

4. STRENGTHENING OF EXISTING REINFORCED CONCRETE (RC) BEAMS USING ULTRA HIGH PERFORMANCE FIBER-REINFORCED CONCRETE (UHPFRC)	92
4.1 Introduction.....	92
4.2 Study of the interface between UHPFRC and concrete.....	92
4.2.1 Preparation of specimens.....	93
4.2.2 Experimental setup	94
4.2.3 Evaluation of the interface characteristics.....	95
4.3 Experimental program for the strengthening of RC beams	99
4.4 Examined strengthening techniques	100
4.4.1 Preparation of the RC beams.....	100
4.4.2 Strengthening of RC beams using UHPFRC layers	101
4.4.3 Strengthening of RC beams using UHPFRC layers and steel bars	102
4.4.4 Strengthening of RC beams using three-side jackets	103
4.4.5 Strengthening of RC beams using an UHPFRC layers and dowels	104
4.5 Preparation of the examined beams	105
4.5.1 Preparation of the concrete beams.....	105
4.5.2 Preparation of the UHPFRC layers	108
4.5.3 Properties of the materials	109
4.5.4 Preparation of the interface	111
4.6 Casting of the examined layers and jackets	113
4.6.1 Casting of the UHPFRC layers.....	113
4.6.2 Casting of the UHPFRC layers with dowels at the interface	114
4.6.3 Casting of the UHPFRC layers with the steel bars.....	115
4.6.4 Casting of the three-side jackets.....	116
4.7 Testing of the strengthened beams.....	117

4.7.1 Experimental setup for the testing of the control beams and the beams strengthened with jackets	117
4.7.2 Experimental setup for the testing of beams strengthened with layers	119
4.8 Experimental results.....	122
4.8.1 Experimental results for the control beams	122
4.8.2 Experimental results for the beams strengthened with UHPFRC layers.....	127
4.8.3 Experimental results for the beams strengthened with UHPFRC layers and dowels	134
4.8.4 Experimental results for the beams strengthened with UHPFRC layers and steel bars	141
4.8.5 Experimental results for the beams strengthened with jackets on three sides.....	149
4.8.6 Comparison of the experimental results for the different techniques.....	155
4.9 Conclusions.....	158
5. THE NUMERICAL MODELING OF ULTRA HIGH PERFORMANCE FIBER REINFORCED CONCRETE (UHPFRC).....	159
5.1 Introduction.....	159
5.2 Modeling of the materials	159
5.3 Validation of the numerical model	163
5.3.1 Initial beam prior to strengthening	163
5.3.2 Numerical modeling of the strengthened beams with UHPFRC layers	165
5.3.3 Numerical modeling of beams strengthened with UHPFRC layers and steel bars	170
5.3.4 Numerical modeling of the strengthened beams with jackets on three sides	173
5.4 Sensitivities Analysis	176
5.4.1 The effect of layer depth on the performance of the strengthened beams.....	176
5.4.2 Coefficients of monolithic behavior	184
5.4.3 The effect the tensile strength of UHFRC on the performance of the strengthened beams	186

5.4.4 The effect of shrinkage on the performance of the strengthened beams	188
5.4.5 Strengthening of RC beams using UHPFRC layers at the compressive side	189
5.4.6 Strengthening of existing RC beams with different configuration of the reinforcement.....	191
5.4.7 The effect of the amount of reinforcement at the UHPFRC layer	193
5.4.8 The effect of steel grade on the performance of the strengthened beams with UHPFRC layers and steel bars	195
5.4.9 Strengthening with various layer depths and various diameters of steel bars	197
5.4.10 Strengthening with jackets and steel bars.....	198
5.5 Conclusions.....	201
6. CONCLUSIONS AND FUTURE WORK.....	203
6.1 Conclusions.....	203
6.2 Future work.....	206
List of References	208

List of Tables

Table 3.1 Examined mixture designs

Table 3.2 Experimental results for the different mixture designs

Table 3.3 Experimental program for the different curing regimes

Table 3.4 Tensile and compressive results for the specimens placed in the water tank

Table 3.5 Tensile and compressive results for the specimens placed in the steam curing tank

Table 3.6 Experimental results for the different types of fibers

Table 3.7 Mixture designs for the preparation of the UHPFRC for the different fiber contents

Table 3.8 Experimental results for the different fiber contents

Table 3.9 Stress and strain values for the different fiber contents

Table 3.10 Stress and crack opening values for the different fiber contents

Table 3.11 Fracture energy for the different fiber contents

Table 3.12 Experimental results for the different depths of the prisms

Table 4.1 Coefficients of friction and cohesion obtained from the push-off tests

Table 4.2 Experimental program for the strengthening of existing full scale RC beams

Table 4.3 Mixture design of concrete

Table 4.4 Results of the compressive tests of the examined concrete mixture

Table 4.5 Results of the compressive tests of the examined UHPFRC mixture

Table 4.6 Measured roughness depths using the sand patch method

Table 4.7 Experimental results for the different strengthening techniques

Table 5.1 Yield and maximum load for the different layer depths and the different types of interface

Table 5.2 Coefficients of monolithic behavior

Table 5.3 Yield and maximum load for the different tensile strengths

Table 5.4 Numerical results for strengthening at the compressive and the tensile sides

Table 5.5 Numerical results for strengthening of a weaker existing RC beam

Table 5.6 Numerical results for different amounts of reinforcement of the layer

Table 5.7 Numerical results for the different steel grades

Table 5.8 Numerical results for the different diameters of the steel bars and the different layer depths

Table 5.9 Numerical results for strengthening with a three-side jacket and a three-side jacket with steel bars

List of Figures

Figure 2.1 Traditional techniques for the strengthening of RC structures: a) Strengthening with jackets, b) strengthening with jackets and shear walls, c) addition of shear walls, d) strengthening of joints

Figure 2.2 Strengthening with FRPs: a) Wrapping of a RC column, b) strengthening of columns with FRPs

Figure 2.3 Concrete versus HPC and UHPFRC mixture design

Figure 2.4 Experimental setup for the investigation of the tensile fracture properties of UHPFRC

Figure 2.5 Proposed tri-linear softening curve for the investigation of fracture mechanism of UHPFRC

Figure 2.6 Experimental setup for the investigation of the flexural performance and the fracture properties of UHPFRC

Figure 2.7 Retrofitting using UHPFRC

Figure 2.8 Proposed configurations for the composite concrete-UHPFRC elements

Figure 2.9 a) Rehabilitation of road bridge using UHPFRC, b) application of the UHPFRC using conventional equipment

Figure 2.10 a) Application of the UHPFRC on a crash barrier, b) rehabilitation of a bridge pier

Figure 2.11 Strengthening of an industrial floor pier

Figure 2.12 Testing setup for the push off tests

Figure 3.1 Preparation of the specimens: a) mixer used for the mixing the materials, b) dog bone shaped and cube specimens after casting and c) dog bone shaped and cube specimens after demolding

Figure 3.2 Dimensions of the dog bone shaped specimens

Figure 3.3 Experimental setup for: a) direct tensile tests, b) compressive tests

Figure 3.4 Stress-strain results for mixture U1 in tension

Figure 3.5 Stress-strain results for mixture U2 in tension

Figure 3.6 Stress-strain results for mixture U3 in tension

Figure 3.7 Stress-strain results for mixture U4 in tension

Figure 3.8 Stress-strain results for mixture U5 in tension

Figure 3.9 Average stress-strain results for the different examined mixture designs

Figure 3.10 Tensile stress-strain results for mixture U5 using cement 52.5 N type I

Figure 3.11 Comparison of the average tensile stress-strain results for the different types of cement

Figure 3.12 Results of the direct tensile tests three days after casting for: a) the specimens placed in the water tank, b) the specimens placed in the steam curing tank

Figure 3.13 Results of the direct tensile tests five days after casting for: a) the specimens placed in the water tank, b) the specimens placed in the steam curing tank

Figure 3.14 Results of the direct tensile tests seven days after casting for: a) the specimens placed in the water tank, b) the specimens placed in the steam curing tank

Figure 3.15 Results of the direct tensile tests ten days after casting for: a) the specimens placed in the water tank, b) the specimens placed in the steam curing tank.

Figure 3.16 Results of the direct tensile tests fourteen days after casting for: a) the specimens placed in the water tank, b) the specimens placed in the steam curing tank

Figure 3.17 Results of the direct tensile tests twenty-eight days after casting for: a) the specimens placed in the water tank, b) the specimens placed in the steam curing tank

Figure 3.18 Results of the direct tensile tests ninety days after casting for the specimens placed in the water tank

Figure 3.19 Average tensile stress-strain results at different time periods for the specimens placed in the water tank

Figure 3.20 Average tensile stress-strain results at different time periods for the specimens placed in the steam curing tank

Figure 3.21 Tensile strengths for the different curing conditions

Figure 3.22 Compressive strengths for the different curing conditions

Figure 3.23 Steel fibers retained from car tires

Figure 3.24 Experimental results for the direct tensile tests using 3% recycled steel fibers

Figure 3.25 Experimental results for the direct tensile tests using 6% recycled steel fibers

Figure 3.26 Comparison of the results for the different types of steel fibers

Figure 3.27 Measurement of the workability of UHPFRC: a) flow table used for the measurement of the workability, b) tamping of the UHPFRC, c) measurement of the flow diameter

Figure 3.28 Flow diameter results for the different fiber contents

Figure 3.29 Tensile stress-strain results for plain UHPC

Figure 3.30 Tensile stress-strain results for the specimens prepared with 1 % steel fibers

Figure 3.31 Tensile stress-strain results for the specimens prepared with 2 % steel fibers

Figure 3.32 Tensile stress-strain results for the specimens prepared with 3 % steel fibers

Figure 3.33 Tensile stress-strain results for the specimens prepared with 4 % steel fibers

Figure 3.34 Tensile stress-strain results for the specimens prepared with 6 % steel fibers

Figure 3.35 Average stress-strain results for the different fiber contents

Figure 3.36 Tensile strengths for the different fiber contents

Figure 3.37 Compressive strengths for the different fiber contents

Figure 3.38 a) Tensile stress-strain model for the specimens with 1 % steel fibers, b) tensile stress-strain model for the specimens with 2 % and 3 % steel fibers, c) tensile stress-strain model for the specimens with 4 % and 6 % steel fibers

Figure 3.39 Strain-hardening for the different fiber contents

Figure 3.40 Stress-crack opening model

Figure 3.41 Fracture energy related to the failure causes the crack

Figure 3.42 Experimental setup for the measurement of shrinkage

Figure 3.43 Results for the drying shrinkage of plain UHPC and UHPFRC with 3 % steel fibers

Figure 3.44 Geometry of the examined prisms

Figure 3.45 Preparation of prisms with different depths

Figure 3.46 Experimental results of the direct tensile tests

Figure 3.47 Experimental setup for the flexural testing of the: (a) 25 mm prisms, (b) 50 mm prisms, (c) 75 mm prisms and (d) 100 mm prisms

Figure 3.48 Characteristic failures of the: (a) 25 mm prisms, (b) 50 mm prisms, (c) 75 mm prisms and (d) 100 mm prisms

Figure 3.49 Load-deflection results for the prisms with a depth of: (a) 25 mm, (b) 50 mm, (c) 75 mm and (d) 100 mm

Figure 3.50 Results of the proposed model versus the experimental results

Figure 3.51 Experimental setup for the cyclic loading tests

Figure 3.52 Examined loading histories

Figure 3.53 Tensile stress-strain results for the specimens with 3% steel fibers

Figure 3.54 Experimental results for: a) loading history 1, b) loading history 2 and c) loading history 3

Figure 3.55 Modulus of elasticity degradation for: a) loading history 1, b) loading history 2 and c) loading history 3

Figure 3.56 Average curves of the modulus of elasticity degradation for all the loading histories

Figure 3.57 Degradation of the modulus of elasticity with the loading cycles

Figure 3.58 Stress-strain curve of UHPFRC under cyclic loading

Figure 3.59 Comparison of the average monotonic curve with the cyclic envelope curves

Figure 3.60 Validation of the proposed model using experimental results for: (a) loading history 1, (b) loading history 2 and (c) loading history 3

Figure 3.61 Stress-strain results of UHPFRC with 2% steel fibers under cyclic loading

Figure 3.62 Validation of the proposed model for 2% steel fibers

Figure 4.1 Preparation of specimens for the push-off tests: a) specimen with a rough interface, b) specimens without any preparation of their surface c) specimens after casting and d) specimens after demolding

Figure 4.2 a) Experimental setup and dimensions of specimens, b) the testing of specimens and c) specimens after testing

Figure 4.3 a) Shear stress versus interface slip for UHPFRC with 3% steel fibers and smooth interface, b) load versus interface slip for UHPFRC with 3% steel fibers and smooth interface, c) shear stress versus interface slip for UHPFRC with 3% steel fibers and rough interface, d) load versus interface slip for UHPFRC with 3% steel fibers and rough interface

Figure 4.4 Reinforced concrete beams

Figure 4.5 Strengthening with UHPFRC layers

Figure 4.6 Strengthening with UHPFRC layers and steel bars

Figure 4.7 Strengthening with three-side jackets

Figure 4.8 Strengthening with UHPFRC layers and dowels

Figure 4.9 Minimum required cover for the dowels based on the Greek Code for Interventions

Figure 4.10 a) Assembling of the reinforcement, b) preparation of the molds and the reinforcement and c) reinforcement in the molds ready for casting

Figure 4.11 a) Dry mixing of the materials, b) concrete ready to cast, c) beam after casting and d) beam after demolding

Figure 4.12 Experimental results of the direct tensile tests of UHPFRC over 2 months

Figure 4.13 a) Roughening of the surface with a pistol grip needle scaler, b) the surface after roughening, c) measurement of the roughness depth using the sand patch method

Figure 4.14 a) Preparation of molds, b) casting of the layers

Figure 4.15 Preparation of the strengthened beams with UHPFRC layers and dowels: a) drilling of the beam, b) the dowels in position and c) strengthened beam after casting

Figure 4.16 a) Preparation of specimen, b) strengthened beam after the demolding

Figure 4.17 Different phases of the preparation of a three-side jacket: a) beam after roughening, b) beam in the mold ready for casting and c) strengthened beam after the demolding

Figure 4.18 Experimental setup for the four point loading tests: a) distance between the two loading points and the span length and b) experimental setup for the control beams

Figure 4.19 Experimental setup for the beams strengthened with three-side jackets: a) experimental setup (side 1) and b) experimental setup (side 2)

Figure 4.20 (a) Distance between the two loading points, span length and position of the LVDTs in side 1 and (b) distance between the two loading points, span length and position of the LVDTs in side 2

Figure 4.21 Experimental setup for the beams strengthened with layers: a) experimental setup (side1), b) experimental setup (side 2) and c) LVDT used for the measurement of slip

Figure 4.22 Load versus deflection for beam P1

Figure 4.23 Different phases during the testing of beam P1: a) appearance of the first flexural cracks, b) propagation of the cracks, c) the failure on both the compressive and the tensile sides and d) the beam at the end of the test

Figure 4.24 Load versus deflection for beam P2

Figure 4.25 Different phases during the testing of beam P2: a) appearance of the first flexural cracks, b) propagation of the cracks, c) the failure on both the compressive and tensile sides and d) the beam at the end of the test

Figure 4.26 Average load versus deflection curve for beams P1 and P2

Figure 4.27 Load versus deflection for beam U1

Figure 4.28 Testing of beam U: a) appearance of the first flexural cracks during the test, b) propagation of the cracks and beginning of local de-bonding, c) failure on both the compressive and tensile sides and d) the de-bonding at the interface

Figure 4.29 Load versus deflection for beam U2

Figure 4.30 a) Load versus slip in different positions for beam U2 and b) slip versus the distance from the supports

Figure 4.31 Testing of beam U2: a) appearance of the first cracks, b) propagation of the cracks, c) failure on both the tensile and compressive sides and d) the beam at the end of the test

Figure 4.32 Average load versus deflection curve for beams U1 and U2

Figure 4.33 Load versus deflection for beam D1

Figure 4.34 a) Load versus slip in different positions for beam D1 and b) slip versus the distance from the support for beam D1

Figure 4.35 Different phases during the testing of beam D1: a) appearance of the first cracks, b) failure of beam on both the compressive and tensile sides and c) beam at the end of the test

Figure 4.36 Load versus deflection for beam D2

Figure 4.37 a) Load versus slip in different positions for beam D2, b) slip versus the distance from the support for beam D2

Figure 4.38 Different phases during the testing of beam D2: a) appearance of the cracks, b) the failure of the beam on both the compressive and tensile sides and c) failure mode at the end of the test

Figure 4.39 Average load versus deflection curve for beams D1 and D2

Figure 4.40 Load versus deflection for beam UB1

Figure 4.41 a) Load versus slip in different positions for beam for beam UB1 and b) slip versus the distance from the support for beam UB1

Figure 4.42 Different phases during the testing of beam UB1: a) appearance of the cracks, b) failure on the compressive side and the propagation of cracks on the UHPFRC layer and c) failure mode at the end of the test

Figure 4.43 Load versus deflection for beam UB2

Figure 4.44 a) Load versus slip in different positions of beam UB2 and b) slip versus the distance from the support for beam UB2

Figure 4.45 Testing of beam UB2: a) appearance of the first cracks, b) propagation of the cracks and c) failure on the compressive side and starting of failure on the UHPFRC layer

Figure 4.46 Average load versus the deflection curve for beams UB1 and UB2

Figure 4.47 Load versus deflection for beam 3SJ1

Figure 4.48 Testing of beam 3SJ1: a) formation of the first cracks, b) propagation of the cracks, c) the failure of the beam and d) the crucial crack for the failure of beam

Figure 4.49 Load versus deflection for beam 3SJ2

Figure 4.50 Different phases during the testing of beam 3SJ2: a) formation of the cracks, b) starting of the failure of the jacket, c) failure of mode of beam 3SJ2 at the failure and d) beam at the end of the test

Figure 4.51 Average load versus deflection curve for beams 3SJ1 and 3SJ2

Figure 4.52 Average load versus deflection curves for all the different techniques

Figure 4.53 Average stiffness of all the examined specimens

Figure 4.54 Maximum values of slips for the different specimens

Figure 5.1 Constitutive model in tension and compression adopted in ATENA software

Figure 5.2 Stress-strain model of the reinforcement

Figure 5.3 Bond-slip model based on the CEB-FIP model code 1990

Figure 5.4 Interface behavior in: a) shear, b) tension

Figure 5.5 Tensile function adopted in ATENA

Figure 5.6 Geometrical model used for the finite element analysis of the initial beams

Figure 5.7 Numerical versus experimental results for the initial beam

Figure 5.8 Crack pattern and strain distribution of the existing RC beam: a) at the first crack load, b) at the maximum load and c) strain distribution at the reinforcement at the maximum load

Figure 5.9 Geometrical model used for the finite element analysis of the strengthened beams with UHPFRC layers

Figure 5.10 Numerical versus experimental results for the beams strengthened with UHPFRC layers for a non-monolithic connection at the interface

Figure 5.11 Crack pattern and strain distribution of the existing RC beam strengthened with an UHPFRC layer and a non-monolithic connection at the interface: a) at the first crack load, b) at the maximum load and c) strain distribution at the reinforcement at the maximum load

Figure 5.12 Numerical versus experimental results for the beams strengthened with UHPFRC layers assuming a monolithic connection at the interface

Figure 5.13 Crack pattern and strain distribution of the strengthened beams with UHPFRC layers considering a monolithic connection at the interface at: a) the first crack load, b) the maximum load and c) strain distribution at the reinforcement at the maximum load

Figure 5.14 Geometrical model used for the modeling of the strengthened beams with UHPFRC layers and steel bars in ATENA

Figure 5.15 Numerical versus experimental results for the strengthened beams with UHPFRC layers and steel bars

Figure 5.16 Crack pattern and strain distribution of the existing RC beam strengthened with UHPFRC layer and steel bars: a) at the first crack load, b) at the maximum load and c) strain distribution at the reinforcement at the maximum load

Figure 5.17 Geometrical model used for the numerical modeling of the beams strengthened with three-side jackets

Figure 5.18 Numerical versus experimental results for the beams strengthened with three-side jackets

Figure 5.19 Crack pattern and strain distribution of the existing RC beam strengthened with a three-side jacket: a) at the first crack load, b) at the maximum load and c) strain distribution at the reinforcement at the maximum load

Figure 5.20 Crack pattern and strain distribution of the existing RC beam inside the jacket: a) at the first crack load and b) at the maximum load

Figure 5.21 Numerical results for the load and the deflection for the different layer depths and a non-monolithic connection at the interface

Figure 5.22 Increase of the load (%) for increasing layer depths

Figure 5.23 Crack pattern and strain distribution of the existing RC beam strengthened with a 30 mm layer at the tensile side for a non-monolithic connection at the interface: a) at the first crack load, b) at the maximum load and c) strain distribution at the reinforcement at the maximum load

Figure 5.24 Crack pattern and strain distribution of the existing RC beam strengthened with a 70 mm layer at the tensile side for a non-monolithic connection at the interface: a) at the

first crack load, b) at the maximum load and c) strain distribution at the reinforcement at the maximum load

Figure 5.25 Numerical results for the load and the deflection for the different layer depths for a monolithic connection at the interface

Figure 5.26 Increase of the load (%) for increasing layer depths for a monolithic connection at the interface

Figure 5.27 Crack pattern and strain distribution of the existing RC beam strengthened with a 30 mm layer at the tensile side and a monolithic connection at the interface: a) at the first crack load, b) at the maximum load and c) strain distribution at the reinforcement at the maximum load

Figure 5.28 Crack pattern and strain distribution of the existing RC beam strengthened with a 70 mm layer at the tensile side and a monolithic connection at the interface: a) at the first crack load, b) at the maximum load and c) strain distribution at the reinforcement at the maximum load

Figure 5.29 Comparison of the performance of a strengthened and a monolithic member

Figure 5.30 Performance of strengthened RC beams with layers with different tensile strengths

Figure 5.31 Numerical results for strengthened beams with UHPFRC layers at the tensile side for different values of shrinkage

Figure 5.32 Numerical results for the existing RC beam and the beam strengthened with a layer at the compressive side

Figure 5.33 Crack pattern and strain distribution of the existing RC beam strengthened with a layer at the compressive side: a) at the first crack load, b) at the maximum load and c) strain distribution at the reinforcement at the maximum load

Figure 5.34 Reinforcement of the weaker existing RC beam

Figure 5.35 Load versus deflection results for the weaker existing RC beam and the strengthened beam

Figure 5.36 Load versus deflection results for the different diameters of steel bars of the UHPFRC layer

Figure 5.37 Load increase for increasing amounts of reinforcement

Figure 5.38 Load versus deflection results for the different steel grades

Figure 5.39 Load versus deflection results for different layer depths and different diameters of steel bars

Figure 5.40 Strengthening with a three-side jacket and steel bars

Figure 5.41 Load versus deflection results for the strengthened beams with a three-side jacket and a three-side jacket and steel bars

Figure 5.42 Crack pattern and strain distribution of the existing RC beam strengthened with a three-side jacket and steel bars: a) at the first crack load, b) at the maximum load and c) strain distribution at the reinforcement at the maximum load

List of Symbols

Latin Lower Case Symbols

b: width of the specimens

c: adhesion factor

c_1 : the depth of the neutral axis

d_b : diameter of dowel

d: depth prisms

d_1 : the effective flexural depth of the section

f_t : maximum stress

f_m : maximum load

f_0 : first crack load

f_{op} : stress at any point at the descending part of the stress-strain curve

f_u : flexural strength

f_t' : maximum stress at the reloading curve

$f_{0,p}$: stress at the end of the hardening branch

f_{yd} : design value for the yield stress of steel

f_{cd} : design value of the compressive strength of concrete

f_{ck} : characteristic compressive strength of the concrete

f_{ctd} : design tensile strength of concrete

$f_{y, str}$: resistance of the strengthened member at the yield load

$f_{y, mon}$: resistance of the monolithic member at the yield point

h : cross section height

l_f : length of steel fibers

n : number of loading cycles

t : depth of concrete

w : crack opening

w_u : crack opening up to the complete separation

w_m : permanent crack opening

Latin Upper Case Symbols

A_s : cross section area of bars

A_f : crack fracture area

E_0 : modulus of elasticity

$E_{0, hard}$: second modulus of elasticity

E_{pl} : modulus of elasticity at the end of the unloading curve

E_s : modulus of elasticity of steel

$E_{0'}$: initial tangent modulus of elasticity at the beginning of the reloading curve

E_n : modulus of elasticity after n cycles

F_t : load applied in tension

G : fracture energy

G_a : dissipated energy during the strain-hardening phase

G_b : dissipated energy during the strain-softening phase

K_f : coefficient of monolithic behavior based on the resistance at the yield load

K_{str} : stiffness of the strengthened member

K_{mon} : stiffness of the monolithic member

K_r : coefficient of monolithic behavior based on the maximum resistance

K_k : coefficient of monolithic behavior based on the stiffness

$K_{\theta,y}$: coefficient of monolithic behavior based on deformation at the yield load

$K_{\theta,u}$: coefficient of monolithic behavior based on deformation at the maximum load

L : effective span length of prism specimens

P : flexural load

S : the slip at the interface

Q : dissipated work needed for the generation of a crack

Greek Symbols

γ_m : safety coefficient

δ_{un} : damage at the unloading point

$\delta_{y,\text{str}}$: deformation of the strengthened beam at the yield load

$\delta_{y,\text{mon}}$: deformation of the monolithic beam at the yield load

$\delta_{u,\text{str}}$: deformation of the strengthened beam at the maximum resistance

$\delta_{u,\text{mon}}$: deformation of the monolithic beam at the maximum resistance

ϵ_0 : strain at the end of the elastic state

ϵ_{cu} : the maximum useable compressive strain

ϵ_t : strain at the maximum stress

ϵ_{op} : strain at any point on the descending part of the stress-strain curve

ϵ_{pl} : residual strain for the unloading curve

ϵ_{un} : unloading axial strain

ϵ_t' : strain for the respective maximum stress at the descending curve

ϵ_0' : the respective maximum axial strain for the tangent modulus of elasticity

ϵ : strain at any point in the linear state

$\epsilon_{0,1}$: strain at the end of the hardening branch of the proposed stress-strain model

ϵ_s : strain of the reinforcement

ϵ_y : yield strain of the reinforcement

τ : bond strength

τ_u : shear strength at the interface

μ : coefficient of friction

σ : any value of stress

σ_N : external vertical to the interface stress

ρ_s : ratio of the reinforcement to the cross section dimensions

Acknowledgements

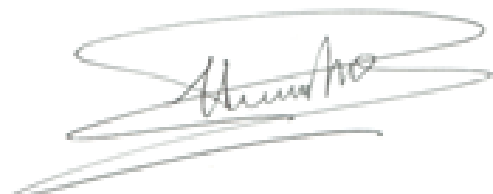
First of all, I would like to express my sincere gratitude to my first supervisor Dr Andreas Lampropoulos for given me the opportunity to work on this research project and also for his patience and motivation. During these years of my PhD, he supported me with all his power and he did his best to create the best working environment for me. His support was very important for me and i feel really grateful for having the opportunity to collaborate with him.

I would like also to express my gratitude to my supervisors, Professor Neil Ravenscroft and Dr Pierfrancesco Cacciola for their support and guidance during these years. Also, I would like to thank the Doctoral College and the School of Environment and Technology of the University of Brighton, and all the people who are involved, for providing me the best working environment. My sincere gratitude also goes to Dr David Pope for his support during the experimental work of my thesis and to Dr Demetres Nicolaides for his guidance during the first steps of my research.

Finally, I would like to thank my father Athanasios, my mother Maria and my sister Danae. In a difficult period for me, they support me with all their power and with every possible way. Without their support I would not be able to complete my PhD.

Declaration

I declare that the research contained in this thesis, unless otherwise formally indicated within the text, is the original work of the author. The thesis has not been previously submitted to this or any other university for a degree, and does not incorporate any material already submitted for a degree.

A handwritten signature in black ink, appearing to read 'Spyridon A. Paschalis', is written over a large, light-colored scribble or smudge.

Spyridon A. Paschalis

Date 18-10-2017

1. INTRODUCTION

1.1 Research significance

The safety of structures is of high importance affecting people's lives. Even though at present there are several methods for the strengthening of Reinforced Concrete (RC) structures, the drawbacks of existing techniques make the decision for the strengthening of existing structures difficult. Hence, the main drawbacks of existing techniques are mainly related to the ease of preparation and application, the high cost, the total time taken to be applied and the disturbance on the occupancy even though relocation is also possible. Finally, in most of the traditional techniques, trained staff is required for the application of the technique (Fardis and Dritsos, 2003). The present research, with the proposal of a new innovative technique for the strengthening of RC structures, aims to take the research in the field of the strengthening of RC structures one step further, to increase the safety level of existing structures and to protect people's lives.

In the present research, an innovative technique for the strengthening of existing RC structures using an advanced material such as Ultra High Performance Fiber Reinforced Concrete (UHPFRC) is investigated. The strengthening of structures is a field which can find application, first of all, in old structures. Most of the new structures which are built currently have a high safety level. However, it is not possible to make the same claim for old structures. An important parameter which should be taken into consideration in is that many old structure were designed without any regulations, or are based on those which have proved to be inadequate (Fardis and Dritsos, 2003). Also, it should considered that a large number of structures built in the past have reached the end of their service life. In many cases, they are used for a different purpose to their original design specification.

Finally, another important parameter which should be taken into consideration is that these structures built in the past make up the majority of the total number of existing structures today. For example, in Greece which is a high seismic risk area, it is estimated that more than 70% of the total number of existing structures were built before 1985 (Technical Chamber of Greece, 2017), period when the regulations which were in force have been proved to be inadequate. Consequently, structural evaluation of these structures is considered necessary. It is worth mentioning that as high seismic risk area can be defined an area with a history of a

major seismicity. The seismic risk on the other hand is defined by the combination of the vulnerability of structures to damages, as well as to people's lives and the economic impact.

Strengthening of RC structures is a crucial issue in high seismic risk areas. Existing structures may have undergone an earthquake with unknown effects. The effects of an earthquake can be devastating in many ways. Hence, earthquakes can affect peoples' lives and can also have an economic impact. The cost of lost property, expenses from medical care through injury, lost income from damaged buildings or expenses if relocation is necessary are some examples of the economic impact from an earthquake. Finally, the strengthening of structures can find application on existing structures which have been submitted to accidental actions during their service life, and in which case their load carrying capacity system needs to be upgraded.

At present, there are several methods for the strengthening and retrofitting of RC structures with different objectives. Some of the most popular methods include the construction of RC layers and jackets, the addition of structural elements, such as braces and shear walls, and the use of Fiber Reinforced Polymers (FRPs). The addition of structural elements is a reliable method which can increase the strength, the stiffness or the ductility of the structure but also presents significant disadvantages (Fardis and Dritsos, 2003). Therefore, it is a method which requires a great deal of time for its application alongside the necessity for trained staff to implement it. Also, the addition of new RC layers and jackets changes the geometry of the elements and consequently the overall behavior of the structure. Finally, a relocation of the occupants is also possible, which has a high economic impact.

Strengthening with FRPs is a popular method which is not time consuming, nor a change in the geometry of the strengthened elements; yet it is able to increase the load carrying capacity of the strengthened members. However, this method also presents crucial disadvantages. Therefore, FRPs have different characteristics from concrete where de-bonding is possible. Also, the FRP do not present ductility and for correct application of the material, experienced and trained staff is required (Triantafillou, 2004). The FRPs present also crucial disadvantages which are related to the use of epoxy resins. More specifically, the main drawbacks of the FRPs are related to the high cost, the difficulty to apply on wet surfaces or at low temperatures, the low permeability to water vapour and the poor behavior at high temperatures.

The disadvantages of existing methods, together with the development of new advanced materials with enhanced properties, make the proposal of new techniques for the strengthening and retrofitting of RC structures necessary. Research in the field of

strengthening of RC structures is now focused on novel techniques which combine strength, cost effectiveness, ease and speed of preparation and application. The present research is focused on an innovative technique for the strengthening of RC structures, using an advanced material, such as UHPFRC.

The main benefit of the proposed technique is the superior mechanical properties of the UHPFRC compared to conventional materials and also the speed and ease of preparation and application of the material. Another important benefit is that for the preparation and the application of UHPFRC only simple tools need to be used. In cases that the addition of layers or jackets, without extra reinforcement is concerned, this is a significantly easier method to apply compared to traditional techniques. These parameters can reduce the total time which is required for the application of the technique and also the total cost. On the contrary, when additional reinforcement is required, a procedure similar to conventional techniques should be followed for the application of the technique. Another important aspect of this technique is that the characteristics of UHPFRC, such as the modulus of elasticity, are close to the characteristics of concrete. Additionally, thin UHPFRC layers with high strength and ductility can be constructed. Consequently, the geometry of the strengthened elements does not change dramatically. Based on existing studies in UHPFRC (Lampropoulos et al., 2015) thin UHPFRC elements can be constructed for the strengthening of RC elements. In the present research, the performance of RC beams strengthened with UHPFRC layer with a layer depth of 3 cm will be investigated numerically. This depth is significantly lower compared to the layer depths which are normally used for RC jackets. Based on the instructions of the Technical Chamber of Greece (2004), a layer depth of at least 7-10 cm should be used for the construction of RC jackets or layers. This layer depth can change the geometry of the elements dramatically. Finally, another benefit of the examined technique is that due to the big volume of fibers in the mixture, the shrinkage of UHPFRC is less significant, which is also a benefit of the examined technique.

The aim of the present research is to investigate the effectiveness of UHPFRC as a strengthening material. This has been achieved through an extensive experimental investigation. More specifically, RC beams have been strengthened with layers and jackets using different strengthening configurations, and the effectiveness of each configuration has been examined experimentally. An objective of the present research is the investigation of crucial parameters of the material, which are missing from the literature, and are required for the application of the material for strengthening purposes. Also, the present research focuses

on the development of an optimum mixture design which can be used for strengthening applications. A further objective is the investigation of the interface characteristics between UHPFRC and concrete. Hence, a study of the interface between UHPFRC and concrete has been conducted through push-off tests, while measurements for the slips at the interface between UHPFRC and concrete have been recorded. Finally, another objective of the present research is to investigate crucial parameters which are required for the design of the examined technique, and how these parameters affect the performance of the technique. Within the design, there are a number of parameters which should be taken into consideration such as; the depth of the layer, the fiber content, the grade and the amount of reinforcement of the layers. Before the application of the technique, it is of high importance that an optimum decision for the design of the material and the examined technique is taken. Hence, in the present research, a numerical model which can predict the behavior of composite UHPFR-concrete elements has been developed, a sensitivity analysis has been conducted, and all these crucial parameters which affect the performance of the examined technique have been analysed.

1.2 Methodology and structure of the present research

1.2.1 Methodology

The present research investigates an innovative technique for the strengthening of RC structures using an advanced material such as UHPFRC. The effectiveness of the examined technique is investigated through an extensive experimental and numerical investigation. The experimental investigation of the present research is, firstly, focused on the mechanical properties of the UHPFRC. Crucial parameters which are related to the mechanical properties of the material are investigated first. Based on the experimental results of this research, an optimum mixture design is proposed, which is adopted for the strengthening of existing RC beams. The next step of the present research is the realistic application of the material for the strengthening of existing RC elements. In order to obtain reliable results, testing of RC beams is conducted. Additionally, the optimum strengthening configuration using UHPFRC is investigated. Finally, certain important parameters concerning the design of the examined technique are investigated numerically.

1.2.2 Structure of the present thesis

The structure of the present thesis is as follows: the first chapter is an introduction to the present research and presents the research significance and the methodology used. The second chapter presents the most important studies on UHPFRC, and also, the existing methods for strengthening of RC structures. This chapter aims to identify the knowledge gaps in UHPFRC and within the strengthening techniques relevant to this research. The third chapter is focused on the experimental investigation into the mechanical properties of the UHPFRC under static and cyclic loading which are missing from the literature, and the optimization of the material. Hence, an optimum mixture design is adopted for the application of the material for the strengthening of RC elements. The next step of the present research is the application of the UHPFRC for the strengthening of RC beams. Therefore, RC beams were constructed and strengthened with additional UHPFRC layers and jackets using different strengthening configurations. The performance of the strengthened beams for the different configurations has been evaluated, and a comparison is presented. An additional study has also been conducted on the interface behavior between concrete and UHPFRC through push-off tests. In chapter five, a finite element model, which has been validated according to the experimental results of a full-scale beam testing, has been developed, and certain significant parameters of the examined technique have also been investigated numerically. Finally, in the last chapter, the conclusions of the present research are presented together with suggestions for further research.

2. LITERATURE REVIEW

2.1 Introduction

In the present chapter, the literature review in UHPFRC is presented. The first part of the present chapter is focused on the presentation of existing techniques for the strengthening of RC structures together with the state-of-the-art in the field. The second part is focused on the presentation of the most important studies in UHPFRC and the applications of the material for repair and strengthening purposes. The present chapter aims, first of all, to identify the knowledge gaps in UHPFRC and the applications of the material for strengthening purposes and to address these gaps in the following chapters. Also, another aim is to obtain all these useful information in the literature which can be used for the purposes of the present research.

2.2 Existing methods for the strengthening and retrofitting of reinforced concrete structures

Traditional techniques for the strengthening and retrofitting of Reinforced Concrete (RC) structures are based on the addition of new structural elements. Once the decision for strengthening is taken, an important aspect to consider is which method is applied. Therefore, one option would be to increase the capacity of the structure to carry the loads as a whole (global strengthening) or alternatively to strengthen the weakest members (local strengthening). Usually, the first option is chosen in cases that there are many weak elements in the structure which need to be strengthened, and the second, in cases that only few members need to be strengthened (Fardis and Dritsos, 2003). In Figure 2.1, traditional techniques for strengthening of RC structures, are presented.



(a)



(b)



(c)

(d)

Figure 2.1 Traditional techniques for the strengthening of RC structures: a) Strengthening with jackets, b) strengthening with jackets and shear walls, c) addition of shear walls, d) strengthening of joints (University of Patras, 2013)

Methods based on the addition of structural elements aim to increase the strength, the stiffness and the ductility of the structure. A popular method includes the addition of braces, which improves primarily the stiffness and the ductility of the structure, and also achieves a moderate increase in the strength. Shear walls in the frames of the structure, are used to increase the stiffness and the strength of the structure. Another strengthening technique, which concern the global strengthening, is the construction of walls connected with the existing columns. This method increases mainly the stiffness and the ductility of the existing members. The construction of jackets is mainly preferred for columns and aims to increase the ductility of the element (Fardis and Dritsos, 2003).

A popular method for the strengthening of RC structures, includes the use of Fiber Reinforced Polymers (FRPs). One of the main benefits of this technique is the ease of application, as well as, the fact that it does not affect the stiffness and the dynamic properties of the structure. Additionally, this technique also can increase the capacity for deformation (Triantafillou, 2004). In Figures 2.2a and 2.2b applications of FRPs for the strengthening of RC columns is presented.



(a)

(b)

Figure 2.2 Strengthening with FRPs: a) Wrapping of a RC column, (Balsamo et al., 2012), b) strengthening of columns with FRPs (Balsamo et al., 2012)

The last decade a cement-based composite material, named textile-reinforced mortar (TRM), has been developed and used for strengthening applications. This material consists of high-strength carbon, basalt or glass fibers embedded into inorganic materials such as cement-based mortars. The main advantages of the TRM are the resistance to high temperatures, the low cost, the ability to be applied in low temperatures or on a wet surface, the permeability to water vapour, and also the compatibility with concrete substrates (Raouf et al., 2017).

Bournas et al. (2009), presented an experimental study on the effectiveness of TRM jackets for the seismic retrofitting of RC columns with continuous and lap-sliced deformed bars. The effectiveness of the examined technique was also compared with the effectiveness of FRP jackets. The experimental results indicated that the retrofitting with TRM jackets is an effective method and the cyclic deformation capacity of the strengthened elements was increased, while the buckling of the steel bars was also delayed. Additionally, it was found that the splitting bond failure in columns with lap-spliced bars was prevented. Finally, compared to strengthening with FRPs, it was found that this is an equally effective technique, as both the strength and the deformation capacity were increased.

Tetta et al. (2016), presented a study on the performance of TRM and FRP jackets for the shear strengthening of beams. In this study two different types of beams were examined; medium-scale rectangular beams, and full scale T beams. All the specimens subjected to ambient and high temperatures. Crucial parameters which were investigated in the study of the medium-scale beam were the performance of the matrix, the level of temperature to which

the specimens were exposed, the strengthening configuration, the number of layers and properties of the textile. In the full scale beams, the effectiveness of non-anchored and anchored TRM jackets in shear strengthening at high temperature was investigated. From the experimental results it was deduced that TRM jackets are more effective compared to FRP jackets for increasing the shear capacity at high temperatures. Also, it was found that the strengthening configuration affects the shear capacity of the TRM and FRP jackets at high temperatures. More specifically, it was found that the most effective configuration was the fully-wrapping, followed by the U-wrapping and side-bonding. Another important finding of this study was that the number of layers affects the failure mode of side-bonding and U-wrapping at high temperatures. On the contrary, the number of layers did not affect the shear capacity and the failure mode of the side bonding and U-wrapping of the FRP jackets. Finally, it was found that the use of anchors increased the effectiveness of the TRM jackets.

Tetta et al. (2016), investigated the effectiveness of TRM jackets for the shear strengthening of full scale RC T-beams. In this study, textile based anchors were used as anchorage systems of the jackets. The parameters which were investigated in this study were the effectiveness of the textile based anchors, the number of TRM layers, the material properties and the strengthening system. The experimental results indicated that the use of textile-based anchors increased the effectiveness of TRM jackets significantly, while the shear capacity of the strengthened beams was increased proportionally for increasing number of layers. Another important finding was that the different textile geometries in non-anchored jackets, with the same amount of reinforcement, had as result the same increase of the capacity. Finally, it was concluded that TRM jackets can present the same effectiveness as the FRP jackets in terms of the shear capacity of the full scale RC T-beams.

Raouf et al. (2017), presented a comparison between the effectiveness of TRM and FRPs, for the flexural strengthening of RC beams. In this study, parameters such as the number of TRM and FRP layers, the textile surface conditions, the textile fiber material and the end anchorage system of the external reinforcement were investigated. The experimental results indicated that the TRM was not as effective as the FRP for the flexural strengthening of the RC beams, with the effectiveness ratio varying from 0.46 to 0.8. Also, it was found that when the number of the TRM layers was increased from one to three the effectiveness of TRM versus the FRP was increased by 100%. Additionally, it was found that the coating to the dry textile had as a result a higher effectiveness for the TRM while the failure mode was also different. On the other hand, the use of different textile material with the same stiffness, had as a result different

increase of the flexural capacity. Finally, another finding of this study was that the end-anchorage did not affect the performance of TRM-retrofitted beams.

2.3 Development of cementitious materials

During the last decades, research has focused on the improvement of the compressive strength of concrete. Consequently, cement based materials with compressive strength higher than 200 MPa are now available (AFGC-SETRA, 2013). This has been achieved with the improved microstructure of the material. These types of materials are known as High Performance Concretes (HPC) and Ultra High Performance Concretes (UHPC). However, the main disadvantage of these concretes remain the brittle behaviour and the low tensile strength. Therefore, fibers have been incorporated in the mixture and new ductile materials with high tensile strength, such as Ultra High Performance Fiber Reinforced Concrete (UHPFRC), are now available.

The main differences between UHPFRC, HPC and concrete are related to the microstructure of the materials. In the mixture of UHPFRC there are not any coarse aggregates. Therefore, silica sand with particle size of less than 500 μm is used for the preparation of the UHPFRC. This has as a result the improved homogeneity of the mixture. The extremely fine particles of silica fume, have as a result the improved density and fluidity of the mixture and also the reduction of the voids. The steel fibers on the other hand, improve the tensile strength and the ductility of the material. The water/cement ratio of the UHPFRC is significantly lower and superplasticizer is added in the mixture to secure the workability. Also, the incorporation of high volume of fibers in the mixture, has as a result a ductile behavior of the material. Finally, in the UHPFRC, Ground Granulated Blast Furnace Slag (GGBS) is used in the mixture as part replacement of cement. In Figure 2.3 a comparison between a typical UHPFRC, HPC and a concrete mixture is presented.

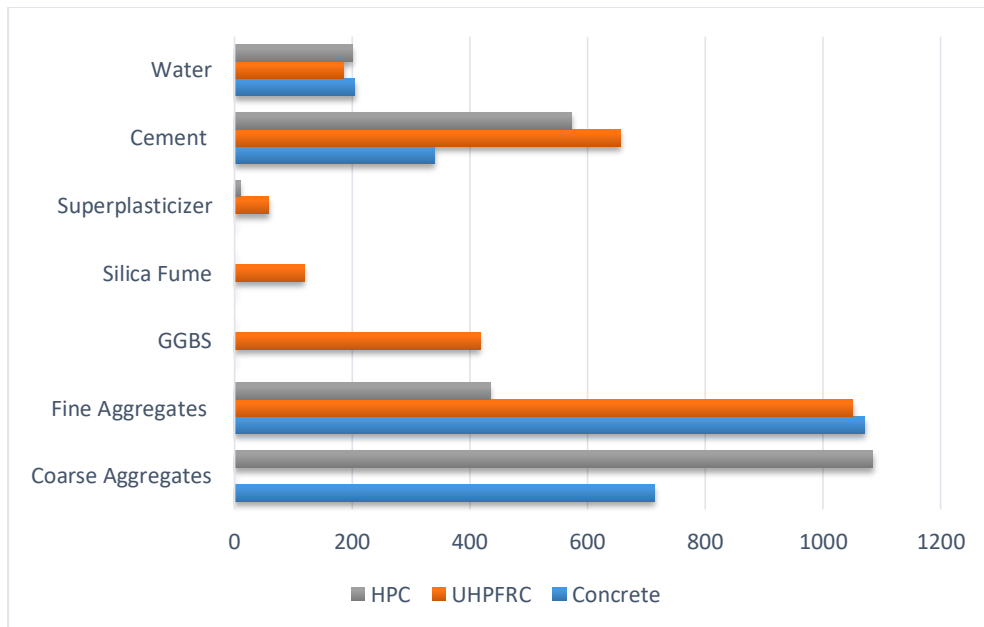


Figure 2.3 Concrete versus HPC and UHPFRC mixture design

2.4 Existing knowledge and applications of UHPFRC

In the present section the most important studies in the investigation of the properties of UHPFRC and the application of the material for strengthening purposes are presented. In the literature there are number of studies on the investigation of the mechanical properties of UHPFRC. Hassan et al. (2012), investigated the tensile and compressive behavior of UHPFRC experimentally. For the investigation of the effect of steel fibers on the tensile and compressive characteristics of UHPFRC, specimens with and without fibers were prepared. For the investigation, dog-bone shaped specimens and cylinder specimens were used for the investigation of the tensile and the compressive characteristics of the material. From the experimental results it was found that the tensile strength of the specimens with steel fibers was increased by 100% compared to specimens without fibers. Additionally, the ductility in tension and compression was improved. On the other hand, the modulus of elasticity and the compressive strength of the material were not affected.

The performance of UHPFRC is highly affected by the amount of fibers in the mixture. Kang et al. (2010), investigated the fracture properties of UHPFRC for different fiber contents. The tensile fracture properties of the material were investigated through three point loading tests. For this investigation notched specimens with dimensions 100x100x400 mm were used, while two Linear Variable Differential Transformers (LVDTs) were placed on both sides of the

prisms for the measurement of the deflection. Finally, the crack width was measured with a clip gauge, which was placed at the bottom of the specimens (see Figure 2.4).

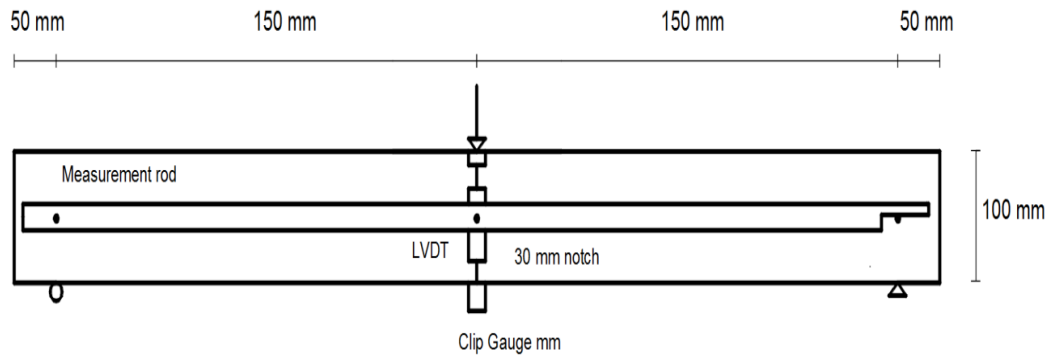


Figure 2.4 Experimental setup for the investigation of the tensile fracture properties of UHPFRC (Kang et al., 2010)

Five groups with fiber contents ranging between 1% and 5% were investigated in this study. From the experimental results the researchers concluded that there is a linear relationship between the increase of the volume ratio of the fibers and the flexural tensile strength. Due to the fact that fiber contents higher than 5% were not investigated in this study, the upper limit of this relationship is for fiber contents up to 5%. For the investigation of the fracture mechanism of UHPFRC, inverse analysis was conducted and a tri-linear softening curve was proposed. The tri-linear curve is illustrated in Figure 2.5. In this figure, three branches can be distinguished. The first is the softening branch, which is characterized by a crack opening and a reduction of the cohesive stress. The second branch is characterized by a bridging plateau, followed by a third softening branch.

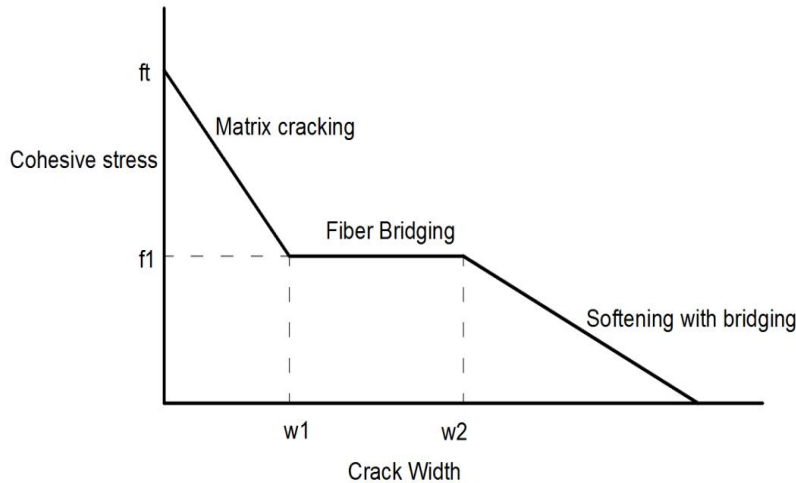


Figure 2.5 Proposed tri-linear softening curve for the investigation of fracture mechanism of UHPFRC (Kang et al., 2010)

Yoo et al. (2013), investigated the effect of fiber content on the properties of UHPFRC. From the investigation of the compressive strength of the material it was found that the maximum compressive strength was achieved using 3% per volume steel fibers. For higher fiber contents the compressive strength was reduced. This was attributed to the non-homogenous distribution of the fibers in the mixture. The fracture properties and the flexural performance of UHPFRC were also investigated in this study. Notched prism specimens, with dimensions 100x100x400 mm, were prepared and flexural tests were conducted. The deflection was measured using two LVDTs, and the crack width was measured with a clip gauge as illustrated in Figure 2.6.

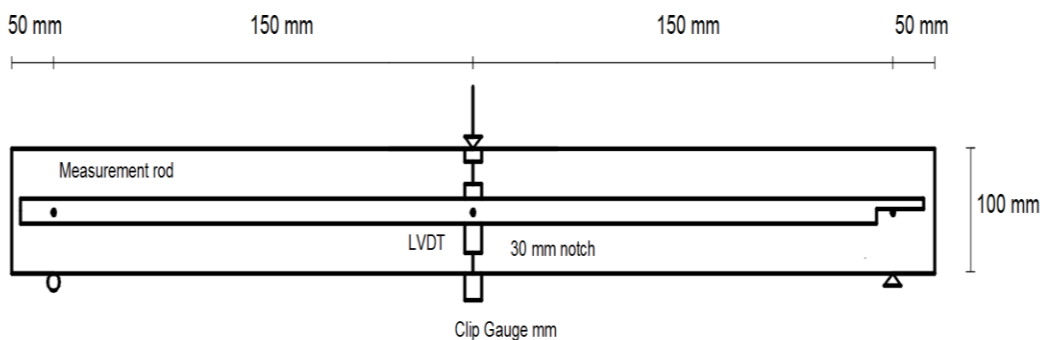


Figure 2.6 Experimental setup for the investigation of the flexural performance and the fracture properties of UHPFRC (Yoo et al., 2013)

From the experimental results the researchers found that the peak load was increased for increasing fiber content. On the contrary, after the maximum load and at the softening region, the ductility was reduced. Also, the initial stiffness was not affected by the different fiber contents. Finally, another finding of this study was that the specimens prepared with 4% steel fibers exhibited higher flexural strength compared to specimens with 3% steel fibers and despite the fact that the specimens with 4% steel fibers exhibited lower compressive strength. This was attributed to the ability of fibers to optimize the post crack behaviour of UHPFRC.

The orientation and distribution of fibers in the mixture are important parameters affecting the mechanical properties of UHPFRC. Kang and Kim (2011), investigated the effect of the fiber orientation on the tensile characteristics of UHPFRC. The tensile behavior was investigated in two phases. The first was the pre-cracking state and the second was the post cracking state. From the analytical and experimental investigation of the material in the first state, it was observed that the behavior was not affected by the distribution of the fibers. Consequently, the study was focused on the post-cracking state. For this investigation two concrete placing directions were investigated; parallel and transverse to the tensile direction of the specimens. From the direct tensile tests, the researchers concluded that the specimens prepared with the different fiber orientations presented different behavior. More specifically, it was observed that the specimens which were cast parallel to the tensile direction, presented better performance. In this study also, the fiber orientation was examined with captured digital images. From these images it was observed that the fibers of the specimens which were cast parallel to the tensile direction, were more uniformly dispersed.

The importance of fiber distribution was also highlighted by Ferrara et al. (2011). In this study, it was shown that the orientation of the steel fibers can be controlled through a well balanced fresh state and a suitable casting process. For the investigation of effect of fiber orientation on the performance of the UHPFRC, slabs with the same sizes but different flowing directions were cast. From these slabs, beam specimens were obtained with their axis parallel and perpendicular to the flow direction. From the experimental results it was evident that the orientation of fibers affected the performance of the material. Hence, the optimum performance was achieved from the specimens with a fiber alignment parallel to the flow direction.

Nicolaidis et al. (2015), development Ultra High Performance Cementitious Composites (UHPC) using constituent material available in Cyprus. Aim of the study was to propose a mixture which exhibits good performance against blast and impact loading. For the

optimization of the material, different parameters were investigated such as; the various fiber contents, the different types of sand, the different water/cement ratio and the different curing regimes. The experimental results indicated that the optimum performance of the material was achieved for curing at 90 °C for 11 days, for a water/binding ratio equal to 0.16 and a volume fraction of fibers equal to 6% per volume.

Farhat et al. (2007), investigated some special characteristics of High Performance Fiber Reinforced Cementitious Composites (HPFRCC), such as the shrinkage of the material and its behavior under thermal cycling. Additionally, the material was applied for the retrofitting of concrete beams under elevated temperature. The volume of fibers in this research was high, namely 8% per volume, which deviates from the fiber contents normally used for the preparation of UHPFRC. The effect of fluctuated temperature on the behavior of HPFRCC was investigated first. Specimens were subjected to thermal cyclic loading ranging between 25°C and 90°C. The results indicated that due to the high volume of fibers in the mixture, the cyclic thermal loading did not affect the mechanical properties of the material. In this study, the behavior of the material under fatigue was also investigated. Specimens with different dimensions tested under various loading conditions. More specifically, the stress was in the range of 10% and 90% of the maximum stress level. From the results obtained, differences in the response between specimens with the different sizes were identified. For the small specimens, and after one million cycles, no special damages were appeared. On the contrary, a variation in the response was noticed for bigger specimens. These differences were attributed to the distribution of the fibers in the mixture. Thicker elements are likely to have a non-even distribution of the fibers in their mass.

HPFRCC was also applied for the retrofitting of RC beams. Retrofitting strips were bonded on both the tensile and vertical sides. In Figure 2.7, the retrofitting procedure of this study is presented.

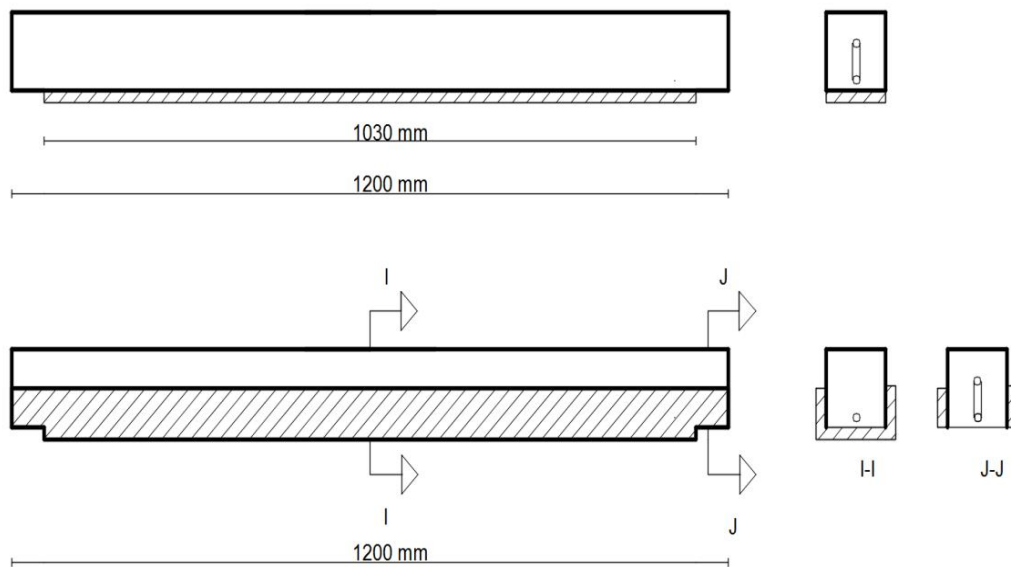


Figure 2.7 Retrofitting using UHPFRC (Farhat et al., 2007)

As shown in Figure 2.7, the retrofit material was applied as wide strips and U shaped jackets. For the bonding of the strips with the beams, an epoxy based adhesive was used. From the testing of the strengthened beams, the researchers concluded that the retrofitting with strips can increase the loading carrying capacity up to 86%, while the strips can also prevent the shear failure of the beams. Finally, in this study, the behavior of the retrofitted specimens under thermal cyclic loading was investigated. The results indicated that the bonding between the two materials was not affected by the thermal cycling loading.

Habel et al. (2006), investigated the flexural performance of composite concrete-UHPFRC elements. In this study, three configurations for the optimum performance of the composites elements were proposed (see Figure 2.8). In the first configuration, the researchers proposed that for the protection of the concrete layer a thin UHPFRC layer, of at least 3 cm, should be cast on the existing RC member (see Figure 2.8a). In the second configuration, steel bars can be added to the UHPFRC layer to replace the deteriorated bars of the RC member (see Figure 2.8b). In this case the layer should have a depth of at least 5 cm. Finally, the aim of the third configuration was to increase the strength of the existing members. Therefore, it was suggested that steel bars should be added to the UHPFRC layer (see Figure 2.8c).

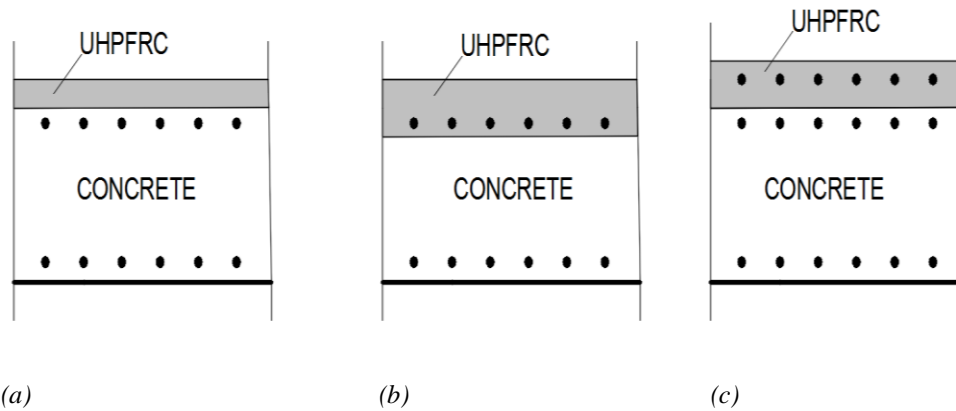


Figure 2.8 Proposed configurations for the composite concrete-UHPFRC elements (Habel et al., 2006)

There are limited applications of UHPFRC for the strengthening and rehabilitation of RC structures. It is worth mentioning that the term strengthening describes the structural intervention which aims to increase the strength of structural components to carry additional loads, while the term rehabilitation is a more general term describes the re-establishment of the safety and the serviceability during a defined time frame. Bruhwiler and Denarie (2008), presented real applications of UHPFRC for the rehabilitation of existing RC structures which were exposed to severe environmental conditions and high mechanical loading. The first application of this study was the rehabilitation and the widening of a road bridge (see Figure 2.9). In this application, the researchers replaced both the upstream and the downstream kerbs of the bridge. The first was replaced by a 3 cm thick UHPFRC layer, and the latter with a prefabricated UHPFRC kerb. The surface of the deck, which was contaminated with chlorides, was replaced by a 3 cm UHPFRC layer and over the layer a bituminous pavement layer was cast. In Figure 2.9b, the casting procedure of UHPFRC for this application is presented. As shown in this figure, for the preparation and the application of the material, only simple tools were used. The low permeability of the material was confirmed with air permeability tests, whereas the good mechanical properties of UHPFRC were validated with uniaxial tests. Finally, from the cost analysis, it was found that the cost was about 10% higher compared to conventional methods. However, the main benefit of this application was the required time, which was substantially shorter compared to conventional techniques.



(a)

(b)

Figure 2.9 a) Rehabilitation of road bridge using UHPFRC, b) application of the UHPFRC using conventional equipment (Bruhwiler and Denarie, 2008)

Another application of UHPFRC in that study was the construction of a protection layer of a crash barrier wall of a highway bridge using UHPFRC (see Figure 2.10a). Due to the exposure of the barrier to severe environmental conditions, high strength and low permeability were required in this application, together with protection from impact actions like crashes. A further application of this study, was the rehabilitation of a bridge pier using UHPFRC (see Figure 2.10b). For this application, thick prefabricated UHPFRC layers were constructed. The layers were transferred to the construction site and placed as an outer layer for the protection of the existing piers. For the connection of the joints, an epoxy resin was used, whereas the gap between the UHPFRC shells and the existing material was filled with a self-compacting mortar.



(a)

(b)

Figure 2.10 a) Application of the UHPFRC on a crash barrier, b) rehabilitation of a bridge pier (Bruhwiler and Denarie, 2008)

The last application was the strengthening of an industrial floor using UHPFRC. A 4 cm thick UHPFR layer was cast over the existing slab in order to increase the load carrying capacity of the slab. As illustrated in Figure 2.11, due to the excellent workability of the material, the casting was easy and only conventional tools were used.



Figure 2.11 Strengthening of an industrial floor (Bruhwiler and Denarie, 2008)

Noshiravani and Bruhwiler (2016), investigated the performance of composite RC-UHPFRC beams subjected to bending and shear in a cantilever beam setup. For this investigation the UHPFRC layer was cast at the tensile side of the beams. The span length, the ratio and the type of the reinforcement were variable. From the experimental results it was found that most of the beams failed due to a flexural failure at a force of 2 to 2.8 higher than the resistance of the control specimens. The medium span specimens on the other hand, which had a low shear reinforcement, failed with a shear-flexural crack. Finally, another finding of this study was that the cracking near to the interface softens the bond between the elements and enhance the deformation capacity.

Safdar et al. (2016), investigated the application of UHPFRC as a repair material and the flexural response of composite UHPFRC-RC elements was examined. In this investigation the RC beams were repaired on both the compressive and the tensile sides. The layers had varying thicknesses, and the specimens were tested under four-point loading. The results indicated that the flexural strength of the repaired beams was increased for increasing UHPFRC layer thicknesses. Also, the experimental results indicated that the stiffness of the repaired beams was increased significantly, while the formation of the cracks under service conditions was delayed.

Basten-Masse and Bruhwiler (2016), investigated the behavior of composite UHPFRC-RC slabs in punching. More specifically, the researchers conducted punching tests on composite

RC-UHPFRC slabs without transverse reinforcement. In these tests the slabs failed in punching mode. Also, another finding of this study was that the UHPFRC layer increased both the rigidity of the slab and the shear resistance of the cracked RC section. This had as a result higher deformations for the RC slabs before the failure occurs. Finally, it was found that the resistance of the composite slab, for a layer depth of 50 mm, was at least 1.69 times greater than the resistance of the reference slab.

The study of the interface between UHPFRC and concrete is missing from the literature. However, Papanicolaou and Triantafyllou (2002) studied the interface behavior between Fiber Reinforced Concrete (FRC) and a lightweight concrete. More specifically, in this study the researchers conducted push-off tests and presented the results for the shear stress and the slip at the interface between Fiber Reinforced Concrete (FRC) and a lightweight concrete. The testing setup for these tests is presented in Figure 2.12. In this study, the length of the interface and the percentage of the reinforcement which was crossing the interface were variable. From the results obtained, the researchers concluded that for higher percentages of reinforcement at the interface, the value of the shear resistance was also higher. Also, for higher lengths of the interface the values of the slip were lower.

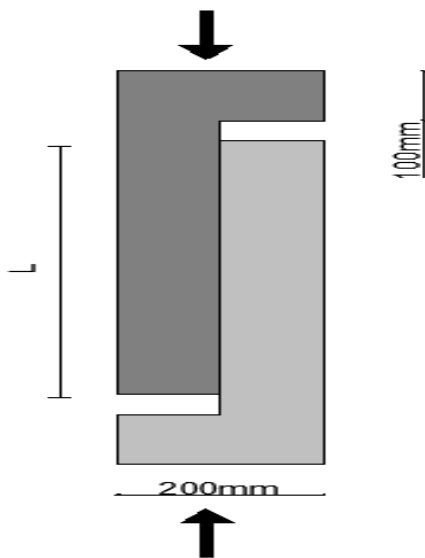


Figure 2.12 Testing setup for the push off tests (Papanicolaou and Triantafyllou, 2002)

2.5 Knowledge gaps

From the presentation of the most important studies in UHPFRC, it can be noticed that there are limited applications of the material for the strengthening of RC structures. Hence, parameters such as the effect of dowels at the interface, the performance of the elements for

strengthening with three-side jackets, the effect of the layer depth and the effect of the reinforcement of the layer have not been investigated. For the application of the material in real structures, further investigation is considered necessary. The present research aims to investigate the performance of UHPFRC as a strengthening material through an extensive experimental and numerical investigation.

The interface behavior between UHPFRC and concrete is of high importance for the performance of strengthened elements using UHPFRC layers. More specifically, in case of RC elements strengthened with additional layers, one of the most crucial parameters is the connection at the interface between the old and the new layer, since inadequate bonding may lead to premature failure of the strengthened elements. The connection at the interface between the existing RC elements and the new UHPFRC layers is a crucial topic which has not been studied and needs investigation. In the present research, the interface connection will be studied through push-off tests, while during the testing of the strengthened beams measurements of the slip at the interface will be recorded.

Most of existing studies in UHPFRC are focused on the investigation of the behavior of UHPFRC under static loading. However, the behavior of the material under cyclic loading, is missing from the literature. In earthquake prone areas, the structures, and subsequently the load-bearing systems are subjected to seismic loads which are normally simulated with a cyclic loading history. The cyclic response of the structural elements is highly affected by the behavior of the materials under cyclic loading. The present research aims to address this research gap by presenting the results of an experimental investigation. These results have been used for the constitutive modelling of the behavior of UHPFRC under cyclic loading.

The superior performance of UHPFRC can be attributed to the enhanced tensile characteristics. Despite the fact that the tensile properties of the material are highly affected by the fiber content and the curing conditions, these parameters have not been investigated thoroughly. More specifically, from the presentation of the most important studies in UHPFRC it can be noticed that the investigation of the performance of the material in direct tension for different fiber contents has not been investigated. Also, despite the fact that the tensile characteristics of the material are highly affected by the fiber content, in the literature there are not any available models for the simulation of the stress-strain behavior for the different fiber contents. In the present research, the effect of fiber content on the tensile characteristics of UHPFRC will be investigated in depth.

3. EXPERIMENTAL INVESTIGATION OF THE PROPERTIES OF ULTRA HIGH PERFORMANCE FIBER REINFORCED CONCRETE (UHPFRC)

3.1 Introduction

Before the application of the UHPFRC for the strengthening of RC beams, it is of high importance that there is an investigation into the significant parameters of the material which are missing from the literature and are required for the application of the material in this field. Hence, the present chapter, aims to investigate crucial parameters of the UHPFRC, related mainly to the properties of the material under various loading conditions, and to select an optimum mixture design which can be applied for the strengthening of RC beams.

The performance of UHPFRC is highly dependent on the properties of the cementitious matrix. Hence, in the present chapter different mixture designs with different proportions of the constituents of the UHPFRC have been investigated, and the mixture with the optimum mechanical properties has been adopted for the subsequent part of the present research. An additional study has been conducted on the performance of UHPFRC for various cement types. Also, the effect of curing time and curing regime on the performance of the cementitious matrix has been investigated in detail in the present chapter. Another important phenomenon which affects the performance of the cementitious matrix is shrinkage. Shrinkage is related to the loss of water from the mass of concrete, which results in a reduction in the volume of concrete and the appearance of cracks in concrete. This can affect the properties and the durability of the material. In the present chapter, shrinkage has been measured in different periods; the effect of steel fibers on the phenomenon has also examined.

The unique properties of UHPFRC are mainly related to the incorporation of steel fibers in the mixture, and the volume of steel fibers is a crucial parameter which affects the performance of UHPFRC. An extensive experimental investigation has been conducted on the effect of various fiber contents on the tensile characteristics and the compressive strength of UHPFRC. Based on the experimental results, different stress-strain and stress-crack opening models have been proposed for the modelling of UHPFRC in tension and the different percentages of steel fibers. Another important parameter which affects the performance of UHPFRC is the type of fibers. In the present chapter, two different types of steel fibers have been examined. The first type is conventional steel fibers with a length of 13

mm, a diameter of 0.16 mm and a tensile strength of 3000 MPa. This is a commonly used type of fibers in UHPFRC, and has as a result good mechanical properties of the material, while these fibers are also wide available in the market. The second type of fibers is recycled steel fibers retained from car tires. This is an environmental friendly solution, and at the same time, it can reduce the total cost of the material, as the cost of these fibers is lower compared to the conventional steel fibers. The performance of UHPFRC for the different types of fibers has been evaluated, and the fiber type with the optimum performance has been adopted for the application of the material for the strengthening of RC beams.

The fiber distribution is an important parameter influencing the performance of the UHPFRC elements. Based on Ferrara et al. (2011), the distribution of the fibers is affected by the mixing and the casting procedure; the depth of the material in conjunction with the length of the layer can also affect the performance of UHPFRC. Thick elements are more likely to have a non-uniform distribution of the fibers in their mass, which can affect their performance. In the present thesis, UHPFRC layers have been cast for the strengthening of the existing RC elements. The selection of the appropriate depth of the layers is of high importance for the performance of the technique. Therefore, this chapter presents the experimental research conducted on the 'size effect' of UHPFRC prisms with various depths. A model for the correlation of the tensile strength with the respective flexural strength of UHPFRC has also been proposed.

Finally, for the application of the examined technique in earthquake prone areas, the study of the behavior of the material under cyclic loading is of high importance. However, the study of the performance of UHPFRC under cyclic loading is missing from the literature. In the present chapter, different loading histories and different percentages of steel fibers have been examined, and the performance of UHPFRC under cyclic loading has been investigated. Based on the experimental results, a constitutive stress-strain model for the UHPFRC under cyclic loading has been proposed. A further model has been suggested for the degradation of the modulus of elasticity with the number of loading cycles. These models can be used for the prediction of the hysteretic characteristics of UHPFRC and the computational analysis of UHPFRC subjected to cyclic loading.

3.2 Investigation of different mixture designs

3.2.1 Examined mixture designs

For the application of UHPFRC for the strengthening of RC structures high mechanical properties are required. A preliminary study has been conducted on the investigation of the properties of different mixture designs of UHPFRC. The mixture with the optimum performance has been adopted for the next investigations and the application of the material for the strengthening of RC beams.

For the preparation of UHPFRC, and in order to improve the homogeneity and the density of the material, only materials with fine particles are used. Therefore, in the present study, silica sand with a maximum particle size of 500 μm was used, together with dry silica fume with retention on 45 μm sieve less than 1.5 %, Ground Granulated Blast Furnace Slag (GGBS) and cement. A low water/cement ratio was also used together with polycarboxylate superplasticizer in order to secure the workability of the mixture. Additionally, 3% per volume steel fibers were incorporated into the mixture. The steel fibers had a length of 13 mm and a diameter of 0.16 mm; the tensile strength was 3000 MPa, while the modulus of elasticity was 200 GPa. Finally, cement 32.5 R type II was used for the preparation of the all the examined mixtures. In the next sections, a detailed investigation on the effect of different fiber contents, different types of fibers and different cement types on the performance of UHPFRC is presented.

The examined mixtures designs of the present investigation were based on a mixture design proposed by Hassan et al. (2012). For the preparation of the different mixture designs, different quantities of cement, GGBS and silica fume were incorporated into the mixture. The rheological properties of the UHPFRC are of high importance for the application of the material for the strengthening of existing RC elements. The large volumes of fibers in the mixture make the compaction of the material difficult using conventional methods. Therefore, effective rheological properties are required for application of UHPFRC for strengthening purposes. This preliminary study has been conducted to obtain a mixture with the correct balance of mechanical properties but also rheological properties. Therefore, apart from the different quantities of the constituents of the UHPFRC, the quantities of water and superplasticizer were adjusted accordingly in order to achieve the target workability of the mixture. More specifically, the target workability of the present investigation was a flow

diameter of 255 mm, in a slump cone with a height of 60 mm, a top diameter of 70 mm and a bottom diameter of 100 mm. This value of workability indicate effective rheological properties, while the procedure for the measurement of the workability is presented in detail in a next section and was based on the BS 1015-3:1999, (1999). All the examined mixture designs are presented in Table 3.1.

Mixture	Cement (Kg)	GGBS (Kg)	Silica Fume (Kg)	Water (Kg)	Silica Sand (Kg)	Superplasticizer (Kg)	Fibers (Kg)	$\frac{\text{Water}}{\text{Cement}}$
U1	657	119	418	235	1051	62	235.5	0.36
U2	500	575	119	135	1051	59	235.5	0.27
U3	600	475	119	185	1051	59	235.5	0.3
U4	880	0	314	290	1051	59	235.5	0.33
U5	657	418	119	185	1051	59	235.5	0.3

Table 3.1 Examined mixture designs

3.2.2 Preparation of specimens

For the mixing of the materials, all the dry ingredients were mixed first for three minutes. Then, water and superplasticizer were added into the mixture. Once the mixture reached the wet stage, steel fibers were incorporated through sieving. The specimens were demolded forty-eight hours after casting and placed in a water tank for twenty-six days. The specimens were tested twenty-eight days after casting. This is a time frame over which the cementitious materials develop strength close to the maximum that they can reach. A detailed investigation of the effect of curing time and curing regime on the properties of UHPFRC is presented in a next section. The preparation of the specimens is presented in Figure 3.1.



Figure 3.1 Preparation of the specimens: a) mixer used for the mixing the materials b) dog bone shaped and cube specimens after casting c) dog bone shaped and cube specimens after demolding

3.2.3 Experimental setup

Dog-bone shaped specimens were prepared for the direct tensile tests. The geometry of the examined specimens is illustrated in Figure 3.2. Since UHPFRC is a material with completely different characteristics compared to concrete and HPC, especially in tension, and there are not any standards for the testing of the material under this loading condition, for the direct tensile tests a similar procedure followed by Hassan et al (2012) and Park et al. (2012) was adopted. Hence, these tests were conducted under a constant displacement rate of 0.007 mm/sec, using a servo-hydraulic testing machine (see Figure 3.3a) leading to comparable results.

The compressive tests of UHPFRC were conducted according to BS EN 12390-3:2009, (2009). The experimental setup for these tests is presented in Figure 3.3b. Four standard cubes with side lengths of 100 mm were used for each investigation and the specimens were tested under a loading rate of 0.6 MPa/s.

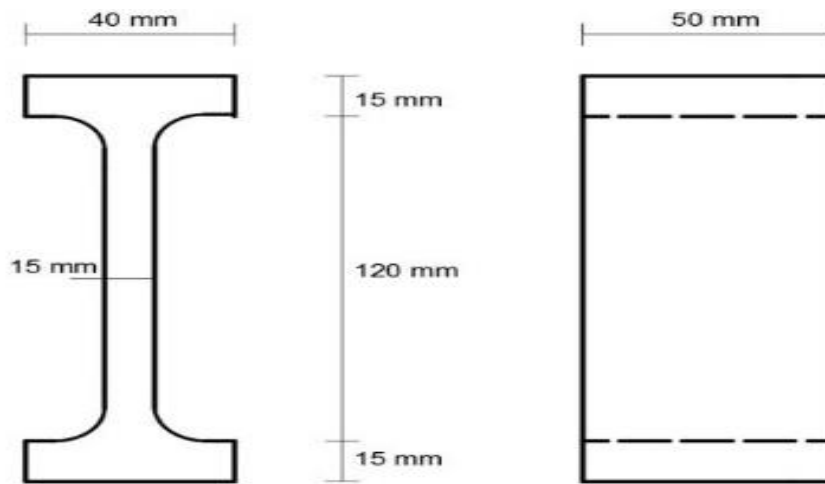


Figure 3.2 Dimensions of the dog bone shaped specimens



(a)

(b)

Figure 3.3 Experimental setup for: a) direct tensile tests, b) compressive tests

3.2.4 Experimental results

The results of the direct tensile tests of mixture U1 are presented in Figure 3.4. As illustrated in this figure, the scatter in the experimental results was between the values of 6.8 MPa and 7.3 MPa. Considering the average curve, the tensile strength was found to be equal to 7 MPa. From the linear part of the stress-strain curve, the modulus of elasticity was calculated equal to 45 GPa. The average compressive strength was 100 MPa.

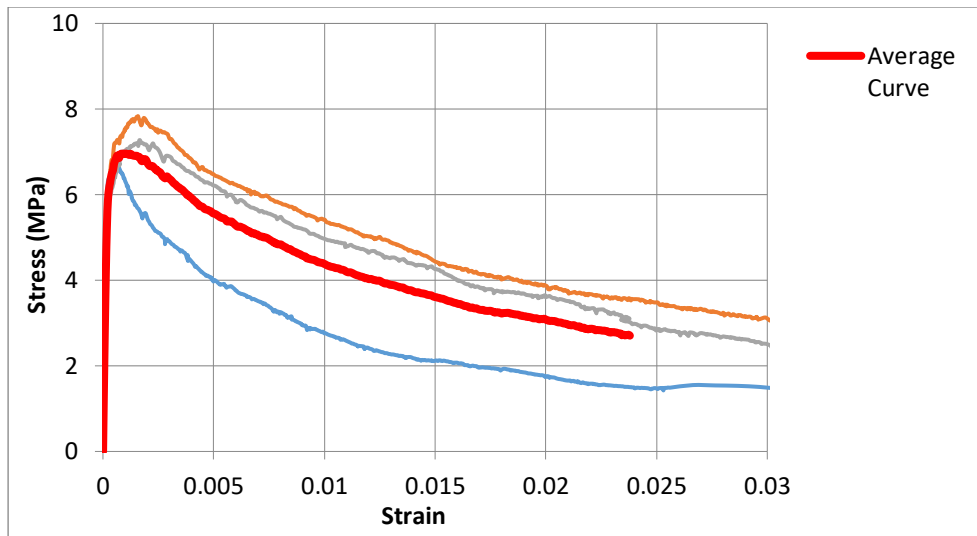


Figure 3.4 Stress-strain results for mixture U1 in tension

The stress-strain results of mixture U2, which was prepared with lower quantities of cement and silica fume and a higher quantity of GGBS compared to mixture U1 (see Table 3.1), are presented in Figure 3.5. Based on the results of Figure 3.5, the tensile strength ranged between the values of 7.1 MPa and 9.2 MPa, and considering the average curve, the tensile strength was found to be equal to 7.8 MPa. The modulus of elasticity, on the other hand, was equal to 48 GPa, and the average compressive strength was 108 MPa. From these results, it is clear that mixture U2 presents higher mechanical properties in comparison with mixture U1.

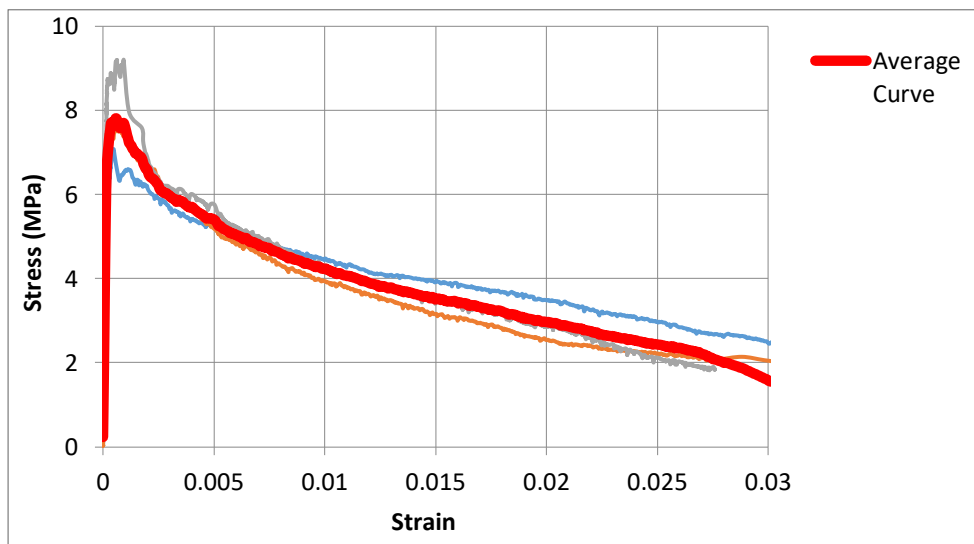


Figure 3.5 Stress-strain results for mixture U2 in tension

The stress-strain results of the direct tensile tests of mixture U3 are presented in Figure 3.6. As shown in this figure, the tensile strength ranged between the values of 6.4 MPa and 8.3 MPa. Based on the average curve, the tensile strength was 7.1 MPa, and the modulus of

elasticity was calculated to be equal to 47 GPa. Finally, the average compressive strength was 95 MPa.

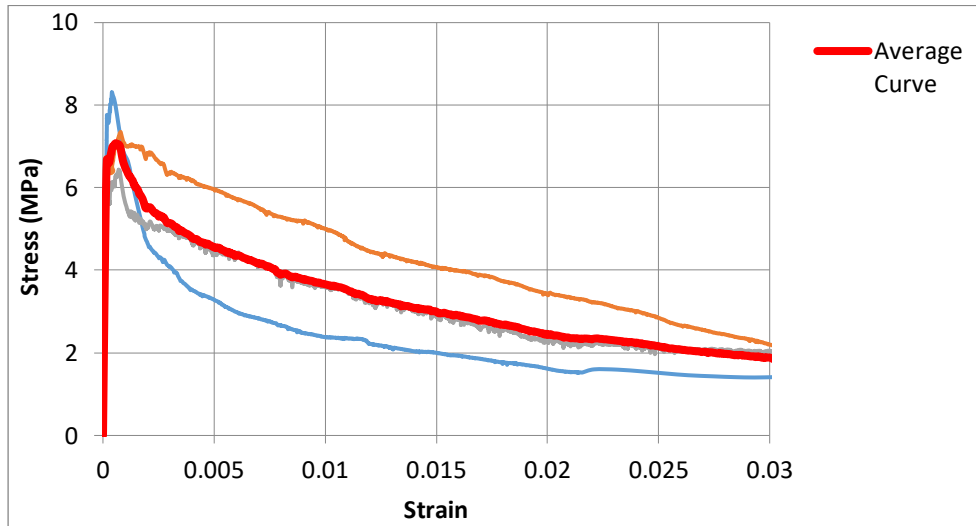


Figure 3.6 Stress-strain results for mixture U3 in tension

Mixture U4 was prepared without the use of GGBS. The experimental results of the direct tensile tests of are presented in Figure 3.7. As presented in this figure, the tensile strength ranged between the values of 7.3 MPa and 8.8 MPa, while the average tensile strength equalled to 7.4 MPa. The modulus of elasticity was calculated to be equal to 49 GPa, and the average compressive strength was 106 MPa.

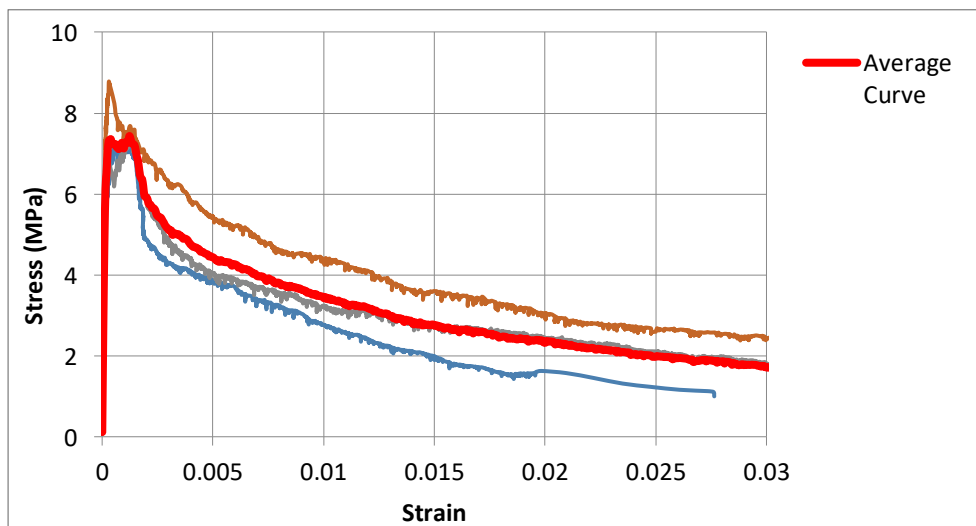


Figure 3.7 Stress-strain results for mixture U4 in tension

Finally, in Figure 3.8, the experimental results of mixture U5 in tension are presented. As shown in this figure, the tensile strength was in the range of 7.7 MPa and 9.9 MPa; from the average stress-strain curve, the tensile strength was found to be equal to 8.5 MPa. The modulus of elasticity, on the other hand, was calculated as 55 GPa, and the average

compressive strength was 126 MPa. These results indicate high mechanical properties for mixture U5.

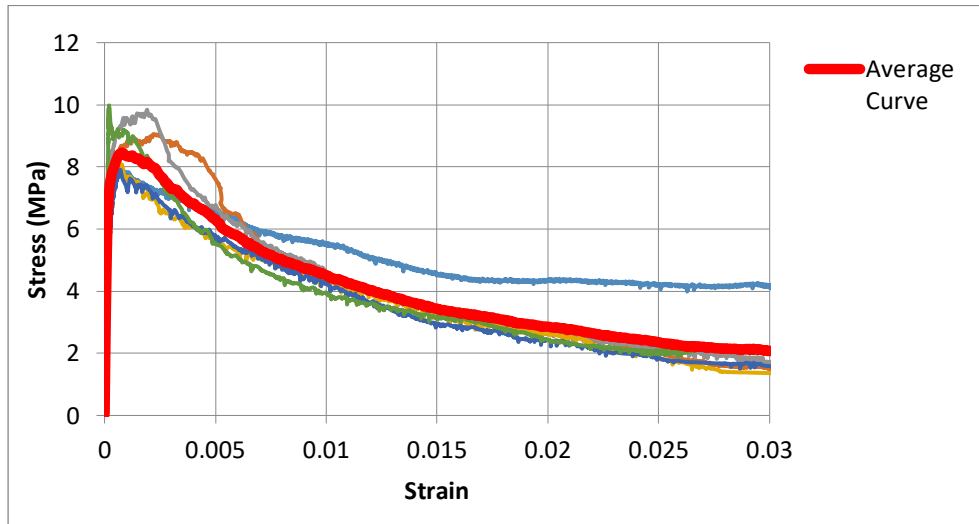


Figure 3.8 Stress-strain results for mixture U5 in tension

All the average stress-strain curves for the different examined mixtures designs are presented in the same graph in Figure 3.9, while in Table 3.2 all the values for the tensile and the compressive strengths are presented.

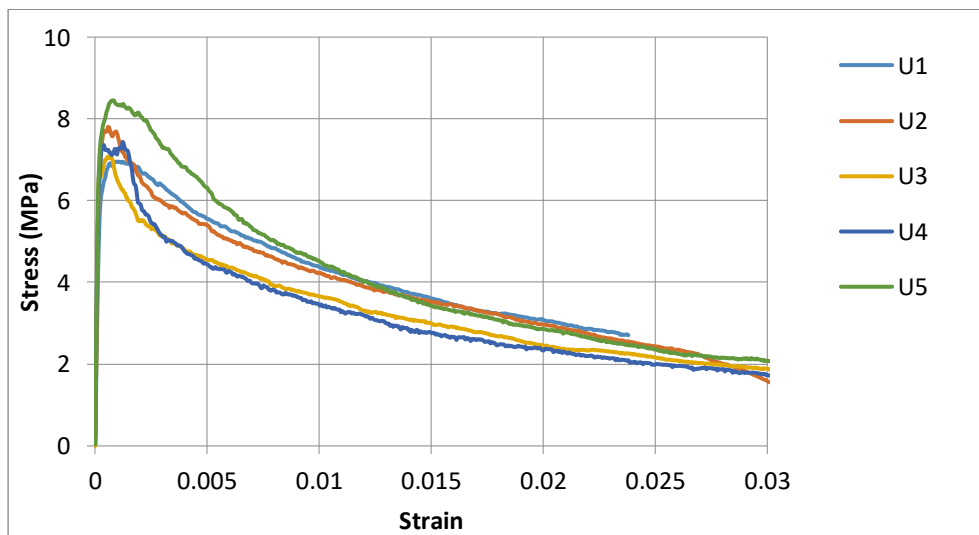


Figure 3.9 Average stress-strain results for the different examined mixture designs

Mixture	Mean Tensile Strength (MPa)	Compressive Strengths (MPa)	Mean Compressive Strength (MPa)
U1	7	95	100
		104	
		103	
		98	
U2	7.8	105	108
		112	
		110	
		105	
U3	7.1	92	95
		93	
		97	
		98	
U4	7.4	102	106
		108	
		106	
		108	
U5	8.5	122	126
		128	
		130	
		124	

Table 3.2 Experimental results for the different mixture designs

The experimental results of the present investigation indicated that the optimum tensile and compressive strengths of the material were achieved for mixture U5. Consequently, for the subsequent investigation within this research, this mixture design is adopted. Finally, it is worth mentioning that from the preparation of the different mixtures, it was observed that the use of GGBS can increase the workability of the mixture without any significant reduction of the strength of the material. Hence, when higher quantities of GGBS were used in the mixture, a lower amount of water/cement was required to achieve the desired workability. For higher quantities of cement, on the other hand, a higher water/cement ratio was necessary to achieve the desired workability.

3.3 The effect of cement type on the performance of UHPFRC

In the present section, the effect of the cement type on the performance of the UHPFRC has been investigated. For this investigation, two different types of cement, were examined; 32.5 R type II and 52.5 N type I cement. These are commonly used types of cement, which are also wide available in the market. For the present study, it was assumed that these two types of

cement present a consistent behavior and act with a similar way. The use of 52.5 N type I cement is expected to increase the performance of UHPFRC. However, an important parameter which should be taken into consideration is that the cost of the 52.5 N type I cement is significantly higher compared to 32.5 R type II cement. Hence, the present investigation aims to quantify the differences in the performance of UHPFRC using the different types of cement. However, it should be noted that the decision to undertake or not the extra cost is dependent on the designer of the technique.

For the preparation of the specimens, the mixture U5 was adopted (see Table 3.1), which presented the optimum performance, together with 3 % steel fibers. For the curing of the specimens, after the demolding two days after casting, the specimens were placed in a water curing tank for twenty-six days and tested after twenty-eight days. The experimental results for cement 32.5 R type II and 3% steel fibers are presented in the previous section (see Figure 3.8 and Table 3.2). The tensile stress-strain results of the dog-bone shaped specimens prepared with cement 52.5 N type I are presented in Figure 3.10. As shown in this figure, the maximum tensile strength was found to be equal to 11.3 MPa, and the modulus of elasticity was calculated as 56.2 GPa. The average compressive strength was 150 MPa. In Figure 3.11 a comparison of the experimental results for the different cement types is presented.

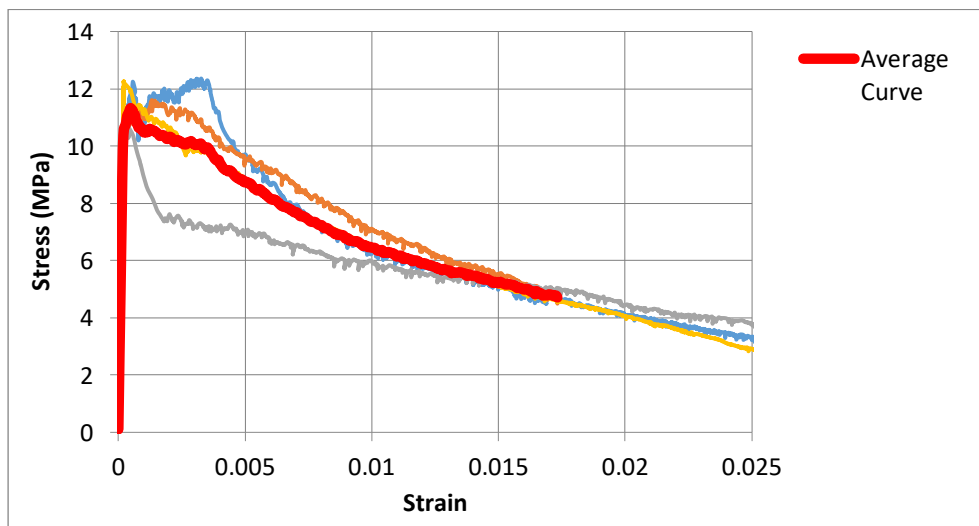


Figure 3.10 Tensile stress-strain results for mixture U5 using cement 52.5 N type I

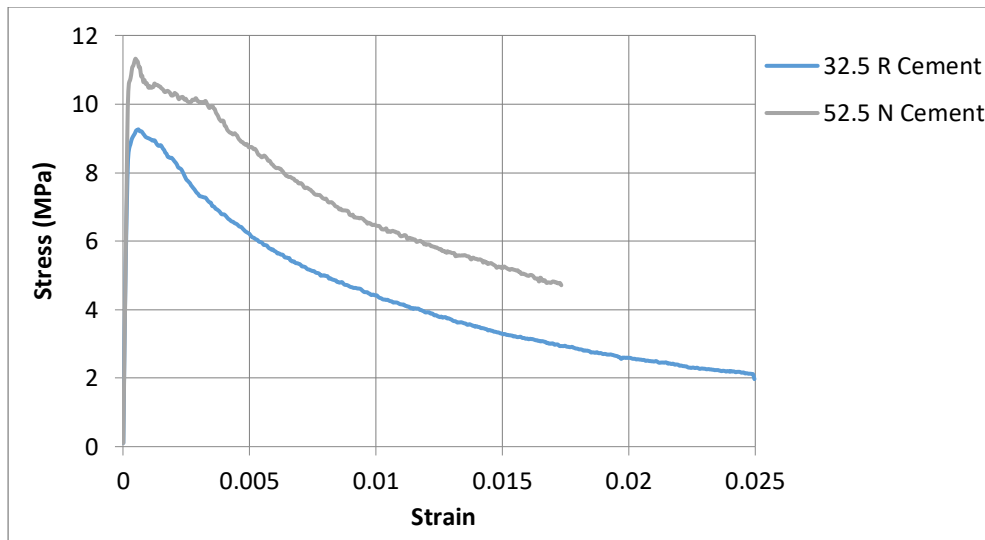


Figure 3.11 Comparison of the average tensile stress-strain results for the different types of cement

Based on the experimental results of the present section, it is clear that the use of high strength cement results in higher compressive and tensile strengths for UHPFRC. Hence, once the 32.5 R type II cement was replaced by 52.5 N type I cement, the tensile strength was increased by 18% and the compressive strength by 16%.

3.4 The effect of the curing time and curing regime on the performance of UHPFRC

3.4.1 Experimental investigation

Crucial parameters that affect the properties of the hardened UHPFRC are the curing regime and the curing duration. Heat curing accelerates the hydration process, activates the pozzolanic reaction of silica fume and reduces the curing time. As a consequence, heat curing has as a result high strength in a short period. In the present research, for the casting of the layers and jackets, first of all the existing beams will be roughened, and later on, the layers and jackets will be cast. When similar strengthening procedures are followed heat curing is difficult to apply. However, there are strengthening applications, in which prefabricated UHPFRC layers can be used. In these cases, heat curing at high temperatures can be applied. Bruhwiler and Denarie (2008), used prefabricated layers for the strengthening of bridge piers, while for the connection of the existing members with the layers epoxy resin was used. Farhat et al. (2007), used UHPFRC for the retrofitting of RC beams. The retrofitting material in this case was applied as wide strips. For the bonding of the strips with the beam, epoxy based adhesive was used. These are cases in which heat curing can be applied.

The present section focuses on the effect of the curing regime and curing time on the tensile stress-strain characteristics and the compressive strength of UHPFRC. Nicolaides et al. (2015), investigated the effect of different curing temperatures and concluded that the optimum performance is achieved for a curing temperature of 90 °C. This temperature was also adopted in the present investigation.

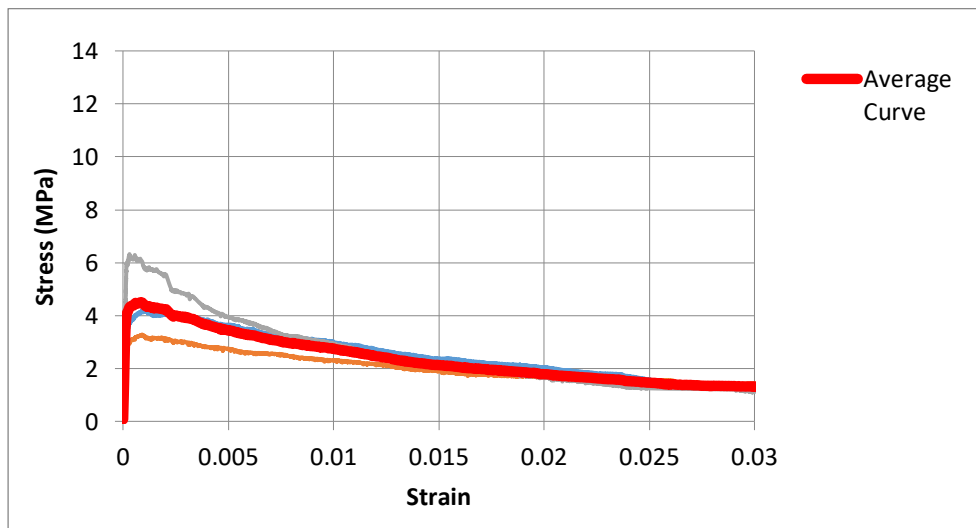
The tensile characteristics of the UHPFRC were investigated through direct tensile tests of dog bone shaped specimens (see Figure 3.2). Four standard cubes with side lengths of 100 mm were also tested in compression for each investigation. For the curing of the specimens, after the demolding two days after casting, some of the specimens were placed in a water tank at a water temperature of 20 °C (± 2 °C) while other specimens were steam-cured at 90 °C (± 2 °C). Testing was conducted on day three, five, seven, ten, fourteen and twenty eight, and a further investigation took place at ninety days for specimens cured in the water tank. The specimens remained in the water tank and the steam curing tank until eight hours prior to testing. The results of Section 3.3 indicated that higher mechanical properties are achieved with the use of high strength cement 52.5 N type I, and this type of cement was adopted in the present investigation together with 3 % per volume steel fibers. The experimental program for this investigation is presented in Table 3.3.

Testing Time	Group A	Group B
	Days in Steam Curing Tank	Days in water tank
3	1	1
5	3	3
7	5	5
10	8	8
14	12	12
28	26	26
90	-	88

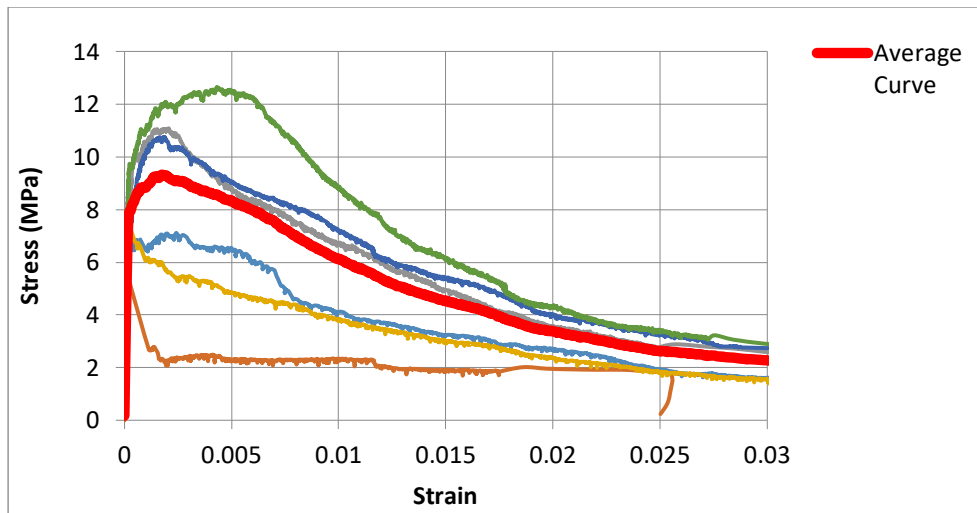
Table 3.3 Experimental program for the different curing regimes

3.4.2 Experimental results

Testing was conducted for the different curing conditions over three days. The experimental results of the direct tensile tests for the specimens placed in the water tank and in the steam curing tank are presented in Figures 3.12a and 3.12b respectively.



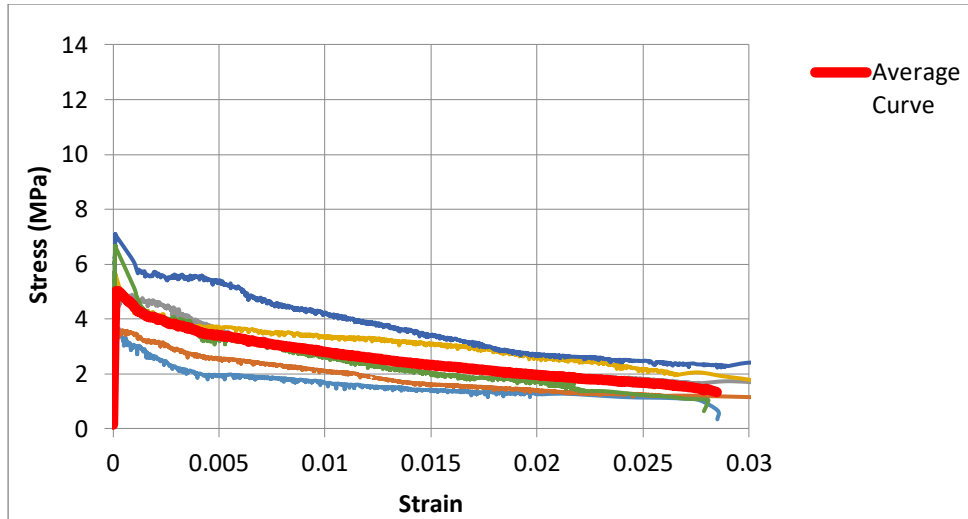
(a)



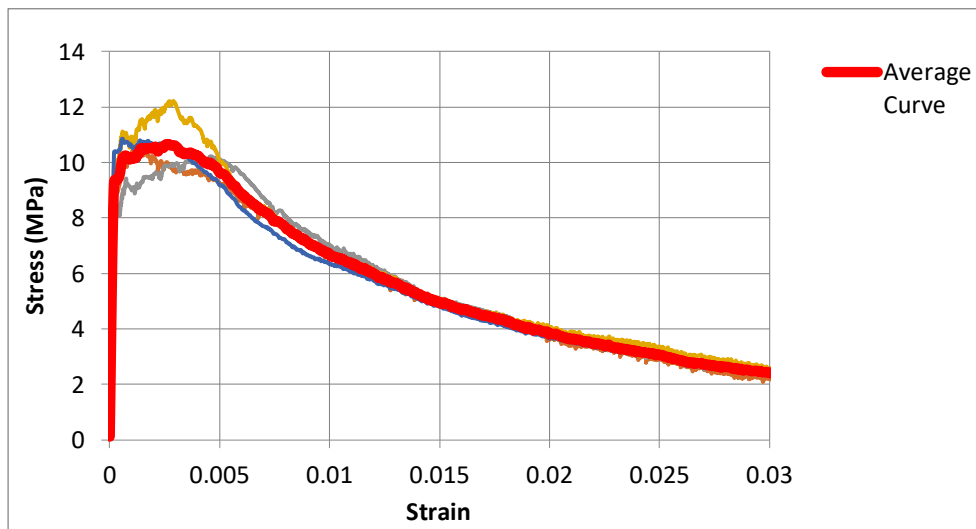
(b)

Figure 3.12 Results of the direct tensile tests three days after casting for: a) the specimens placed in the water tank, b) the specimens placed in the steam curing tank

The results of Figure 3.12a indicate a scatter in the experimental results between the values of 3.3 MPa and 6.3 MPa. Considering the average curve, the maximum tensile strength was found to be 4.5 MPa, and from the linear part of the stress-strain curve, the modulus of elasticity was equal to 31.8 GPa. The average compressive strength was 83 MPa. The results of Figure 3.12b, for the specimens placed in the steam curing tank, indicate a scatter in the results between the values of 7.1 MPa and 11.1 MPa, and the average maximum tensile strength was equal to 8.5 MPa. The modulus of elasticity, was calculated to be 46.8 GPa, while the average compressive strength was 156 MPa. These experimental results indicate the effectiveness of the steam curing on the acceleration of the tensile and compressive strengths of the material. It can be noticed that the tensile and the compressive strength of the specimens placed in the steam curing tank for one day were almost 90% higher in comparison with the respective strengths obtained for curing in the water tank for the same time. In Figures 3.13a and 3.13b, the tensile experimental results of the specimens tested in five days are presented.



(a)

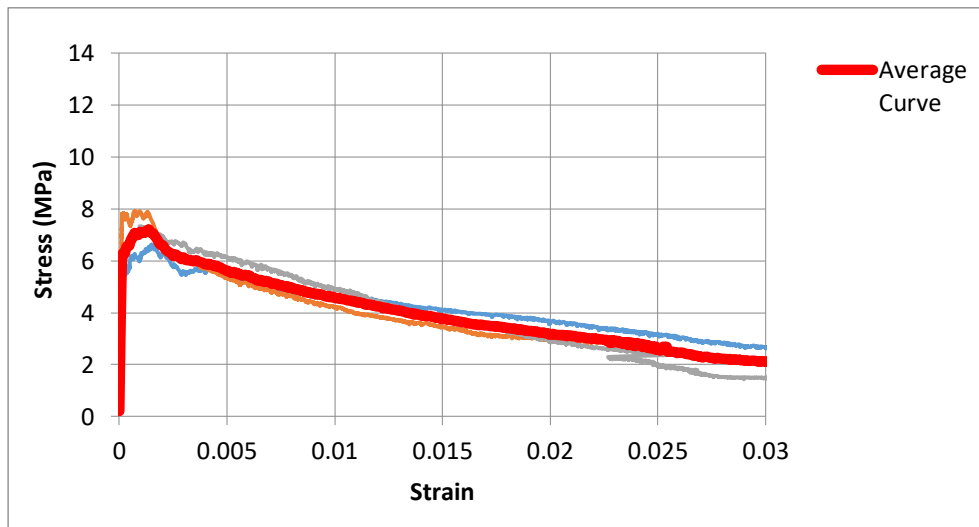


(b)

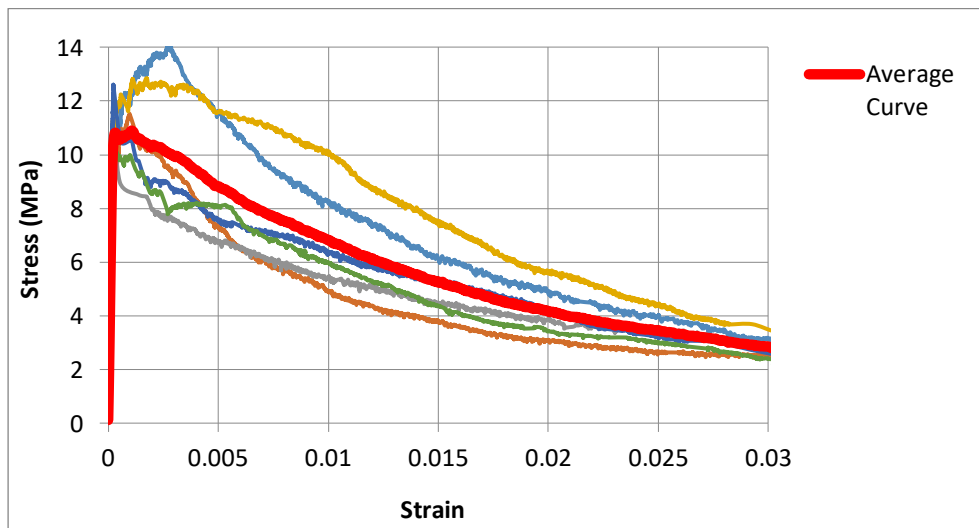
Figure 3.13 Results of the direct tensile tests five days after casting for: a) the specimens placed in the water tank, b) the specimens placed in the steam curing tank

As illustrated in Figure 3.13a, the tensile strength of the specimens placed in the water tank ranged between the values of 3.7 MPa and 7.1 MPa; based on the average stress-strain curve, the tensile strength was found to be 5 MPa. The modulus of elasticity was equal to 50 GPa, and the average compressive strength was 106 MPa. For the specimens placed in the steam curing tank, on the other hand, the scatter in the results was in the range of 10.2 MPa and 12.2 MPa. From the average stress-strain curve, the maximum tensile strength was equal to 10.7 MPa. Finally, the modulus of elasticity was calculated to be 56 GPa, and the average compressive strength was 164 MPa. From these results, it can be seen that two more days in the water tank (from one day to three days) resulted in an increase of 11% on the tensile strength and 27% on the compressive strength of the UHPFRC. For the specimens placed in

the steam curing tank, however, two more days in the steam curing tank showed an increase of 26% in the tensile strength and 5% in the compressive strength. The next investigation took place over seven days. The results of the direct tensile tests are presented in Figures 3.14a and 3.14b.



(a)

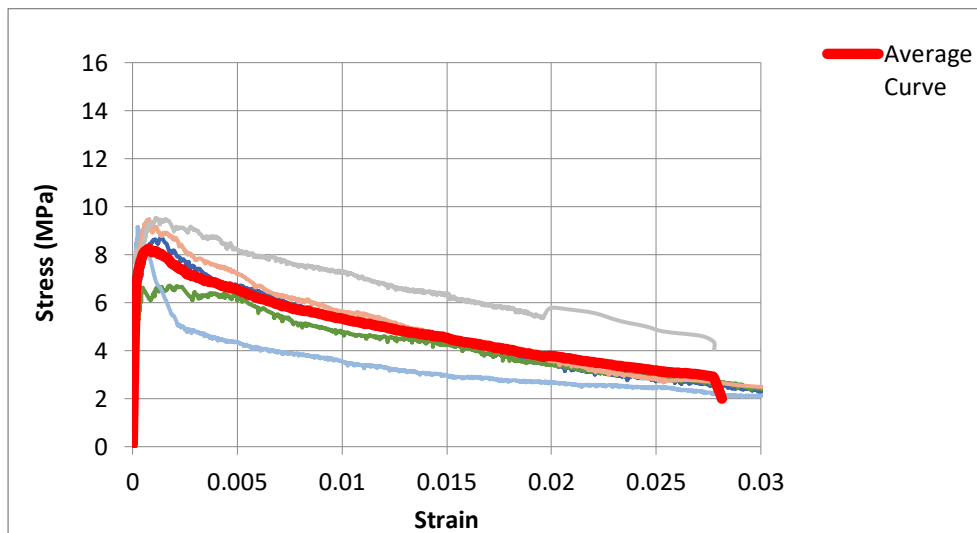


(b)

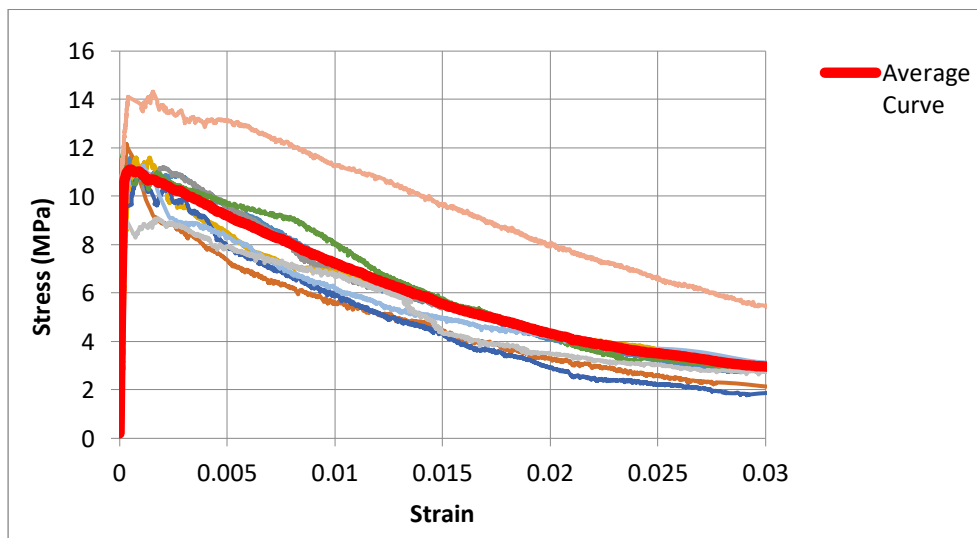
Figure 3.14 Results of the direct tensile tests seven days after casting for: a) the specimens placed in the water tank, b) the specimens placed in the steam curing tank

The experimental results of Figure 3.14a for the specimens placed in the water tank, indicate a scatter in the experimental results between the values of 6.6 MPa and 7.9 MPa. Considering the average stress-strain curve, the maximum tensile strength equalled 7.2 MPa while the modulus of elasticity was calculated to be 53.4 GPa. The average compressive strength was 114 MPa. By contrast, from the experimental results of Figure 3.14b, the tensile strength

ranged between 10.5 MPa and 14.2 MPa. Additionally, the average tensile strength was 10.9 MPa, and the modulus of elasticity was 56.1 GPa. Finally, the average compressive strength was 168 MPa. The experimental results at seven days indicate a steady upward trend on both the tensile and compressive strength of the specimens placed in the water tank. The mechanical properties of the specimens placed in the steam curing tank, on the other hand, were also slightly improved. The next investigation took place ten days after casting and the stress-strain results of the direct tensile tests for the different curing conditions are presented in Figures 3.15a and 3.15b.



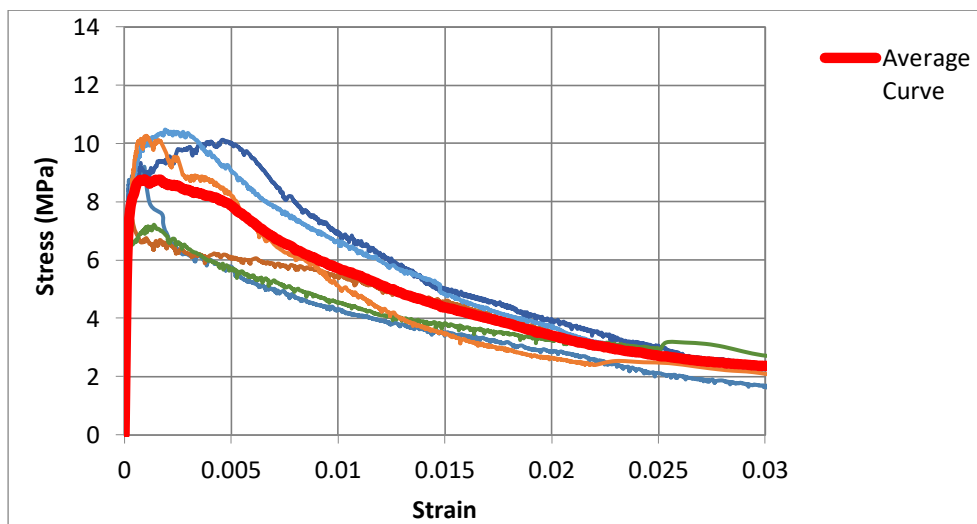
(a)



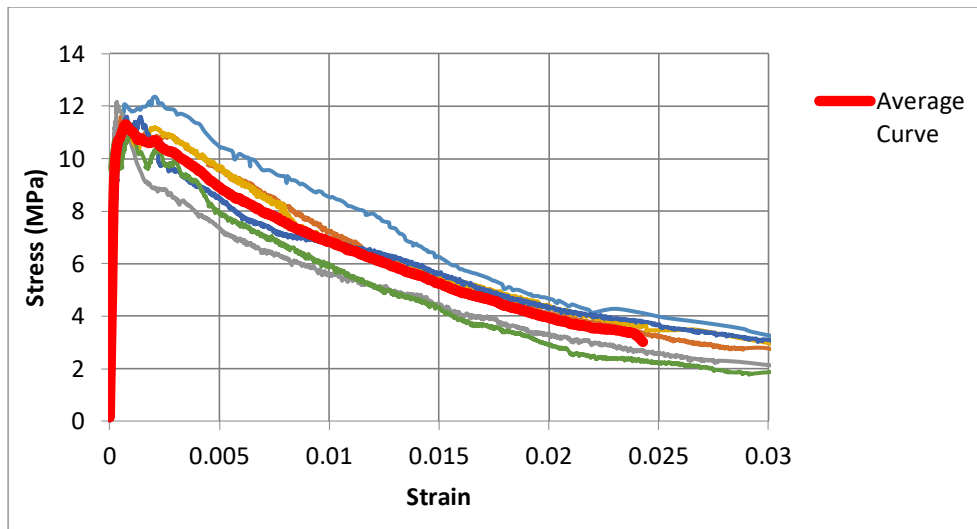
(b)

Figure 3.15 Results of the direct tensile tests ten days after casting for: a) the specimens placed in the water tank, b) the specimens placed in the steam curing tank

As shown in Figure 3.15a, the scatter in the experimental results for the specimens placed in the water tank was in the range of 6.7 MPa and 9.5 MPa. The average tensile strength was equal to 8.3 MPa. On the other hand, the modulus of elasticity was calculated to be 52 GPa, and the average compressive strength was 130 MPa. The experimental results for the specimens placed in the steam curing tank indicated a scatter in the experimental results between the values of 11.1 MPa and 12.4 MPa, and the average maximum tensile strength was 11.3 MPa. The modulus of elasticity was equal to 56 GPa, and the average compressive strength was 177 MPa. From these results, the same upward trend of the mechanical properties of UHPFRC for the different curing conditions can be distinguished. Comparing the mechanical properties obtained at seven and ten days for the specimens placed in the steam curing tank, it is evident that three more days results in 4% higher tensile strength and 5% higher compressive strength. A higher increase was noticed for the specimens placed in the water tank. In this case, the compressive strength increased by 15.3% and the tensile strength by 12.8%. The next investigation was conducted fourteen days after casting, and the experimental results for the different curing conditions are presented in Figures 3.16a and 3.16b.



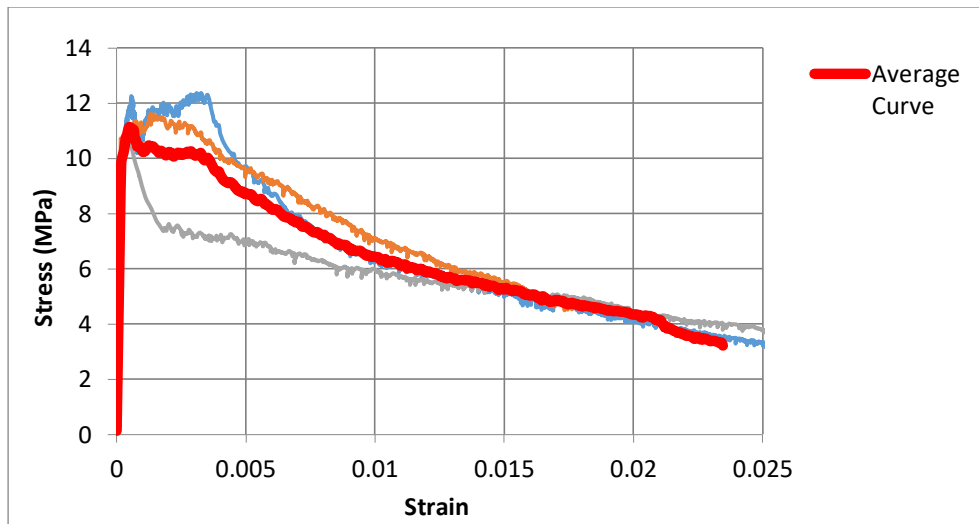
(a)



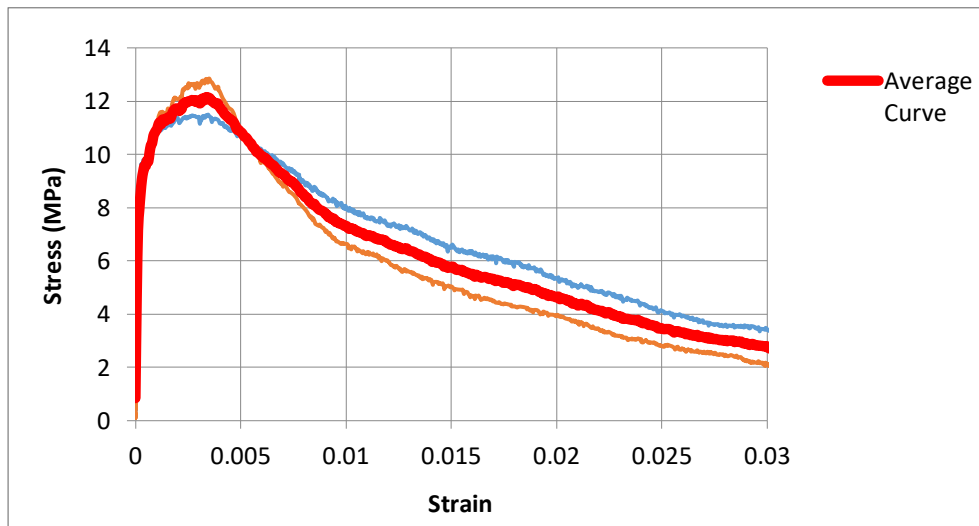
(b)

Figure 3.16 Results of the direct tensile tests fourteen days after casting for: a) the specimens placed in the water tank, b) the specimens placed in the steam curing tank

The results for the specimens placed in the water tank was in the range of 6.4 MPa and 11.4 MPa. Based on the average stress-strain curve, the maximum tensile strength was found to be 8.8 MPa, and the modulus of elasticity was calculated as 52.4 GPa. The average compressive strengths was 135 MPa. The results of Figure 3.16b for the specimens placed in the steam curing tank, indicate a lower scatter in the experimental results with the tensile strength in the range of 12 MPa and 14 MPa. The average maximum tensile strength in this case was found to be 12.3 MPa, and the modulus of elasticity was equal to 60.8 GPa. Finally, the average compressive strength was 180 MPa. From the experimental results of Figure 3.16b, it is clear that the heat curing produces very high mechanical properties for the UHPFRC over a short period of time. For the mechanical properties achieved fourteen days after casting for the different curing conditions, the tensile and compressive strength of the specimens placed in the steam curing tank were 40% and 34% higher respectively. This is in comparison with the respective strengths obtained from the specimens placed in the water tank for the same period. The following investigation involved the study of the performance of UHPFRC twenty-eight days after casting for the different curing conditions. The experimental results are presented in Figures 3.17a and 3.17b.



(a)



(b)

Figure 3.17 Results of the direct tensile tests twenty-eight days after casting for: a) the specimens placed in the water tank, b) the specimens placed in the steam curing tank

The results of Figure 3.17a indicate a scatter on the tensile strength between the values of 10.7 MPa and 12.4 MPa. From the average stress-strain curve, the average tensile strength was found to be 11.1 MPa while the modulus of elasticity was calculated to be 57 GPa. Moreover, the average compressive strength was 150 MPa. By contrast, the scatter in the experimental results for the specimens placed in the steam curing tank was in the range of 11.5 MPa and 12.9 MPa, and the average tensile strength was 12.2 MPa. The modulus of elasticity was equal to 57 GPa while the average compressive strength was 183 MPa. The experimental results of the specimens tested twenty-eight days after casting indicated that the heat curing does not have any further effect after the first fourteen-day period as it seems that during this period the material has reached its maximum properties. Therefore, the mechanical properties of the

specimens placed in the steam curing tank for twenty-six days were almost same as the mechanical properties obtained from the specimens with twelve days in the steam curing tank. On the contrary, in the same period, the mechanical properties of the specimens placed in the water tank increased. More specifically, the tensile and the compressive strength of the specimens tested twenty-eight days after casting increased by 26% and 11% respectively compared to the values obtained from the specimens tested fourteen days after casting with the same curing conditions.

The last investigation constitutes the study of the performance of UHPFRC ninety days after casting. From the results over twenty eight days, it was noticed that the heat curing has not any further effect after twelve days period in the steam curing tank. Consequently, for this investigation, only the properties of the specimens placed in the water tank were examined. Additionally, heat curing for ninety days does not have any practical application. The tensile experimental results for the specimens placed in the curing tank and tested at the ninety-day point are presented in Figure 3.18.

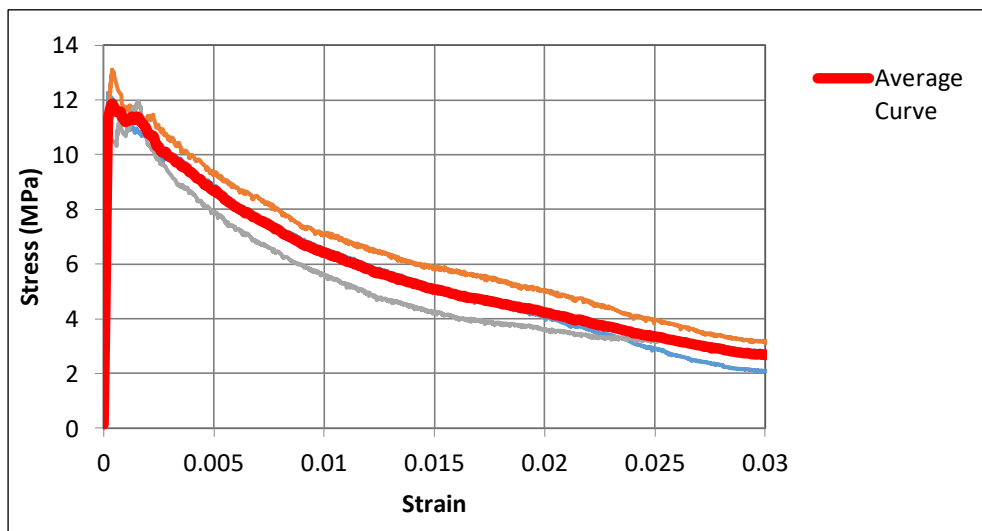


Figure 3.18 Results of the direct tensile tests ninety days after casting for the specimens placed in the water tank

As shown in Figure 3.18, the tensile strength ranged between the values of 11.9 MPa and 13 MPa. In view of the average curve, the tensile strength was equal to 11.9 MPa, and the modulus of elasticity was calculated as 58 GPa. Additionally, the average compressive strength equalled 161 MPa. The results of Figure 3.18 indicate an upward trend of the mechanical properties of the UHPFRC after a twenty-eight day period. Hence, the tensile and the compressive strength of the UHPFRC after the twenty-eight period increased by 7.2% and 7.3% respectively. All the average stress-strain curves of the specimens placed in the water tank and tested at different times are presented in the same graph, Figure 3.19. The average

stress-strain curves of the specimens placed in the steam curing tank, are presented in Figure 3.20.

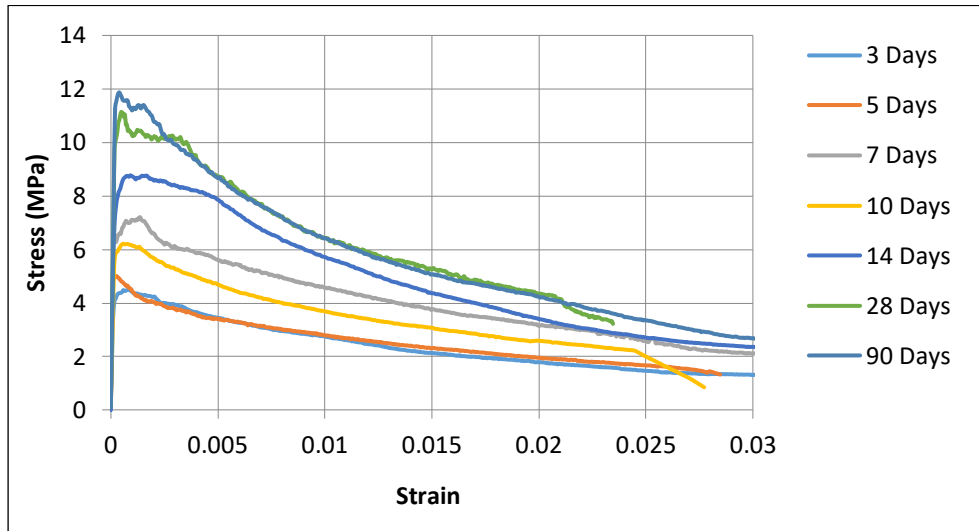


Figure 3.19 Average tensile stress-strain results at different time periods for the specimens placed in the water tank

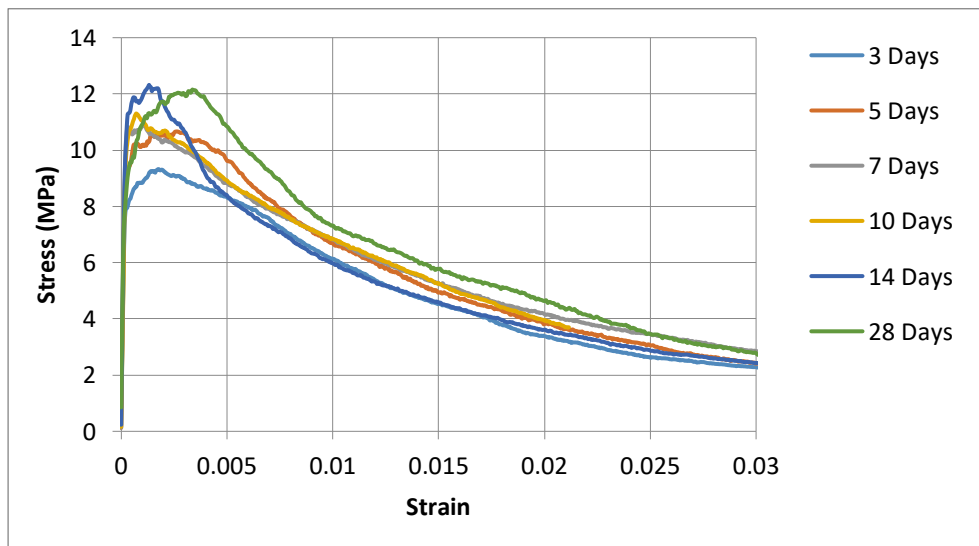


Figure 3.20 Average tensile stress-strain results at different time periods for the specimens placed in the steam curing tank

In Figures 3.21 and 3.22, the maximum tensile and compressive strengths for the differing lengths of time and curing conditions are presented. In the same figures the scatter in the experimental results is also presented.

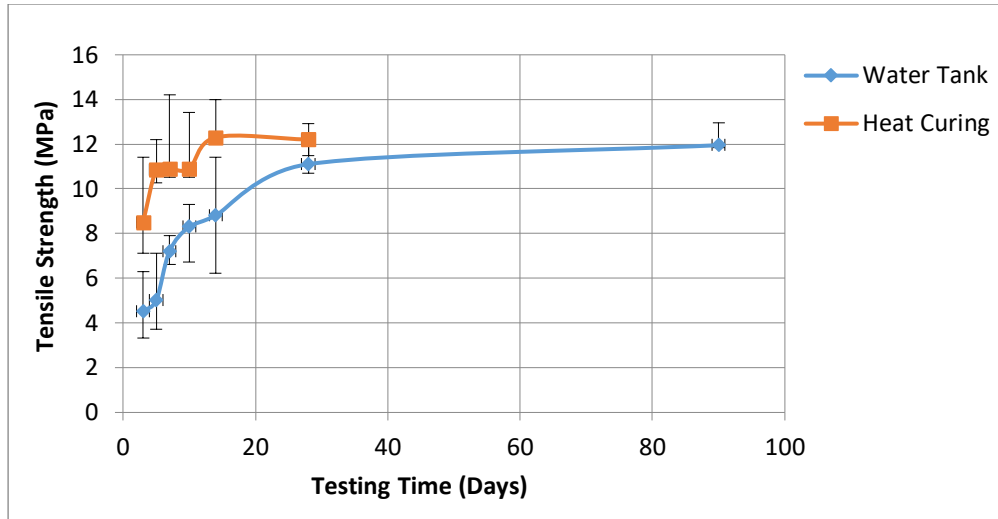


Figure 3.21 Tensile strengths for the different curing conditions

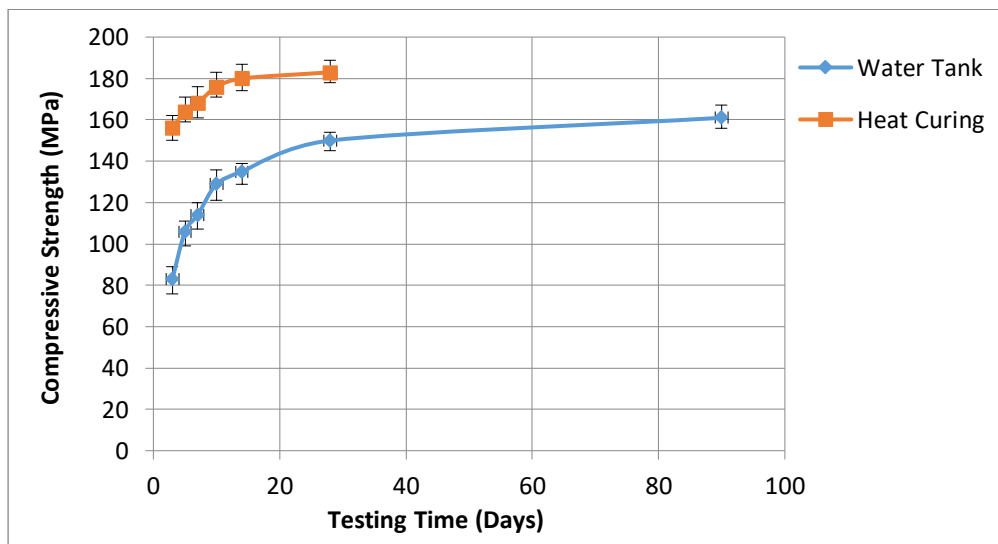


Figure 3.22 Compressive strengths for the different curing conditions

The results of Figures 3.19-3.22 indicate that the tensile and compressive strength of the specimens placed in the water tank presented an upward trend for the entire ninety day period. From the same figures, the effectiveness of the steam curing on the acceleration of the strength development is also clear. As shown in Figure 3.21, the fourteen-day tensile strength of the steam-cured specimens is almost the same as the ninety-day tensile strength of specimens cured under normal curing conditions. This trend is also confirmed from the results of Figure 3.22 for the compressive strengths. As shown in this figure, the compressive strength of the specimens placed in the water tank for ninety days is almost the same as the compressive strength achieved with steam curing for three days. Also, from the experimental results, it can be noticed that the scatter in the experimental results for the compressive tests is not so high compared to the scatter in the experimental results for the direct tensile tests. The distribution

of the fibers is a very important parameter which affects the results of the mechanical testing of the UHPFRC and especially the direct tensile tests. Hence, a local deficiency of the specimens, such as a non-uniform distribution of the fibers, may lead to a premature failure. This has as a result a big scatter in the experimental results. Also, a drawback of these test is that a misalignment of the specimens during the testing is also possible, which can affect the failure mode of the specimens. In Tables 3.4 and 3.5, all the tensile and compressive experimental results for the different curing conditions are presented.

Testing Day	Normal Curing Conditions			
	Mean Tensile Strength (MPa)	Compressive Strengths (MPa)	Mean Compressive Strength (MPa)	Modulus Of Elasticity (GPa)
3	4.5	76	83	31.8
		85		
		82		
		89		
5	5	99	106	44
		108		
		106		
		111		
7	7.2	107	114	51
		116		
		113		
		120		
10	8.3	121	129	50.2
		131		
		128		
		136		
14	8.8	129	135	51.4
		136		
		137		
		139		
28	11.3	145	150	57
		154		
		151		
		150		
90	11.95	156	161	58
		160		
		161		
		167		

Table 3.4 Tensile and compressive results for the specimens placed in the water tank

Testing Day	Steam Curing			
	Mean Tensile Strength (MPa)	Compressive Strengths (MPa)	Mean Compressive Strength (MPa)	Modulus Of Elasticity (GPa)
3	8.5	150	156	46.8
		153		
		159		
		162		
5	10.7	159	164	56
		164		
		171		
		164		
7	10.9	161	168	56.1
		176		
		166		
		169		
10	11.3	171	176	56
		173		
		177		
		183		
14	12.3	174	180	59
		187		
		181		
		178		
28	12.2	178	183	57
		184		
		181		
		189		

Table 3.5 Tensile and compressive results for the specimens placed in the steam curing tank

Comparing the experimental results of the present research for the different curing conditions, it can be noticed that the optimum mechanical properties are achieved for curing in the steam curing tank for twelve days. For normal curing conditions on the other hand, similar properties can be achieved for a curing period longer than twenty-eight days. For the strengthening of the existing RC beams, and in order to achieve the optimum performance of the examined technique, high mechanical properties of the UHPFRC are required. Hereby, considering that for the full scale testing of the present research heat curing cannot be applied, curing with conventional methods (water spraying) for a period higher than twenty eight days must be applied. Consequently, a period of two months is adopted for the curing of the constructed layers and jackets of the present research. This is a time frame which combines both good

mechanical properties, and also it is a reasonable time frame within the purposes of the present research.

3.5 Investigation of different types of fibers

For the previous investigations, conventional steel fibers with a length of 13 mm, a diameter of 0.16 mm and a tensile strength of 3000 MPa were used. In the present section, the performance of UHPFRC using recycled steel fibers retained from car tires has also been investigated. The main benefits of the use of recycled steel fibers are related to the low cost of the fibers, and the fact that this is an environmental friendly solution. More than one billion used tires arise annually globally of which 250.000 in the European Union (EU), and approximately 50 million reach the end of their lives in the United Kingdom per year (European Tire Recycling Association, 2015). It is estimated that more than 500.000 tons of high quality steel fibers could be recovered annually from these used tires in the EU. Tire shredding can be used to recover steel fibers from used tires. During this process, the tires are shredded to pieces. Then, the rubber pieces which contain steel, are placed into a second shredder and shredded to smaller pieces while magnets are used to separate the steel from the rubber. During the final stage, the rubber is granulated to the desired size, in the range of 1 to 10 mm (Pilakoutas et al., 2004).

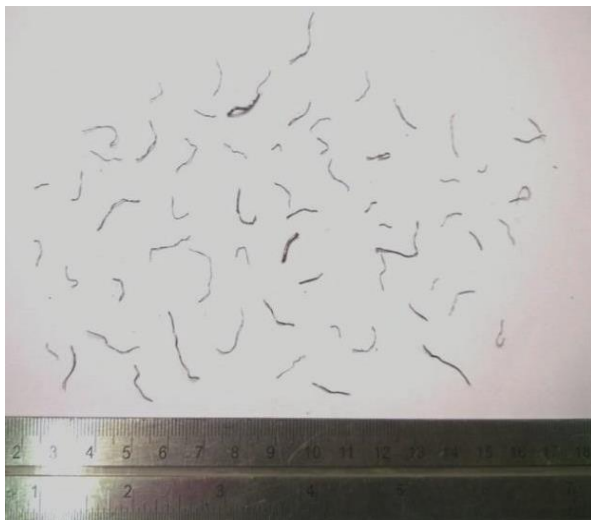


Figure 3.23 Steel fibers retained from car tires

The shredded recycled steel fibers contain small amounts of rubber; careful washing of the fibers is suggested before the mixing of the material. Also, it is important that the long bid wires will be removed before the casting. The shape and size of the fibers is not consistent

(see Figure 3.23), and the fibers tend to become entangled. For this reason, in the present investigation only, short fibers were investigated.

For the investigation of the properties of UHPFRC using recycled steel fibers, both tensile and compressive tests were executed. The experimental setup for these tests is presented in Figure 3.3. For the preparation of the specimens, the mixture design U5 of Table 3.1 and cement 52.5 N type I were used. The results of the previous section have been used for the selection of the curing time and curing regimes of present investigation. In order to achieve high mechanical properties in short period, heat curing has been selected. From the results of the previous section it was found that heat curing for three days has as a result properties of the material which can be achieved with normal curing conditions in twenty-eight days. Hence, three days in the steam curing has been selected for the curing of the specimens. Consequently, after the demolding and casting stage, the specimens were cured by being placed in a steam curing tank at 90 °C (± 2 °C) for three days. In Figure 3.24, the tensile experimental results of the specimens prepared with 3 % recycled steel fibers are presented. In the same figure, the average stress-strain curve is also presented.

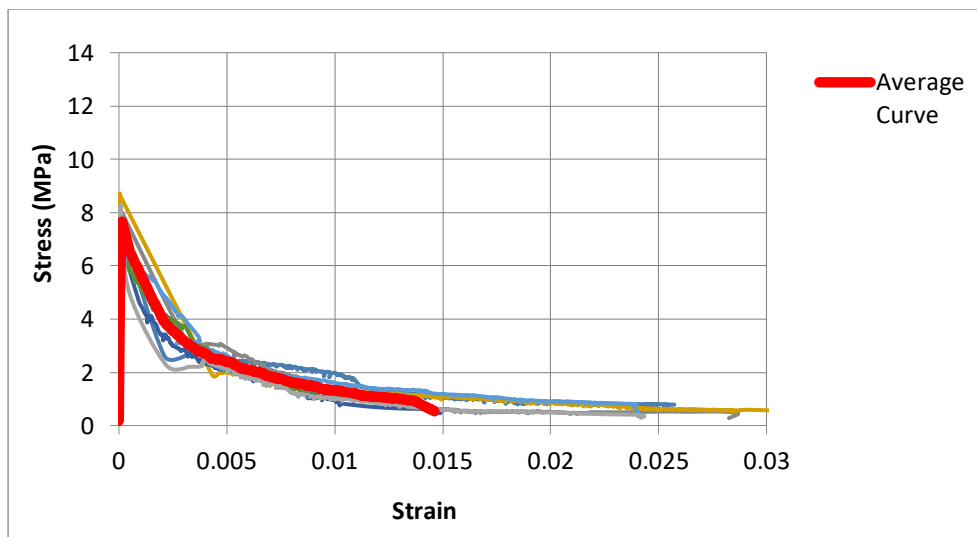


Figure 3.24 Experimental results for the direct tensile tests using 3% recycled steel fibers

The results of Figure 3.24 indicate a scatter in the experimental results between the values of 6.7 MPa and 8.7 MPa. Considering the average curve, the maximum tensile strength was found to be 7.6 MPa, and the modulus of elasticity was calculated equal to 56 GPa. Finally, the average compressive strength of four standard cubes was 167 MPa. Based on the results of Figure 3.24, a strain softening behavior in tension and relatively low tensile strength can be distinguished. Consequently, a higher percentage of recycled steel fibers has also been investigated, namely 6 % per volume. Considering that only short fibers were used in this

investigation, the large volume of fibers in the mixture did not affect the workability of the mixture significantly. In Figure 3.25, the tensile stress-strain results of the specimens prepared with 6% steel fibers are presented.

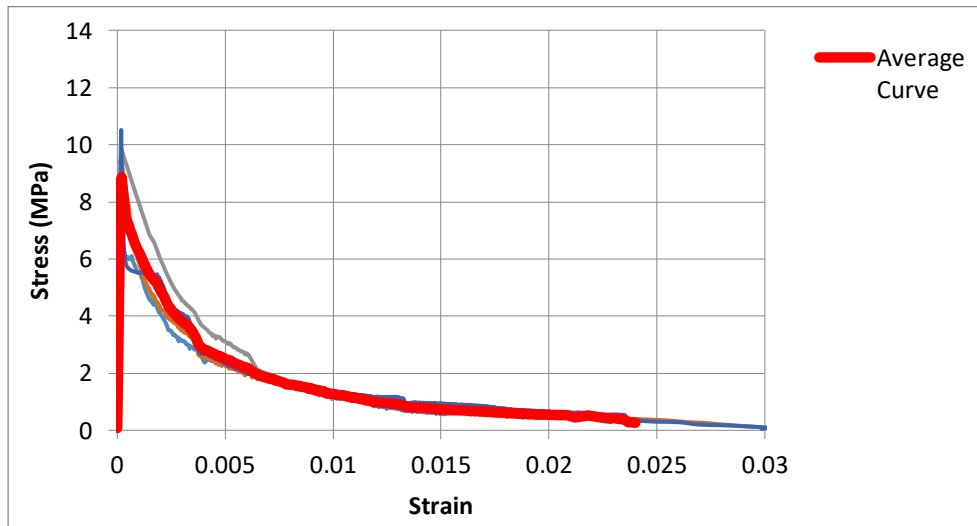


Figure 3.25 Experimental results for the direct tensile tests using 6% recycled steel fibers

As shown in Figure 3.25, the tensile strength was ranged between the values of 6.6 MPa and 10.5 MPa, while the average maximum tensile strength was found to be 8.9 MPa and the modulus of elasticity was calculated equal to 57 GPa. Finally, the average compressive strength of four standard cubes was 184 MPa. The stress-strain results of the specimens prepared with 3 % per volume conventional steel fibers, the same curing conditions and cement 52.5 N type I are presented in Figure 3.13b. All the average stress-strain curves for the different types of fibers and the different fiber contents are presented in the same graph in Figure 3.26, and the experimental results are presented in Table 3.6.

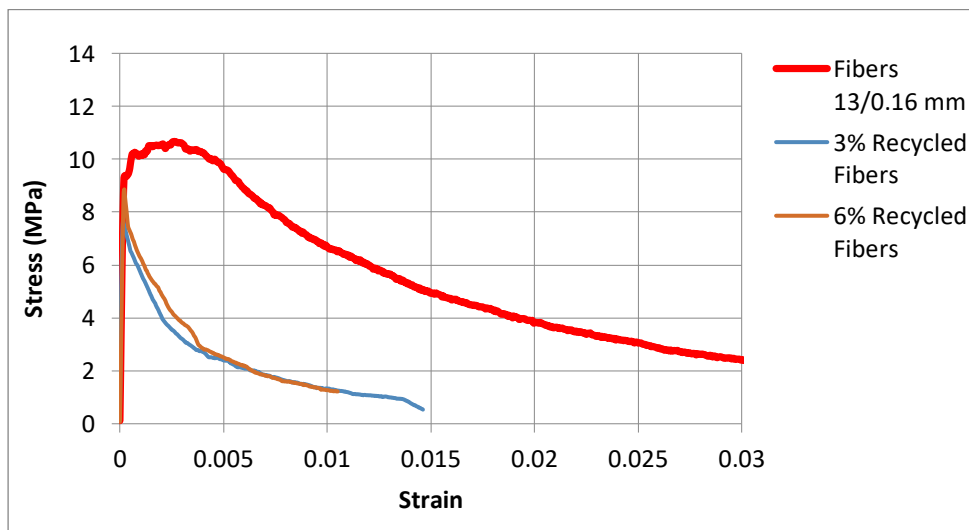


Figure 3.26 Comparison of the results for the different types of steel fibers

Fiber Type and Content	Mean Tensile Strength (MPa)	Compressive Strengths (MPa)	Mean Compressive Strength (MPa)	Modulus Of Elasticity (GPa)
3% Recycled Fibers	7.6	164	167	56
		168		
		165		
		171		
6% Recycled Fibers	8.9	175	184	57
		188		
		182		
		191		
3% Conventional Fibers	10.7	161	164	56
		167		
		169		
		159		

Table 3.6 Experimental results for the different types of fibers

From the results of Figure 3.26 and Table 3.6, it is clear that the optimum performance of the UHPFRC was achieved using the conventional steel fibers (13/0.16 mm). It is also evident that the performance of the specimens prepared with 3% conventional steel fibers is better compared to the performance achieved using 6% recycled steel fibers. Even with this fiber content, strain-softening in tension was observed. In this case, and after the formation of the first cracks, the fibers did not create a bridging of the cracks and the material could not undertake a higher load. This can be attributed, first of all, to the poor bonding between the fibers and the matrix. The recycled fibers contain amounts of rubber. The small amounts of rubber could have affected the bonding. Further, the orientation and the distribution of the fibers is an important parameter, which affects the performance of UHPFRC. Hence, the inconsistent size and shape of the recycled fibers could also affect the orientation and the distribution of the fibers. Due to the fact that the longer recycled steel fibers tend to become entangled, for the preparation of the specimens, only short fibers were used. According to Tlemat et al. (2004), the tensile stress, using this type of fibers, is increasing linearly for increasing length to diameter aspect ratio. Hence, the short fibers and the low aspect ratio of the present investigation could also explain the strain-softening and the low tensile strength of the material.

From the comparison of the compressive strengths, on the other hand, it can be seen that the specimens prepared with 3 % recycled fibers presented almost the same compressive strength as the specimens prepared with the same fiber content using conventional fibers. The optimum

compressive strength was achieved from the specimens prepared with 6 % recycled fibers. From these results, it is clear that the type and the length of the fibers is not crucial for the compressive strength of the material, and similar values were achieved for the same fiber contents.

Based on the experimental results of the present section, conventional steel fibers with a length of 13mm, a diameter of 0.16 mm, a tensile strength of 3000 MPa and a modulus of elasticity of 200 GPa are adopted for the next investigations and the application of the material for the strengthening of existing RC beams.

3.6 The effect of fiber content on the performance of UHPFRC

3.6.1 Experimental investigation

The fiber content is a crucial parameter which affects the performance of UHPFRC. The selection of the appropriate fiber content is related to the desired mechanical properties of the material, the workability of the mixture, the ease of preparation and application of the material and the total cost. The unique properties of UHPFRC are attributed to the incorporation of steel fibers in the mixture and the enhanced tensile characteristics of the material. Different fiber content affect the tensile characteristics of the material, the compressive strength, the workability, the ductility, the fracture energy and the shrinkage of UHPFRC. UHPFRC is a ductile material, which presents strain-hardening and high energy absorption. However, up to date, the effect of fiber content on the tensile characteristics of the material has not been investigated thoroughly. In the literature there are not any studies focused on the performance of UHPFRC in direct tension for different fiber contents. Also, the effect of fiber content on parameters such as the fracture energy, the strain-hardening, the workability and the maximum strength is missing from the literature. The available models in the literature for the modelling of the stress-strain behavior of UHPFRC in tension cannot accurately simulate the response of the material for the different fiber contents. In the present research, different models for the different fiber contents have been proposed for the simulation of the stress-strain behavior of UHPFRC in tension. Finally, the experimental results of the present investigation have been used for the selection of the appropriate fiber content of the realistic application of the material for the strengthening of existing RC members.

In the present section, direct tensile tests and compressive tests were conducted on a number of specimens with various fiber contents and the performance of the material in tension has

been evaluated. Based on the experimental results, different models have been proposed for the modelling of the material in tension for the various fiber contents. An additional investigation has been conducted on the effect of fiber content on the workability and the fracture energy of UHPFRC.

3.6.2 Preparation of the material

The present investigation focuses on the effect of steel fibers on the performance of UHPFRC. Hence, for the preparation of the material, cement 32.5 R type II and the mixture U5 (see Table 3.1) have been adopted. In the present investigation, six different fiber contents were examined, namely 0%, 1%, 2%, 3%, 4% and 6%. The incorporation of higher fiber contents in the mixture results in an ineffective workability of the mixture, and also it is not a cost-effective solution for the preparation of UHPFRC and the application of the material for the strengthening of RC elements. Consequently, higher percentages have not been investigated in the present research. The specimens demolded two days after casting. For the curing, the specimens were placed in a water tank for twenty-six days and tested after twenty-eight days. The mixture designs for the different fiber contents are presented in Table 3.7.

Material	Mixture Proportions (Kg/m ³)					
Cement	657					
GGBS	418					
Silica Fume	119					
Silica Sand	1051					
Superplasticizer	59					
Water	185					
Mixture	D0	D1	D2	D3	D4	D6
Steel Fibers	0 (0%)	78.5 (1%)	157 (2%)	235.5 (3%)	314 (4%)	471 (6%)

Table 3.7 Mixture designs for the preparation of the UHPFRC for the different fiber contents

3.6.3 Measurement of the workability for the different fiber contents

In the present section, the results of the measurement of the workability of UHPFRC for the different fiber contents are presented. The workability of UHPFRC without fibers, and also, with 3 % and 6 % per volume has been measured with a flow table following the procedure described by BS 1015-3:199 (1999). The applied cone had a height of 60 mm, a top diameter of 70 mm and a bottom diameter of 100 mm (see Figure 3.27a). The flow table was filled in two layers, and each layer was tamped ten times with a tamper (see Figure 3.27b). Then, the cone was lifted, and the table was jolted 15 times at a rate of one jolt per second. The diameter of the UHPFRC was determined in two perpendicular diameters, and the average value was considered (see Figure 3.27c). The results of the flow diameter for the different fiber contents are presented in Figure 3.28.

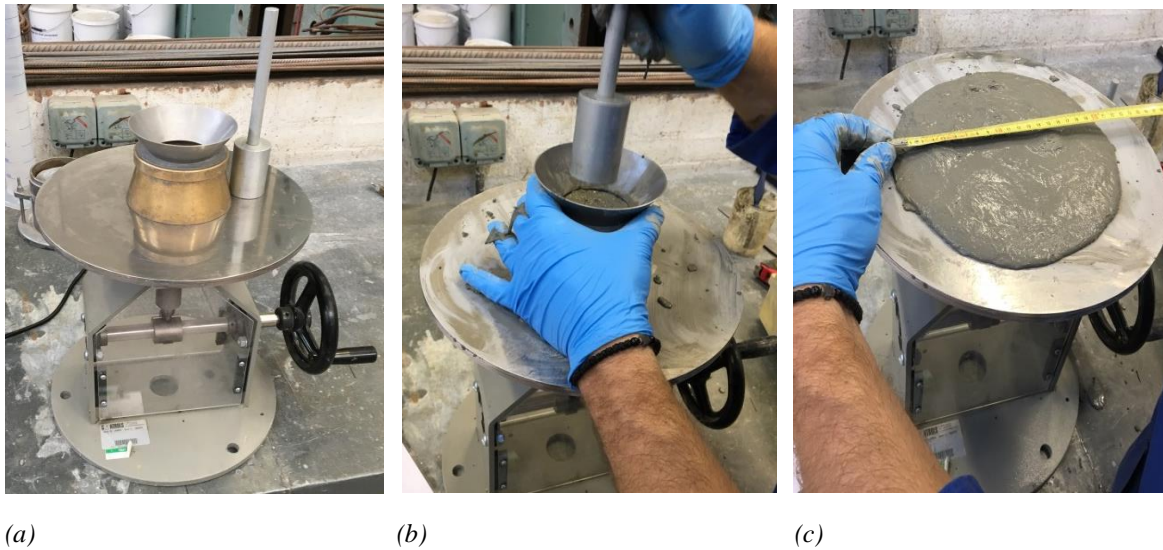


Figure 3.27 Measurement of the workability of UHPFRC: a) flow table used for the measurement of the workability, b) tamping of the UHPFRC, c) measurement of the flow diameter

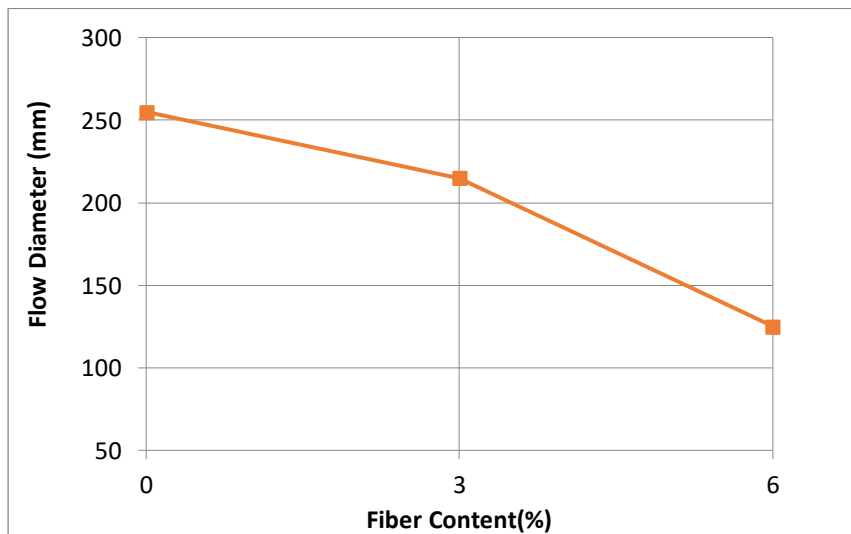


Figure 3.28 Flow diameter results for the different fiber contents

The results of Figure 3.28 indicate that the volume of steel fibers in the mixture affects the workability of UHPFRC significantly. More specifically, while the flow diameter of the Ultra High Performance Concrete (UHPC) mixture without fibers was 255 mm, the respective values for the mixtures with 3 % and 6 % steel fibers were 215 mm and 125 mm. These results indicate a good workability of the mixture without fibers as well as for the mixture with 3 % steel fibers. By contrast, the high volume of steel fibers in the mixture prepared with 6 % steel fibers, caused a pronounced reduction in flow.

3.6.4 Testing of the UHPFRC for the different fiber contents

For the investigation of the tensile characteristics of UHPFRC for the different fiber contents, dog bone shaped specimens were prepared and tested in tension (see Figures 3.2 and 3.3a). Additionally, for each investigation, four standard cubes with side lengths of 100 mm were prepared and tested in compression (see Figure 3.3b). The first examined mixture was the mixture D0 (see Table 3.7), which was prepared without the use of steel fibers. In Figure 3.29, the experimental results of the direct tensile tests are presented. As shown in this figure, a brittle behavior of the material can be determined. Once the specimens reached their maximum strength, a sudden failure occurred. The maximum tensile strength ranged between the values of 2.2 MPa and 5.1 MPa. In view of the average curve, the maximum stress was found to be equal to 4.5 MPa while the modulus of elasticity was calculated to be 46 GPa. Finally, the average compressive strength was 101 MPa.

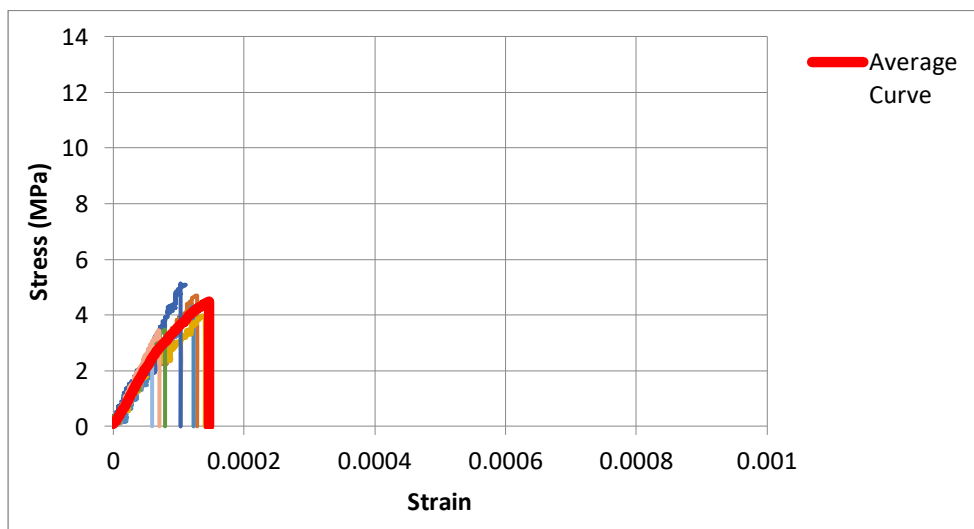


Figure 3.29 Tensile stress-strain results for plain UHPC

The next investigation constitutes the study of the properties of UHPFRC using 1 % steel fibers. The tensile results are presented in Figure 3.30. As illustrated in this figure, the maximum stress ranged between 5.5 MPa and 8.2 MPa. Based on the average curve, the maximum tensile strength was equal to 6.5 MPa. From the linear part of the stress-strain curve, the modulus of elasticity was calculated to be 52.4 GPa. The average compressive strength was 102 MPa.

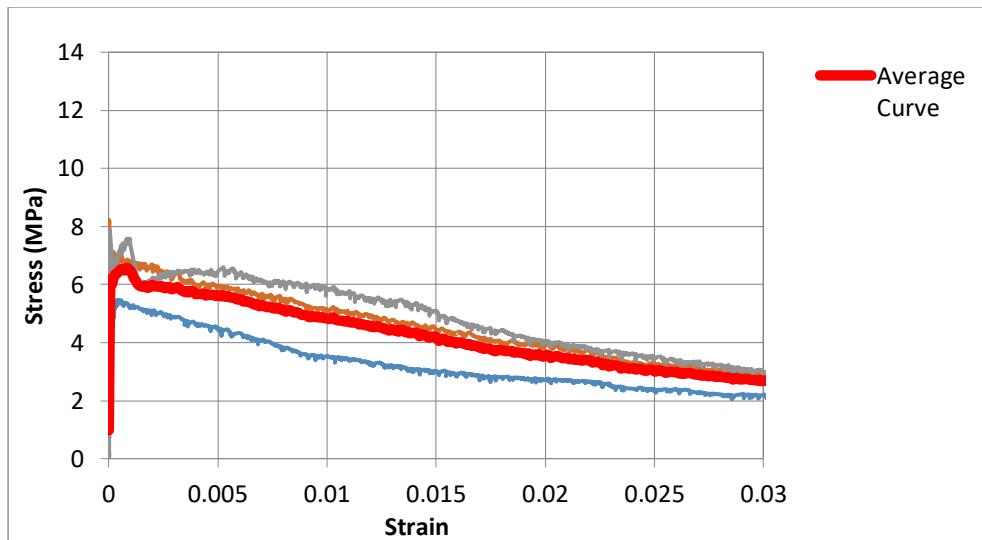


Figure 3.30 Tensile stress-strain results for the specimens prepared with 1 % steel fibers

For the next investigation, a higher percentage of steel fibers was incorporated into the mixture; 2 % per volume. The experimental results in tension are presented in Figure 3.31. The results of this figure indicate a scatter in the experimental results between the values of 8.1 MPa and 9.7 MPa. Considering the average curve, the maximum tensile strength was found to be equal to 8.4 MPa, and the modulus of elasticity was 53.3 GPa. The average compressive strength was 116 MPa. From these results, an upward trend of the tensile and compressive strength can be observed for increasing fiber contents.

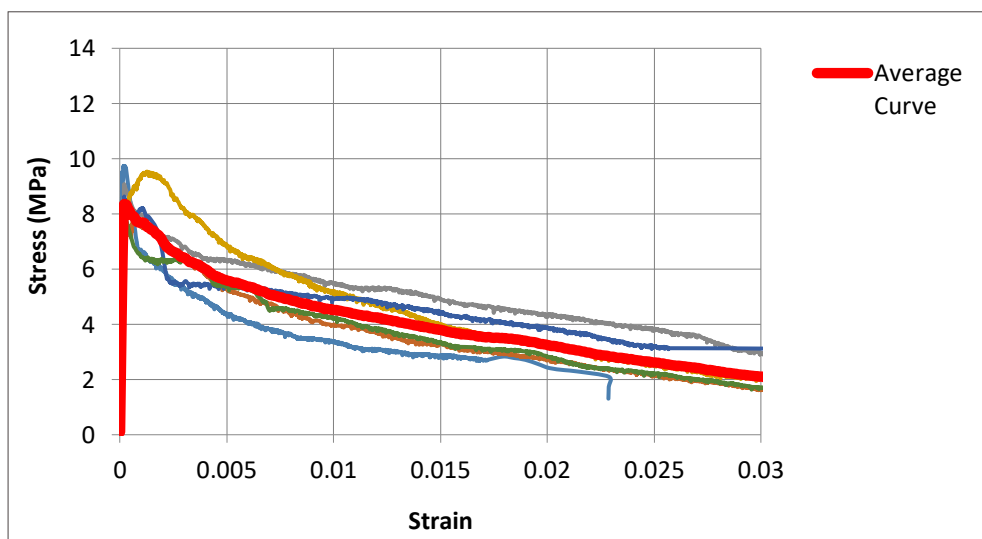


Figure 3.31 Tensile stress-strain results for the specimens prepared with 2 % steel fibers

The next investigation involved the preparation of specimens using 3 % steel fibers. The experimental results are presented in Figure 3.32. As illustrated in this figure, the maximum tensile strength ranged between the values of 7.9 MPa and 11.4 MPa, and based on the average curve, the maximum tensile strength was equal to 9.6 MPa. The modulus of elasticity was

calculated to be 52.3 GPa, and the average compressive strength was 126 MPa. Comparing the results obtained for the specimens prepared with 2% and 3% steel fibers, an increase of 14% on the tensile strength and 7% on the compressive strength can be seen with the incorporation of a 1% higher quantity of steel fibers in the mixture. On the contrary, the modulus of elasticity was not affected.

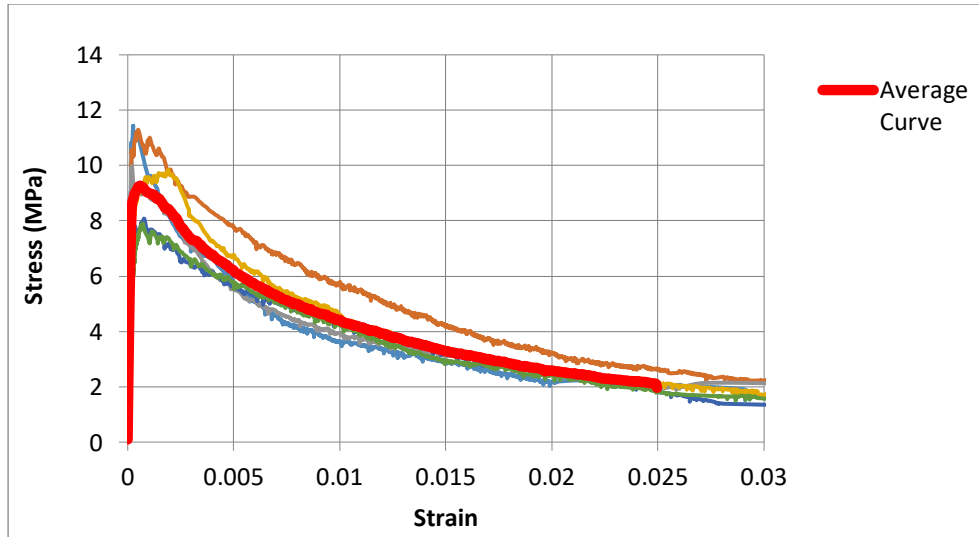


Figure 3.32 Tensile stress-strain results for the specimens prepared with 3 % steel fibers

The next investigation constitutes the study of the performance of UHPFRC using 4% per volume steel fibers. The experimental results in tension are presented in Figure 3.33. As shown below, the maximum tensile strength was in the range of 10.3 MPa and 16.8 MPa. Taking into account the average curve, the maximum tensile strength was found to be equal to 11.3 MPa. The modulus of elasticity, was calculated to be 53.5 GPa, and the average compressive strength was 136.1 MPa. The results of mixture D4 confirm the effectiveness of the steel fibers to increase the strength of the specimens. Hence, when the fiber content was increased from 0% to 4%, an increase of 151% on the tensile strength and 29% on the compressive strength was noticed. For this reason, an even higher percentage of steel fibers was investigated, namely 6%.

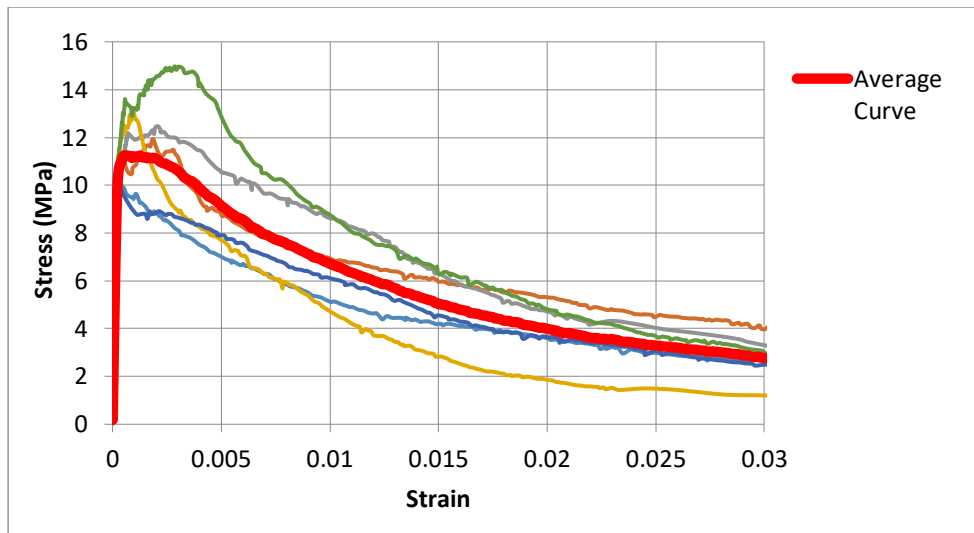


Figure 3.33 Tensile stress-strain results for the specimens prepared with 4 % steel fibers

The stress-strain results of mixture prepared with 6 % steel fibers are presented in Figure 3.34. The scatter in the experimental results was between the values of 10.2 MPa and 17.3 MPa. Based on the average stress-strain curve, the maximum load was found to be equal to 12.5 MPa. From the linear part of the stress-strain curve, the modulus of elasticity was calculated to be 53.1 GPa. An extremely high value of compressive strength was also achieved for this percentage of fibers with 176 MPa.

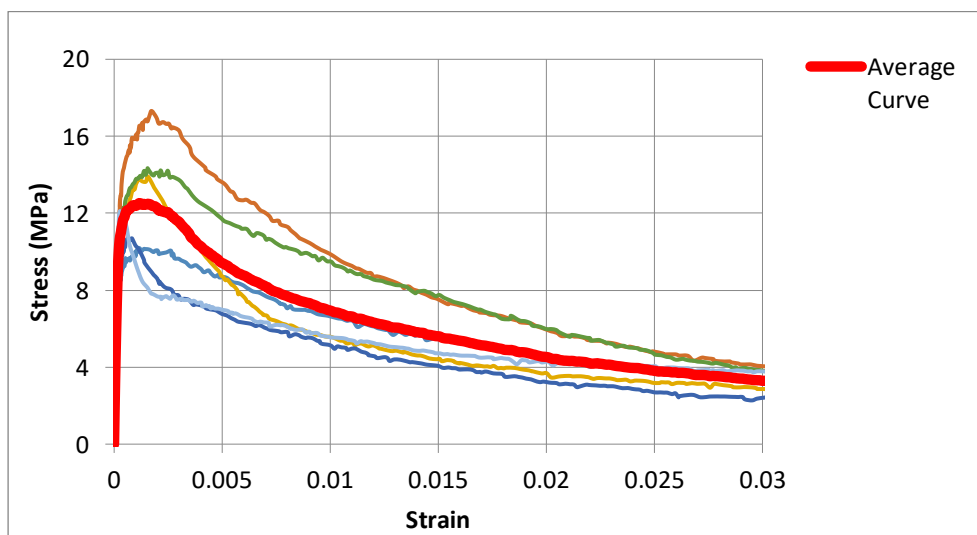


Figure 3.34 Tensile stress-strain results for the specimens prepared with 6 % steel fibers

All the average stress-strain curves, for the different fiber contents are presented in the same graph in Figure 3.35. The maximum tensile strength and the maximum compressive strength for the different fiber contents are presented in Figures 3.36 and 3.37 respectively. In these figures the scatter in the experimental results is also presented.

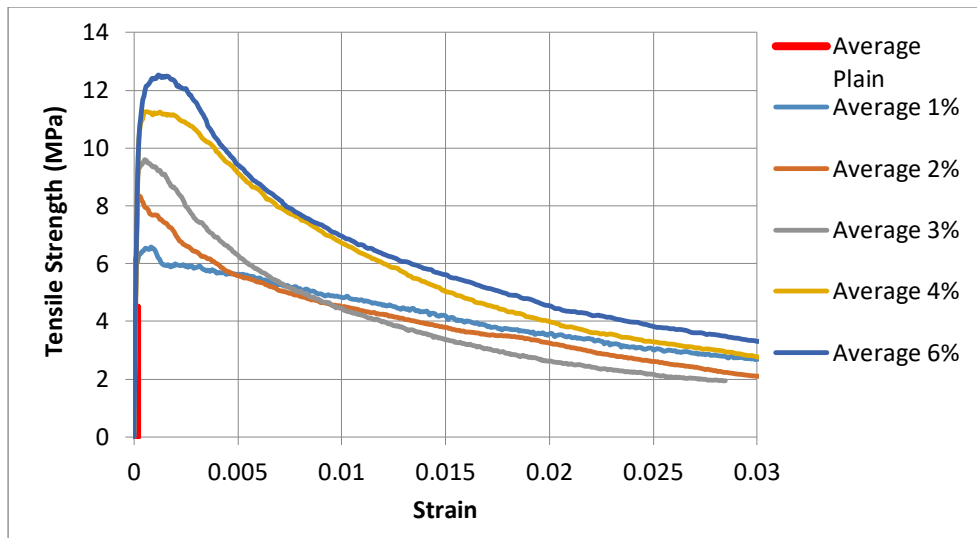


Figure 3.35 Average stress-strain results for the different fiber contents

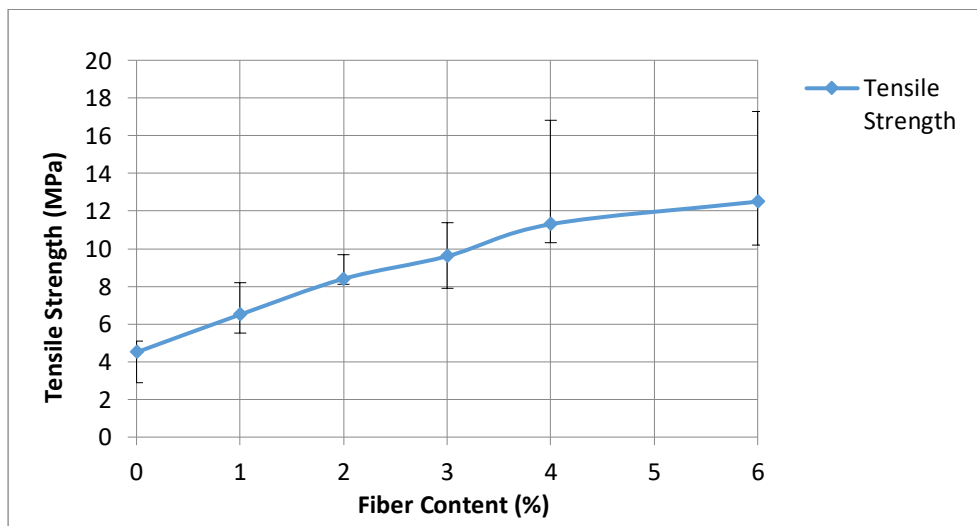


Figure 3.36 Tensile strengths for the different fiber contents

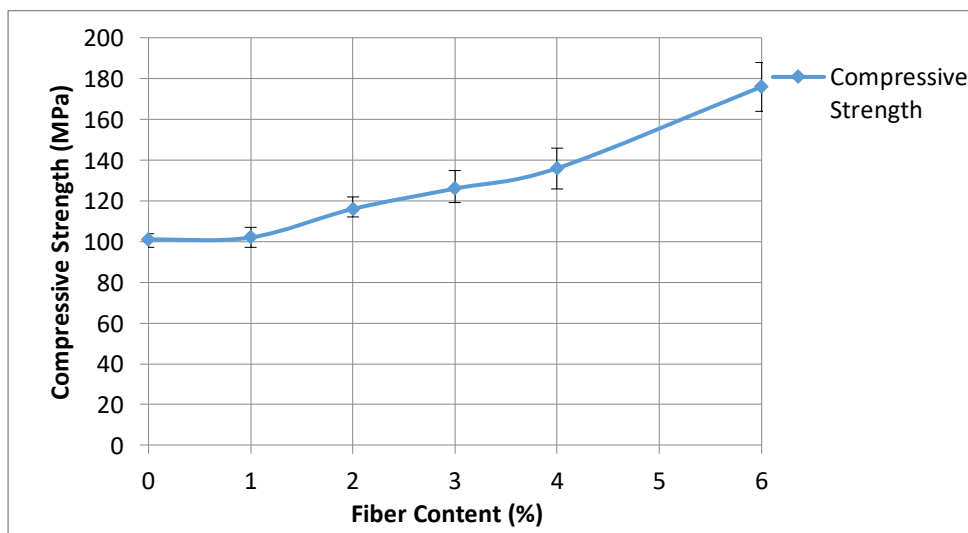


Figure 3.37 Compressive strengths for the different fiber contents

From the results of the figures above, it is clear that the steel fiber content affects not only the tensile strength of the UHPFRC, but also the tensile characteristics of the material, such as the post elastic state. Hence, when the fiber content increased from 0 % to 6 %, the tensile strength increased by 178% while the post-elastic state was also increased. The high volume of fibers in the mixture had, as a result, after the formation of the first cracks, more fibers to undertake the load and to create a strong bridging of the cracks. Consequently, a higher load carrying capacity was achieved for higher percentages of steel fibers. From Figure 3.37 also, it is evident that fiber content affects the compressive strength, and for increasing fiber contents, higher compressive strength was achieved. The steel fibers in the mixture creates a strong matrix, which increases the crack resistance of the material. Therefore, a higher compressive strength is achieved. Also, it can be noticed that for increasing fiber content there is a higher scatter in the experimental results. This can be attributed to the non-uniform distribution of the fibers in the mixture for higher fiber contents. In Table 3.8 all the values for the tensile and compressive strengths for the different fiber contents are presented.

Fiber Content (%)	Mean Tensile Strength (MPa)	Compressive Strengths (MPa)	Mean Compressive Strength (MPa)
0	4.5	98	101
		102	
		101	
		104	
1	6.5	97	102
		104	
		101	
		107	
2	8.4	114	116
		112	
		117	
		121	
3	9.6	119	126
		124	
		135	
		130	
4	11.3	126	136
		135	
		139	
		146	
6	12.5	164	176
		188	
		183	
		169	

Table 3.8 Experimental results for the different fiber contents

3.6.5 Modelling of the stress-strain and the stress-crack opening behavior of UHPFR in tension for the different fiber contents

The experimental results of the investigation of the effect of different fiber contents on the tensile performance and on the stress-strain response of UHPFRC, were used to model the behavior of the material in tension. The behavior of the material is divided in two parts. The parts are; first up to a maximum stress level and second after the maximum stress level is reached, when the response of the material is governed by the formation of a single crack. The direct tensile results show that the stress-strain behavior up to a maximum stress level depend on the amount of steel fibers in the mixture. Hence, for the different fiber contents, different ascending branches can be distinguished as presented in Figures 3.38a-3.38c.

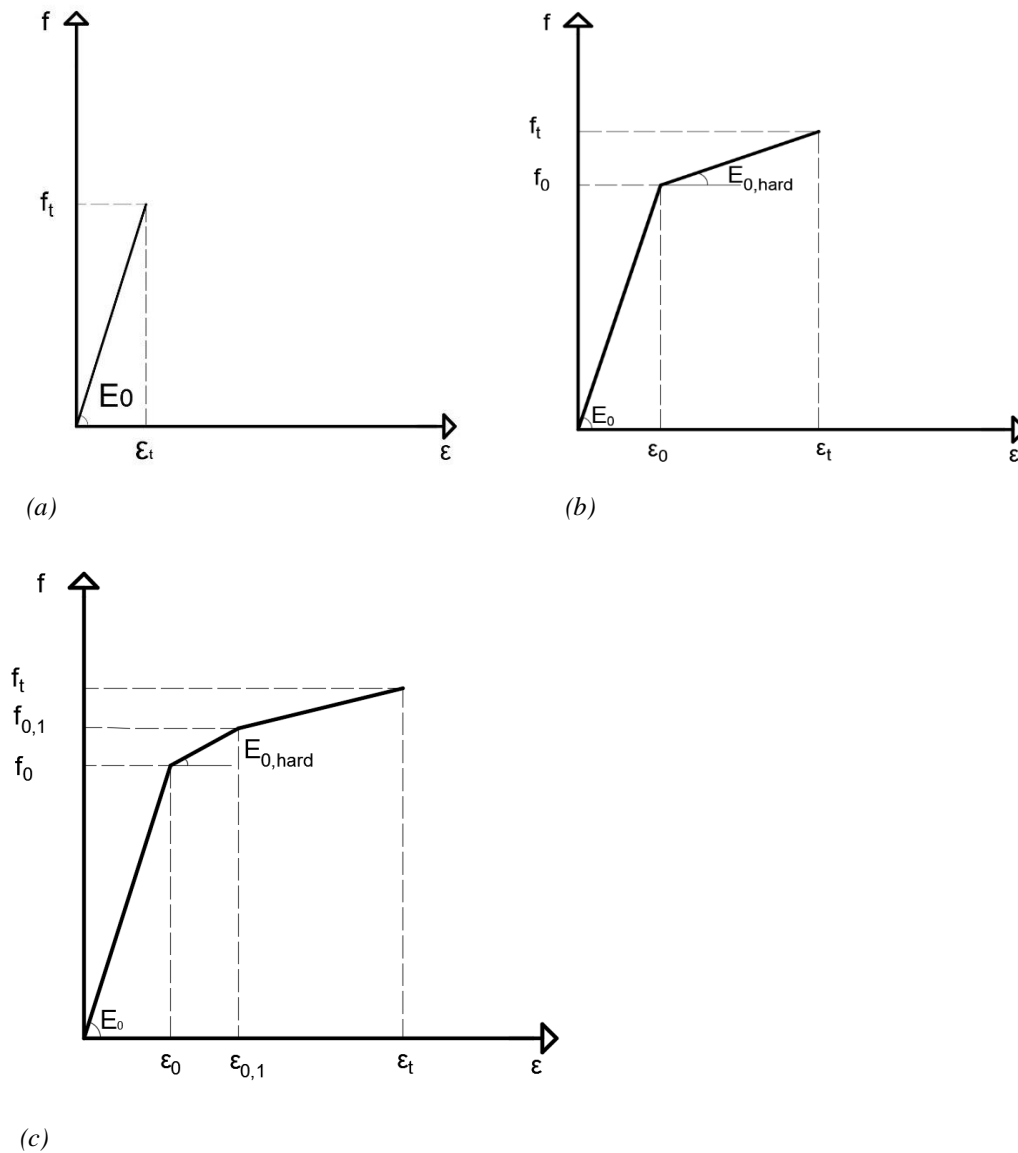


Figure 3.38 a) Tensile stress-strain model for the specimens with 1 % steel fibers, b) tensile stress-strain model for the specimens with 2 % and 3 % steel fibers, c) tensile stress-strain model for the specimens with 4 % and 6 % steel fibers

The tensile behavior of specimens with 1% steel fibers is characterized by strain-softening behavior and the initial response was simulated with one linear branch up to a maximum stress level (Figure 3.38a). Specimens with 2 and 3% steel fibers on the other hand, presented strain-hardening behavior and two branches were used to represent the stress-strain behavior up to a maximum stress level (Figure 3.38b). The first branch was limited to the end of the elastic state (f_0, ϵ_0) and the second ended at the maximum stress (f_t, ϵ_t). Finally, the incorporation of high percentages of steel fibers (4 and 6 %) caused a pronounced strain-hardening state. Hence, a third branch ($f_{0,1}, \epsilon_{0,1}$) was inserted in the ascending branch in order to simulate the behavior of the material up to the maximum stress level (Figure 3.38c).

The effect of fiber content in the post-elastic state, is shown in Figure 3.39. In this figure, the strain-hardening of the average curves of specimens with 3, 4 and 6% steel fibers is presented. As shown in this figure, the strain-hardening of the specimens with 3% can be represented with one branch. However, for specimens with 4 and 6 % steel fibers, a second branch in the post-elastic state can be distinguished and is required in this state to model the strain-hardening of the specimens with this fiber contents.

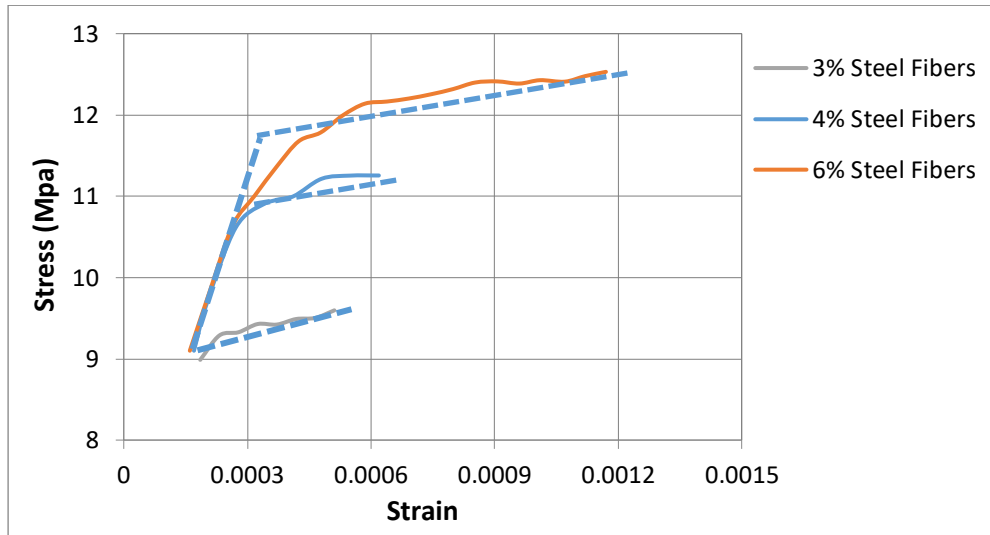


Figure 3.39 Strain-hardening for the different fiber contents

Similar models for the modelling of the stress-strain behavior proposed by Habel et al. (2006) for UHPFRC and RILEM TC 162-TDF (2002) for SFRC. The experimental results of the present study indicate that the responses of specimens up to a fiber content of 3%, are in good agreement with the shape of existing models available in the literature (Habel et al., 2006). However, existing models could not accurately model the response of specimens with higher fiber contents. Therefore, in the present study, the response of mixtures with fiber contents higher than 3%, was modelled with a tri-linear model. The characteristic values of the proposed models of Figures 3.38a-3.38c are presented in Table 3.9.

Fibers (%)	f_0 (MPa)	ε_0	$f_{0,1}$ (MPa)	$\varepsilon_{0,1}$	f_t (MPa)	ε_t	E_0 (GPa)	$E_{0,hard}$ (GPa)
1	-	-	-	-	6.5	0.00012	52.4	-
2	8.0	0.00015	-	-	8.4	0.00036	53.3	1.9
3	8.9	0.00017	-	-	9.6	0.00050	52.3	2.1
4	9.1	0.00017	10.6	0.00027	11.3	0.00055	53.5	15
6	8.5	0.00016	11.5	0.00030	12.5	0.00120	53.1	21.4

Table 3.9 Stress and strain values for the different fiber contents

In all the examined cases, in which the tensile response was characterized by a strain-hardening behavior (2-6%), the second modulus elasticity ($E_{0,hard}$) was calculated. This can be defined as the ratio of the stress to strain in the hardening state (Figures 3.38b and 3.38c). From the calculation of the second modulus of elasticity, it was evident that as the volume fraction of the fibers increased the second modulus of elasticity also increased.

The stress-crack opening behavior can be modelled with a bi-linear curve, as illustrated in Figure 3.40, and the obtained characteristic values are presented in Table 3.10. The proposed values of the present study in this state are in good agreement with the findings of other researchers for similar models. Based on the model proposed by Habel et al. (2006), it is considered that at approximately half of the fiber length, no more stresses are transferred through the crack. This assumption is in good agreement with the proposed values of the current study, which are based on the experimental results, and have been found to be in the range of 5.3-6.6 mm, for a fiber length of 13 mm.

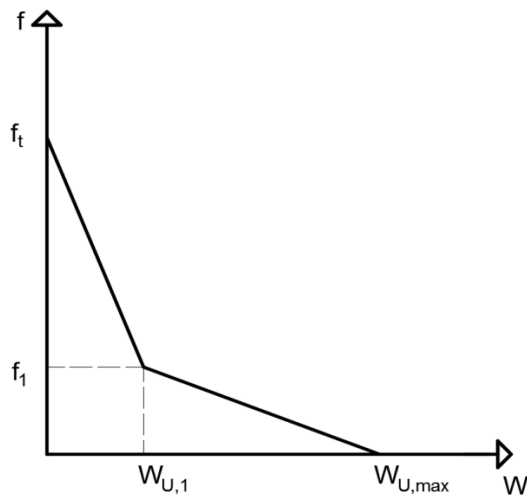


Figure 3.40 Stress-crack opening model

Fibers (%)	σ_1 (MPa)	$W_{u,1}$ (mm)	$W_{u,max}$ (mm)
1	3.8	1.2	6.6
2	3.5	1.2	5.6
3	3.6	0.9	5.3
4	4.2	1.6	5.7
6	5.2	1.2	6.1

Table 3.10 Stress and crack opening values for the different fiber contents

3.6.6 The effect of fiber content on the fracture energy of UHPFRC

The steel fiber content apart from the mechanical properties may affect the dissipated energy of the material until their failure. In the present section, the effect of fiber content on the fracture energy of UHPFRC has been investigated. More specifically, the fracture energy has been calculated based on the average tensile stress-strain curves, for the different fiber contents. The fracture energy can be defined as the dissipated work which is necessary for the separation of two crack surfaces (Wille and Naaman, 2010). The fracture energy can be calculated by the following equation:

$$G = \frac{Q}{A_f} = \frac{\int_{w=0}^{w=w_u} F_t(w) \cdot dw}{A_f} \quad (3.1)$$

Where Q is the dissipated work needed for the generation of a crack; A_f is the crack fracture area; F_t is the load applied in tension; w is the crack opening; w_u is the crack opening up to complete separation; w_m is the permanent crack opening.

The fracture energy can be distinguished in the energy dissipated during the strain hardening (G_a) and the strain softening (G_b), as presented in Figure 3.41.

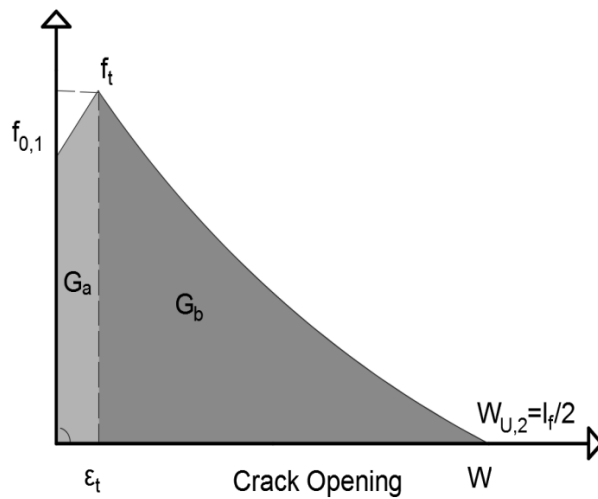


Figure 3.41 Fracture energy related to the failure causes the crack

Based on Figure 3.41, the fracture energy is given from the equation below:

$$G = G_a + G_b \quad (3.2)$$

The fracture energy for the different fiber contents has been calculated and it is presented in Table 3.11.

Steel Fibers (%)	Fracture Energy (KJ/m ²)
1	18.2
2	18.4
3	18.5
4	24.4
6	28.4

Table 3.11 Fracture energy for the different fiber contents

The results of Table 3.11 indicate that high values of fracture energy can be achieved for high percentages of steel fibers. For fiber contents between 1-3 % the fracture energy presented a minor upward trend at increasing fiber dosage. Fracture energy values equal to 24.4 KJ/m² and 28.4 KJ/m² were obtained for specimens with 4 and 6 % steel fibers respectively. These values are in the range of reported values in the literature for similar investigations. Benson and Karihaloo (2005), recorded a value of fracture energy equal to 20 KJ/m² using 6 % steel fibers, while for the same fiber content, a value of 24 KJ/m² was recorded by Habel et al. (2006). Wille and Naaman (2010), conducted a research on the improvement of the fracture energy of UHPFRC, and with an optimized UHPFRC with a compressive strength of 200 MPa they found a fracture energy which exceeded 30 KJ/m² using 1.5 % twisted steel fibers.

3.7 Measurement of shrinkage of UHPFRC

An important phenomenon for the cementitious materials is shrinkage, which is related to the loss of water from the mass of the materials and results in the reduction of the volume. This produces cracks, which can affect the mechanical properties and the durability of the materials. The shrinkage is divided into two categories; free and constrained shrinkage. The main types of free shrinkage are plastic, drying, autogenous and carbonation shrinkage. Plastic shrinkage is related to the loss of moisture in fresh concrete. This is attributed to the evaporation of water from the surface or with the fact that the aggregates in the mixture absorb the water. Drying shrinkage refers to the loss of water due to the drying of concrete in hardened concrete. As a result, a change in the volume of the concrete occurs. Autogenous shrinkage concerns the shrinkage in conservative systems. This happens during the hydration process. At this stage, fine capillaries are shaped. Finally, carbonation shrinkage is due to the

reaction of the ingredients of concrete to carbon dioxide. Constrained shrinkage, on the other hand, is where the elements cannot deform freely because of their connection to another element (Sahinagic-Isovic et al., 2012).

In the present section, the drying shrinkage of UHPFRC has been investigated. Six UHPFRC prisms with dimensions of 75x75x280 mm were prepared in total. More specifically, three prisms were prepared using 3 % per volume steel fibers, and three specimens were prepared without the use of steel fibers. The shrinkage was measured at different points in time. Mixture U5 (see Table 3.1) was used for the preparation of the specimens. The specimens were stored in a room with a relative humidity of 42 % and a temperature of 20 °C, conditions similar to the standard climate, as proposed by DIN 50014 (1985) (temperature 23 ± 2 °C and relative humidity RH 50 ± 5).

After the demolding of the specimens two days after the casting, the prisms were placed in a metal frame and the shrinkage was measured using dial gauges. The experimental setup for these tests is presented in Figure 3.42.

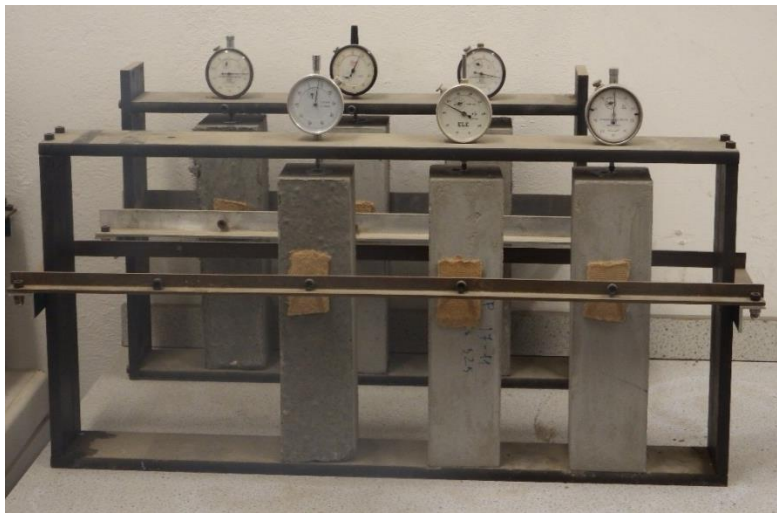


Figure 3.42 Experimental setup for the measurement of shrinkage

The average measurements of shrinkage over different time periods for the different percentages of steel fibers are presented in Figure 3.43.

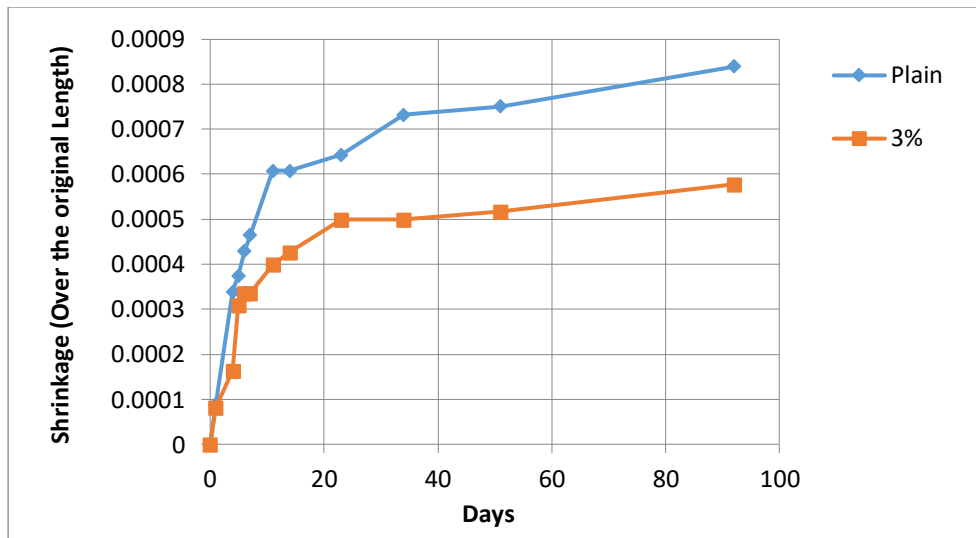


Figure 3.43 Results for the drying shrinkage of plain UHPC and UHPFRC with 3 % steel fibers

As shown in the figure above, the specimens prepared with 3 % steel fibers presented significantly lower values of shrinkage compared to the specimens without fibers. Consequently, the drying shrinkage of the specimens prepared with 3 % steel fibers over three months was 29 % lower compared to the value of shrinkage obtained for the specimens without fibers. The steel fibers in the mixture increases the crack resistance of the material and can reduce the shrinkage of the material. Also, it can be noticed that, in all the examined cases, the drying shrinkage during the first month increased rapidly. After this period, higher values of shrinkage were recorded, but the shrinkage increased with a lower rate.

3.8 Investigation of the ‘size effect’ of UHPFRC

In the present research, UHPFRC layers and jackets will be cast for the strengthening of the existing RC beams. An important parameter which may affect the performance of the technique is the depth of the layer. Thick elements are more likely to have a non-uniform distribution of the fibers in their mass, which can affect their performance. The non-uniform distribution of the fibers can be related to parameters such as; the compaction of the material, the type and the dimensions of the fibers or the casting procedure. In the present section the ‘size effect’ of UHPFRC prisms with various depths has been investigated and a model for the correlation of the tensile strength with the respective flexural strength of UHPFRC has been proposed.

3.8.1 Specimens and Materials

The present investigation concerns the performance of UHPFRC prisms with various layer depths. More specifically, prisms with four different depths were prepared for the investigation of the ‘size effect’ of the UHPFRC ranging between 25 mm and 100 mm. The length and breath for all the examined prisms was the same with 500 mm and 100 mm respectively. Hereby, the dimensions of the prisms were: 25x100x500 mm, 50 x100x500 mm, 75 x100x500 mm, and 100x100x500mm. In Figure 3.44, the examined prisms are presented.

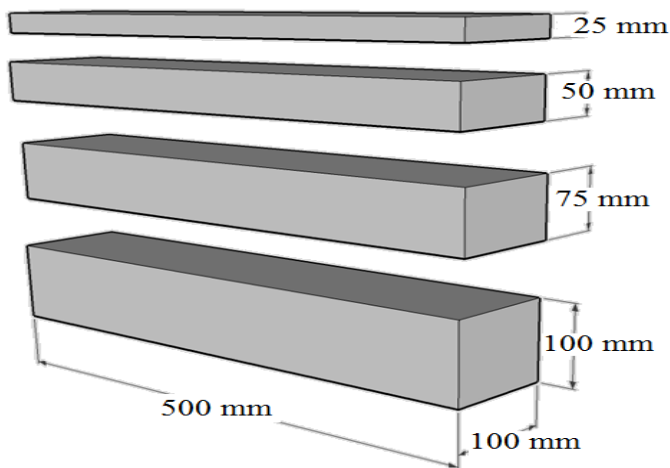


Figure 3.44 Geometry of the examined prisms

For the preparation of the specimens, the mixture U5 (see Table 3.1) was used together with high strength cement 52.5 N type I. The preparation of the prisms with the different depths is presented in Figure 3.45.

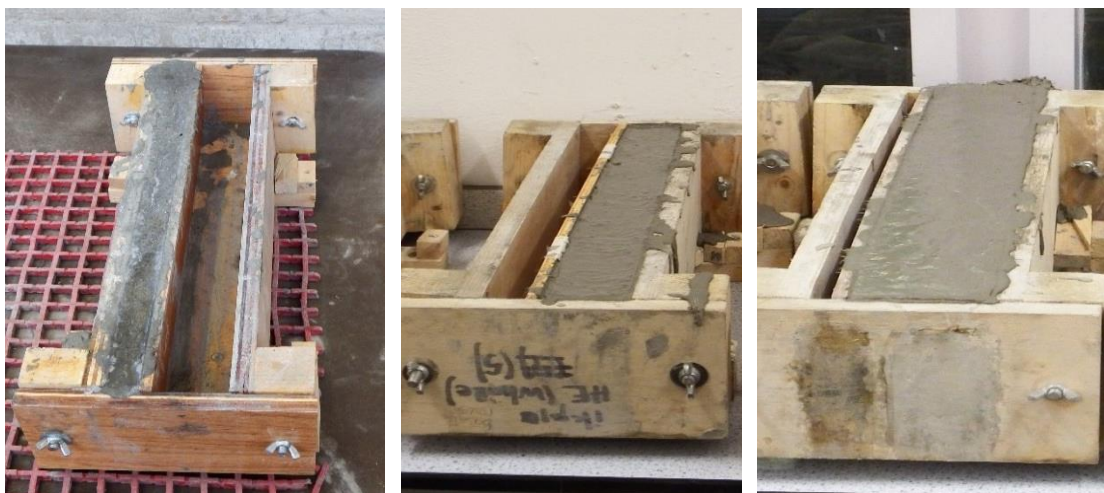


Figure 3.45 Preparation of prisms with different depths

For the curing of the specimens, after the demoulding two days after the casting, the specimens were placed in the steam curing tank for three days in 90 °C ($\pm 2^\circ\text{C}$). From the investigation of the effect of curing time and curing regime on the performance of UHPFRC, it was found that curing for three days in the steam curing tank has as a result high mechanical properties for the material, almost the same obtained for curing in a water tank for twenty eight days. Hereby, this time frame was also adopted in the present investigation.

3.8.2 Testing Setup and Experimental Results

Direct tensile tests of dog bone shaped specimens were conducted using the setup of Figure 3.3a. Due to the scatter in the experimental results six specimens were tested. The tests were conducted under the same displacement control with the previous investigations, namely of 0.007 mm/sec. The stress-strain results of all the direct tensile tests are presented in Figure 3.46.

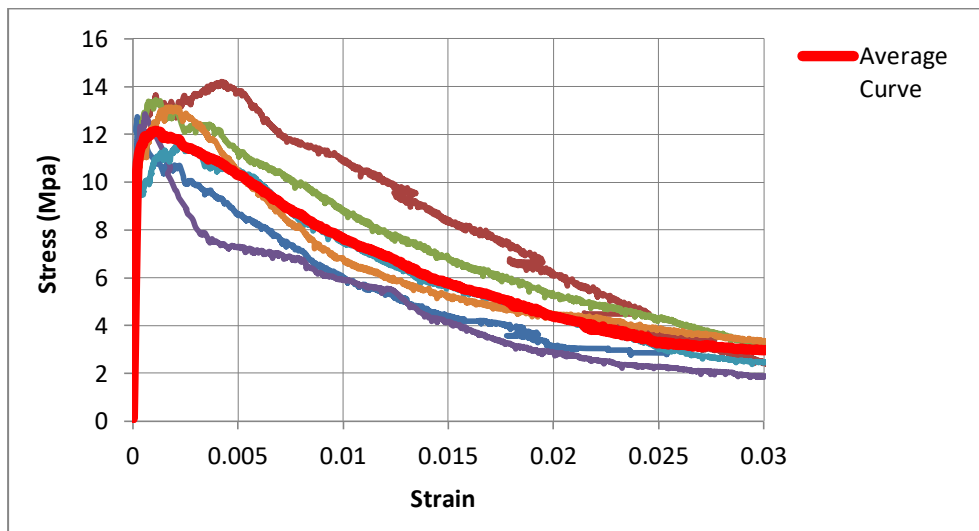


Figure 3.46 Experimental results of the direct tensile tests

The experimental results indicate a scatter in the experimental results between the values of 11.74 MPa and 14.20 MPa. An average stress-strain curve was calculated and the average tensile strength was found to be 12.10 MPa, while the modulus of elasticity was calculated to be 54 GPa.

3.8.3 Flexural Tests of Prisms

For the investigation of the ‘size effect’ on the flexural performance of UHPFRC, three flexural tests were performed for each different depth value. The tests were conducted under four point loading with a span length of 300 mm and a distance of 100 mm between the two loading points. Two LVDTs were used to record the deflection of the prisms on both sides and the tests were conducted using a displacement control of 0.001 mm/sec, as proposed by JSCE-SF4 (1984). An external yoke was used in order to exclude any additional displacement at the support. The testing setup for these tests is presented in Figure 3.47.

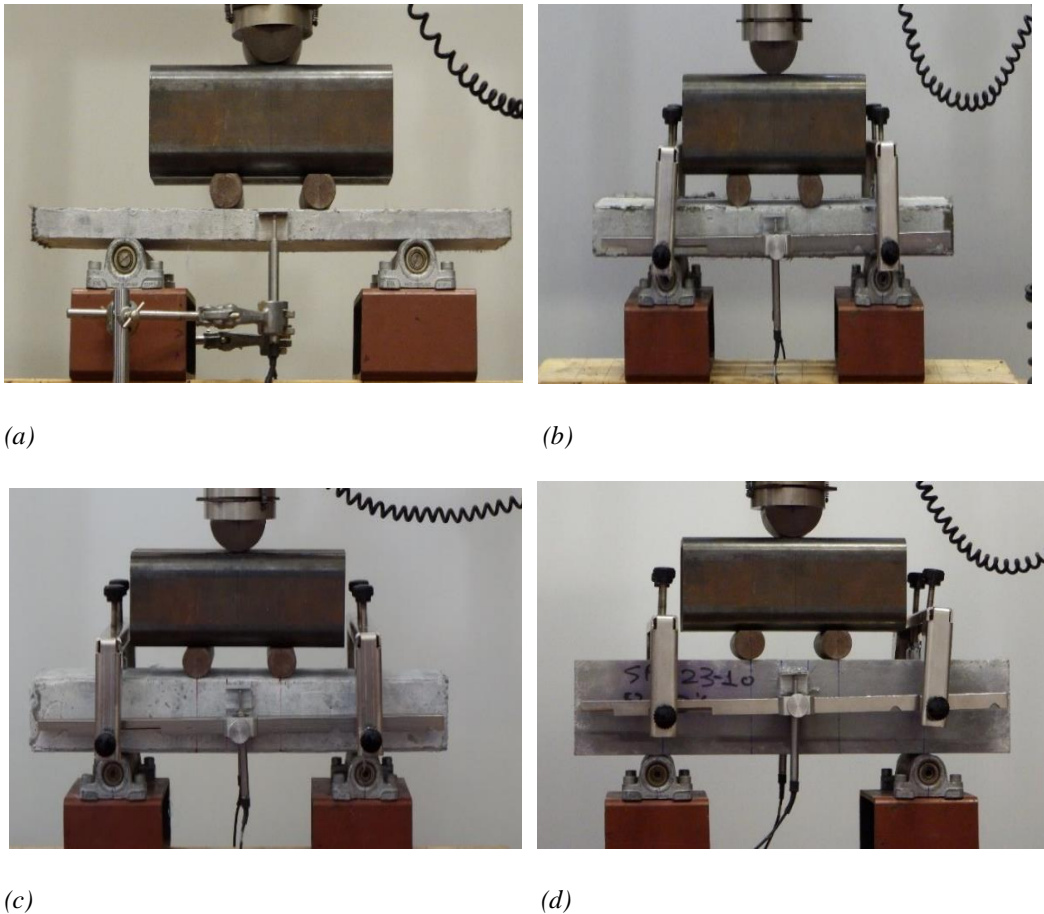


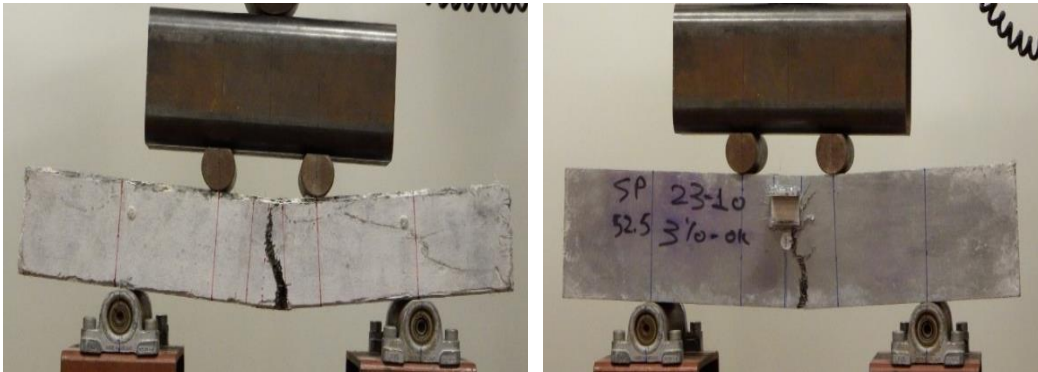
Figure 3.47 Experimental setup for the flexural testing of the: (a) 25 mm prisms, (b) 50 mm prisms, (c) 75 mm prisms and (d) 100 mm prisms

The majority of the specimens failed in the middle of the span length with a typical vertical flexural crack. The typical failure mode for the specimens with the different thickness values are presented in Figure 3.48.



(a)

(b)

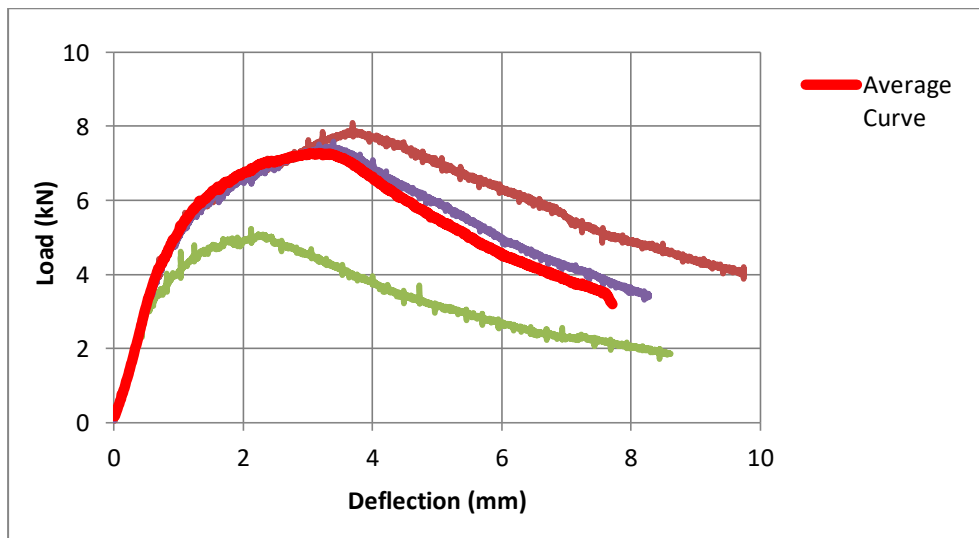


(c)

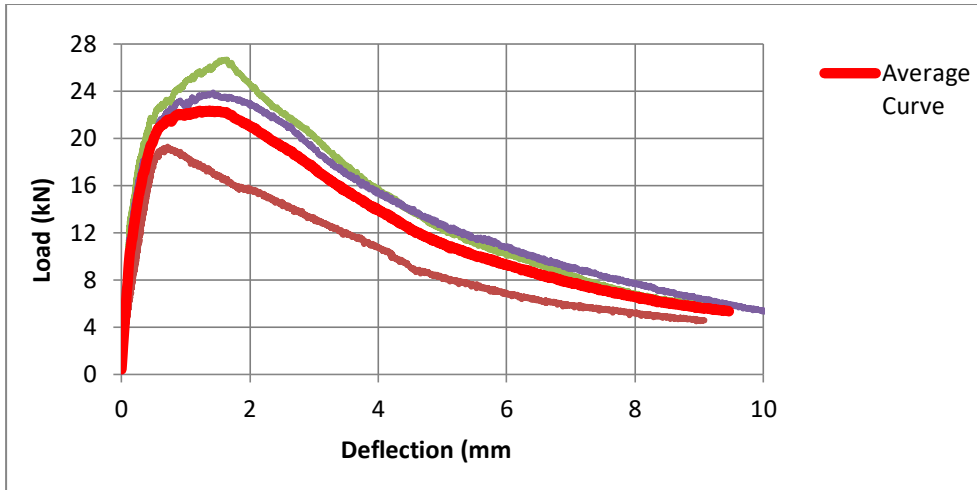
(d)

Figure 3.48 Characteristic failures of the: (a) 25 mm prisms, (b) 50 mm prisms, (c) 75 mm prisms and (d) 100 mm prisms

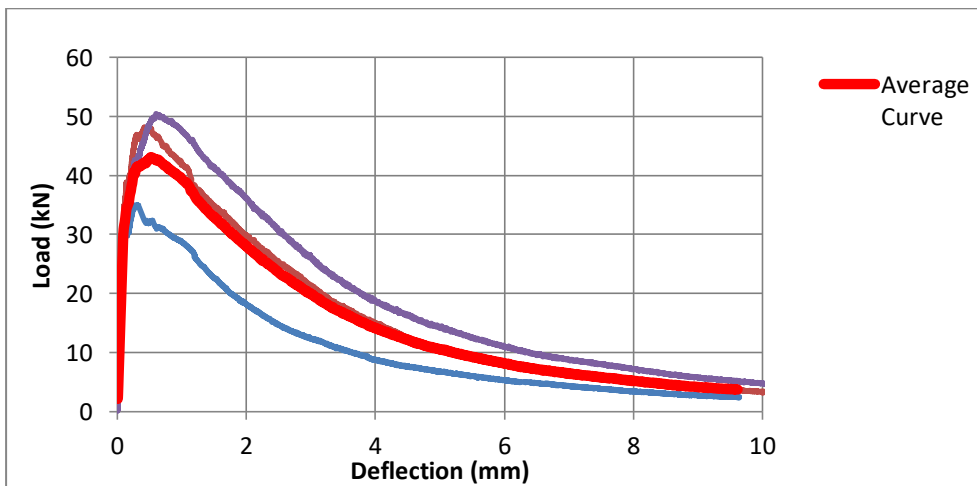
The load-deflection results of all the examined specimens together with the average curves are presented in Figures 3.49a-3.49d.



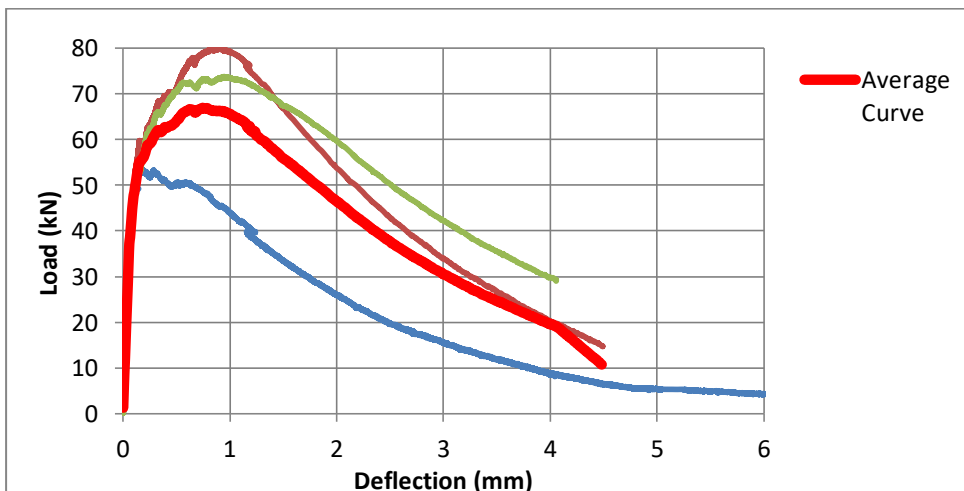
(a)



(b)



(c)



(d)

Figure 3.49 Load-deflection results for prisms with a depth of: (a) 25 mm, (b) 50 mm, (c) 75 mm and (d) 100 mm

The results of Figure 3.49 indicate that there is a scatter in the experimental results, since for the 25 mm depth prisms the maximum load was ranged between 5.3 KN and 8.1 KN, for the 50 mm depth the maximum load was between 19.3 KN and 26.7 KN, for the 75 mm depth the maximum load was between 35 KN and 49.2 KN, and for the 100mm depth prism the range was between 50.5 KN and 80.3 KN.

From the average load-deflection curves, the average maximum load was calculated to be equal to 6.5 KN for the 25mm prisms, 22.3 KN for the 50 mm prisms, 43.1 KN for the 75 mm prisms, and 66.7 KN for the 100 mm prisms.

3.8.4 Proposed Equation for the ‘size effect’

The flexural strength of each specimen was determined according to JSCE-SF4 (1984) (Equation 3.3).

$$f_u = \frac{P \cdot L}{b \cdot d^2} \quad (3.3)$$

Where f_u is the flexural strength (in MPa); P is the peak load; L is the effective span length (300 mm); b is the width of the specimens (100 mm); d is the depth varies from 25 to 100 mm.

The flexural strength results for all the different examined thicknesses are presented in Table 3.12. These values have been calculated using the average maximum load values.

Beam Depth (mm)	Flexural strength (MPa)
25	31.2
50	26.8
75	23.0
100	20.1

Table 3.12 Experimental results for the different depths of prisms

The results of Table 3.12 indicate that there is a ‘size effect’ on the flexural performance of UHPFRC and an increment of the flexural strength as the depth is reduced, can be distinguished. This can be attributed to the non-uniform distribution of the fibers for higher depths. In order to correlate the average tensile strength of UHPFRC calculated from the direct

tensile tests, with the flexural strength, the following equation (3.4) is proposed. This equation has been calibrated to fit the experimental results.

$$f_t = \frac{f_u}{2.85 \cdot (1 - 4.2 \cdot h)} \quad (3.4)$$

Where f_t is the tensile stress (MPa); h is the cross section height (in m); f_u is the flexural tensile strength. A comparison between the experimental results and the results obtained using equation 3.4 is presented in Figure 3.50.

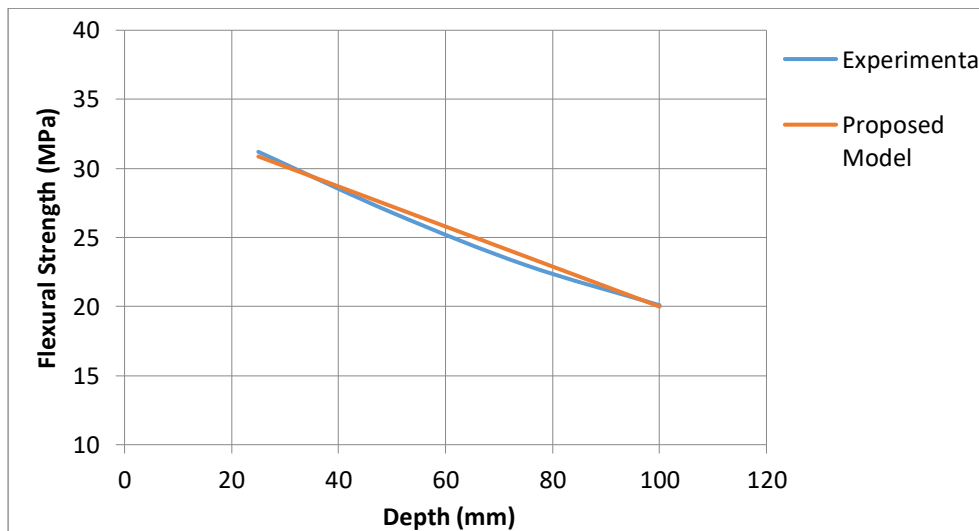


Figure 3.50 Results of the proposed model versus the experimental results

The proposed model could be used to correlate the flexural with the direct tensile strength of UHPFRC for specimens with depth up to 100 mm thickness.

3.9 UHPFRC under Cyclic Loading

The experimental results of the previous sections indicated that the UHPFRC is a cementitious material with enhanced strength in tension and compression. The use of UHPFRC for earthquake strengthening of RC structures is a novel application. In earthquake prone areas the structures are subjected to seismic loads that are usually simulated with a cyclic loading history. However, there are not any studies on UHPFRC under cyclic loading. In the present investigation the hysteretic characteristics of UHPFRC under cyclic loading were investigated and a model which can predict the hysteretic characteristics of UHPFRC was proposed. The proposed model of the present investigation, can be used for the computational analysis of the UHPFRC subjected to cyclic loading.

3.9.1 Experimental Investigation

In the current experimental investigation, direct tensile tests of UHPFRC under monotonic and cyclic loading were conducted. More specifically, cyclic loading tests under various loading histories were performed and a model for the response of UHPFRC under cyclic loading was proposed. The proposed model was validated for the different loading histories and the different percentages of steel fibers. For the preparation of the specimens three different percentages of steel fibers were investigated, namely 1%, 2% and 3%. The mixture designs for the various fiber contents are presented in Table 3.7, while for the preparation of the material cement 32.5 R type II was used. For the curing, after the demolding two days after casting, the specimens placed in a water tank for twenty-six days and tested over twenty-eight days.

3.9.2 Experimental Setup

Dog-bone specimens were used for the direct tensile tests. Twenty-five identical dog bone specimens were examined in total in tension, using different percentages of steel fibers and different loading histories. The tests were controlled by the LVDT measurements, using the same displacement rate with the previous investigations, namely 0.007 mm/sec (see Figure 3.51).



Figure 3.51 Experimental setup for the cyclic loading tests

The three different loading histories which were applied in this investigation are presented in Figure 3.52. Extension step of 0.2 mm was used for loading history 1, while for loading histories 2 and 3 the step was equal to 0.4 mm and 0.8 mm respectively.

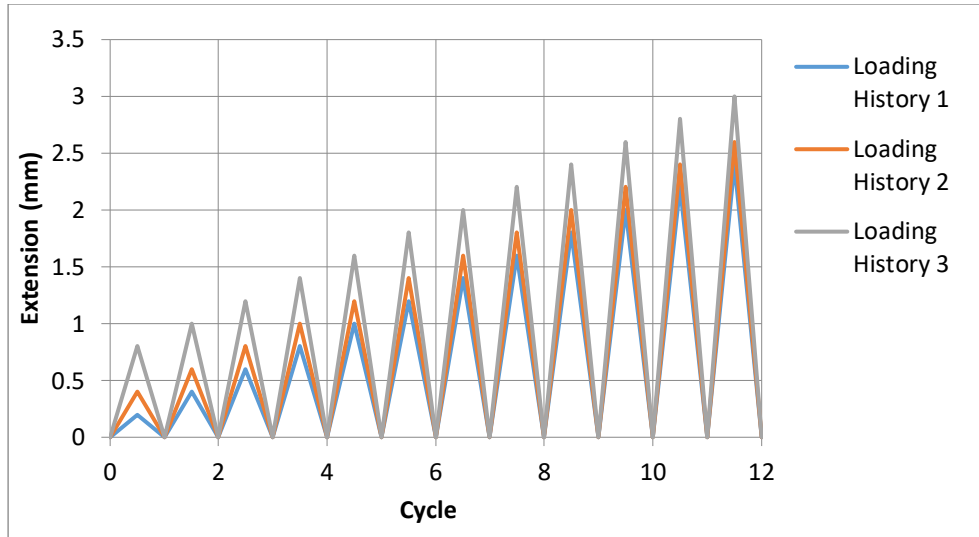


Figure 3.52 Examined loading histories

3.9.3 Experimental results and discussion

Initially, the performance of UHPFRC under monotonic loading was investigated. For this reason, six monotonic tests of dog bone specimens with 3% steel fibers were conducted and the stress-strain curves together with the average curve are presented in Figure 3.53.

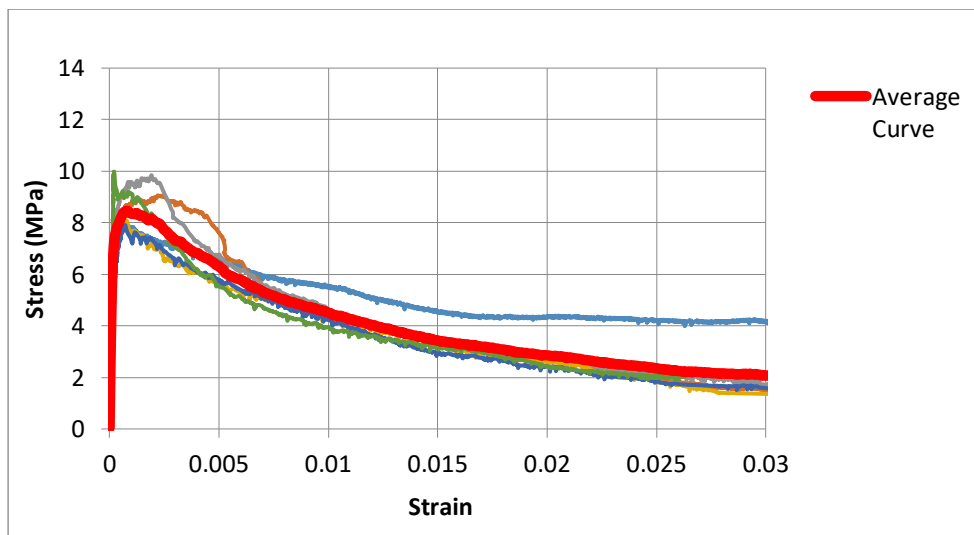
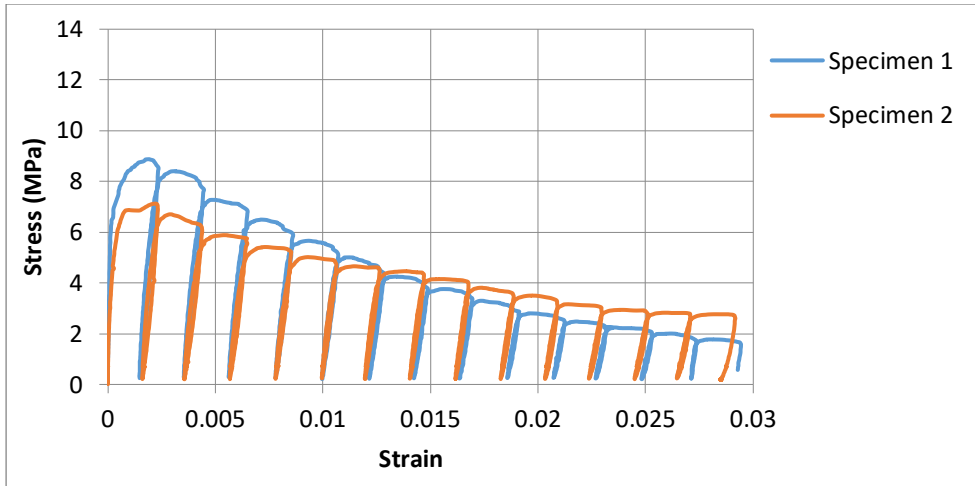
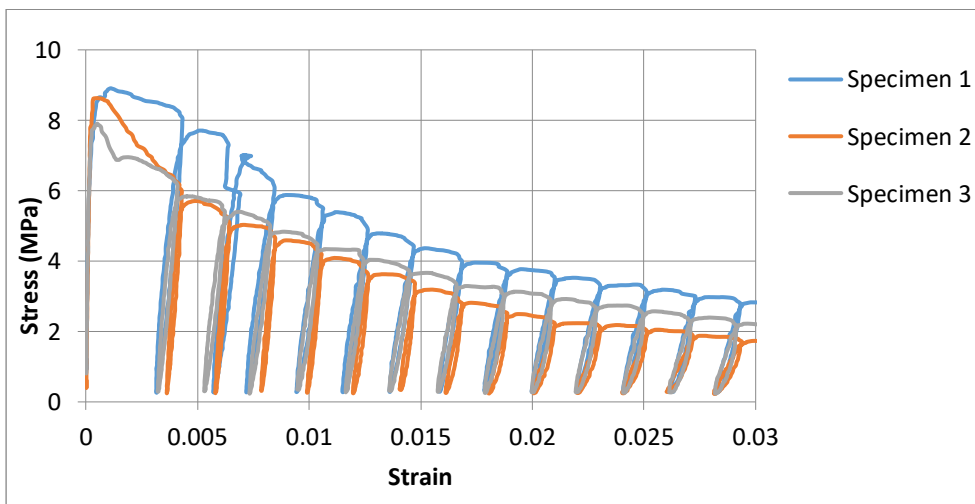


Figure 3.53 Tensile stress strain results for the specimens with 3% steel fibers

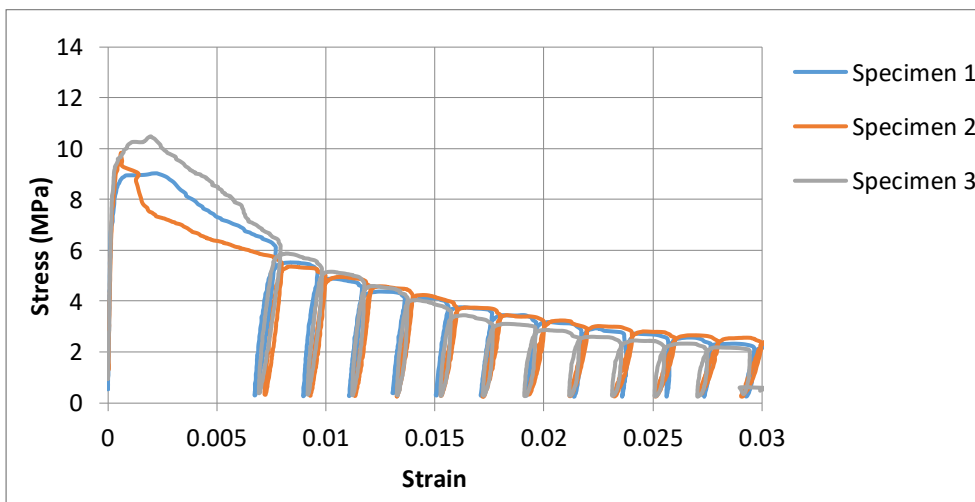
The respective stress-strain results for the specimens tested under cyclic loading for the loading histories 1, 2 and 3 are presented in Figures 3.54a-3.54c. Due to the fact that during the testing of specimen 3 of loading history 1, the failure commenced on the grips, the results of this specimen were ignored.



(a)



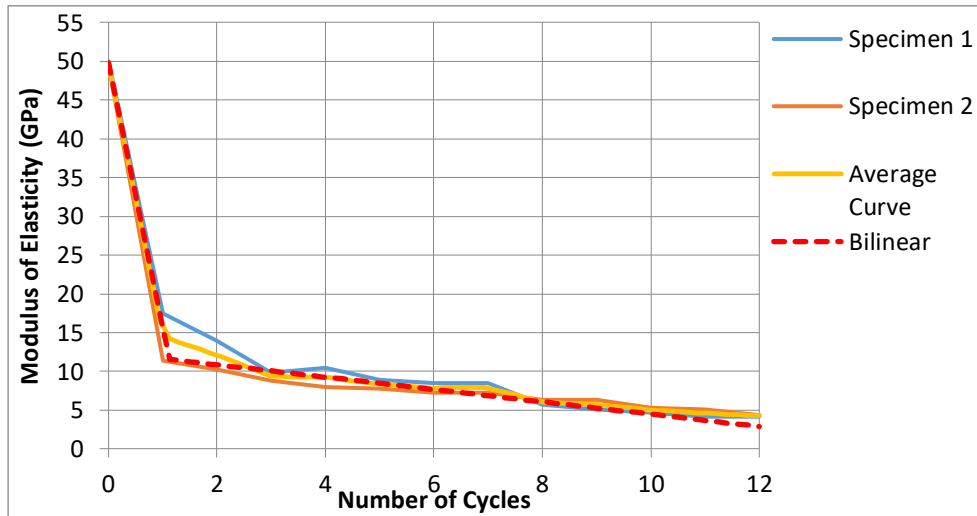
(b)



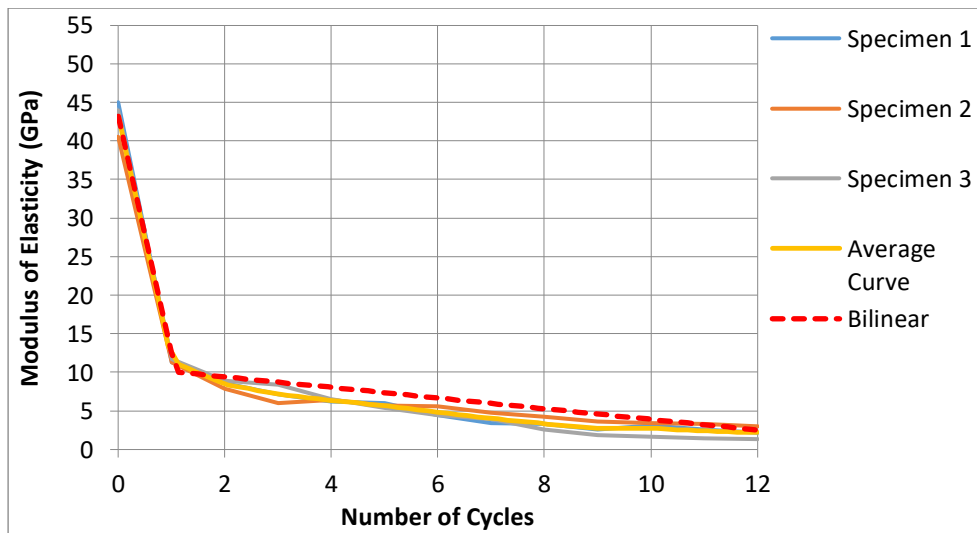
(c)

Figure 3.54 Experimental results for: a) loading history 1, b) loading history 2, and c) loading history 3

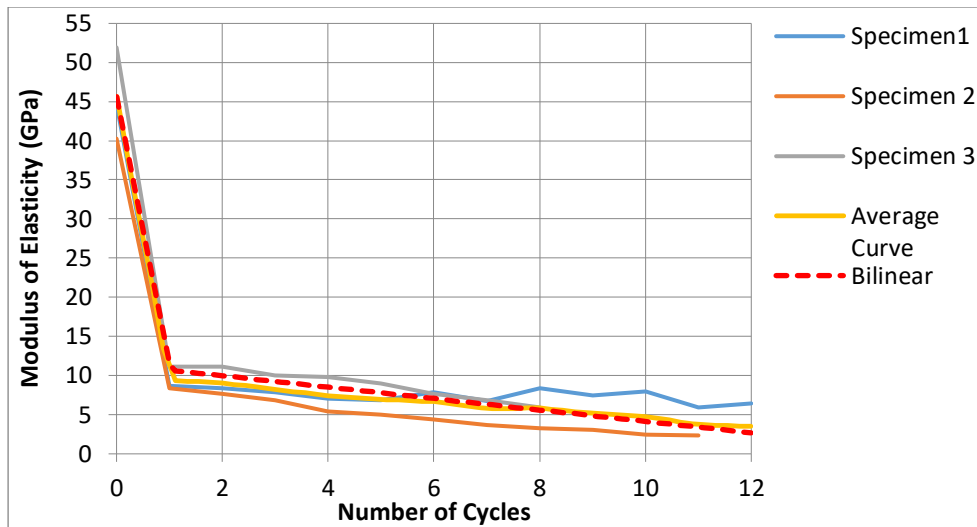
The experimental results of Figure 3.54 were used for the calculation of the modulus of elasticity degradation with the number of cycles. The results for all the identical specimens together with the average results and the bilinear approximations, for loading histories 1, 2 and 3 are presented in Figures 3.55a, 3.55b and 3.55c respectively.



(a)



(b)



(c)

Figure 3.55 Modulus of elasticity degradation for: a) loading history 1, b) loading history 2 and c) loading history 3

From Figure 3.55a-3.55c it is clear that, in all the examined loading cases, the modulus of elasticity was considerably reduced after the first loading cycle, and then it was slightly further reduced as the number of cycles was increased. In all the examined cases the modulus of elasticity was approximately reduced to the 25% of its initial value after the first loading cycle. This significant reduction is mainly attributed to the fact that in all the examined loading histories, the response of the specimens reached the post-cracking phase at the first loading cycle (see Figure 3.54).

The average curve of all the examined cases is presented in Figure 3.56. Based on this curve, equation 3.5 is proposed for the reduction of the modulus of elasticity with the loading cycles. This equation was also used for the bilinear approximations of Figure 3.55 and it can be observed that the results obtained using this equation are in very good agreement with the experimental results.

$$\frac{E_n}{E_0} = 0.25 - 0.016 \cdot n \quad (3.5)$$

Where n is the number of cycles ($n > 1$); E_0 is the initial modulus of elasticity; E_n is the modulus of elasticity after n cycles.

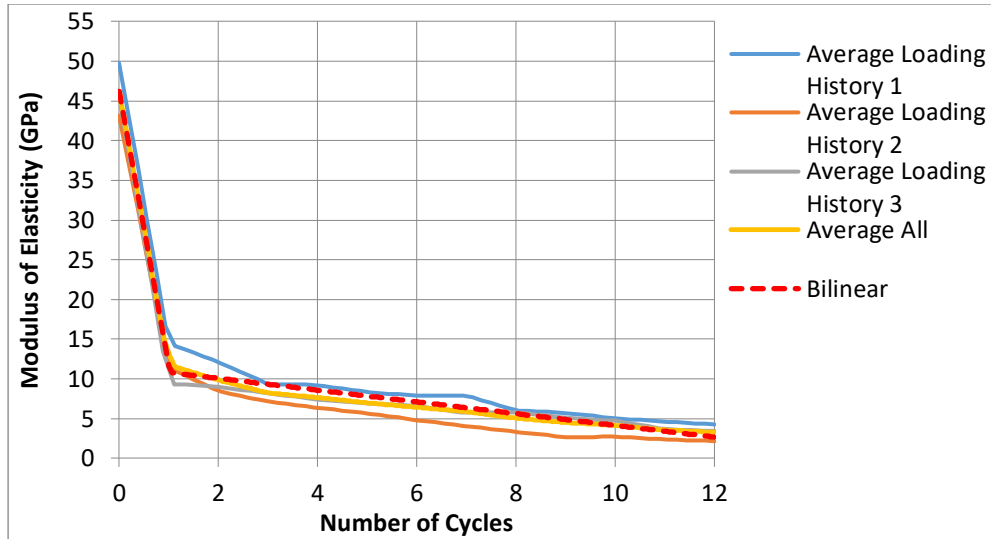


Figure 3.56 Average curves of the modulus of elasticity degradation for all the loading histories

The comparison between the average experimental results and the proposed model is presented in Figure 3.57. The results of the bilinear models indicate that the behavior is not affected by the loading history and is governed by the same equation 3.5 in all the examined cases.

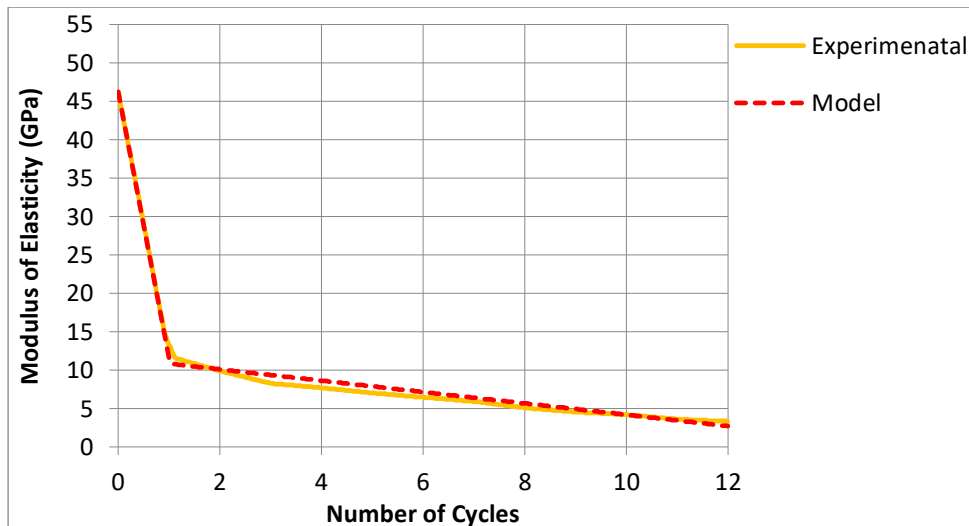


Figure 3.57 Degradation of the modulus of elasticity with the loading cycles

3.9.4 Analytical investigation

The response of UHPFRC in direct tension is dissimilar to the response of conventional plain concrete under the same loading condition. The behavior of concrete in tension is considered linear up to the maximum level of stress and after this point a sudden failure occurs. On the contrary, for UHPFRC after the linear part in which the steel fibers don't have any effect, the first crack appears and a non-linear behavior transpires up to the maximum load. After this

point the stress drops gradually. These phases of UHPFRC under tension can be distinguished in Figure 3.58.

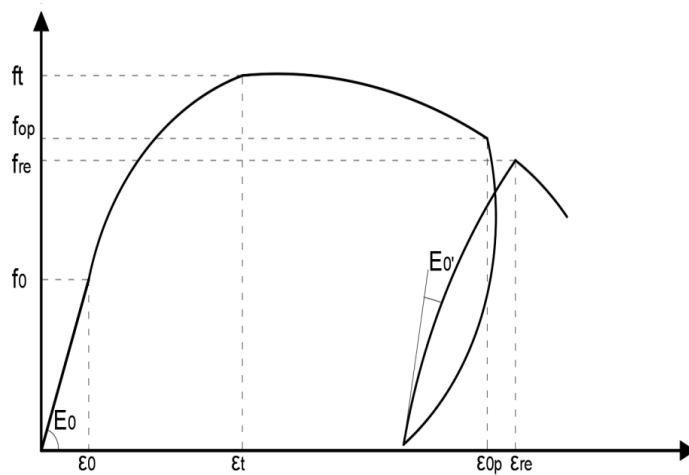


Figure 3.58 Stress-strain curve of UHPFRC under cyclic loading

In the present study, the envelope curve for cyclic loading was assumed identical to the monotonic stress-axial strain response. This assumption has also been adopted by other researchers for conventional concrete (Yankelevsy and Reinhardt, (1989) and Bahn and Hsu, (1998)). In Figure 3.59, the average monotonic curve is presented together with the respective results of the cyclic loading tests. The results indicate that the average monotonic curve is approaching the cyclic response of the specimens.

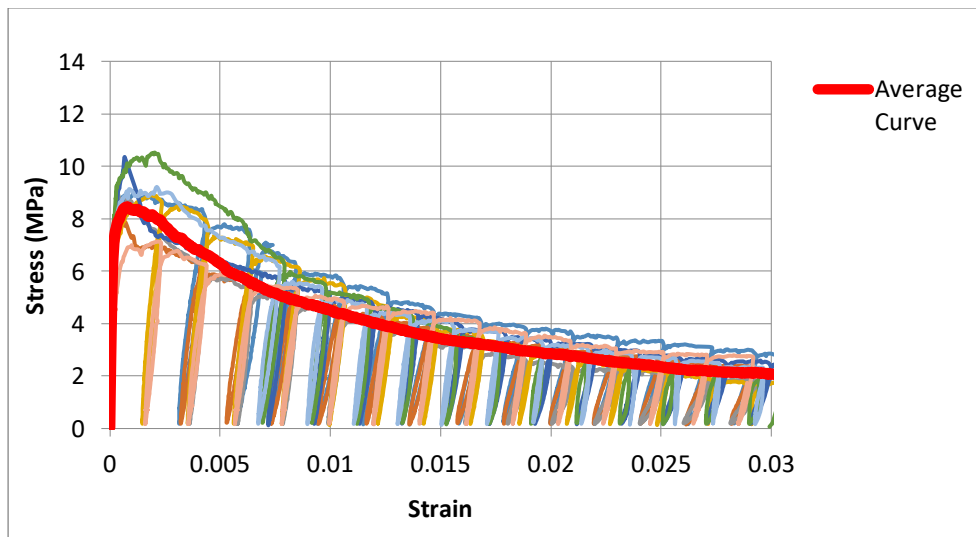


Figure 3.59 Comparison of the average monotonic curve with the cyclic envelope curves

The proposed model is consisted of five various phases, as presented in Figure 3.59. The first is the linear phase up to a level of stress f_0 and axial strain ϵ_0 . The second is the non-linear phase up to a maximum stress of f_t and axial strain ϵ_t . The third is the descending phase until

the unloading point (f_{op} , ε_{op}), and finally the next two phases are the unloading and the reloading phases. In the first part, the stress-strain relation is linear, hence it is given from equation 3.6.

$$\sigma = \varepsilon \cdot E_0 \quad \text{for } \varepsilon < \varepsilon_0 \quad (3.6)$$

Where ε is the strain and E_0 is the modulus of elasticity

After the elastic part, the behavior of the material is characterized by an ascending non-linear branch until the maximum stress. This is the phase where the cracking of the matrix occurs and the steel fibers are bridging the micro-cracks. After this point, the stress falls gradually due to the localization of the damage. This non-linear behavior can be described by an exponential curve. Hence, two equations are proposed for both the ascending part (from the elastic limit until the maximum stress limit), as well as the descending branch from the maximum stress limit up to the unloading point. Therefore, for the ascending part the following equation 3.7 is proposed. This equation was also proposed by Mazars and G. Pijaudier-Cabot (1989) and also used by other researchers (Sima et al. 2008, Faria et al. 1999, Saetta et al., 1999).

$$\sigma = \varepsilon_0 \cdot (1-A) + A \cdot \varepsilon \cdot e^{\frac{\varepsilon_0 - \varepsilon}{\varepsilon_t}} \quad (3.7)$$

Where ε_0 is the strain at the end of the linear part; ε_t is the respective strain for the maximum stress; A is given from the equation (3.8):

$$A = \frac{f_t - \varepsilon_0 \cdot E_0}{E_0 \cdot (\varepsilon_t \cdot e^{\frac{\varepsilon_0 - 1}{\varepsilon_t}} - \varepsilon_0)} \quad (3.8)$$

Where f_t is the maximum stress.

For the descending branch and taking into consideration the softening part, Sima et al. (2008), considered an exponential curve and took into consideration a point on the envelope curve. This exponential curve is also adopted for UHPFRC in the descending branch. Therefore, the descending curve is described by the equation 3.9:

$$\sigma = (B + C \cdot \varepsilon \cdot e^{\frac{\varepsilon_0 - \varepsilon}{\varepsilon_t}}) \cdot E_0 \quad \text{for } \varepsilon > \varepsilon_0 \quad (3.9)$$

Where:

$$B = \frac{f_{op} \cdot \varepsilon_t \cdot e^{\left(\frac{\varepsilon_0 - 1}{\varepsilon_t}\right)} - \varepsilon_{op} \cdot f_t \cdot e^{\frac{\varepsilon_0}{\varepsilon_t} \left(1 - \frac{\varepsilon_{op}}{\varepsilon_0}\right)}}{E_0 \cdot \left(\varepsilon_t \cdot e^{\left(\frac{\varepsilon_0 - 1}{\varepsilon_t}\right)} - \varepsilon_{op} \cdot e^{\frac{\varepsilon_0}{\varepsilon_t} \left(1 - \frac{\varepsilon_{op}}{\varepsilon_0}\right)}\right)} \quad (3.10)$$

$$C = \frac{f_t - f_{op}}{E_0 \cdot \left(\varepsilon_t \cdot e^{\left(\frac{\varepsilon_0 - 1}{\varepsilon_t}\right)} - \varepsilon_{op} \cdot e^{\frac{\varepsilon_0}{\varepsilon_t} \left(1 - \frac{\varepsilon_{op}}{\varepsilon_0}\right)}\right)} \quad (3.11)$$

Where ε_{op} is the strain at any point on the descending part of the stress-strain curve; f_{op} is the respective stress at any point on the descending part of the stress-strain curve.

Previous studies on plain concrete (Sinha et al., 1964) indicate that during the unloading phase, the modulus of elasticity is high at the beginning, then gradually drops, and finally becomes flat. Based on the experimental results of the present study, the unloading branch of UHPFRC exhibits a different behavior which is attributed to the presence of steel fibers in the mixture. For this reason, the experimental results have been used for the calibration of the constitutive model. The equation proposed by Sima et al. (2008), for the unloading part has been calibrated in order to fit the experimental results (see equation 3.12). From the validation of the proposed model, and using all the experimental results of the various mixes, it was evident that this equation can accurately predict the behavior of UHPFRC in this branch.

$$\sigma = D \cdot e^{\frac{F \cdot \left(1 - \frac{\varepsilon - \varepsilon_{pl}}{\varepsilon_{un} - \varepsilon_{pl}}\right)}{22}} \cdot E_0 \cdot (\varepsilon - \varepsilon_{pl}) \quad (3.12)$$

Where:

$$D = \frac{r \cdot (1 - \delta_{un})}{r - 1} \quad (3.13)$$

$$r = \frac{\varepsilon_{un}}{\varepsilon_{pl}} \quad (3.14)$$

Where ε_{pl} is the residual strain for the unloading curve for zero stress; ε_{un} is the unloading strain; δ_{un} is the compressive damage at the unloading point and is given in equation 3.15.

$$\delta_{un}=1-\frac{B}{\varepsilon}-C \cdot e^{\left(\frac{\varepsilon_0-\varepsilon}{\varepsilon_t}\right)} \quad (3.15)$$

F is given in equation (3.16)

$$F=Ln \left(\frac{R \cdot (1-\delta_{un}) \cdot (r-1)}{r} \right) \quad (3.16)$$

R: is given in equation (3.17)

$$R = \frac{E_{pl}}{E_0} \quad (3.17)$$

Where E_{pl} is the Modulus of elasticity at the end of the unloading curve.

The experimental results presented in the present investigation, indicated that the modeling of the re-loading part with a linear stress-strain equation, which is adopted for conventional concrete, can't accurately predict the response of UHPFRC. Hence, an exponential equation, which is a modification of equation 3.7, is proposed in order to describe the behavior of the reloading curves of UHPFRC .

$$\sigma=(\varepsilon_{0'} \cdot (1-A') + A' \cdot \varepsilon \cdot e^{\frac{\varepsilon_0'-\varepsilon}{\varepsilon_t'}}) \cdot E_0 \quad (3.18)$$

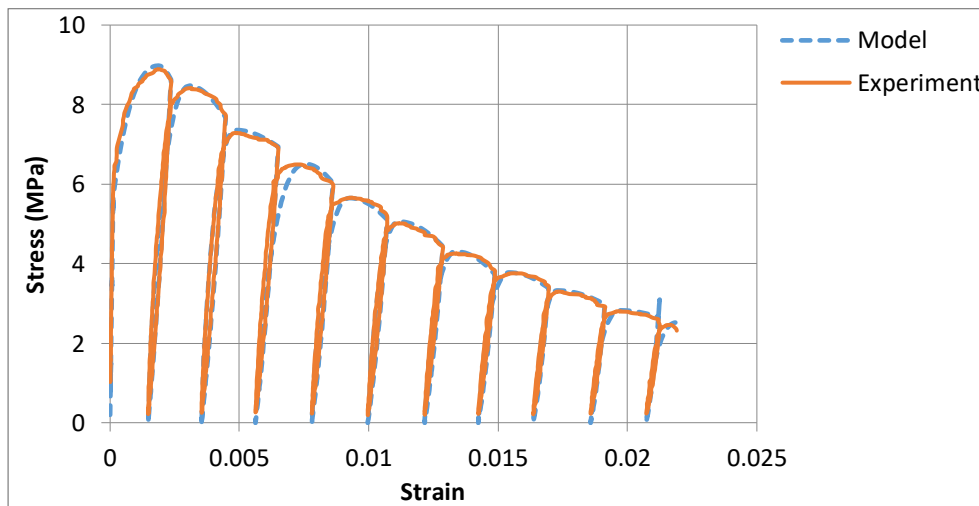
Where A' is given in equation (3.19)

$$A' = \frac{f_t' - \varepsilon_{0'} \cdot E_{0'}}{E_{0'} \cdot (\varepsilon_t' \cdot e^{\left(\frac{\varepsilon_0'-1}{\varepsilon_t'}\right)} - \varepsilon_{0'})} \quad (3.19)$$

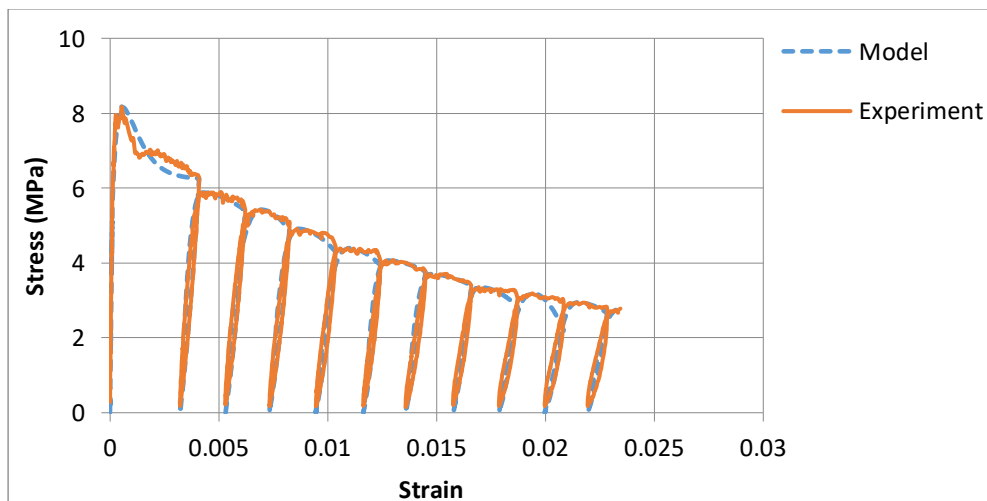
Where f_t' is the maximum stress at the reloading curve; ε_t' is the strain for the respective maximum stress in the descending curve; $\varepsilon_t' = \varepsilon - \varepsilon_{pl}$; E_0' is the initial tangent modulus of elasticity; ε_0' is the respective maximum strain for the tangent modulus of elasticity.

3.9.5 Validation of the proposed constitutive model

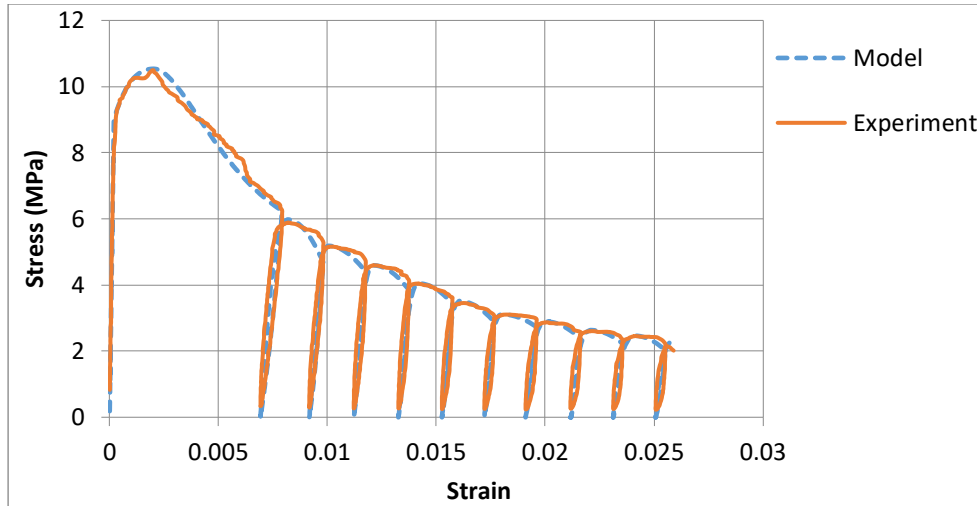
Experimental results of all the examined loading histories for specimens with 3% steel fibers were used for the validation of the model. In Figures 3.60a, 3.60b and 3.60c the results of the proposed constitutive model are compared with experimental results for loading histories 1, 2 and 3 respectively. From these figures, it is clear that the results of the proposed model are in very good agreement with the respective experimental results. Therefore, it can be concluded that the proposed model can accurately predict the cyclic response of UHPFRC. The proposed model concerns UHPFRCs that present strain hardening behavior.



(a)



(b)



(c)

Figure 3.60 Validation of the proposed model using experimental results for: (a) loading history 1, (b) loading history 2, (c) loading history 3

3.9.6 UHPFRC under cyclic loading for different fiber contents

The experimental results of Figures 3.30 and 3.31, for the specimens prepared with 1% and 2% per volume steel fibers and tested under monotonic loading, indicated that strain hardening behavior can be achieved with a minimum percentage of steel fibers 2%. Therefore, in order to investigate the reliability of the proposed model for percentages other than 3%, cyclic loading tests (see loading history 2, Figure 3.52) were conducted for specimens with 2% steel fibers. The experimental results are presented in Figure 3.61 and the validation of the proposed model is presented in Figure 3.62. From Figure 3.62 it is clear that the proposed model can accurately predict the response of UHPFRC for percentage of steel fibers 2%.

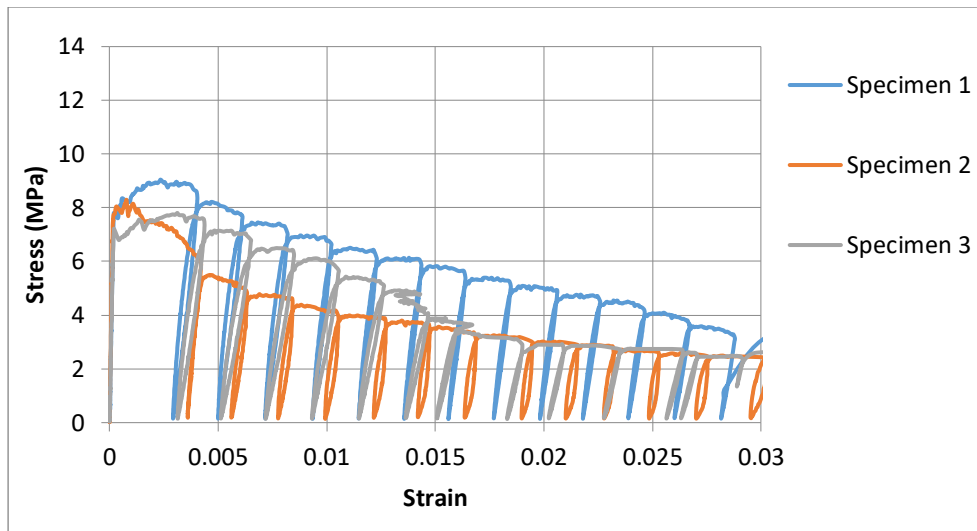


Figure 3.61 Stress-strain results of UHPFRC with 2% steel fibers under cyclic loading

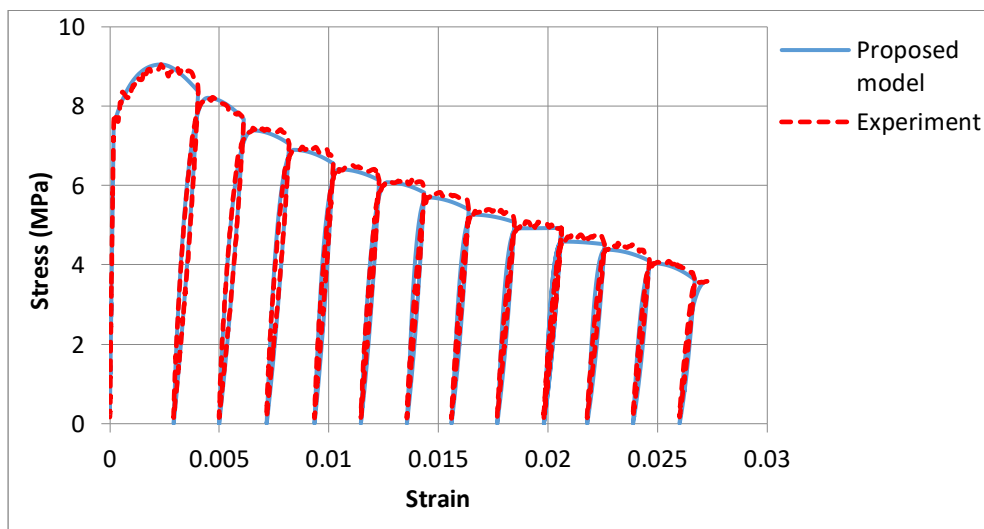


Figure 3.62 Validation of the proposed model for 2% steel fibers

3.10 Conclusions

From the investigation of the properties of UHPFRC of the present section, it was clear that the use of high strength cement can increase both the tensile and the compressive strength of UHPFRC. Consequently, for the preparation of the UHPFRC layers and jackets of the experimental investigation of the full scale testing, cement 52.5 N type I cement is adopted. From the investigation of the different types of fibers on the other hand, it was evident that the specimens prepared with conventional steel fibers with a length of 13 mm, a diameter of 0.16 mm and a tensile strength of 3000 MPa presented better mechanical properties compared to specimens prepared with recycled steel fiber retained from car tires. Hereby, this type of fibers is adopted for the next investigations. Also, the experimental results of the present

chapter indicated that steel fiber content in the mixture affected the compressive strength, the tensile characteristics and the fracture energy of the UHPFRC and different models are required for the simulation of the tensile stress-strain response of the material for the different fiber contents. However, the big volume of fibers in the mixture (higher than 4 %), causes a pronounced reduction in the flow . Consequently, for the next investigations and in order to secure the good workability of the mixture, a fiber content of 3 % is adopted . Also, a further finding of the present research was that the fiber content affects the shrinkage of the material, since lower values of shrinkage were recorded for increasing fiber contents.

From the investigation of the effect of curing time and curing regime on the properties of UHPFRC, it was clear that the optimum performance was achieved with heat curing for twelve days. After this period the heat curing has not any further effect on the properties of the material. On the contrary, for curing with normal curing conditions, it was noticed that the properties of the material are further increased after the twenty-eight days period. Considering that for the full scale testing of the present research heat curing cannot be applied, curing with conventional methods (water spraying) for a period higher than twenty eight days must be applied on the strengthened members, in order to achieve the optimum performance of the strengthened elements.

From the investigation of the flexural performance of UHPFRC prisms with various depths, it was clear that there is a 'size effect'. Hence, an increment of the flexural strength at decreasing depths was noticed. Finally, from the study of the performance of UHPFRC under cyclic loading and various loading histories, it was noticed that the modulus of elasticity was considerably reduced after the first loading cycle, and then, it was slightly further reduced as the number of cycles was increased. Also, comparing the monotonic with the cyclic response of the material, it was noticed that the monotonic response of the specimens was approaching the cyclic response. Consequently, this assumption can be adopted for the earthquake strengthening of existing RC members.

4. STRENGTHENING OF EXISTING REINFORCED CONCRETE (RC) BEAMS USING ULTRA HIGH PERFORMANCE FIBER-REINFORCED CONCRETE (UHPFRC)

4.1 Introduction

In the previous chapter, the results of an extensive experimental investigation on the study of crucial parameters of the UHPFRC, which are related to the mechanical properties of the material, were presented. The experimental results have been used for the development of an optimum mixture design, in terms of strength, ease of preparation and application of the material. The present chapter aims to investigate the effectiveness of UHPFRC as a strengthening material and to study if the examined strengthening technique can increase the load carrying capacity of existing RC elements. Additionally, the present chapter aims to study the interface behavior of composite UHPFRC-concrete members and to investigate if these members can exhibit a monolithic behavior.

A crucial parameter for the performance of the examined technique is the bonding at the interface between the new layer and the existing member. As a result, the first part of the present research is focused on the study of the connection at the interface between UHPFRC and concrete. For this investigation push-off tests have been executed. The second part of the present chapter is focused on a realistic application of the UHPFRC for the strengthening of RC beams. Most of the examined beams have been strengthened with an additional layer at the tensile side and the efficiency of a jacket on three sides has also been studied. An additional analysis has been performed on the effectiveness of dowels to improve the bonding at the interface and the load carrying capacity of the strengthened beams. Also, during the testing of the composite UHPFRC-concrete beams, measurements for the slip at the interface have been recorded and the results obtained have been evaluated based on available existing models in the literature for concrete to concrete interfaces. In the following sections, the extensive experimental investigation of the performance of UHPFRC as a strengthening material is presented.

4.2 Study of the interface between UHPFRC and concrete

A crucial parameter for the performance of the technique is the bonding at the interface between the existing member and the new layer. In the present section, a further investigation

on the interface characteristics between UHPFRC and concrete has been conducted through push-off tests. The experimental results of the present section have also been used for the modeling of the interface of the numerical investigation.

4.2.1 Preparation of specimens

For the study of the interface between UHPFRC and concrete, two different types of interfaces were prepared. Rough interface, with a roughness level equal to 2-2.5 mm, and smooth interface without any preparation. For the roughening of the cubes' surface, a pistol grip needle scaler was employed following exactly the same procedure followed for the preparation of the interface of the full scale beams. The preparation of the specimens is illustrated in Figure 4.1. As shown in this figure, two concrete cubes were prepared first and placed in the timber molds, and later on, the UHPFRC cube was cast. For each investigation three specimens were examined. The specimens were demolded two days after casting and placed in a water tank until the testing day. The specimens were tested over two months.



(a)



(b)



(c)

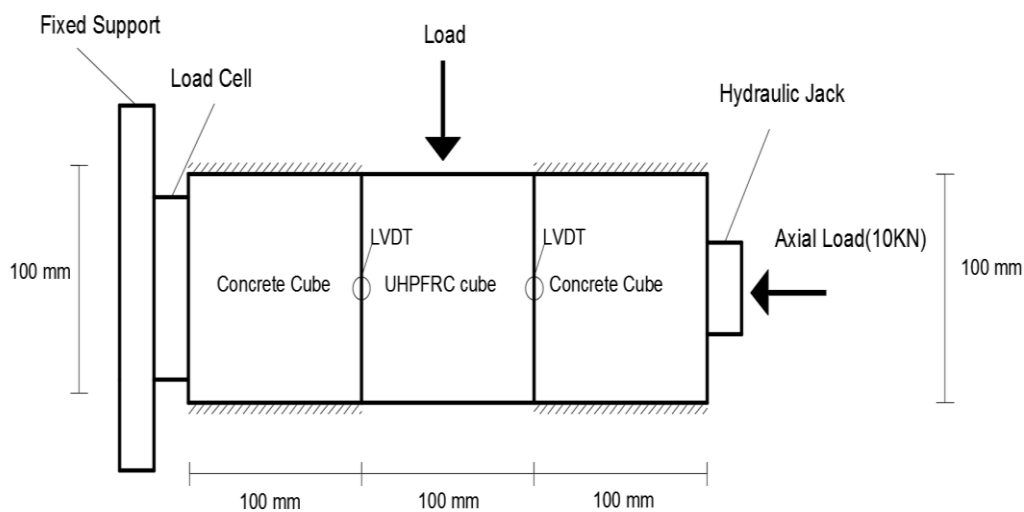


(d)

Figure 4.1 Preparation of specimens for the push-off tests: a) specimen with a rough interface, b) specimens without any preparation of their surface c) specimens after casting and d) specimens after demolding

4.2.2 Experimental setup

The geometry and the experimental setup which was used for the push off tests is presented in Figures 4.2a-4.2c. As illustrated in these figures, a constant axial load equal to 10 KN was applied to the specimens through a hydraulic jack. A load cell in contact with the specimens was also used to record the load and to secure a constant value during the testing. At the same time, a vertical load was also applied to the UHPFRC cube through an actuator under a constant displacement control of 0.001 mm/sec. Finally, two LVDTs were placed on each side of the specimens for the measurement of the slip at the interface.



(a)



(b)

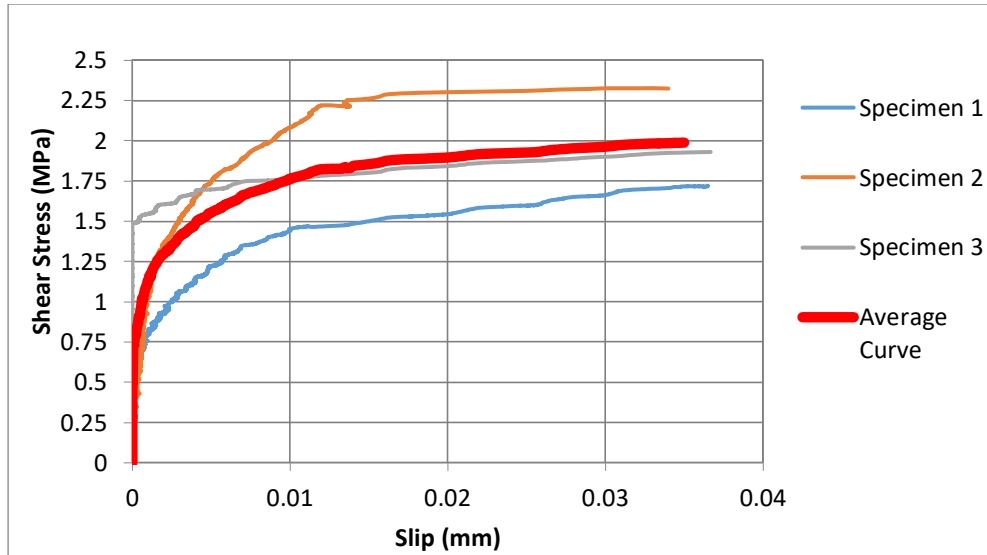


(c)

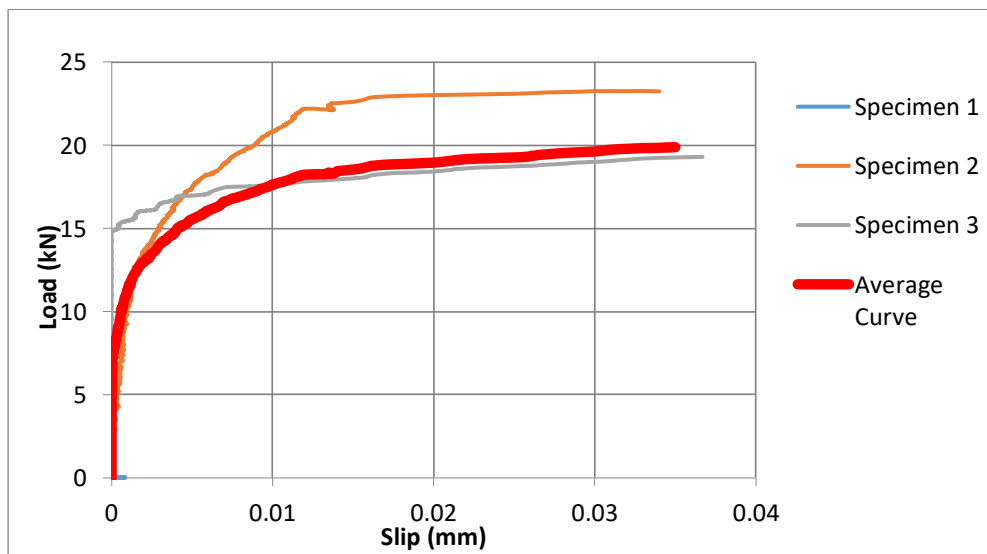
Figure 4.2 a) Experimental setup and dimensions of specimens, b) the testing of specimens and c) specimens after testing

4.2.3 Evaluation of the interface characteristics

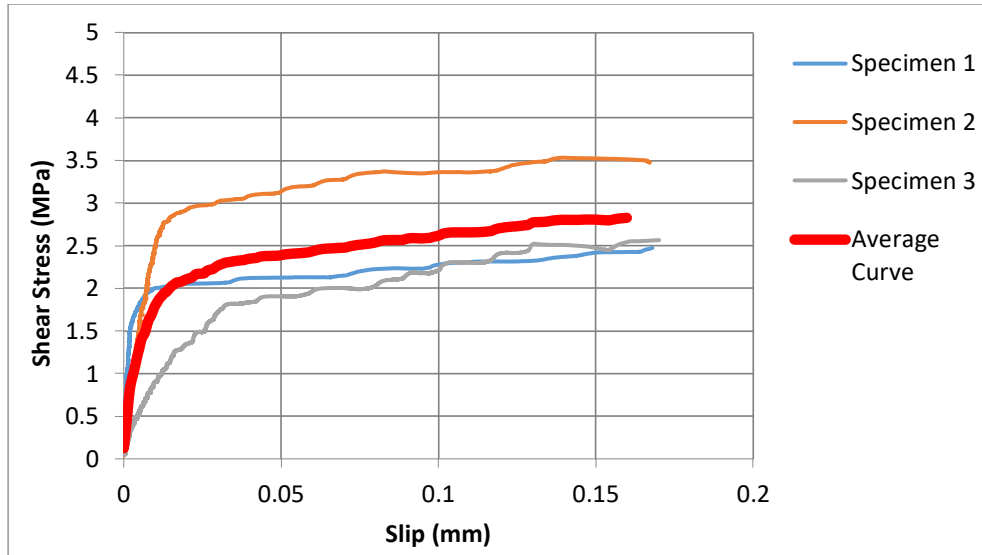
In Figures 4.3a-4.3d, the results of the shear stress and the shear load versus the interface slip for the different types of interface and the different fiber contents, are presented.



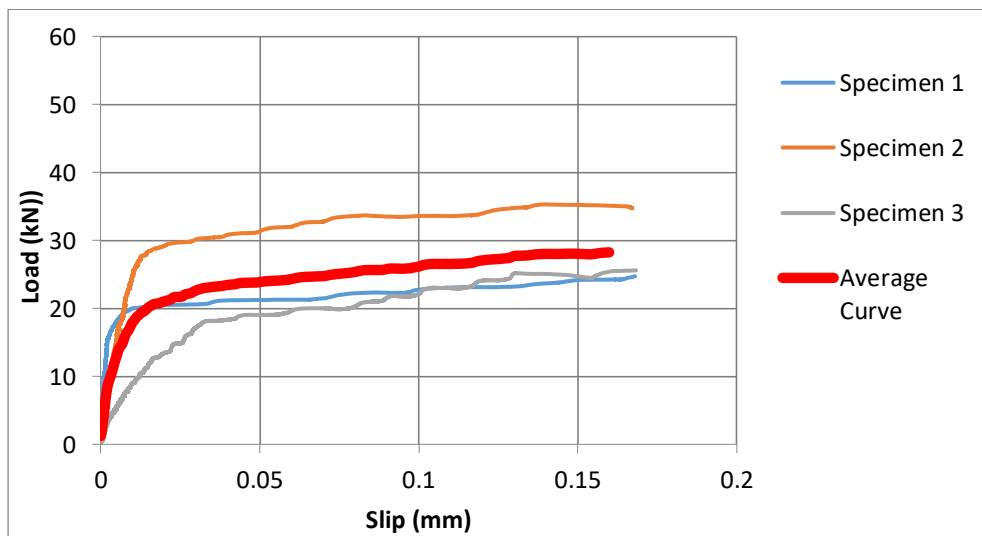
(a)



(b)



(c)



(d)

Figure 4.3 a) Shear stress versus interface slip for UHPFRC with 3% steel fibers and smooth interface, b) load versus interface slip for UHPFRC with 3% steel fibers and smooth interface, c) shear stress versus interface slip for UHPFRC with 3% steel fibers and rough interface, d) load versus interface slip for UHPFRC with 3% steel fibers and rough interface

According to BS EN 1992-1-1:2004 (2004), shear strength can be calculated using Equation 4.1.

$$\tau_{ud} = c \cdot f_{ctd} + \mu \cdot \sigma_N \leq 0.5 \cdot v \cdot f_{cd} \quad (4.1)$$

Where τ_{ud} is the shear strength at the interface; c is the adhesion factor; μ is the coefficient of friction; σ_N is the external normal to the interface stress (1 MPa); v is equal to $0.6 \cdot (1 - f_{ck}/250)$ and f_{ck} is the characteristic compressive strength of the concrete; f_{ctd} is the design tensile

strength of concrete with the lower strength (between the old and the new concrete; f_{cd} is the concrete compressive strength and is given by f_{ck}/γ_c with $\gamma_c=1.5$).

The coefficients of friction and cohesion for the UHPFRC were calculated using Equation 4.1. Hence, for the different types of interface, cohesion ($c \cdot f_{ctd}$) was considered as the shear stress at the interface for a slip value equal to 0.01 mm following the available code provisions (Greek Code for Interventions, 2013) and CEB Fib Model Code, 1993). Coefficients of friction were then calculated using Equation 4.1. In this equation, the externally applied normal to the interface stress was equal to 1 MPa, while the maximum shear stress was the value obtained from the push off tests. The interface characteristics for all the examined specimens are presented in Table 4.1.

	UHPFRC (3% Smooth)	UHPFRC (3% Rough)
τ_u	1.95	2.8
$c \cdot f_{ctd}$	1.65	1.82
c	0.58	0.63
μ	0.3	0.98
σ_N	1	1
$0.5 \cdot v \cdot f_{cd}$	21.61	21.61

Table 4.1 Coefficients of friction and cohesion obtained from the push-off tests

As expected, for smooth interface the coefficient of friction μ presented significantly lower value compared to rough interface, which indicates the good level of preparation of the interface. Also, higher value of the coefficient of adhesion was observed for rough interface compared to interface without any preparation. According to BS EN 1002-1-1:2004 (2004), a value of 0.7 for the coefficient of friction and a value of 0.45 is suggested for concrete and rough interface. Based on the results of the present investigation, an effective bonding between UHPFRC and concrete can be identified.

Based on the experimental results of the present investigation, a value of 0.98 for the coefficient of friction and a value of 1.82 MPa for the cohesion are adopted for the modeling of the interface between UHPFRC and concrete, of the numerical investigation of the following chapter.

4.3 Experimental program for the strengthening of RC beams

In the present investigation, ten identical RC beams were constructed and used for the evaluation of the performance of UHPFRC as a strengthening material. Two beams were used as control beams for the evaluation of the performance of existing RC beams prior to strengthening, while eight beams were strengthened with layers and jackets at the tensile side. More specifically, two beams were strengthened with an UHPFRC layer, two beams were strengthened with an UHPFRC layer and steel bars, two beams were strengthened with a jacket on three sides, and finally two beams were strengthened with an UHPFRC layer and dowels were used at the interface.

The UHPFRC layer is expected to increase the stiffness under service conditions of the strengthened beams. Steel bars, on the other hand, are normally used in traditional strengthening techniques to increase the load carrying capacity of the strengthened members. Hence, this technique has also been adopted, in the present thesis, to achieve the optimum performance of the strengthened beams. The addition of jackets on existing members changes the geometry of the existing members. Therefore, this technique, apart from the load carrying capacity, is expected to increase the stiffness of the existing members. Finally, a common practice, which is used in traditional techniques to improve the bonding at the interface is the use of dowels at the interface. Hence, this technique has also been adopted, in the present investigation, to achieve an effective bonding at the interface and a monolithic behavior of the strengthened members. In all the examined specimens the interface between the existing element and the UHPFRC was roughened with a procedure, which is presented in a next section. The experimental program for the strengthening of existing RC beams together with the testing age of each one of the examined RC beams and layers is presented in Table 4.2.

Beam	Strengthening Technique	Testing time (months)	
		Reinforced Concrete Beam	Layer/ Jacket
P1	Control beam	4	-
P2	Control beam	4	-
U1	UHPFRC layer	4	2
U2	UHPFRC layer	4	2
D1	UHPFRC layer and dowels	4	2
D2	UHPFRC layer and dowels	4	2
UB1	UHPFRC layer and bars	4	2
UB2	UHPFRC layer and bars	4	2
3SJ1	Three-side jacket	4	2
3SJ2	Three- side jacket	4	2

Table 4.2 Experimental program for the strengthening of existing full scale RC beams

As can be seen in Table 4.2, all the examined beams were tested over four months while the testing time of UHPFRC in all of these cases was two months. As presented in the previous chapter, in this time frame the UHPFRC develop high mechanical properties close to maximum that it can achieve.

4.4 Examined strengthening techniques

4.4.1 Preparation of the RC beams

In present investigation a realistic application of the UHPFRC for the strengthening RC beams has been conducted and beams with dimensions similar to those which can be found in real structures have been constructed. The geometry and the reinforcement of the ten identical RC beams is presented in Figure 4.4.

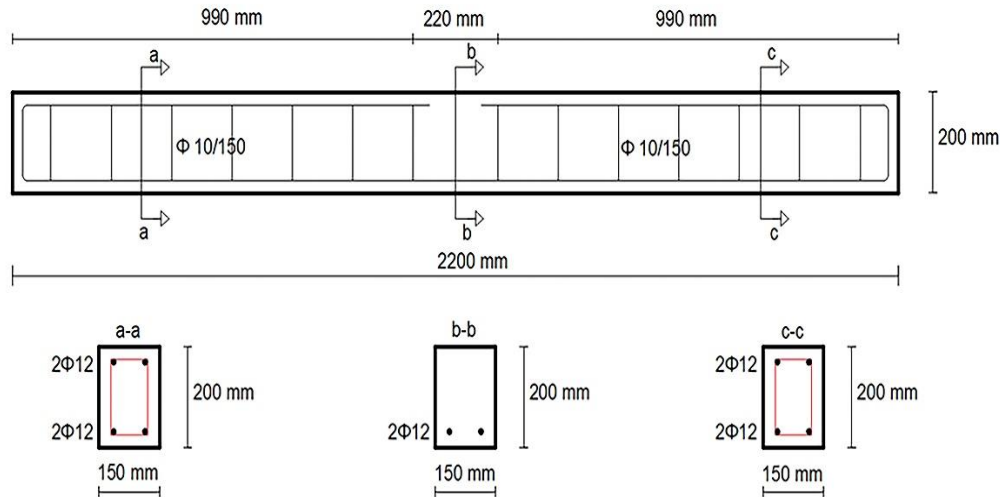


Figure 4.4 Reinforced concrete beams

The existing RC beams were reinforced with steel bars only at the tensile side in order to represent relatively weak beams. Hence, two longitudinal ribbed steel bars with a diameter of 12 mm and length of 2150 mm were placed at the tensile side of each beam. On the contrary, the reinforcement at the compressive side of beams was used only to support the stirrups. The examined techniques set as a target the flexural strengthening of beams. As a consequence, in order to avoid shear failure of the beams, shear reinforcement, according to EN 1992-1-1:2004 (2004), was placed along the whole length of the beams. More specifically, stirrups with a diameter of 10 mm and spacing of 150 mm were placed as shear reinforcement. Finally, plastic spacers were used in order to ensure the required concrete cover of the reinforcement, which was equal to 30 mm, and represents the real measured cover of the reinforcement after the placement of the reinforcement in the molds. In the next chapter, different configurations for the existing RC beams are also examined.

4.4.2 Strengthening of RC beams using UHPFRC layers

The first application of UHPFRC as a strengthening material was the addition of an UHPFRC layer at the tensile side of the beams. In Figure 4.5, the geometry of the strengthened RC beams is presented.

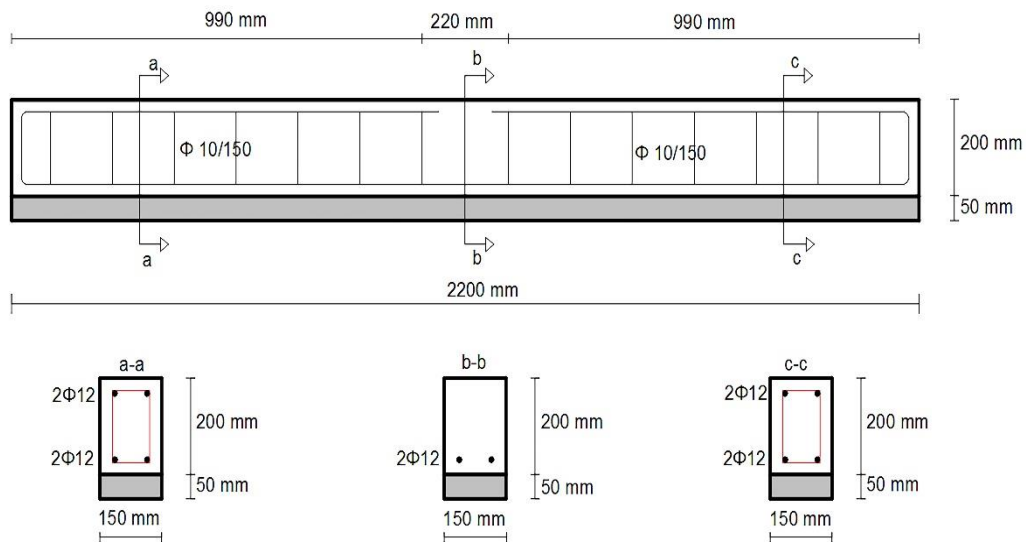


Figure 4.5 Strengthening with UHPFRC layers

As illustrated in Figure 4.5, an UHPFRC layer with a depth of 50 mm, a breath of 150 mm and a length of 2200 mm was constructed at the tensile side of beams. Also, as can be seen in the same figure, the layer was placed along the whole length of the beam. The performance of the existing RC beams for strengthening with different layer depths is investigated numerically in the next chapter.

4.4.3 Strengthening of RC beams using UHPFRC layers and steel bars

The next strengthening technique concerned the addition of steel bars to the UHPFRC layer. The concept of this technique is similar to conventional techniques for strengthening of RC beams using RC layers. However, the unique properties of UHPFRC is expected to increase dramatically the performance of the strengthened beams. The strengthening technique is presented in Figure 4.6.

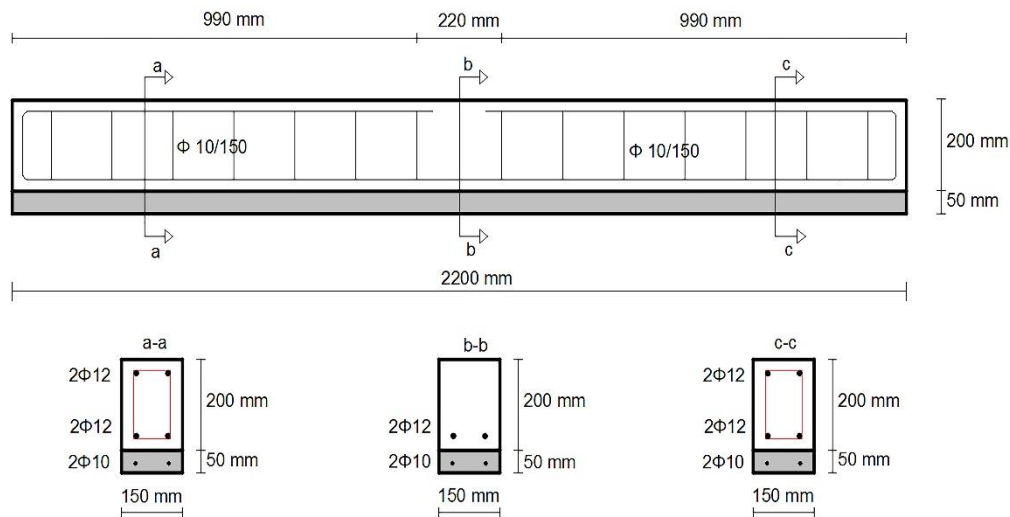


Figure 4.6 Strengthening with UHPFRC layers and steel bars

As illustrated in Figure 4.6, the geometry of the UHPFRC layer was the same with the previous investigation, with a breadth equal to 150 mm, a depth equal to 50 mm and a length equal to 2200 mm. Additionally, two ribbed steel bars with a diameter of 10 mm and a length equal to 2150 mm were added to the UHPFRC layer. The same amount of reinforcement was also used by Tsioulou et al (2013), for strengthening of RC beams with RC layers, leading to comparable results. The effect of the amount of reinforcement on the performance of the strengthened beams is investigated numerically in detail in the next chapter. Finally, the cover of reinforcement was equal to 25 mm, and it was achieved with the use of plastic spacers.

4.4.4 Strengthening of RC beams using three-side jackets

The next application of the present thesis was the strengthening of existing RC beams with a jacket on three sides. The strengthening technique and the geometry of the strengthened beams is presented in Figure 4.7.

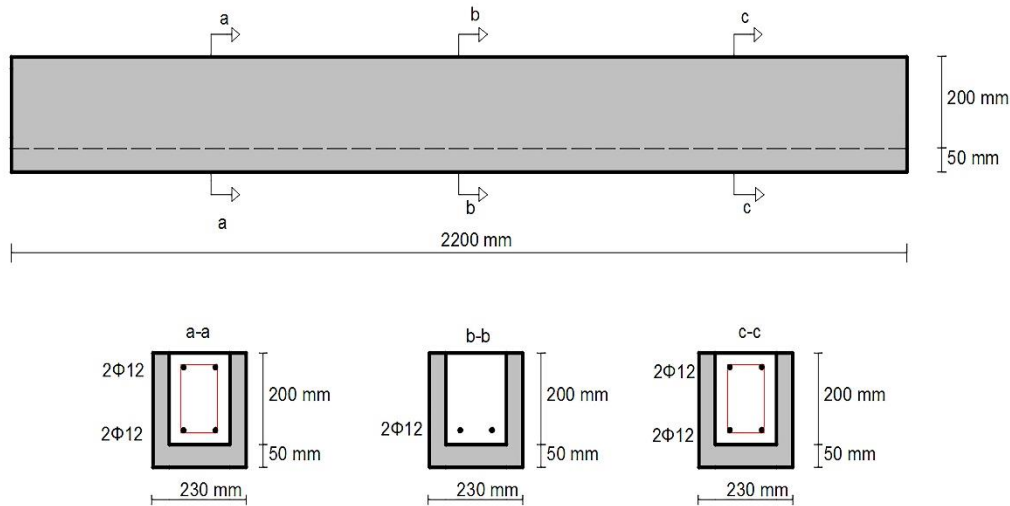


Figure 4.7 Strengthening with three-side jackets

The depth of the layer at the tensile side was equal to 50 mm, while the thickness on both sides of the beam was equal to 40 mm. Hence, the total breadth of the strengthened beam was 230 mm, and the total height was 250 mm. These values represent the real measured dimensions of the strengthened beams and the jacket after the demolding of the beams.

4.4.5 Strengthening of RC beams using an UHPFRC layers and dowels

The next strengthening technique constitutes the addition of dowels at the interface. The geometry and the reinforcement of the strengthened beams are illustrated in Figure 4.8.

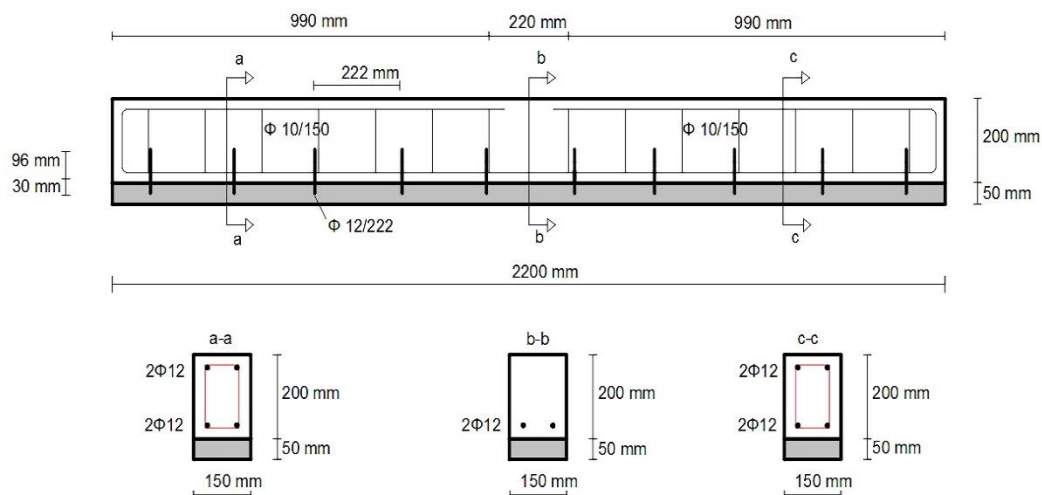


Figure 4.8 Strengthening with UHPFRC layers and dowels

As can be seen in Figure 4.8, the layer had the same geometry to the previous investigations, while ribbed steel bars with a length equal to 126 mm, a diameter equal to 12 mm and a spacing of 222 mm were used as dowels. The dowels were placed along the whole length of the beam, and the embedment length was equal to 96 mm. During the testing of the strengthened beams high shear stresses at the interface are expected. The design of the dowels was based on the Greek Code of Interventions (2013), and three types of shear failure were considered; failure of steel, failure of concrete and concrete cone failure.

In Figure 4.9 the minimum required cover of the dowels for directions parallel and perpendicular to the loading direction according to the Greek Code of Interventions (2013) is presented.

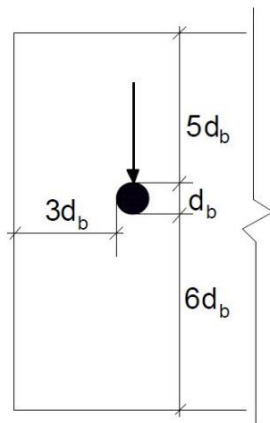


Figure 4.9 Minimum required cover for the dowels based on the Greek Code for Interventions

Based on the Greek Code of Interventions (2013), the embedment length of the dowels should be at least eight times higher than the diameter of the dowel ($8d_b$). In cases that this length cannot be achieved, the embedment length is suggested to be at least six times higher than the diameter of the dowel, in which case, the shear resistance should be reduced to 60% of the maximum value. For embedment length between $6d_b$ and $8d_b$ linear interpolation can be used for the calculation of the shear resistance. Finally, the minimum distance between the dowels should not be lower than five times the diameter of the dowels ($5d_b$).

4.5 Preparation of the examined beams

4.5.1 Preparation of the concrete beams

The first step for the experimental investigation of the performance of UHPFRC as a strengthening material was the construction of the initial beams. The reinforcement of the

examined beams was assembled first (see Figures 4.10a and 4.10b), and then the reinforcement was placed in the timber molds (see Figure 4.10c). As illustrated in these figures, plastic spacers were attached on the reinforcement not only to achieve the desired cover on both sides of the beams (30 mm), but also to avoid toppling and movement of the reinforcement during the casting. In order to secure the constant breadth of the beams and to avoid the opening of the molds during the casting, wooden wedges together with steel bolts were placed on top of the molds (see Figure 4.10c). Due to the increased length of the molds (2300 mm), expanded polystyrene was placed to achieve the desired length of the beams (2200 mm). Finally, standard plastic-cube molds, with side lengths of 100 mm, were used for the investigation of the compressive strength of the concrete mixture (see Figure 4.10b).



(a)



(b)



(c)

Figure 4.10 a) Assembling of the reinforcement, b) preparation of the molds and the reinforcement and c) reinforcement in the molds ready for casting

Once the reinforcement and the moulds were ready, the concrete mixture was prepared. The mixture design used in the present study, was designed based on Teychenne et al. (1997), and it is presented in Table 4.3.

Material	Quantity (kg/m ³)
Cement	340
Fine Aggregates	1071
Coarse Aggregates	714
Water	205

Table 4.3 Mixture design of concrete

A high shear mixer was used for the mixing of the materials. All the dry ingredients were initially mixed for 3 minutes, and then water was added gradually. Once the mixture reached the wet stage and it was ready, it was placed in the molds. The compaction of the mixture was carried out using a hand-held vibrator. The beams were demoulded twenty-four hours after the casting. The preparation of the RC beams is presented in Figures 4.11a-4.11d.



(a)



(b)

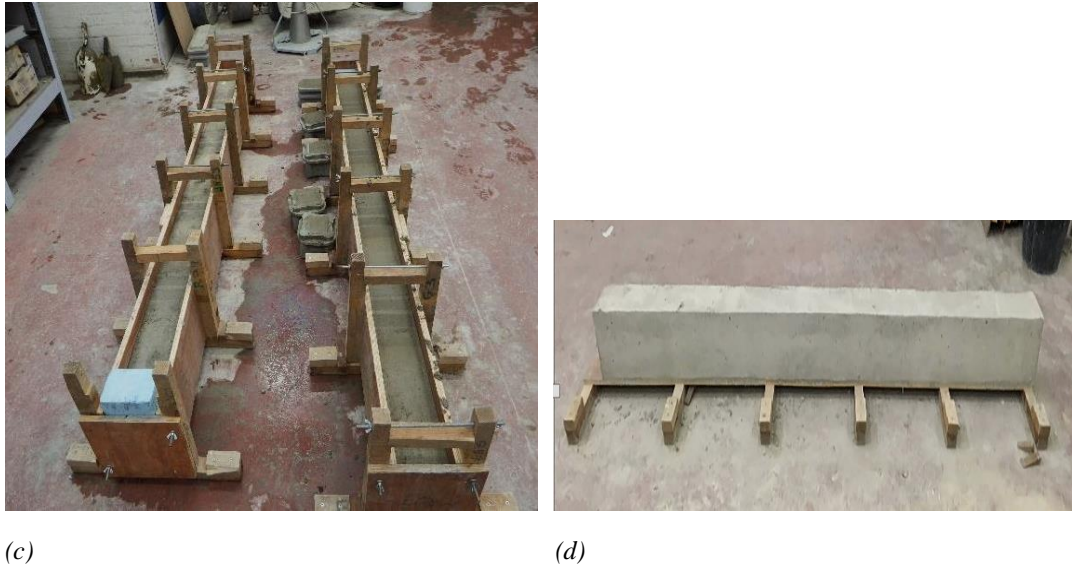


Figure 4.11 a) Dry mixing of the materials, b) concrete ready to cast, c) beams after casting and d) beam after demolding

For the curing of the specimens, the specimens were wet cured daily for a period of twenty-eight days, while after this period when the effect of shrinkage is less significant, the specimens were wet cured every two days. Considering that a period of two months is required for the curing of the layers and jackets, the existing strengthened RC beams were tested over four months.

4.5.2 Preparation of the UHPFRC layers

For the selection of the appropriate fiber content three different parameters were taken into consideration. The workability, the mechanical properties and the cost of the material. Based on Paschalis and Lampropoulos (2016), the cost of the material is increased dramatically for increasing fiber contents. More specifically, while the cost of the material with 1% steel fibers is 1212 £/m³, the cost of the material for 6% steel fibers is 2861 £/m³. Considering that the workability of the material using 6% steel fibers is not effective, and also, the cost of the material is extremely high, this fiber content was rejected. For 1% and 2% steel fibers on the other hand, the properties of the material were not the desired. Consequently, a fiber content between 3% and 4% was considered as optimum for the present investigation. Finally, considering the total cost of the material, a fiber content of 3% was selected for the present investigation. Therefore, the mixture design U5 of Table 3.1 was adopted for the construction of the examined layers and jackets together with 3% steel fibers. Finally, from the investigation of the different types of steel fibers, it was clear that the performance of

UHPFRC using conventional steel fibers with a length of 13 mm, a diameter of 0.16 mm and a tensile strength of 3000 MPa was the optimum. Therefore, this type of fiber was chosen for the preparation of UHPFRC layers and jackets.

4.5.3 Properties of the materials

In the following table the experimental results of the compressive tests for the concrete mixture are presented. Based on the results of this table, the compressive strength was in the range of 26.7-35.2 MPa and the average compressive strength was found to be equal to 30.9 MPa.

Specimen	Compressive Strength (MPa)
C1	32.4
C2	31.6
C3	31.5
C4	30.2
C5	30.5
C6	28
C7	30.5
C8	31.9
C9	26.7
C10	35.2

Table 4.4 Results of the compressive tests of the examined concrete mixture

For the investigation of the properties of the constructed layers and jackets, dog bone shaped specimens and cube specimens were prepared from the same batch with the constructed layers. For the curing, the specimens were wet-cured for twenty-eight days and tested in the same time frame with the layers, namely in two months. The geometry and the procedure for the preparation of the specimens is the same as presented in Section 3.2.2 while the testing procedure is presented in Section 3.2.3. The tensile stress-strain results of six dog-bone specimens are presented in Figure 4.12.

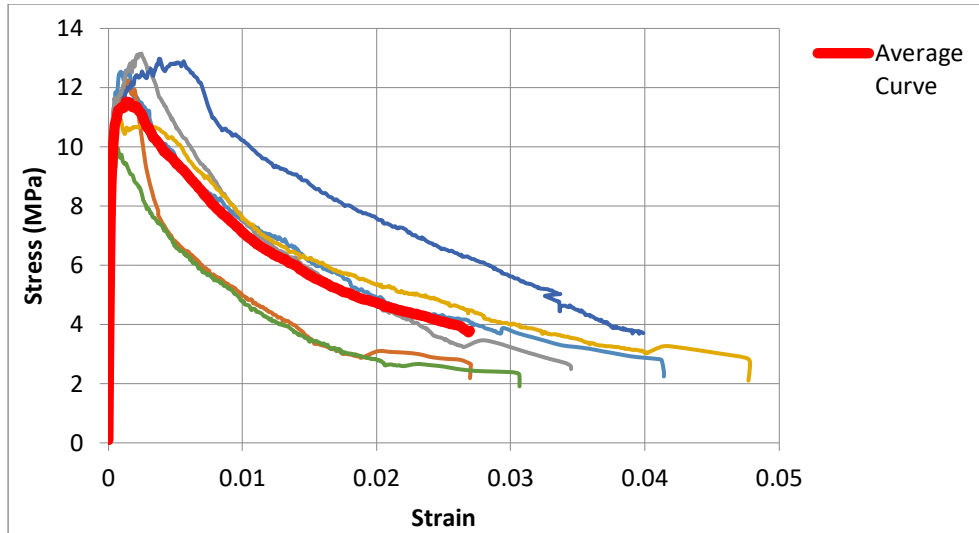


Figure 4.12 Experimental results of the direct tensile tests of UHPFRC over 2 months

The experimental results of Figure 4.12 indicate a scatter in the experimental results for the tensile strength between the values of 9.9 MPa and 13.1 MPa. Considering the average stress-strain curve, the maximum load was found to be equal to 11.5 MPa, and from the linear part of the stress-strain curve, the modulus of elasticity was calculated to be equal to 51 GPa. For the investigation of the compressive strength of the examined UHPFRC mixture, ten standard cubes were tested. The experimental results are presented in Table 4.5.

Specimen	Compressive Strength (MPa)
C1	135
C2	136
C3	137
C4	137
C5	132
C6	143
C7	145
C8	138
C9	128
C10	137

Table 4.5 Results of the compressive tests of the examined UHPFRC mixture

Based on the experimental results of Table 4.5, the compressive strength was in the range of 128-143 MPa and the average compressive strength was found to be equal to 137 MPa. Finally, as a reinforcement of the existing RC beams and the layers, steel bars grade B 500 C were used. The effect of steel grade on the performance of the strengthened beams is investigated in the next chapter. According to BS 4449:2005 (2005), for the steel bars grade B 500 C, the yield stress is equal to 500 MPa, while the ratio of the maximum tensile stress to the yield stress, is in the range of 1.15-1.3. Finally, the elongation at the maximum load is equal to 7.5%.

4.5.4 Preparation of the interface

A crucial parameter for the performance of the examined strengthening technique is the bonding at the interface between the existing members and the UHPFRC layers. The first step before the application of any layer or jacket was the roughening of the surface of the RC beams. For the preparation of the surface, a pistol grip needle scaler was used (see Figure 4.13a), and the sand patch method was used to quantify the concrete surface texture (see Figure 4.13c).



(a)



(b)



(c)

Figure 4.13 a) Roughening of the surface with a pistol grip needle scaler, b) the surface after roughening, c) measurement of the roughness depth using the sand patch method

As can be seen in Figure 4.13a, the coating was removed using a pistol grip needle scaler until the aggregates were exposed (see Figure 4.13b). Before the casting of the additional layers and jackets, the surface was cleaned carefully using high pressure water. As can be seen in Figure 4.13c, only fine sand with a maximum particle size of 500 μm was used in this process. In the present thesis, the interface for all the strengthened beams was roughened to a depth of 2-2.5 mm, which according to the fib bulletin 55 (2012), can be characterized as a rough interface. The average measured depths for each beam are presented in Table 4.6.

Beam	Measured Depth (mm)
U1	2.4
U2	2.2
UB1	2.35
UB2	2.2
3SJ1	2.1
3SJ2	2.2
D1	2.3
D2	2.5

Table 4.6 Measured roughness depths using the sand patch method

4.6 Casting of the examined layers and jackets

4.6.1 Casting of the UHPFRC layers

The first application of UHPFRC as a strengthening material was the construction of a layer at the tensile side of the beams. Two identical RC beams were strengthened with a 50 mm layer at the tensile side of the beams. The preparation of the beams for the addition of the UHPFRC layers is presented in Figures 4.14a and 4.14b. Once the surface was ready and the desired roughening depth was achieved (see Table 4.6), the beams were placed in the molds (see Figure 4.14a) and the UHPFRC layers were cast (see Figure 4.14b). As illustrated in these figures, in lab conditions, the layer was cast at the tensile side and before the testing, the specimens were turned upside down. The effect of pre-compression in this case was considered to be negligible.

One of the main advantages of the examined technique is the ease of preparation of the material. As can be seen in Figure 4.14b, only simple tools were used for both the mixing and casting of the layer. Due to the high volume of fibers, for the compaction of the mixture a hand-held vibrator was used and placed in contact with the outer surface of the molds and not within the mass of the UHPFRC.



(a)

(b)

Figure 4.14 a) Preparation of molds, b) casting of the layers

The strengthened beams were demolded forty-eight hours after the casting of the layers, and the specimens were wet cured daily for twenty-eight days. After this period the specimens were wet cured every two days and until the testing.

UHPFRC is a material with effective rheological properties. Hence, in real practise the layer can be cast with the special arrangement of the formwork. Also, in practise, there are applications where the steel fiber reinforced concrete has been cast as shotcrete and the same procedure can be followed for the casting of the layers. In this case, limitations such as the length of the fibers, the rheological properties and the fiber content should be taken into consideration.

4.6.2 Casting of the UHPFRC layers with dowels at the interface

The last investigation was the study of the performance of strengthened RC beams using UHPFRC layer with dowels crossing the interface. The preparation of the strengthened beams is presented in Figures 4.15a-4.15c.

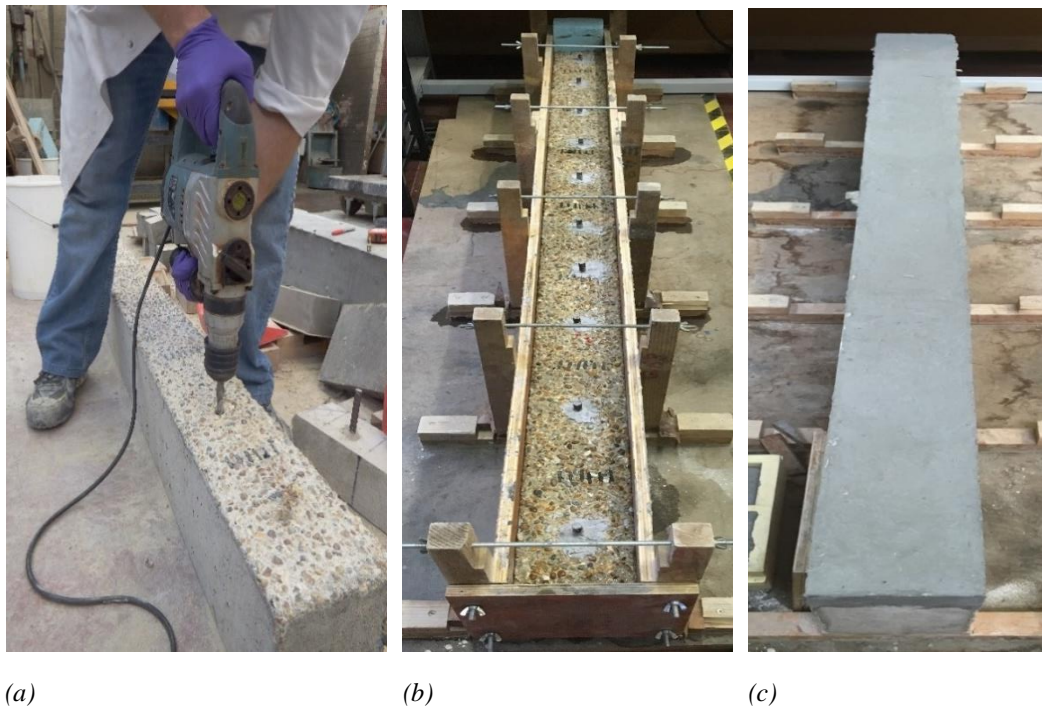


Figure 4.15 Preparation of the strengthened beams with UHPFRC layers and dowels: a) drilling of the beam, b) the dowels in position and c) strengthened beam after casting

As shown in Figure 4.15a, once the desired roughening depth was achieved and the surface was ready, the beams were drilled, using an impact drill, and the dowels were placed in position (see Figure 4.15b). For the connection of the dowels with the beams, a thixotropic

structural two-part adhesive, based on a combination of epoxy resins and special filler was used. According to the specifications of the manufacturer (Sika Limited, 2017), the compressive strength of the epoxy over 14 days and at +15°C is in the range of 70-80 MPa, and for the same conditions, the shear strength is in the range of 15-18 MPa. The tensile strength on the other hand, is in the range of 25-28 MPa and the bond strength with steel is higher than 21 MPa. Finally, the modulus of elasticity in compression is 9.6 GPa and in tension 11.2 GPa. To secure the good properties of the epoxy, the casting of the new layer took place fourteen days after the addition of the dowels.

4.6.3 Casting of the UHPFRC layers with the steel bars

The following technique to be investigated involves the addition of steel bars to the UHPFRC layer. The procedure for the construction of the layers is presented in Figures 4.16a and 4.16b. As illustrated in these figures, once the desired roughening depth was achieved, the surface was cleaned and the RC beams were placed in the molds (see Figure 4.16a). In Figure 4.16b a strengthened beam after the demolding is presented.



(a)

(b)

Figure 4.16 a) Preparation of specimen, b) strengthened beam after the demolding

For the application of a reinforced UHPFRC layer or jacket in real practice the first step is to expose the existing reinforcement, and later on to attach the new reinforcement. In cases that stirrups are used as shear reinforcement, these should be attached on the existing RC beams,

and later on, the layer or jacket should be cast. However, it should be noted that the new reinforcement must not be attached directly on the existing reinforcing bars. Also, in cases of jackets, and in order to secure the anchorage, the slab should be drilled at the position where the jacket will be constructed. The procedure for the strengthening of RC beams with reinforced layers and jackets is described in detail by the Technical Chamber of Greece (2004).

4.6.4 Casting of the three-side jackets

The next application constitutes the addition of a jacket on three sides of the RC beams. The different phases during the preparation of the examined beams are presented in Figures 4.17a-4.17c. The first step before the application of the jacket was the roughening of all the three sides of beams (see Figures 4.17a and 4.17b). Once the coating was removed and the desired depth was achieved, the beam was cleaned carefully and placed in the molds (see Figure 4.17b). A strengthened beam after the casting of the jacket is presented in Figure 4.17c.

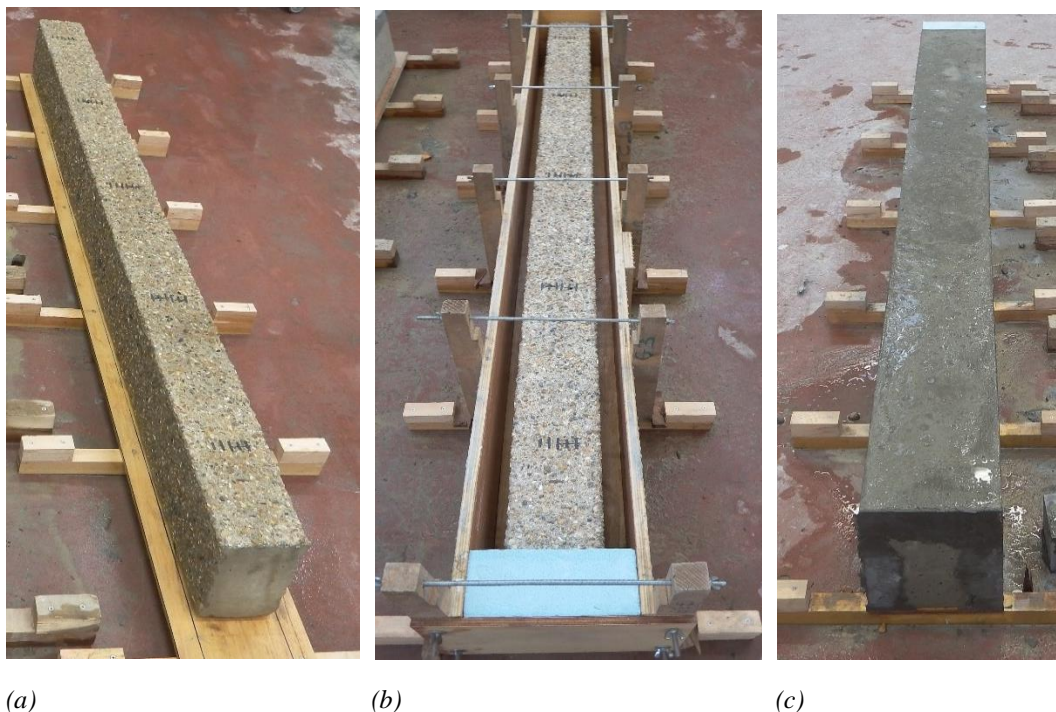
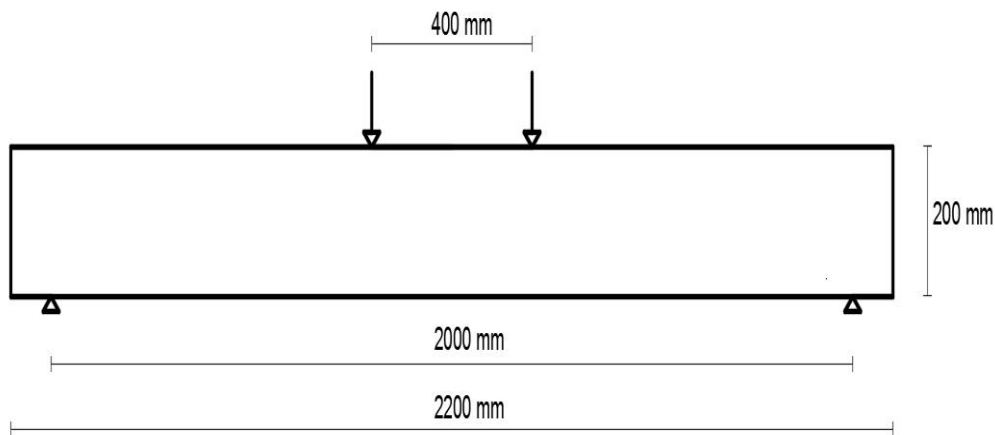


Figure 4.17 Different phases of the preparation of a three-side jacket: a) beam after roughening, b) beam in the mold ready for casting and c) strengthened beam after the demolding

4.7 Testing of the strengthened beams

4.7.1 Experimental setup for the testing of the control beams and the beams strengthened with jackets

In the literature there are limited applications of UHPFRC for strengthening and retrofitting of RC beams using UHPFRC. For the present experimental investigation and the testing of the strengthened beams, a similar method used by Tsioulou et al. (2013) and Safdar et al. (2016) has been selected. Therefore, the RC beams were tested under for point loading test with a constant displacement rate of 0.008 mm/sec (Tsioulou et al., 2013) leading to comparable results. The experimental setup for these tests is presented in Figures 4.18a and 4.18b . As can be seen, the span length was equal to 2000 mm while the distance between the two loading points was equal to 400 mm. During the testing, measurements for the load and the deflection at the middle of the span length and on both sides of the beams were also recorded. The deflection was measured using two LVDTs with an accuracy of 0.001 mm.



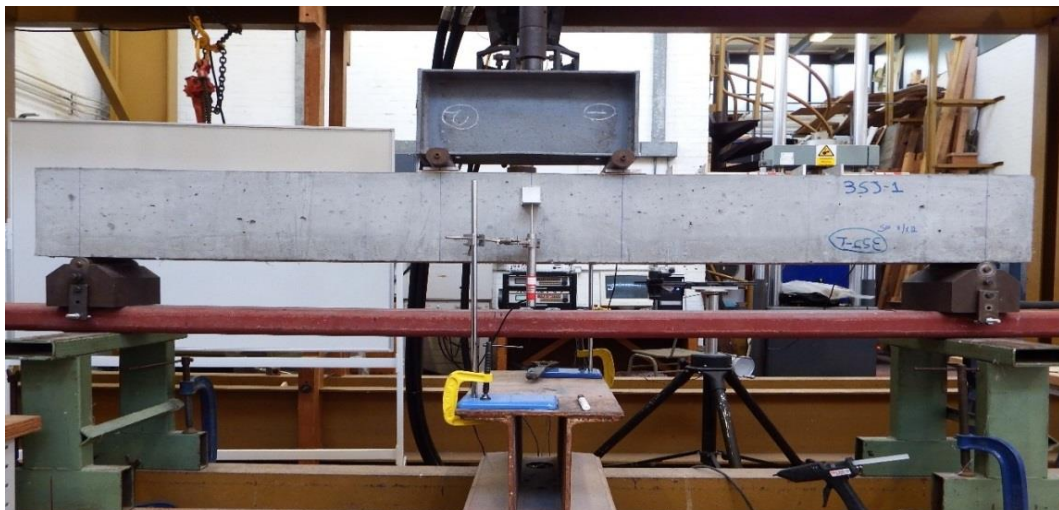
(a)



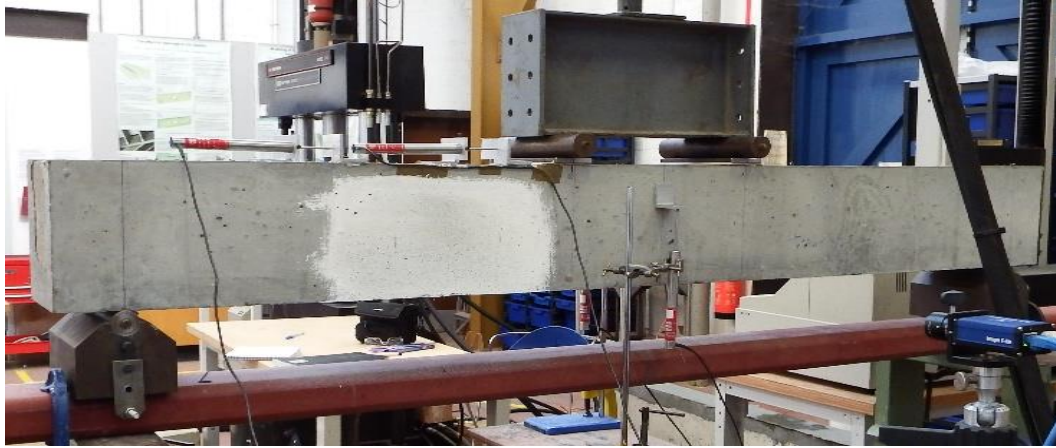
(b)

Figure 4.18 Experimental setup for the four point loading tests: a) distance between the two loading points and the span length and b) experimental setup for the control beams

The experimental setup of Figure 4.18 was also adopted for the testing of the beams strengthened with a three-side jacket. The setup for these tests is presented in Figures 4.19a and 4.19b.



(a)

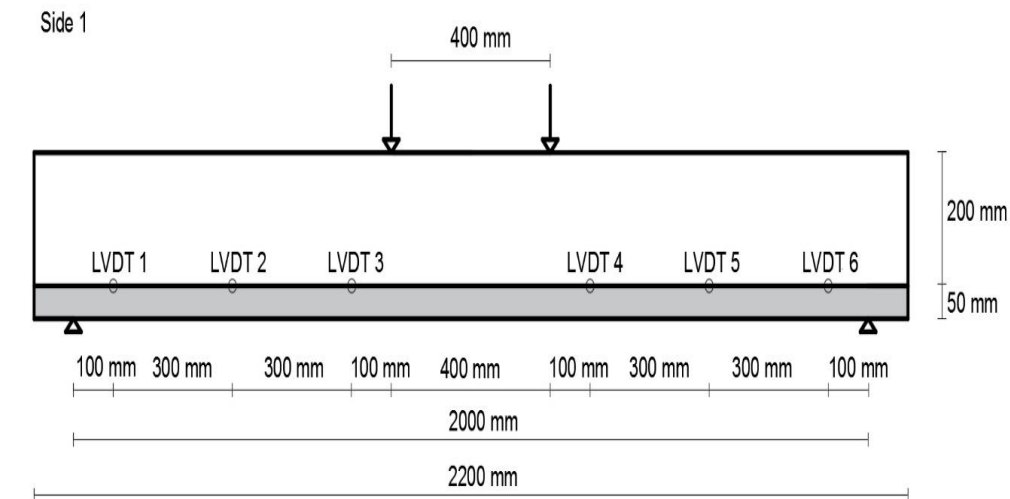


(b)

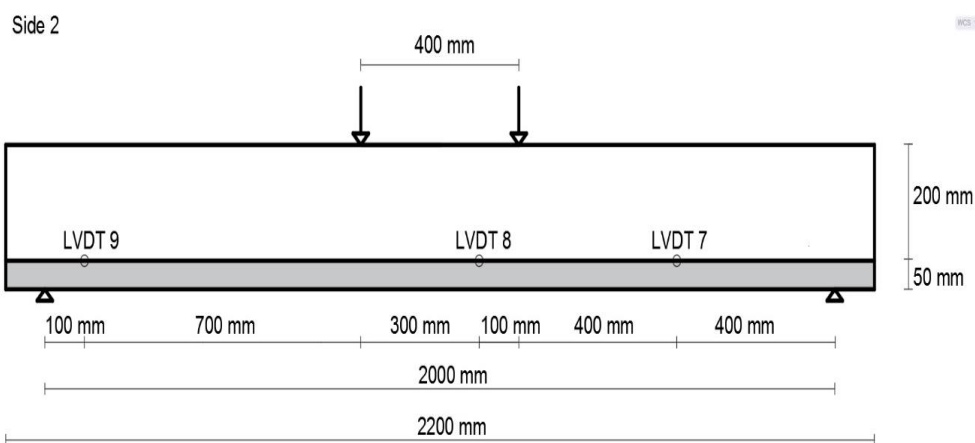
Figure 4.19 Experimental setup for the beams strengthened with three-side jackets: a) experimental setup (side 1) and b) experimental setup (side 2)

4.7.2 Experimental setup for the testing of beams strengthened with layers

For the testing of beams strengthened with UHPFRC layers at the tensile side, apart from the measurements for the load and the deflection in the middle of the span length, measurements were also recorded for the slip at the interface. These measurement were recorded using nine LVDTs, which were placed along the whole length of the beam and on both sides. The position of the LVDTs is presented in Figures 4.20a and 4.20b. As can be seen in Figure 4.20a, the LVDTs were placed symmetrically between the supports and the two loading points in side 1, while in side 2 (see Figure 4.20b) three LVDTs were used for the validation of the results obtained in side 1. Finally, as illustrated in Figures 4.20a and 4.20b, the span length and the distance between the two loading points during the testing were the same with the experimental setup of Section 4.7.1 for the control beams and the beams strengthened with three-side jackets.



(a)



(b)

Figure 4.20 (a) Distance between the two loading points, span length and position of the LVDTs in side 1 and (b) distance between the two loading points, span length and position of the LVDTs in side 2

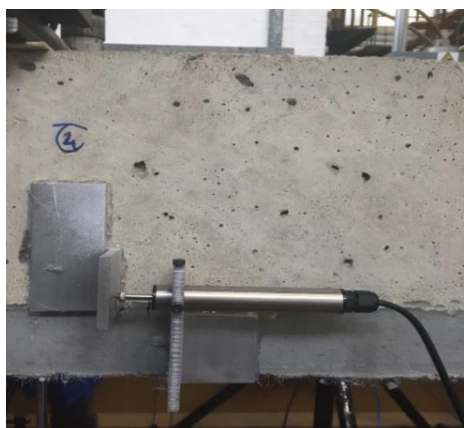
The experimental setup for the beams strengthened with layers is also presented in Figure 4.21. As can be seen, the LVDTs were attached on the beams with metal angle sections, which were glued on the RC beams. Any additional slips due to the rotation of the LVDTs during the testing were found to be negligible.



(a)



(b)



(c)

Figure 4.21 Experimental setup for the beams strengthened with layers: a) experimental setup (side 1) and, b) experimental setup (side 2) and c) LVDT used for the measurement of slip

4.8 Experimental results

4.8.1 Experimental results for the control beams

The experimental results for the load and the deflection of the control beam P1 are presented in Figure 4.22.

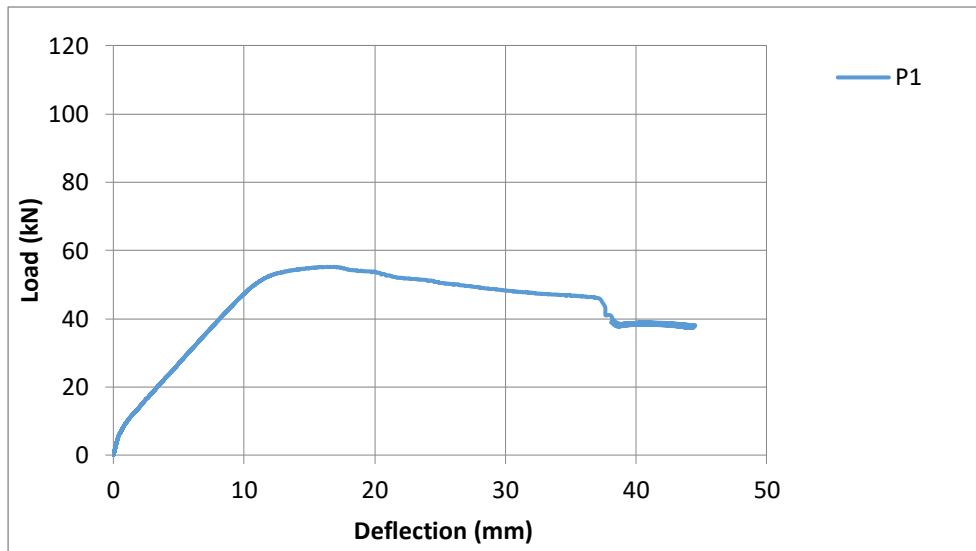


Figure 4.22 Load versus deflection curve for beam P1

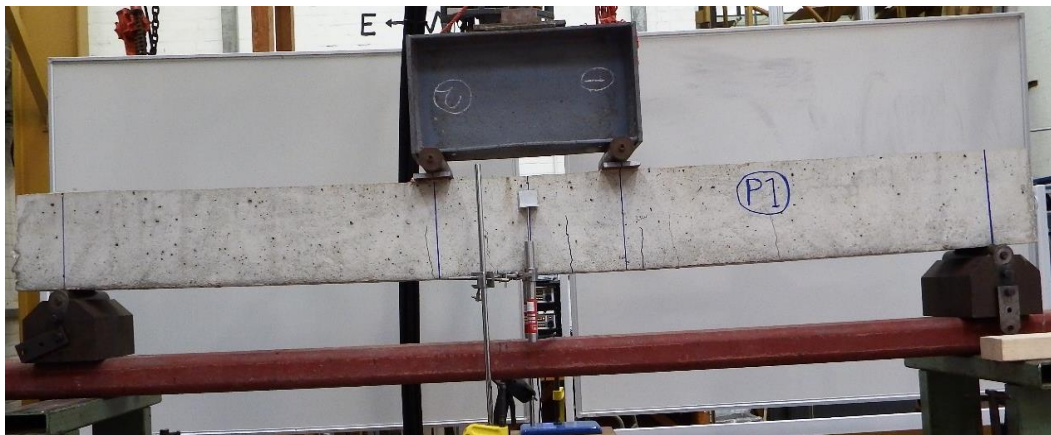
As shown in this figure, the maximum load was equal to 55.18 kN while, from the linear part of the load-average deflection curve, the stiffness was calculated to be equal to 10.5 kN/mm. Finally, the deflection at the maximum and at the failure was found to be equal to 16.64 mm and 37.4 mm respectively. From the graph, it can also be distinguished, that the slope of the load-deflection curve changes at 50 kN, at which point the reinforcement reached yielding; after this point a plateau can be distinguished. The yield of the reinforcement has also been verified analytically. The yield strain of the reinforcement ϵ_y can be defined as:

$\epsilon_y = \frac{f_y}{E_s}$, where f_y is the yield stress (500 MPa) and E_s is the modulus of elasticity (200 GPa).

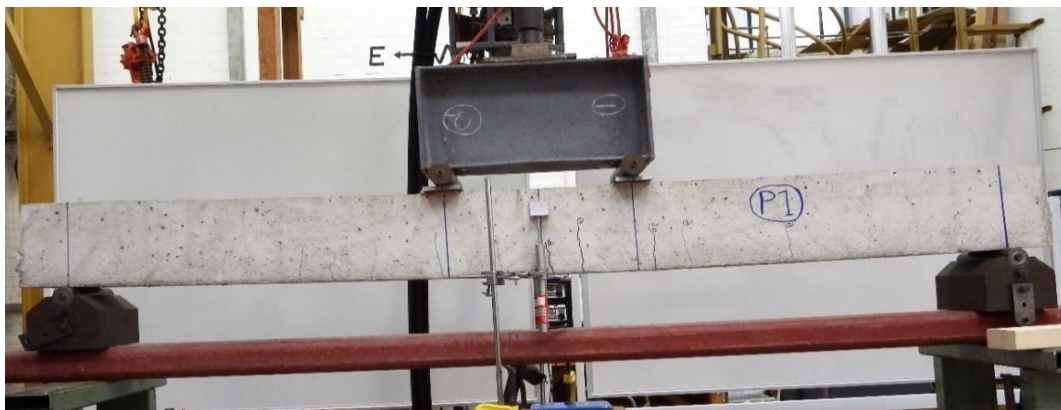
According to Wight and MacGregor (2012), and based on ACI Code Section 10.2.7, the strain of the reinforcement ϵ_s can be found from the following equation: $\epsilon_s = \left(\frac{d_1 - c_1}{c_1}\right) \cdot \epsilon_{cu}$, where ϵ_{cu} is the maximum useable compressive strain (3.5 ‰), d_1 is effective flexural depth of the section, c_1 is depth of the neutral axis. Also, c_1 is given from $c_1 = \frac{a}{\beta_1}$, where $a = \frac{A_s f_y}{0.85 f_c b}$. Finally, b is the breadth of the column (150 mm), A_s is the amount of reinforcement (226.2 mm²), while based on Whitney (1937) for compressive strength up to 28 MPa the coefficient β_1 can be considered equal to 0.85, while for values between 28 MPa and 56 MPa it is given from the following

equation: $\beta_1 = (0.85 - 0.05 \frac{f_c - 28 \text{ MPa}}{7 \text{ MPa}})$. From the above equations it has been calculated that $\epsilon_s = 0.01 > \epsilon_y$, so the steel yields.

Finally, from Figure 4.22, it can be noticed that once the beam reached its maximum load carrying capacity, the load dropped gradually. The different phases during the testing of beam P1 are presented in Figures 4.23a-4.23d.



(a)



(b)



(c)



(d)

Figure 4.23 Different phases during the testing of beam P1: a) appearance of the first flexural cracks, b) propagation of the cracks, c) failure on both the compressive and the tensile sides and d) the beam at the end of the test

From the figures above, it is clear that a flexural failure has occurred. Hence, a crack in the middle of the span length was crucial for the failure of the beam. The first flexural cracks start appearing when the load was equal to 24 kN, and the crucial crack for the failure of the beam appeared when the load was equal to 31 kN in the middle of the span length (see Figure 4.23a). After this point, a localization of the damage could be distinguished while more flexural cracks propagated along the whole length of the beam (see Figure 4.23b). As shown in Figure 4.23c, a failure at the compressive side of the beam occurred during the testing. This failure started once the beam had reached its maximum load carrying capacity, and it was at the descending branch of the load-deflection curve. This resulted in the damage to the beam on both the compressive and the tensile sides at the end of the test (see Figures 4.23c and 4.23d).

A second beam, identical with beam P1, was prepared and tested in order to validate the reliability of the results obtained from beam P1. The results for the load and the deflection of beam P2 are presented in Figure 4.24.

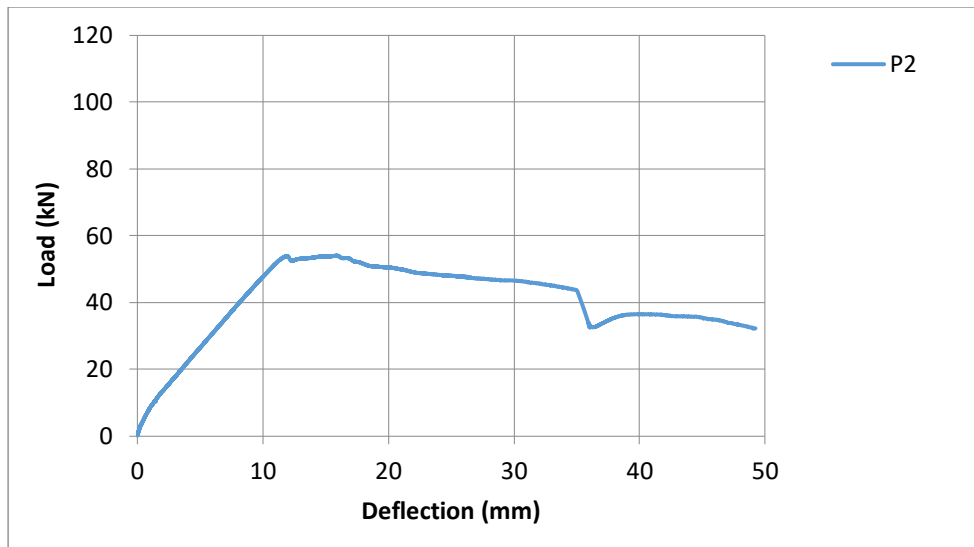


Figure 4.24 Load versus deflection for beam P2

Based on the results of Figure 4.24, the maximum load was found to be equal to 53.98 kN, the stiffness was calculated to be 7.4 kN/mm and the deflection at the maximum load and the failure was equal to 15.89 mm and 35.1 mm respectively. Also, from the graph it can be distinguished that the reinforcement reached yielding at 53 kN; a plateau can be distinguished after this point. The different phases during the testing of beam P2 are presented in Figures 4.25a-4.25d.



(a)



(b)



(c)



(d)

Figure 4.25 Different phases during the testing of beam P2: a) appearance of the first flexural cracks, b) propagation of the cracks c) failure on both the compressive and tensile sides and d) the beam at the end of the test

The failure mode of beam P2 was identical with beam P1. Hence, flexural cracks in the middle of the span length were crucial for the failure of the beam (see Figures 4.25c and 4.25d). The

first cracks start appearing when the value of load was equal to 20 kN while the crucial cracks appeared for a value of a load equal to 25 kN. After this point, the damage localised, and also, more flexural cracks propagated progressively along the whole the length of the beam (see Figure 4.25b). Once the beam had reached its maximum load carrying capacity and it was at descending part of the load-deflection curve, a failure at the compressive side occurred (see Figure 4.25c). Both the compressive and the tensile sides of the beam were damaged as a result at the end of the test (see Figure 4.25c).

The experimental results for the identical beams P1 and P2 are presented in the same graph in Figure 4.26. The same figure also presents the average load-deflection curve of both beams. As illustrated, there is a positive agreement in the experimental results for the two beams, and similar values were achieved for the maximum load (55.18 kN for beam P1 versus 53.98 kN for beam P2) and the stiffness (10.5 kN/mm for beam P1 versus 7.4 kN/mm for beam P2). Finally, considering the average load-deflection curve, the maximum load was found to be equal to 54.6 kN, the stiffness was calculated to be 9.2 kN/mm and the deflection at the maximum load and the failure was equal to 15.89 mm and 35.4 mm respectively.

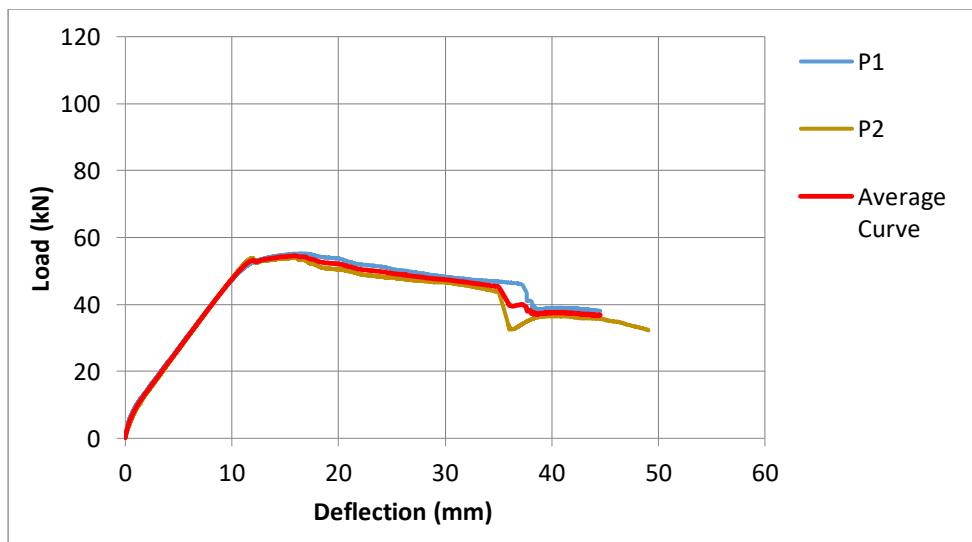


Figure 4.26 Average load deflection curve for beams P1 and P2

4.8.2 Experimental results for the beams strengthened with UHPFRC layers

The beam U1 was strengthened with an UHPFRC layer at the tensile side (see Figure 4.5), and the experimental setup is presented in Section 4.7.2. The load-deflection results are presented in Figure 4.27.

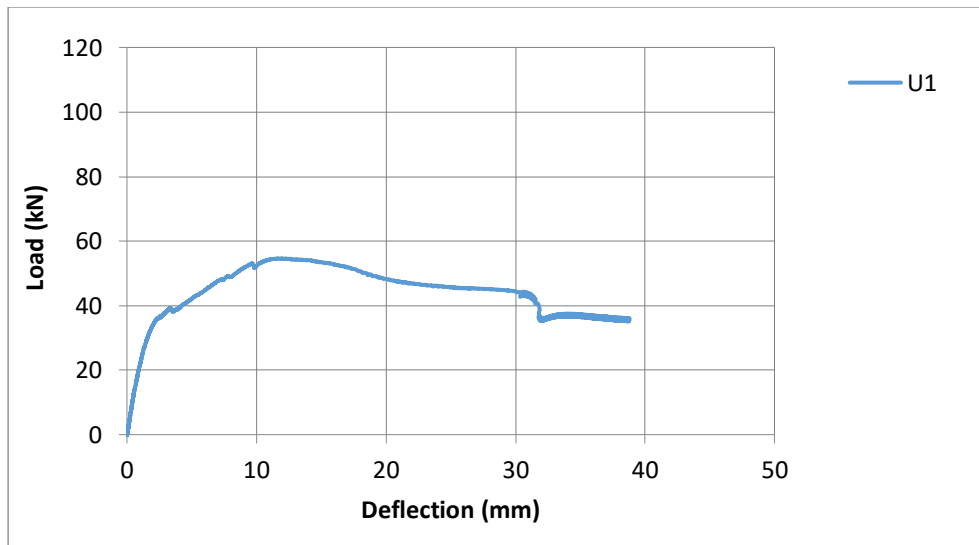


Figure 4.27 Load versus deflection for beam U1

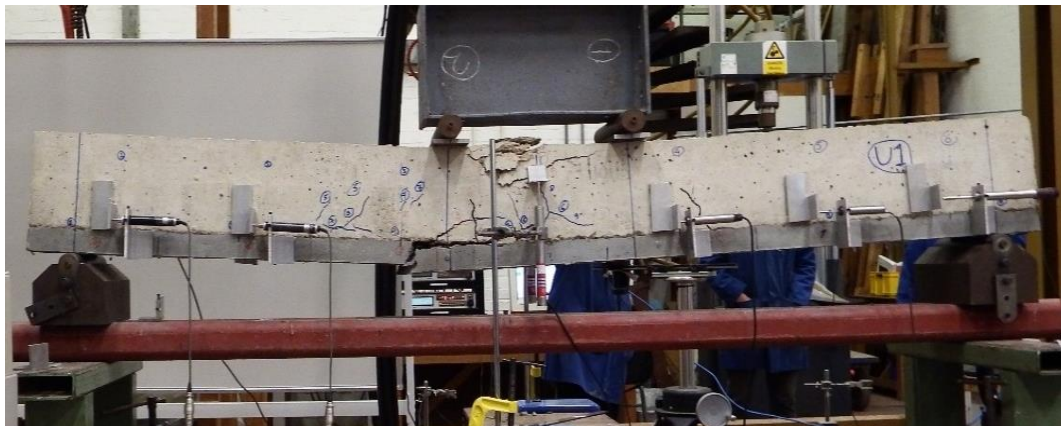
Based on the experimental results of Figure 4.27, the maximum load of beam U1 was found to be equal to 54.6 kN, and from the linear part of the load-deflection curve, the stiffness was calculated to be equal to 24.2 kN/mm. Finally, the deflection at the maximum load was equal to 11.89 mm, while at the failure was equal to 31.1 mm. Due to the fact that there was a local de-bonding at the interface, which affected the measurements of the LVDTs, these recordings for beam U1 were ignored. The different phases during the test are illustrated in Figure 4.28.



(a)



(b)



(c)



(d)

Figure 4.28 Testing of beam U1: a) appearance of the first flexural cracks during the test, b) propagation of the cracks and beginning of local de-bonding, c) failure on both the compressive and tensile sides and d) the de-bonding at the interface

The first crack during the testing, which was also crucial for the failure of the beam, appeared for a value of load equal to 32 kN on the UHPFRC layer and progressively propagated along the RC beam. During the testing, more flexural cracks appeared along the whole length of the beam while shear cracks, which were not crucial for the failure of the beam, could also be

distinguished (see Figures 4.28b and 4.28c). For a value of load equal to 48 kN and before the beam reach its maximum load capacity, a local de-bonding began at the interface, which could be distinguished (see Figures 4.28b, 4.28c and 4.28d). As the beam reached its maximum load carrying capacity and was at the descending branch of the load-deflection curve, a failure at the compressive side of the beam began, which had as a results the damage the compressive side at the end of the test (see Figure 4.28c). During the testing higher deformations on the compressive side occurred. At the point where the limit compressive strain of 3.5 ‰ was exceeded, the failure at the compressive side started. This had as a result the progressive damage of the compressive side and the reduction of the level arm, which had as a result the reduction of the load carrying capacity of the beam.

The second identical beam with U1 was tested under the same loading conditions. The load-deflection results of beam U2 are presented in Figure 4.29.

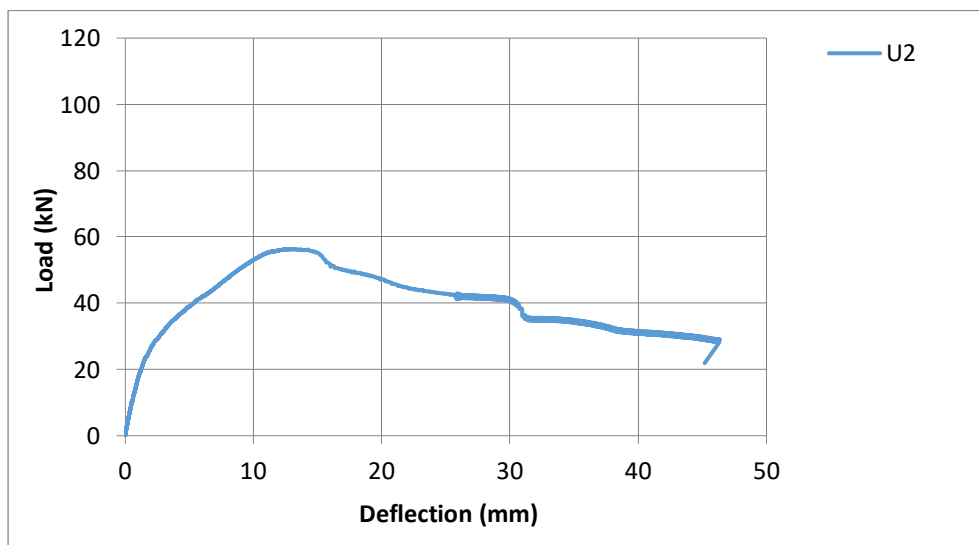
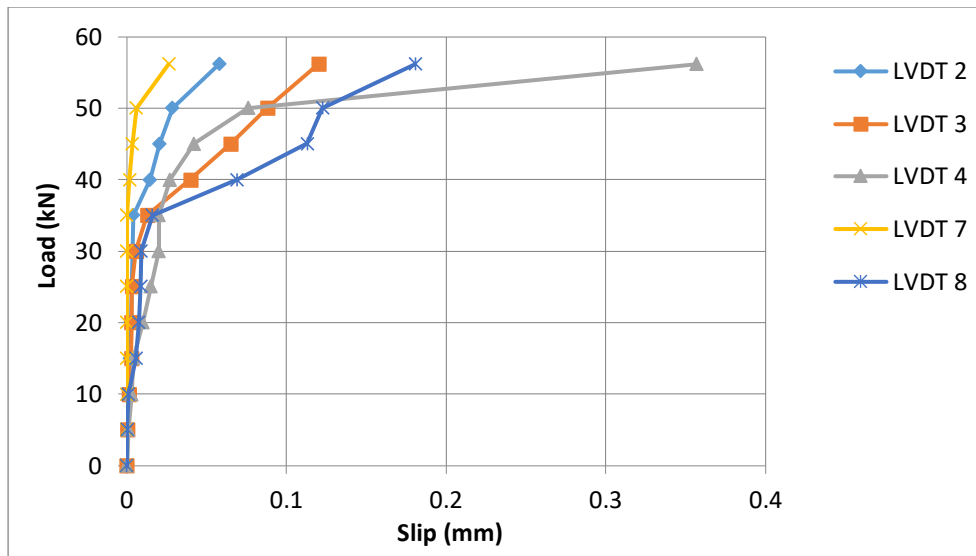
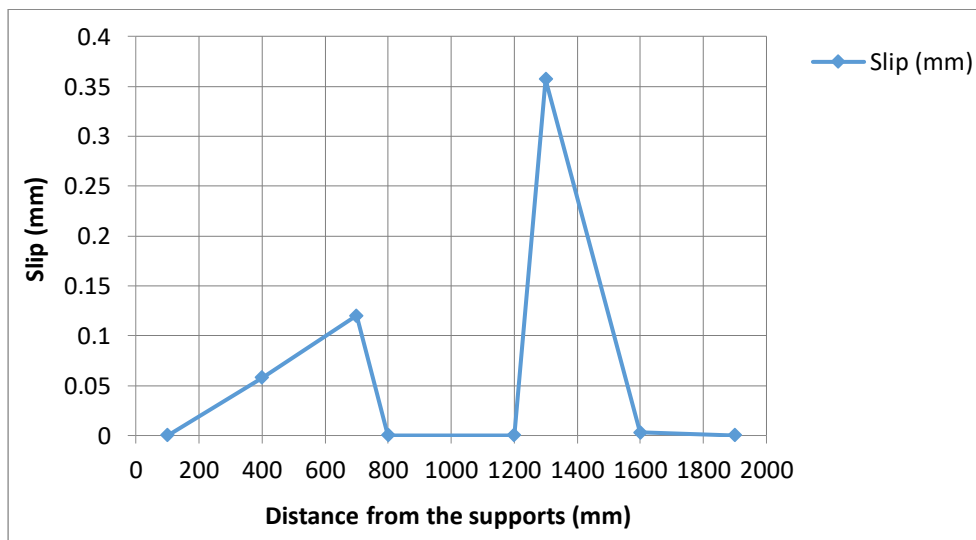


Figure 4.29 Load versus deflection for beam U2

Based on the results of Figure 4.29, the maximum load was equal to 56.3 kN, the stiffness was calculated equal to 19.2 kN/mm and the deflection at the maximum load and at the failure was equal to 13.1 mm and 21.8 mm respectively. In Figures 4.30a and 4.30b the results for the load versus the slip and the slip versus the distance from the support for the maximum load are presented.



(a)



(b)

Figure 4.30 a) Load versus slip in different positions for beam U2 and b) slip versus distance from the supports

Based on the measurements for the slip, the slip close to the supports was equal to zero since at these points the normal to the interface stresses and subsequently the friction action was significantly lower compared to the other points. Hence, slips were recorded at positions 2, 3, 4, 5, 7 and 8. The positions of the LVDTs, where the measurements of slips were recorded, are presented in Figure 4.20. As shown in Figures 4.30a and 4.30b, small values for the slip were recorded at positions close to the supports, ranging between 0.026 mm and 0.062 mm, and higher values were recorded at positions 4 (where the shear is maximum) and at position 8 (where the moment is maximum). As illustrated in Figure 4.20, the geometry and the loading conditions of the beams were symmetrical, while the preparation of the surface was the same

along the whole length of the beam (see Table 4.6). However, the slip measurements were not symmetrical, which can be attributed to the asymmetrical crack pattern at the interface. The different phases during the testing of beam U2 are presented in Figure 4.31.



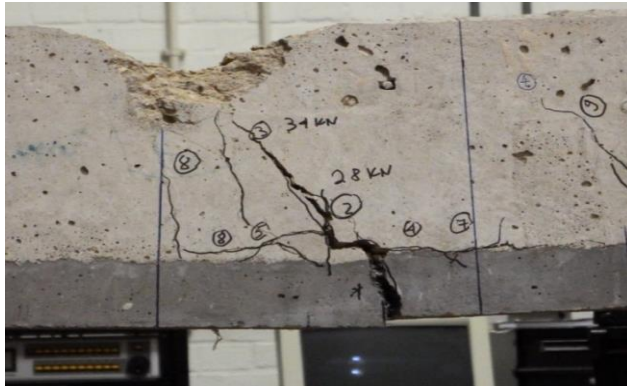
(a)



(b)



(c)



(d)

Figure 4.31 Testing of beam U2: a) appearance of the first cracks, b) propagation of the cracks, c) failure on both the tensile and compressive sides and d) the beam at the end of the test

The failure mode of beam U2 was identical with the failure mode of beam U1. Hereby, the first crack during the testing, occurred as result of the value of a load equal to 28 kN on the UHPFRC layer and progressively propagated on the RC beam. During the testing and for the higher values of a load, more minor flexural and shear cracks appeared on the strengthened beam (see Figure 4.31b). When the beam had reached its maximum load carrying capacity and was at the descending branch of the load-deflection curve, a failure at the compressive side commenced, which led to the failure of both the compressive and the tensile side at the end of the test (see Figures 4.31c and 4.31d). As can be seen in Figure 4.31d, the bonding at the interface for beam U2 was effective, and no de-bonding at the interface was noticed between the UHPFRC layer and the RC beam during the testing.

The load-deflection results obtained for both the identical beams U1 and U2 are presented in the same graph in Figure 4.32. From this figure, it is clear that there is a strong agreement in the experimental results for both the identical beams U1 and U2, and despite the local de-bonding at the interface of beam U1. This indicates that this local de-bonding did not affect the load carrying capacity of the beam significantly, and similar values for the maximum load and the stiffness were obtained for both beams U1 and U2. Based on the experimental results, an average load-deflection curve was calculated, which is also presented in Figure 4.32. Thus, considering the average curve, the maximum load was found to be equal to 55.3 kN, the stiffness was calculated to be equal to 21.5 kN/mm, while the deflection at the maximum load and at the failure was equal to 12.26 mm and 25.1 mm respectively.

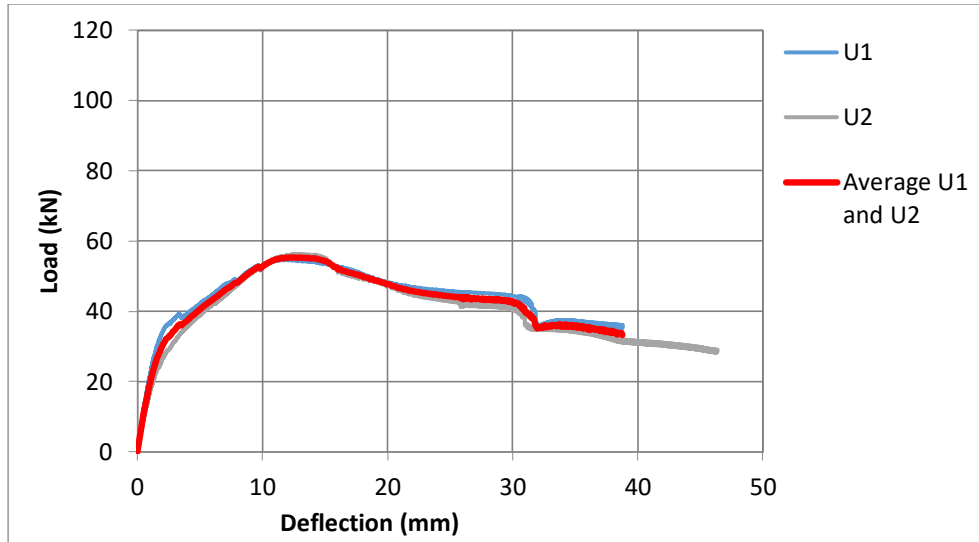


Figure 4.32 Average load versus deflection curve for beams U1 and U2

4.8.3 Experimental results for the beams strengthened with UHPFRC layers and dowels

In the following section the experimental results of the strengthened beams with UHPFRC layers and dowels are presented. The experimental setup for these tests is the same with the setup used for the strengthening of beams with UHPFRC layers, and it is presented in Section 4.7.2. The experimental results for the first examined strengthened beam D1 are presented in Figure 4.33.

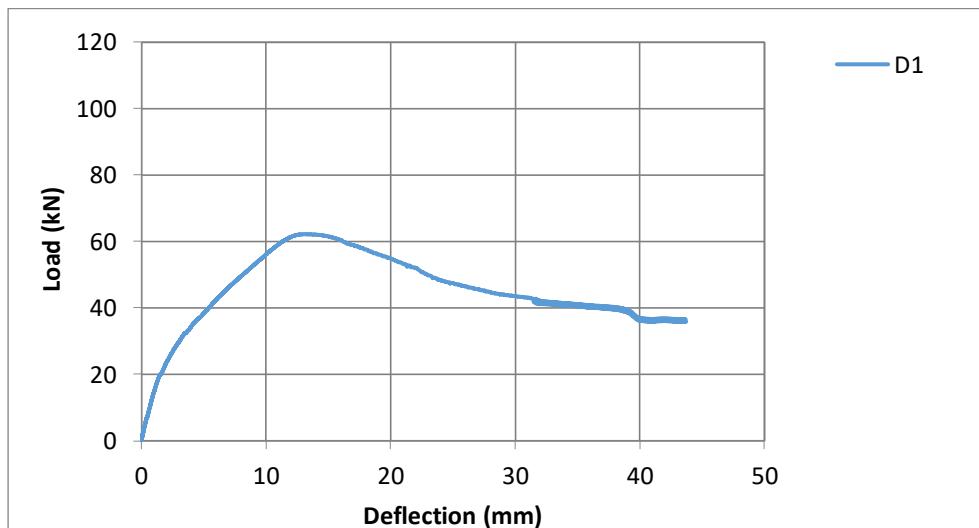
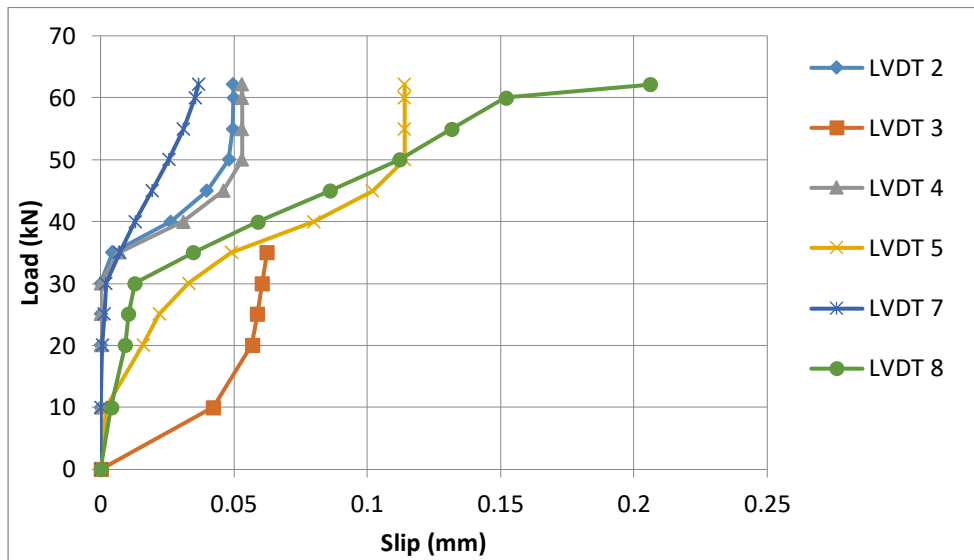


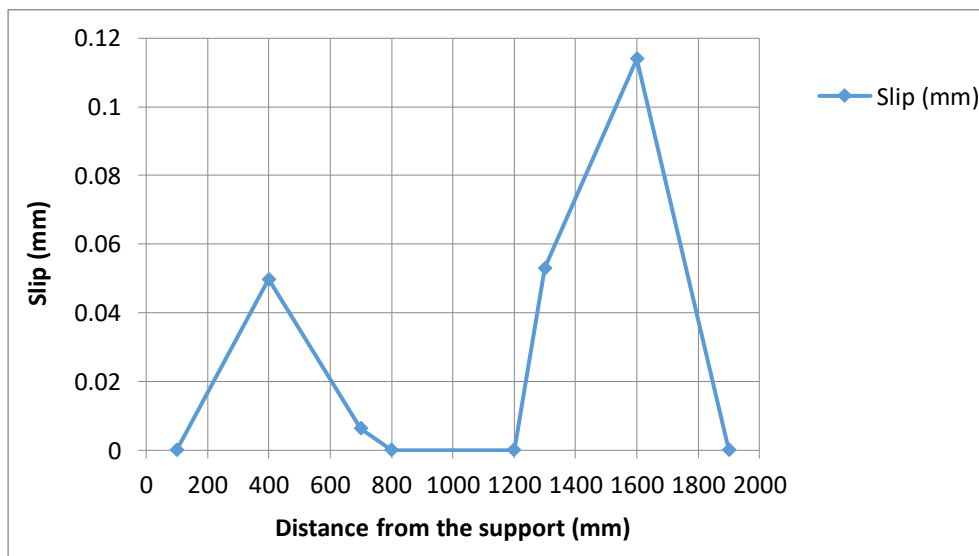
Figure 4.33 Load versus deflection for beam D1

Based on the experimental results of Figure 4.33, the maximum load was found to be equal to 62.2 kN, the stiffness was calculated to be equal to 15 kN/mm, while the deflection at the maximum load and at the failure was equal to 13.5 mm and 23.1 mm respectively. The measurements for the slip at the interface in different positions are presented in Figure 4.34a

and the measurement for the slip versus the distance from the support at the maximum load are presented in Figure 4.34b.



(a)

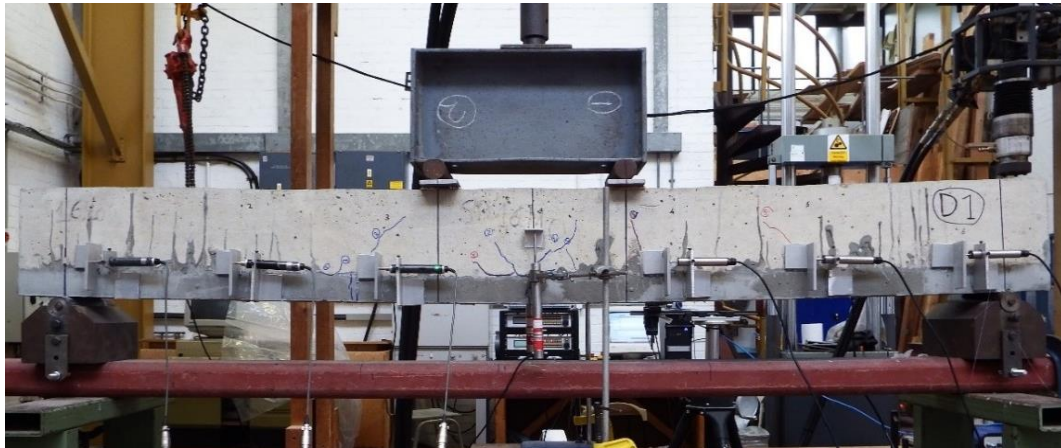


(b)

Figure 4.34 a) Load versus slip in different positions for beam D1 and b) slip versus the distance from the supports for beam D1

As shown in Figure 4.34a, the maximum value of the slip was recorded at position 8, located between the two loading points, while the slip at the area close to the supports was equal to zero. By contrast, values between 0.036 mm and 0.055 mm were recorded at positions 2, 4 and 7. Due to the fact that at position 3, the metal angle section was detached from the beam, measurements higher than 35 kN were lost at this position. It can be noticed, that apart from the higher load carrying capacity of beam D1, compared to beams U1 and U2, lower values

of slip at the interface were also recorded. Finally, it is worth mentioning that, as illustrated in Figure 4.34a, the slip at positions 2, 3, 4, and 5 and despite the fact that the load was increased, the values of slip remained the same. This can be attributed to the effect of the dowels which prevented any further slip. Also, these readings could be affected by the development of cracks at the interface. The different phases during the testing of beam D1 are presented in Figures 4.35a-4.35c.



(a)



(b)



(c)

Figure 4.35 Different phases during the testing of beam D1: a) appearance of the first cracks, b) failure of beam on both the compressive and tensile sides and c) beam at the end of the test

Figures 4.35b and 4.35c illustrates that a flexural crack in the middle of the span length of the strengthened beam was crucial for the failure of the layer and subsequently of the beam. This crack began on the UHFRC layer and progressively propagated along the RC beam. More specifically, this crack was appeared for a value of load equal to 30 kN; after this point, more flexural and shear cracks propagated along the whole length of the beam (see Figure 4.35b). At the descending branch of the load-deflection curve, a failure at the compressive side commenced (see Figure 4.35b). Once the maximum tensile strength of the layer was reached, the layer could not further contribute to the load carrying capacity. During the testing higher deformations at the compressive side occurred and at the point where the limit compressive strain of 3.5 ‰ at the compressive side was exceeded, the damage on the compressive side started. This had as a result the progressive damage of the compressive side, the reduction of the level arm and the reduction of the load carrying capacity. Finally, as can be seen in Figure 4.35c, there was a strong bonding at the interface with no de-bonding at the interface.

A second beam, identical with beam D1, was constructed and tested under the same loading conditions in order to validate the experimental results obtained from beam D1. The experimental results for the load and the deflection are presented in Figure 4.36.

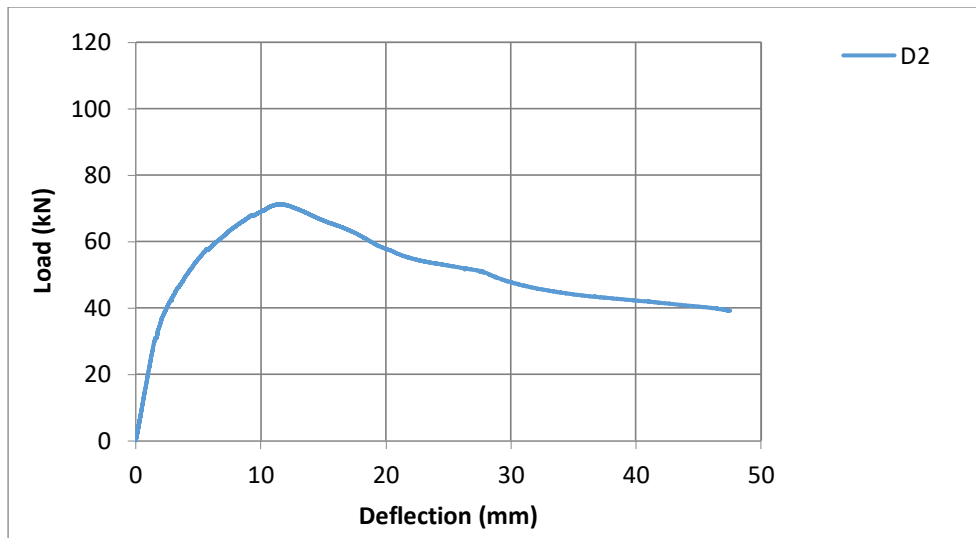
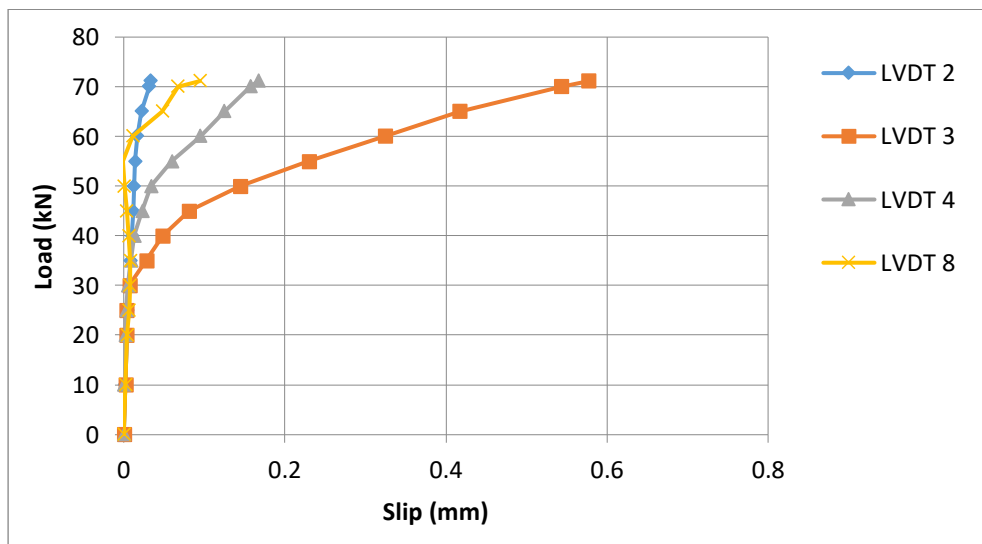
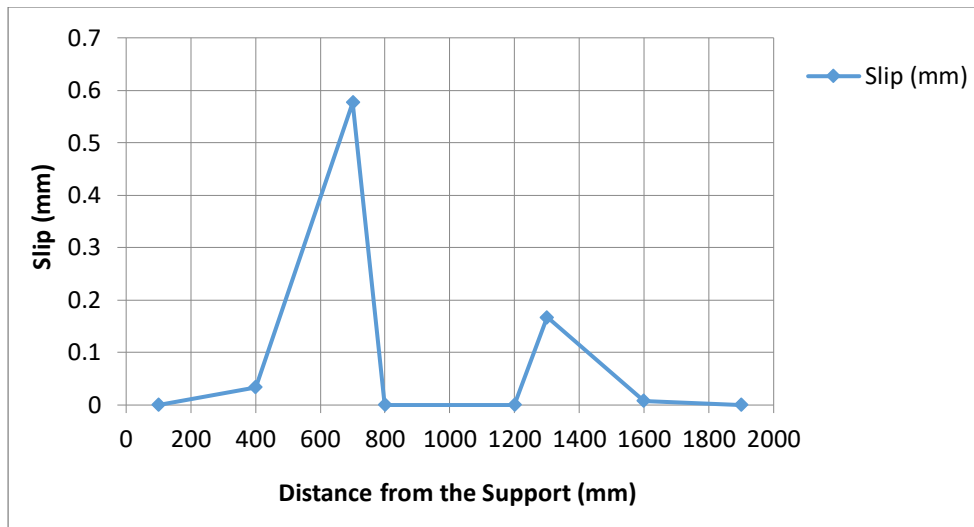


Figure 4.36 Load versus deflection for beam D2

Based on the results of Figure 4.36, the maximum value of a load was equal to 71.3 kN, the stiffness was calculated at 20.5 kN/mm and the deflection at the maximum load and at the failure was equal to 11.54 mm and 20.62 mm respectively. The measurements for the load versus the slip and the slip versus the distance from the support for the maximum load are presented in Figures 4.37a and 4.37b respectively.



(a)



(b)

Figure 4.37 a) Load versus slip in different positions for beam D2 and b) slip versus the distance from the support for beam D2

As shown in Figure 4.37a, slip was recorded only at the positions 2, 3, 4 and 8. More specifically, small values between 0.033 mm and 0.088 mm were recorded at positions 2 and 3 and also at position 8. The higher values of slip were recorded at the positions 3 and 4 (where the shear is maximum), which are located close to the two loading points. Hence, a high value of the slip was recorded at position 4, which is located close to the failure area of the beam. This could have affected the reading for the slip. The different phases during the testing of beam D2 are represented in Figures 4.38a-4.38c.



(a)



(b)



(c)

Figure 4.38 Different phases during the testing of beam D2: a) appearance of the cracks, b) the failure of beam on both the compressive and tensile sides and c) beam at the end of the test

The failure mode of beam D2 was identical with beam D1 and the crucial crack for the failure of the beam appeared on the UHFRC layer for a value of a load equal to 51 kN. As presented in Figures 4.38a and 4.38b, more flexural and shear cracks appeared along the whole length of the beam during the testing, while the failure at the compressive side commenced at the descending part of the load-deflection curve (see Figures 4.38b and 4.38c) The experimental results for both the identical beams D1 and D2 are presented in the same graph in Figure 4.39.

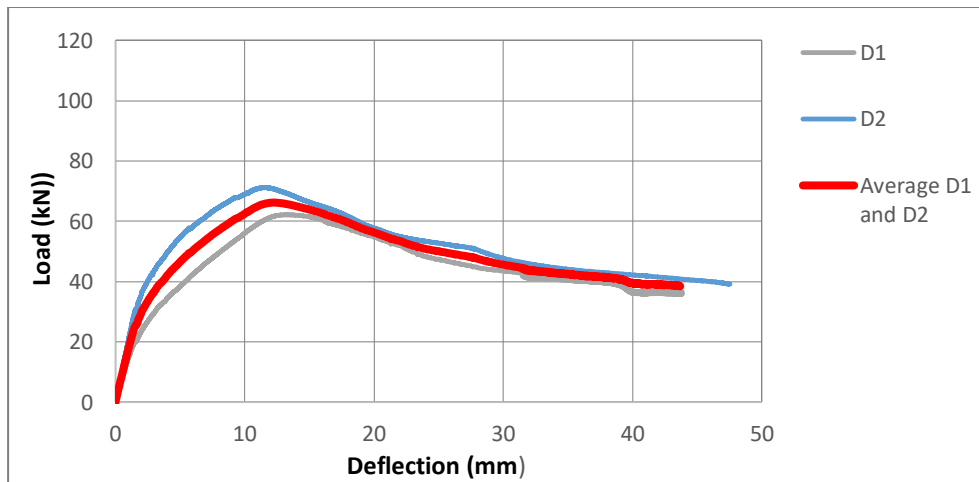


Figure 4.39 Average load versus deflection curve for beams D1 and D2

According to Figure 4.39, beam D1 presented at slightly lower values for both the maximum load (62.2 kN versus 71.3 kN) and the stiffness (15 kN/mm versus 20.5 kN/mm) in comparison with beam D2. This can be attributed to local deficiencies of the UHPFRC, such as the fiber distribution, and also with factors which are related to deficiencies during the preparation and the construction of the strengthened beam. Based on the average curve, the maximum load was found to be equal to 66.2 kN, the stiffness was calculated at 17.8 kN/mm, the deflection at the maximum load was 12.22 mm and the deflection at the failure was 22.3 mm.

4.8.4 Experimental results for the beams strengthened with UHPFRC layers and steel bars

The following RC beams to be examined were strengthened with an UHPFRC layer and steel bars. The experimental setup for these tests is presented in Section 4.7.2, and the load-deflection results for the first strengthened beam UB1 are presented in Figure 4.40.

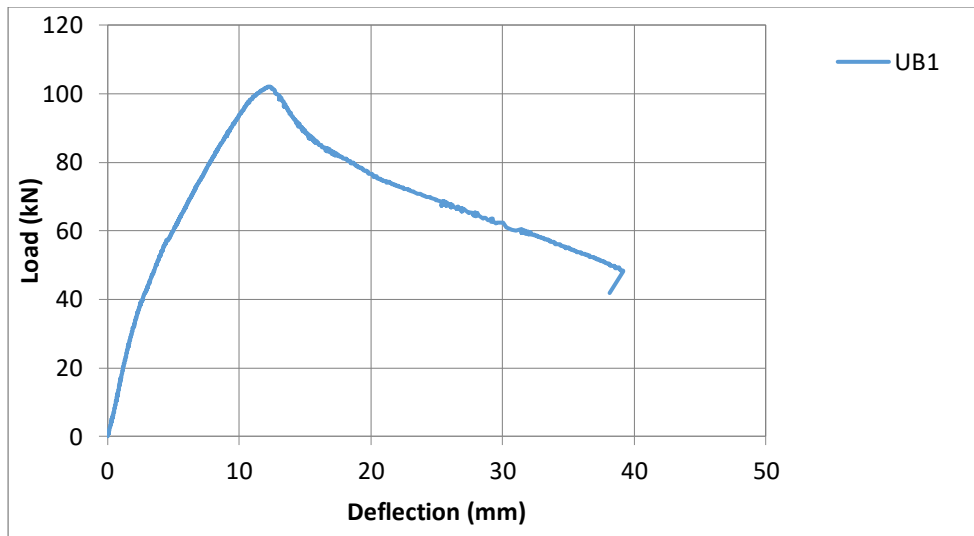
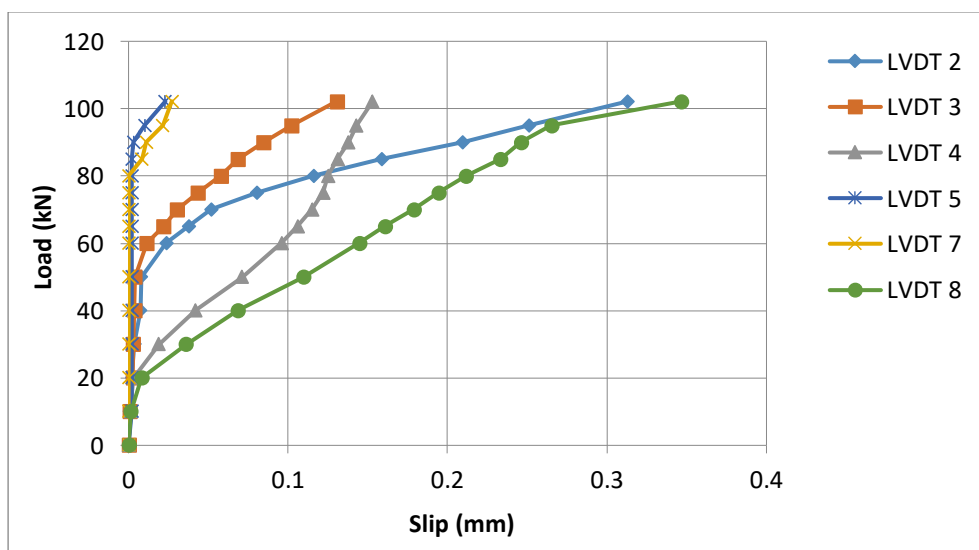
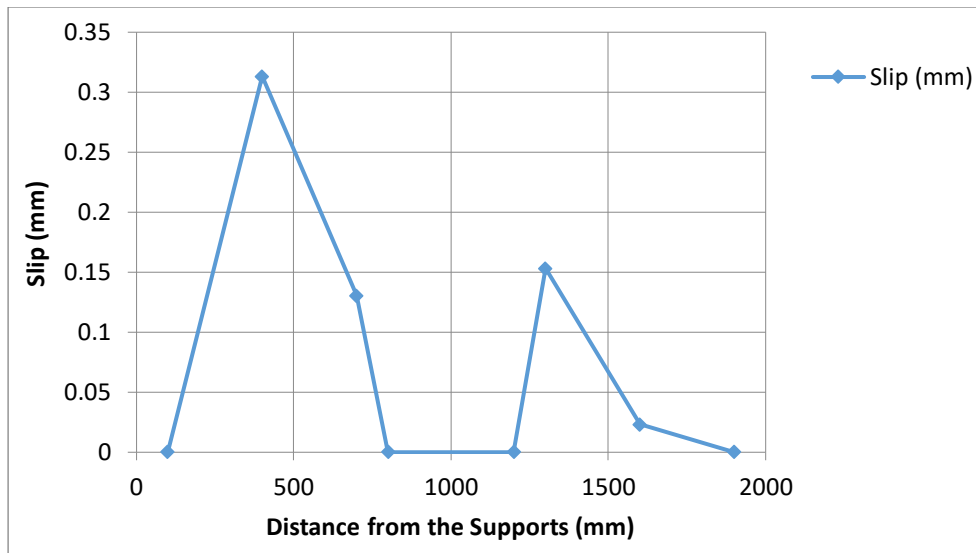


Figure 4.40 Load versus deflection for beam UB1

Based on the experimental results, the maximum load was found to be equal to 102.1 kN, and the stiffness equalled to 18.1 kN/mm; these values are significantly higher in comparison with the respective values obtained from beams U1, U2, D1 and D2, which indicates the effectiveness of the steel bars to increase the load carrying capacity of the strengthened beams. Finally, the deflection at the maximum load and at the failure was equal to 12.23 mm and 17.57 mm respectively. The results for the slip at the interface in different positions, as well as the measurements for the slip versus the distance from the support for the maximum load are presented in Figures 4.41a and 4.41b respectively.



(a)



(b)

Figure 4.41 a) Load versus slip in different positions for beam UB1 and b) slip versus the distance from the support for beam UB1

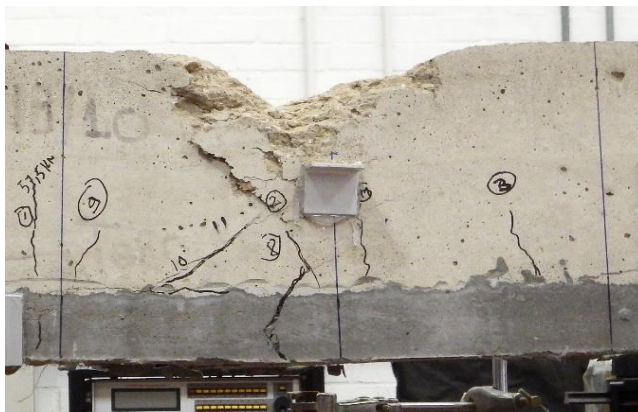
As expected, the slip close to the supports was almost zero, and small values were recorded at positions 5 and 7. By contrast, values between 0.13 mm and 0.15 mm were recorded at positions 3 and 4, which are located close to the two loading points. Finally, a high value of the slip was recorded at position 8, located in the area between the two loading points, and a value of the slip equal to 0.32 was also recorded at position 2. The different phases during the testing of beam UB1 are presented in Figures 4.42a-4.42c.



(a)



(b)



(c)

Figure 4.42 Different phases during the testing of beam UB1: a) appearance of the cracks, b) failure on the compressive side and the propagation of cracks on the UHPFRC layer and c) failure mode at the end of the test

Crucial for the failure of the beam was the failure at the compressive side of the beam. Accordingly, once the maximum load carrying capacity of the beam at the compressive side was reached, the damage at this side commenced and the beam could not carry any more load. The steel bars, on the other hand, improved the load carrying capacity of the strengthened beam significantly. From the graph it can be distinguished that the slope of the load-deflection curve changes at 30 kN, at which point the first cracking started. The first visible cracks during the testing start appearing when the value of the load was equal to 57.5 kN on the RC beam (see Figure 4.42a), and once the beam had reached its maximum load carrying capacity, a single crack progressively propagated along the UHPFRC layer (Figures 4.42b and 4.42c). This crack resulted in the failure of the layer at a later stage. From the graph also it can be distinguished that the bars did not reach yielding and a sudden failure of the beam at the compressive side was commenced. The failure mode and from the graph it can be distinguished that the cross section was over-reinforced. Finally, from Figure 4.42c, it can be noticed that

the bonding at the interface for beam UB1 was strong, and there was not any debonding even at the failure of the beam.

A second beam, identical with beam UB1, was strengthened with an UHPFRC layer and steel bars at the tensile side. The experimental results for the load and deflection are presented in Figure 4.43.

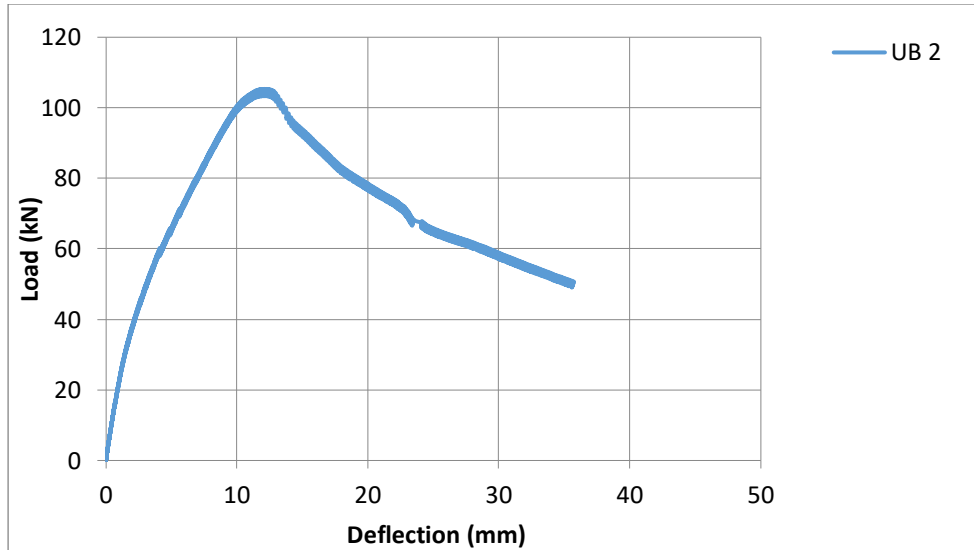
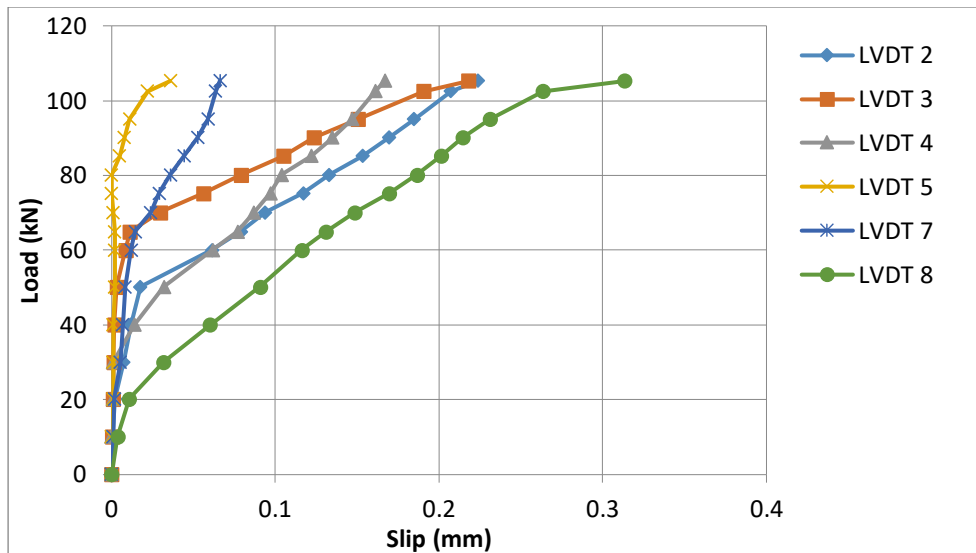
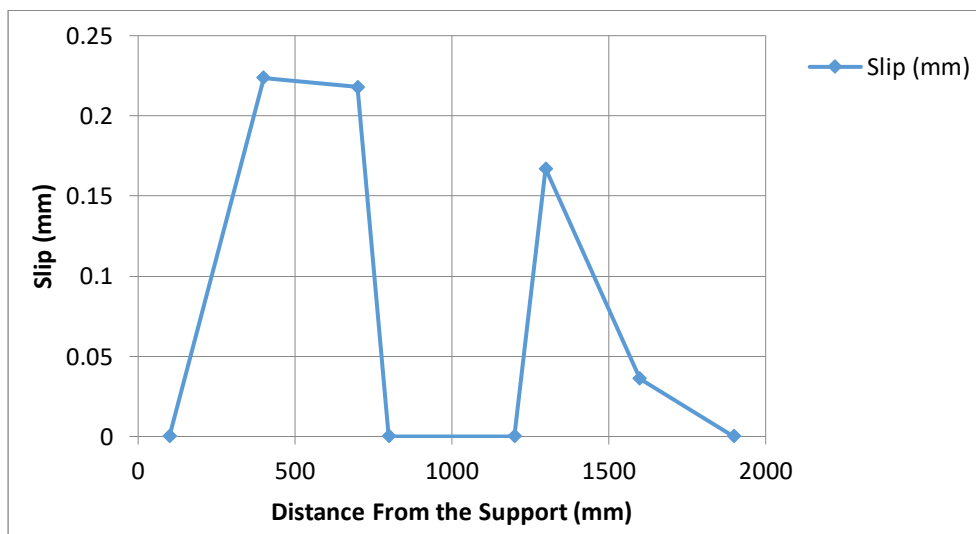


Figure 4.43 Load versus deflection for beam UB2

The maximum load for beam UB2 was found to be equal to 105.4 kN, the stiffness was calculated to be equal to 24 kN/mm, while the deflection at the maximum load was equal to 11.92 mm and the deflection at the failure was equal to 17.13 mm. The measurements for the load versus the slip and the slip versus the distance from the support for the maximum load are presented in Figures 4.44a and 4.44b respectively.



(a)



(b)

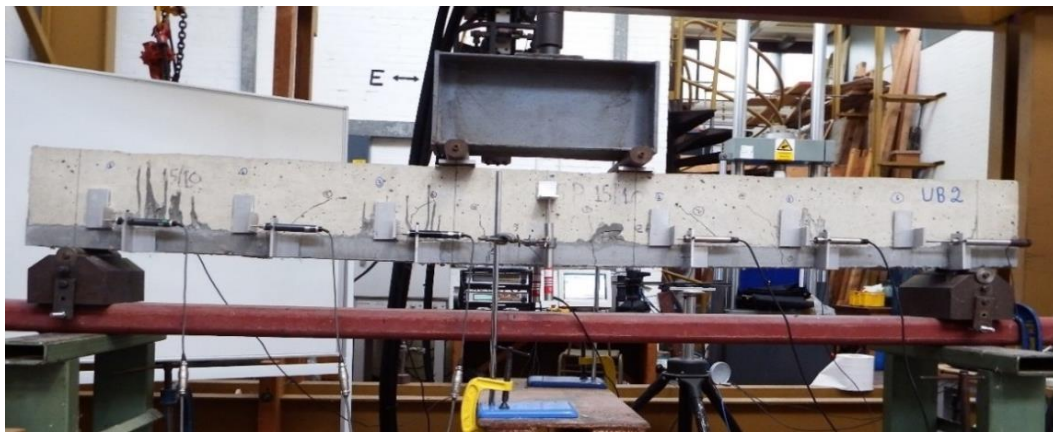
Figure 4.44 a) Load versus slip in different positions of beam UB2 and b) slip versus the distance from the support for beam UB2

The results in Figure 4.44 indicate that the slip in the area close to the supports was equal to zero, and that the higher values were obtained at positions 3 and 4 which are located in the area close to the two loading points. However, the maximum value of the slip was recorded at position 8 in between the two loading points.

In existing codes (Greek Code for Interventions (2013) and fib Bulletin (2008)), limit state values for the design of composite structures, are proposed. According to the Greek Code of Interventions (2013), a maximum slip value of 0.2 mm is proposed for the immediate occupancy performance level, while values of 0.8 mm and 1.5 mm are proposed for the life

safety performance level and the collapse prevention performance level, respectively. According to the fib Bulletin 43 (2008), on the other hand, a maximum interface slip of 0.2 mm is suggested for the serviceability limit state and 2.0 mm for the ultimate limit state. The measurements of slip at the interface of the present study indicate an effective bonding between the UHPFRC layer and the existing RC beam with low values of slip. Hence, in all the examined cases and for all the different strengthening configurations, the recorded values in different positions were lower than 0.8 mm, which according to the Greek Code of Interventions (2013), corresponds to the life safety performance level. The effective bonding between the UHPFRC layer and the existing RC beams is also evident comparing the recorded values of slip at the interface, with the reported values in the literature for concrete to concrete interfaces. Tsioulou et al. (2013), recorded values of slip equal to 1.1 mm for concrete to concrete interfaces for strengthening of full scale RC beams with RC layers at tensile side and along the whole length of the beam. This value corresponds to the collapse prevention performance level and it is significantly higher compared to the recorded values of the present study, for strengthening with UHPFRC layers at the tensile side.

The different phases during the testing of beam UB2 are presented in Figure 4.45.



(a)



(b)



(c)

Figure 4.45 Testing of beam UB2: a) appearance of the first cracks, b) propagation of the cracks and c) failure on the compressive side and starting of failure on the UHPFRC layer

The failure mode of beam UB2 was identical to beam UB1. Hence, the failure at the compressive side of the beam was crucial for the failure of the strengthened beam. The first cracks during the testing could be distinguished when the value of load was equal to 75 kN (see Figure 4.45a); after this point, more cracks were propagated along the whole length of the beam. At the point at which the beam had reached its maximum load carrying capacity, the crack in the middle of the span length spread along the UHPFRC layer (Figure 4.45b). Therefore, it led to the progressive failure of the layer. The bonding at the interface for beam UB2 was also strong, and no de-bonding was noticed during the testing. The experimental results for both the identical beams UB1 and UB2 are presented in the same graph in Figure 4.46. The same Figure also presents the average load-deflection curve.

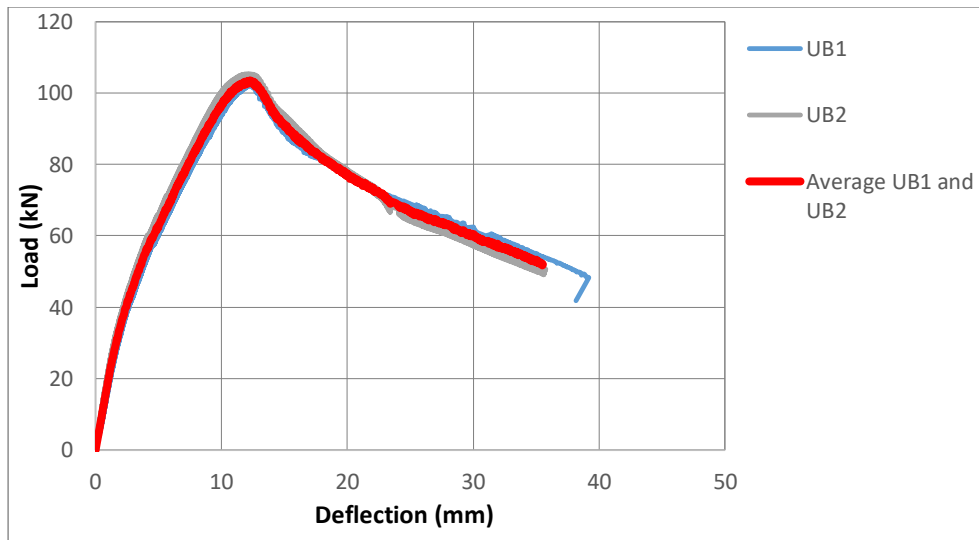


Figure 4.46 Average load versus deflection curve for beams UB1 and UB2

As shown in Figure 4.46, there is a positive agreement in the experimental results for both beams UB1 and UB2, and also extremely high values for the maximum load were achieved. Based on the average curve, the maximum load was found to be equal to 103.5 kN while, from the linear part of the load-deflection curve, the stiffness was found to be equal to 19.5 kN/mm. The deflection at the maximum load and the failure on the other hand, was equal to 12.1 mm and 17.5 mm respectively.

4.8.5 Experimental results for the beams strengthened with jackets on three sides

The next technique relates to the performance of RC beams strengthened with three-side jackets. The experimental setup for these tests is presented in Section 4.7.1. The experimental results for the load and the deflection for the beam 3SJ1 are presented in Figure 4.47.

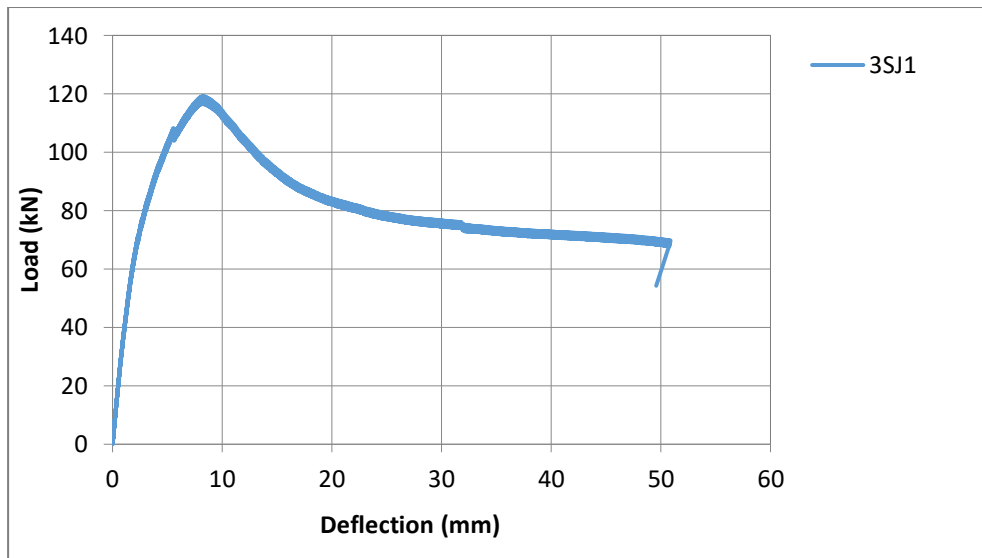


Figure 4.47 Load versus deflection for beam 3SJ1

As illustrated in Figure 4.47, it is clear that the performance of the strengthened beam increased dramatically. Hence, the maximum load was found to be equal to 119.2 kN while the stiffness was calculated to be equal to 38.8 kN/mm. The deflection at the maximum load and the failure on the other hand was found to be equal to 8.27 mm and 14.24 mm respectively. The different phases during the testing of beam 3SJ1 are presented in Figure 4.48.



(a)



(b)



(c)



(d)

Figure 4.48 Testing of beam 3SJ1: a) formation of the first cracks, b) propagation of the cracks, c) the failure of beam and d) the crucial crack for the failure of beam

As can be seen, the beam failed due to a single crack in the middle of the span length. The first visible cracks during the testing appeared when the load was equal to 85 kN, and the crucial crack for the failure of the beam occurred for a value of a load equal to 97 kN in the

middle of the span length (see Figures 4.48b and 4.48d). This crack progressively opened, as illustrated in Figure 4.48d.

A second beam, identical to beam 3SJ1, was prepared and strengthened with a three-side jacket in order to validate the experimental results obtained from beam 3SJ1. The load-deflection results for this test are presented in Figure 4.49.

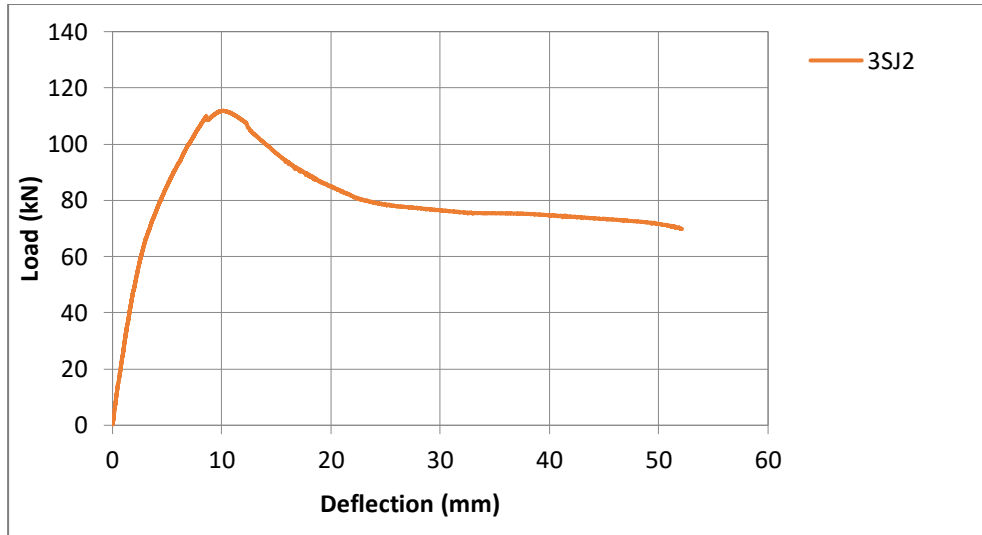
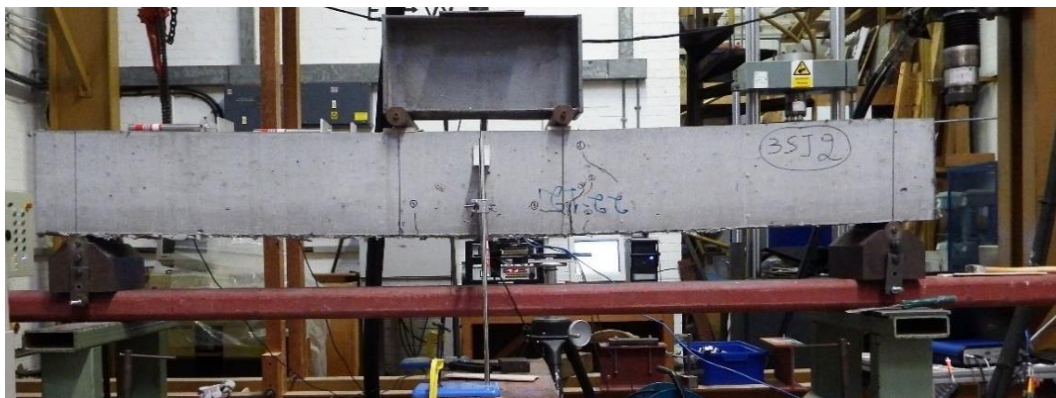


Figure 4.49 Load versus deflection for beam 3SJ2

The experimental results obtained from beam 3SJ1 are confirmed from the experimental results of beam 3SJ2. As a result, high values for both the maximum load and the stiffness were achieved. In particular, the maximum load was found to be equal to 112 kN, and the stiffness was calculated to be equal to 29.5 kN/mm. The deflection at the maximum load on the other hand was found to be equal to 10.19 mm, while the deflection at the failure was equal to 17.62 mm. The different phases during the testing of beam 3SJ2 are presented in Figure 4.50.



(a)



(b)



(c)

Figure 4.50 Different phases during the testing of beam 3SJ2: a) formation of the cracks, b) beginning of the failure of the jacket and c) beam at the end of the test

From Figure 4.50, it can be noticed that a single crack was crucial for the damage of the beam. This crack could be distinguished when the value of the load was equal to equal to 71 kN, and the damage was progressively localized at this crack and resulted in the failure of the beam (see Figure 4.50c). However, the position of the crack was not identical to the previous investigations and it was not located in between the two loading points. After the failure of the beam it was noticed that the fibers in this area were not uniformly distributed which affected the failure mode.

For the present investigation a thickness of 40 mm was adopted on both sides of the jacket. The selection of the appropriate thickness of the jacket (or the layer) is related to the requirements of the strengthening technique. Parameters such as the dimensions of the existing members, the decision to increase dramatically the dimensions of the elements or not, the target of the strengthening technique (to increase the stiffness, the load carrying capacity or both), the total cost of the material, and also architectural reasons should be taken into consideration. An aspect which should also be taken into consideration, is that there is a “size

effect” on the flexural performance of UHPFRC. As presented in Section 3.8 thick elements are more luckily to have a non-uniform distribution of the fibers in their mass, which affects the performance of the UHPFRC elements. Hence, even if the strengthening technique concern elements with higher dimensions, jackets and layer with thicknesses higher than 100 mm are not suggested. The effect of layer depth on the performance of UHPFRC is investigated in depth numerically in the next chapter.

The experimental results of the two identical RC beams which were strengthened with three-side jackets together with the average load-deflection curve are presented in the same graph in Figure 4.51. The results indicate a positive agreement in the experimental results for the two beams. Therefore, similar values for the maximum load were achieved (119.2 kN for beam 3SJ1 versus 112 kN for beam 3SJ2), and the stiffness of beam 3SJ2 was found to be slightly lower in comparison with the respective value obtained for beam 3SJ1 (29.5 kN/mm for beam 3SJ1 versus 38.8 kN/mm for beam 3SJ2). Based on the average load-deflection curve, on the other hand, the maximum load was found to be equal to 114 kN, the stiffness was calculated to be equal to 34 kN/mm, while the deflection at the maximum load and the failure was equal to 8.56 mm and 16.2 mm respectively. From these results, it can be noted that high mechanical properties were achieved for the beams strengthened with three-side jackets, and due to the change of the dimensions of the strengthened beams, very high values of stiffness were also obtained.

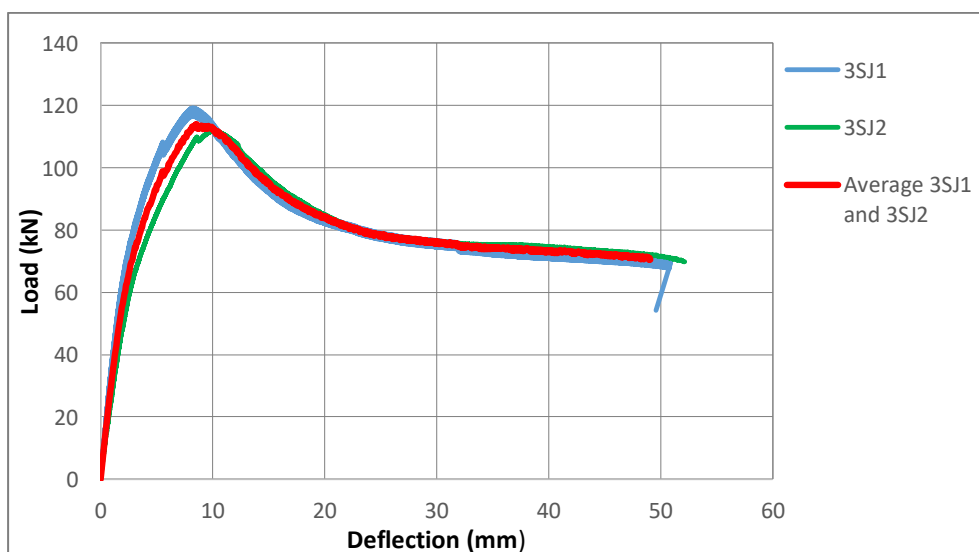


Figure 4.51 Average load versus deflection curve for beams 3SJ1 and 3SJ2

4.8.6 Comparison of the experimental results for the different techniques

For the evaluation of the effectiveness of each one of the examined techniques and to be able to draw a comparison between them, all the average load-deflection curves are presented in the same graph in Figure 4.52.

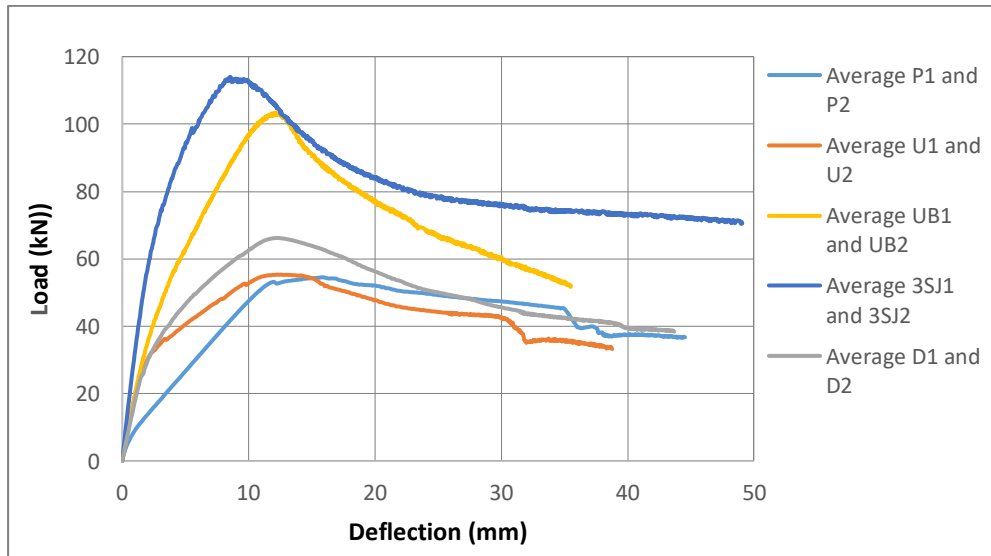


Figure 4.52 Average load versus deflection curves for all the different techniques

The average stiffness of all the examined specimens is presented in the same graph in Figure 4.53. As can be seen, the addition of layer produced a remarkable increase in the stiffness of the strengthened elements, while due to big increase in the dimensions, the stiffness was increased dramatically with the addition of three-side jackets.

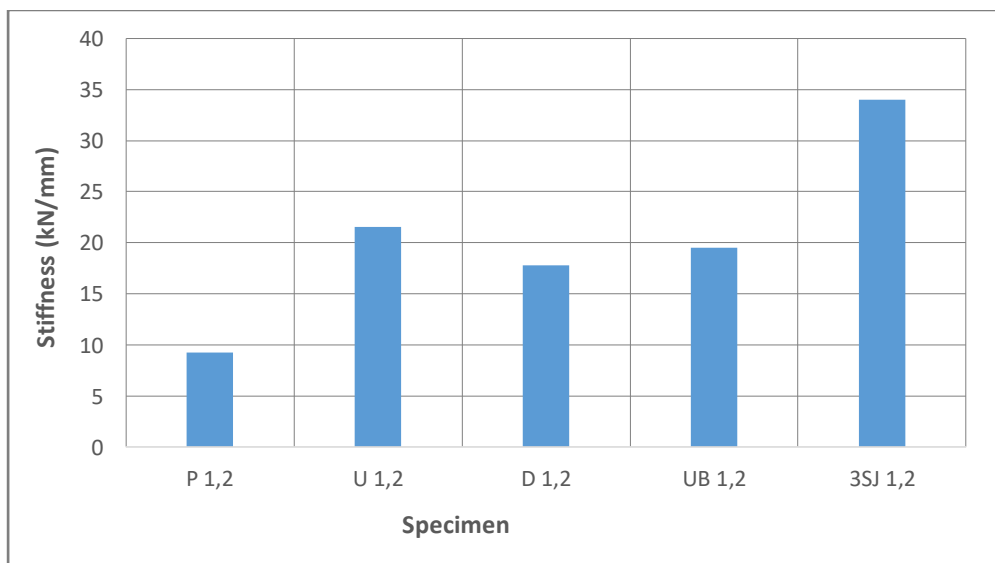


Figure 4.53 Average stiffness of all the examined specimens

The maximum recorded values for the slips (at the maximum load), for the different specimens are presented in Figure 4.54.

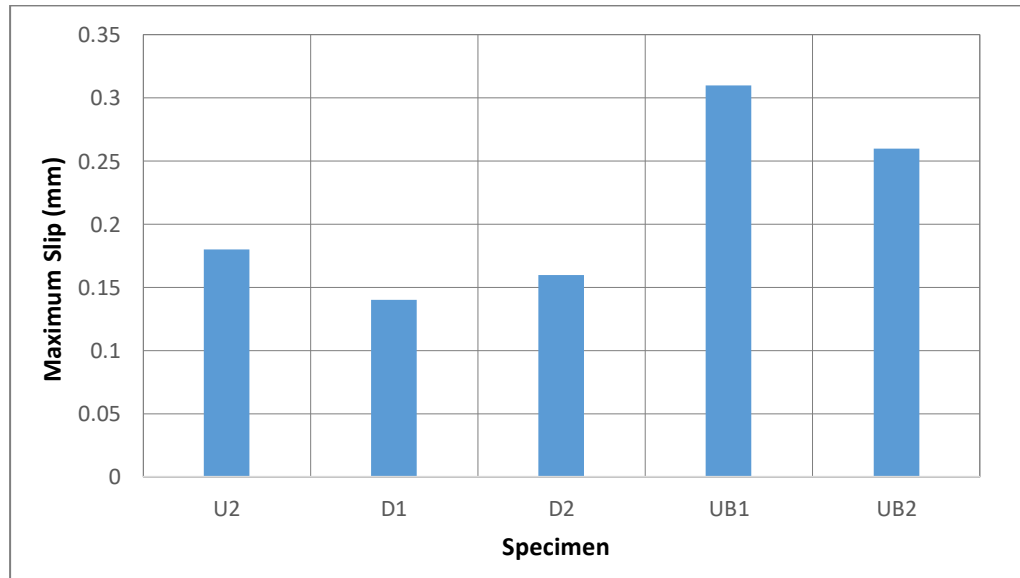


Figure 4.54 Maximum values of slips for the different specimens

The experimental results for the average maximum load, the stiffness, the deflection at the maximum load, the deflection at the failure and the ratio of the average maximum load to the load of the control beam, for the different strengthening techniques, are presented in Table 4.7.

Beams	Average Maximum Load (kN)	Stiffness (kN/mm)	Deflection at maximum load (mm)	Deflection at failure (mm)	Load ratio of strengthened to control beam
P 1,2	54.5	9.2	15.88	35.4	1
U 1,2	55.4	21.5	12.26	25.1	1.02
D 1,2	66.2	17.8	12.22	22.3	1.22
UB 1,2	103.5	19.5	12.1	17.5	1.9
3SJ 1,2	114.5	34	8.56	16.2	2.1

Table 4.7 Experimental results for the different strengthening techniques

From Table 4.7 it can be noticed that the deflection at the maximum load and the failure was reduced as the load carrying capacity of the strengthened beams with the different techniques was increased. After the intervention, the stiffness and the resistance of beams to the imposed

loads was increased. This had as a result a more brittle behavior of the strengthened elements with lower deformation capacity.

The results of Figures 4.52, 4.53 and Table 4.7 indicate that the strengthening with UHPFRC layers at the tensile side had as a result a big increase of the stiffness of the strengthened elements. Hence, lower deformations for the imposed loads could be distinguished, while the formation of the cracks under service conditions was also delayed. The load carrying capacity on the other hand, was also increased slightly. However, for weaker elements higher contribution of the layers can be achieved. This is investigated in detail numerically in the following chapter.

The addition of dowels at the interface, on the other hand, had as a result the improvement of the bonding at the interface between UHPFRC and concrete. Therefore, besides an increase in stiffness, produced a remarkable increase in the load carrying capacity of the beams. As can be seen in Table 4.7, the load carrying capacity of the strengthened beams was increased by 22% with the use of dowels, which indicates the effectiveness of dowels. Also, from Figure 4.54 it can be noticed that the lower values of slip were recorded with the use of dowels even for higher values of load. This indicates the effectiveness of dowels to improve the bonding at the interface.

The load carrying capacity of the strengthened beams was increased dramatically with the addition of steel bars to the layer. Hence, an increase of 90 % was noticed when steel bars added to the layer. The steel bars on the other hand did not affect significantly the stiffness. Also, as can be seen in Figure 4.54, higher values of slip were recorded for the specimens which were strengthened with layers and steel bars. However, the recorded values of slip are significantly lower compared to the reported values in the literature for concrete to concrete interfaces (Tsioulou et al., 2013).

Finally, the optimum performance between the different strengthening configurations was achieved with the construction of three-side jackets. Hence, an increase of 110 % in the load carrying capacity of the strengthened beams was recorded, compared to the load carrying capacity of the control beams. The addition of jacket on three sides, had as a result the increase in the dimensions of the existing beam, which resulted in a big increase in the stiffness of the beam. More specifically, the stiffness of the strengthened elements was increased by 270 % compared to control beams. Finally, it should be noted that this technique could also be used for the shear strengthening of beams.

4.9 Conclusions

The experimental results of the present investigation indicated that the strengthening with UHPFRC is a well promising technique. More specifically, the strengthening with UHPFRC layers, had as a result a big increase in the stiffness of the strengthened elements. Hence, lower deformations for the imposed loads could be distinguished, while the formation of the cracks under service conditions was also delayed. The addition of the dowels at the interface on the other hand, had as a result the improvement of the bonding at the interface between the UHPFRC and normal concrete. Therefore, besides an increase in the stiffness, produced a remarkable increase in the load carrying capacity of the beams. More specifically, the maximum load of the strengthened beams was increased by almost 21.5 % compared to the maximum load obtained for the existing RC beams. The load carrying capacity of the strengthened beams was increased dramatically with the addition of steel bars to the layer. Thus, the maximum load of the strengthened beams with UHPFRC layers and steel bars was increased by 90% compared to the maximum load of the existing RC beams. Finally, the optimum performance between the examined strengthening configurations was achieved with the construction of three-side jackets. Hence, apart from a large increase in the stiffness, which was increased by 270%, an increase of 110 % on the maximum load was achieved with the construction of three-side jackets.

From the measurement of the slips at the interface, it was clear that the bonding between UHPFRC and concrete was effective and small values of slip at the interface were recorded. Also, comparing the recorded values of slip at the interface with reported values in the literature for concrete to concrete interfaces, it was noticed that the values of slip for UHPFRC to concrete interfaces were significant lower. Hereby, a better bonding at the interface can be deduced.

5. THE NUMERICAL MODELING OF ULTRA HIGH PERFORMANCE FIBER REINFORCED CONCRETE (UHPFRC)

5.1 Introduction

In the previous chapters, the results of an extensive experimental study on the evaluation of the properties and the performance of UHPFRC as a strengthening material were presented. The present chapter aims to investigate numerically crucial parameters of the examined technique, which have not been investigated experimentally. More specifically, in the present chapter, a numerical model which can predict the behavior of composite UHPFR-Reinforced Concrete (RC) elements has been developed, and crucial parameters which affect the performance of the examined technique have been analysed. Parameters, which are mainly related to the design of this technique, such as the depth of the layer, the fiber content, the steel grade, the amount of reinforcement of the layers and the shrinkage, have been analysed in the present section. The reliability of the numerical model used in the present investigation has been validated using the experimental results of the full-scale beam testing.

5.2 Modeling of the materials

For the numerical modeling of the examined technique, the finite element analysis software ATENA has been used. Concrete was simulated with an eight-node element with nonlinear behavior and softening branches under both tension and compression (see Figure 5.1), using SBETA constitutive model (Cervenka et al., 2003). The ascending compressive branch is based on the formula recommended by the CEB-FIP model code 90 (1993). Its softening law, linearly descended from the peak stress until it reached a limit compressive strain, which was defined by the plastic displacement and the band size, using a fictitious compression plane model. In tension, the linear ascending branch and exponential softening branch, based on the fracture energy needed to create a unit area of stress-free crack, were used. The properties of concrete described in Section 4.5.3 were adopted for the numerical modeling of concrete.

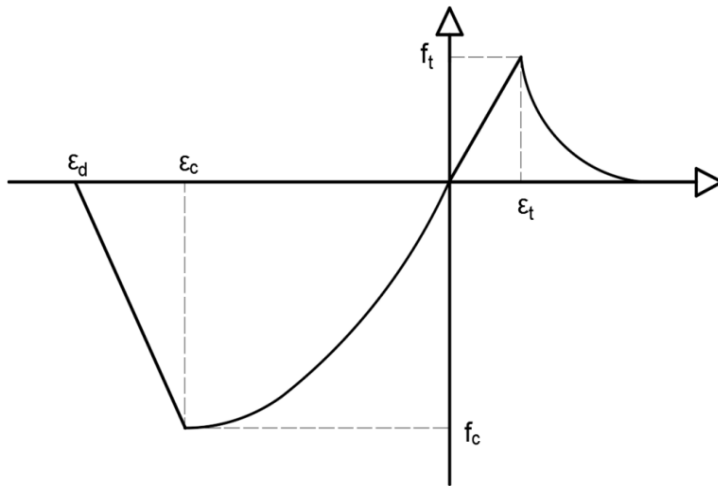


Figure 5.1 Constitutive model in tension and compression adopted in ATENA software (Cervenka et al., 2003)

The steel bars were simulated using linear elements with bi-linear behavior and hardening, as presented in Figure 5.2. The properties of steel grade B500C according to BS 4449:2005 (2005) were adopted for the modeling of the steel bars, and the cover of the steel bars was the same as the experimental investigation.

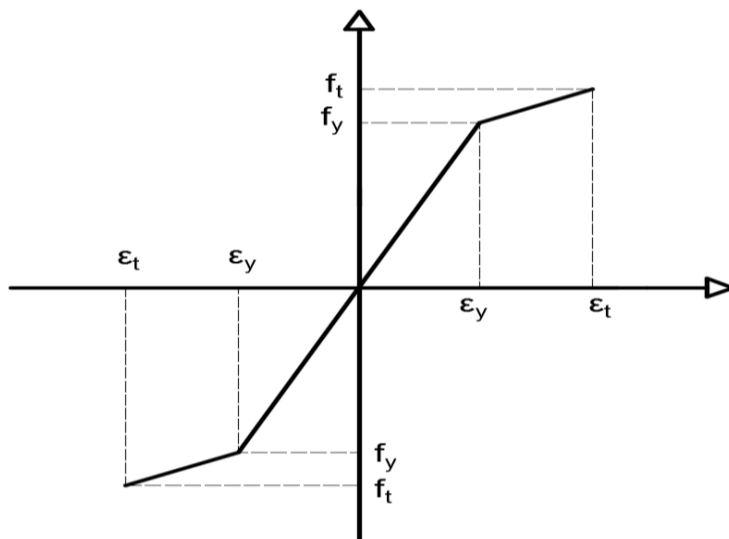


Figure 5.2 Stress-strain model of the reinforcement

The bond model between the reinforcement and the surrounding concrete was taken into consideration during the analysis. More specifically, the bond-slip model according to the CEB-FIB model code 90 (1993) was adopted for the analysis (see Figure 5.3). According to this model, the generated law is dependent on the concrete compressive strength, the reinforcement diameter and the reinforcement type.

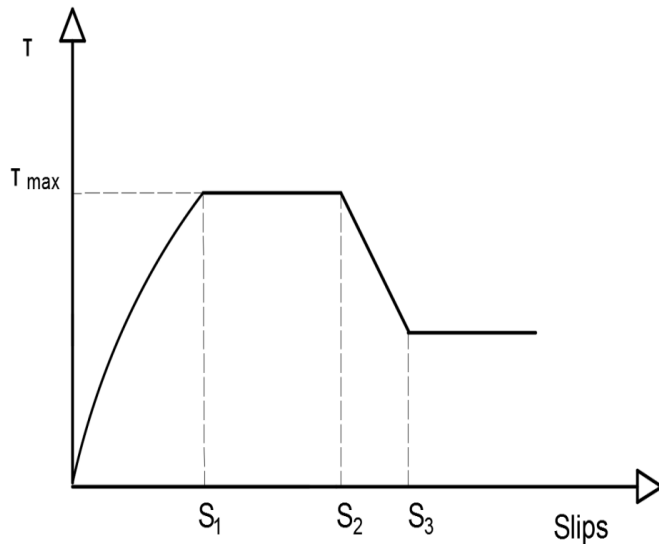
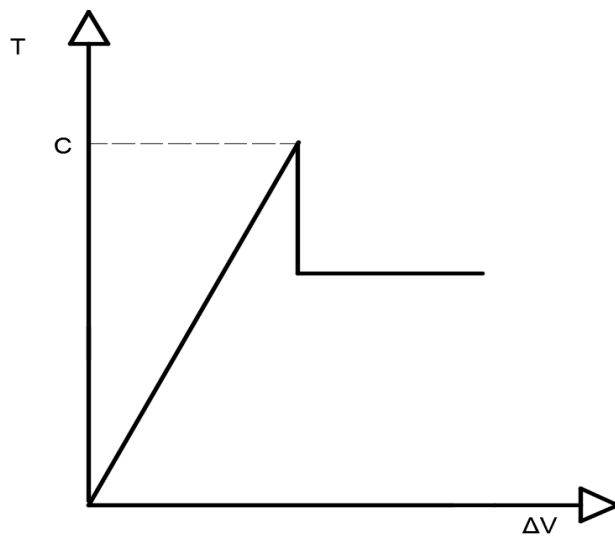


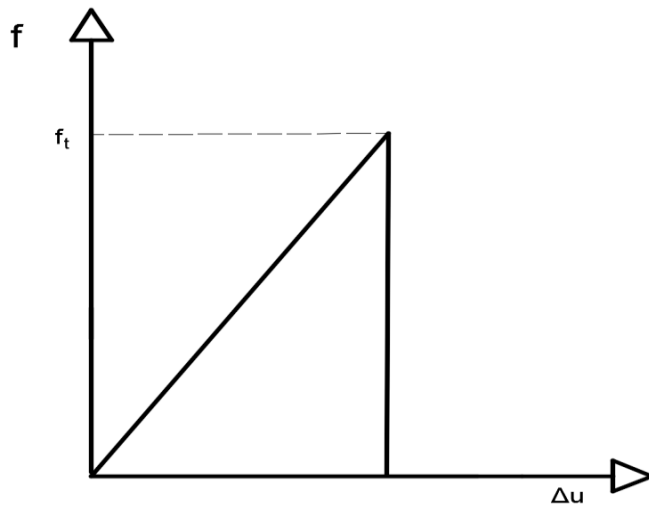
Figure 5.3 Bond-slip law based on CEB-FIP model code 1990

In all the examined cases of the present investigation, the interface between the initial beam and the UHPFRC layer was modeled based on the calculated values from the push off tests of the previous section, using two-dimensional elements. Hence, a coefficient of friction equal to 0.98 and a cohesion of 1.8 MPa, were adopted in the present investigation. An additional investigation has been conducted for strengthening with UHPFRC layers assuming a monolithic connection at the interface.

Important for the interface behavior is the bond strength. Once the bond strength is reached, the response of the interface depends on dry friction. The interface behavior in shear and tension, adopted in the ATENA software, can be seen in Figure 5.4.



(a)



(b)

Figure 5.4 Interface behavior in: a) shear, b) tension

For the numerical modeling of the UHPFRC, the material properties described in Section 4.5.3 were adopted. Therefore, a compressive strength of 136.5 MPa and Young's modulus of 51 GPa were used for the modeling of UHPFRC in compression using the SBETA constitutive model (Cervenka et al., 2003). The tensile response of the material was modeled using the experimental results of the direct tensile tests of the dog-bone shaped specimens, which were obtained from the same batch used for the preparation of the UHPFRC layers. The experimental results of the testing of the dog-bone specimens indicated that the response of the material was linear up to the stress level, equal to 5 MPa. Hence, the response of the UHPFRC was modeled with an elastic behavior up to this stress level, followed by a second linear branch into the phase of strain hardening with multiple microcracking. Then, after the formation of the macrocrack at ultimate resistance, there is the strain-softening phase which was modeled using a bi-linear model (see Figure 5.5).

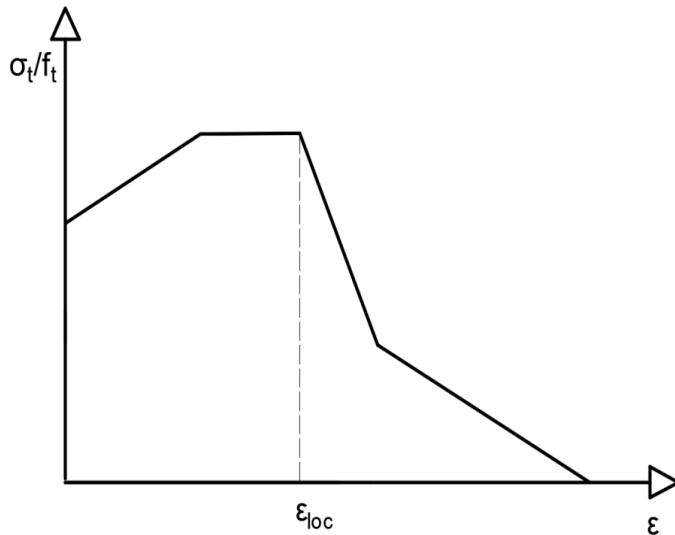


Figure 5.5 Tensile function adopted in ATENA

Finally, for the modeling of the UHPFRC, the shrinkage of the material was also taken into consideration using a negative volumetric strain value to the UHPFRC elements. Therefore, based on the measurement of shrinkage, as presented in Section 3.7, a value of shrinkage equal to 565 microstrain was applied to the elements of the UHPFRC layers.

5.3 Validation of the numerical model

5.3.1 Initial beam prior to strengthening

The geometrical model used for the modeling of the initial RC beam prior to strengthening, as well as the properties and the dimensions of the reinforcement, were identical to the constructed RC beam (see Figure 4.4). The geometrical model used for the finite element analysis is presented in Figure 5.6.

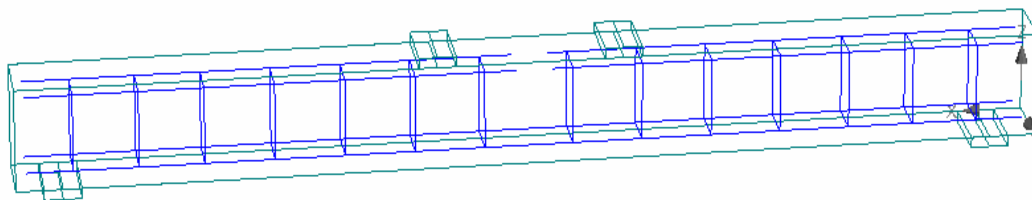


Figure 5.6 Geometrical model used for the finite element analysis of the initial beams

The numerical results of the initial RC beam prior to strengthening together with the average experimental results of the existing RC beam are presented in the same graph in Figure 5.7. In most graphs of the present chapter, and especially in cases that coefficients μ and c are taken into consideration, the post-peak branch is presented at a load almost 90% of the maximum. After this point there are numerical instabilities, which are related to convergence problems at high levels of damage. Hence, these results were ignored. However, it should be noted that all of the investigations of the present chapter concern the performance up to the maximum load. Consequently, these instabilities do not affect the obtained results.

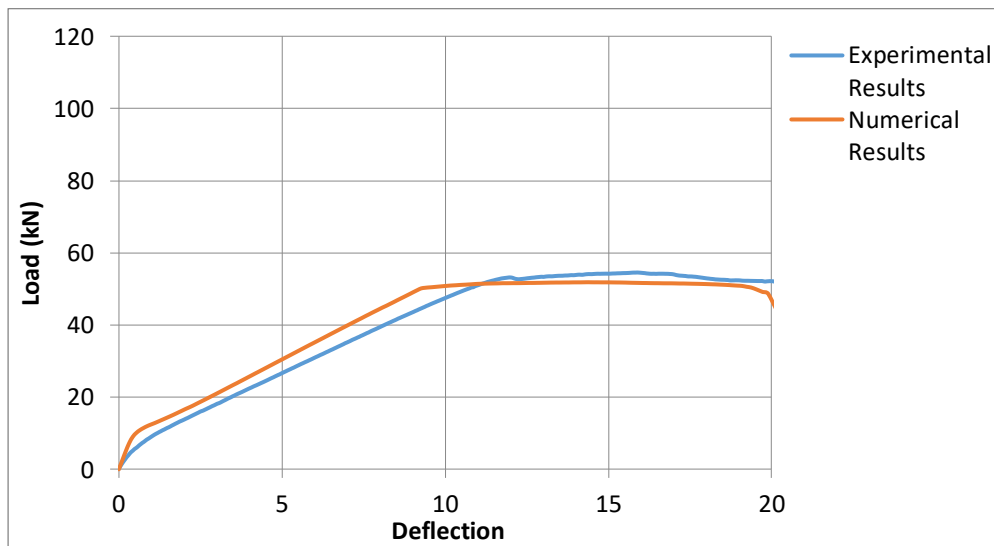
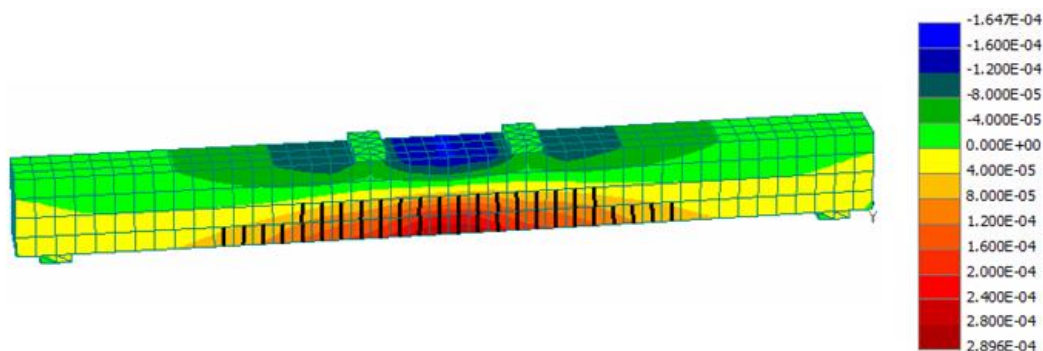
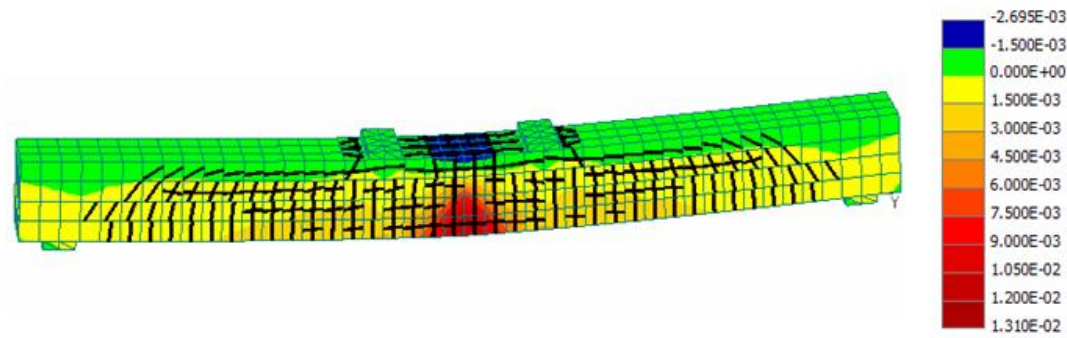


Figure 5.7 Numerical versus experimental results for the initial beam

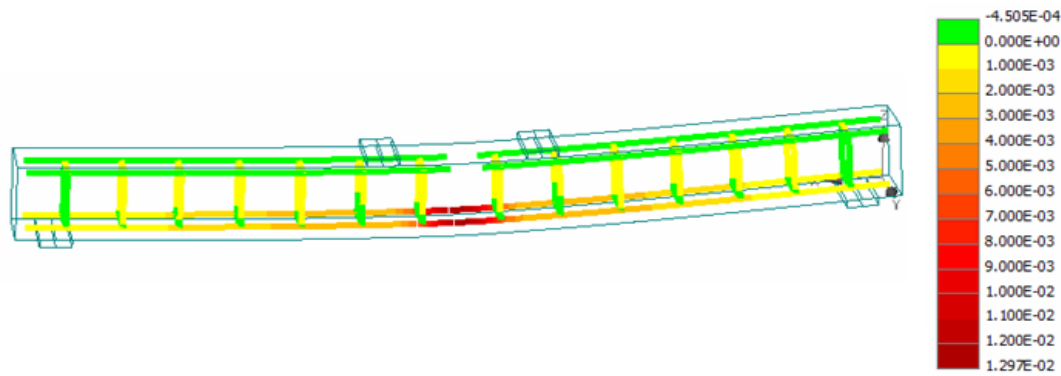
Based on Figure 5.7, a positive agreement between the numerical and the experimental results can be observed and similar values for the load carrying capacity were achieved (51.9 kN for the numerical analysis versus 54.6 kN for the experimental investigation). The crack pattern and the strain distribution of the initial beam prior to strengthening are presented in Figures 5.8a-5.8c.



(a)



(b)



(c)

Figure 5.8 Crack pattern and strain distribution of the existing RC beam: a) at the first crack load, b) at the maximum load and c) strain distribution at the reinforcement at the maximum load

As shown in Figure 5.8, high values of strain can be distinguished in the middle of the span length and at the tensile side of the beam, for both the beam and the reinforcement. From the same figure, it can be observed that the major cracks were localized in the same area. This is in agreement with the experimental results, as the damage of the existing RC beam in the experimental investigation was localized in this area (see Figures 4.23 and 4.25).

5.3.2 Numerical modeling of the strengthened beams with UHPFRC layers

For the validation of the numerical model used for the modeling of the existing RC beams strengthened with UHPFRC layers, the numerical results were compared with the respective experimental results. The UHPFRC layers were simulated using eight-node elements and the properties, as presented in Section 5.2, were adopted for the modeling of the material. The geometrical model used for this investigation is presented in Figure 5.9.

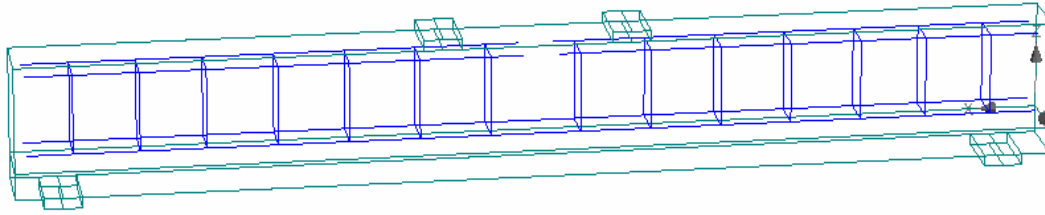


Figure 5.9 Geometrical model used for the finite element analysis of the strengthened beams with UHPFRC layers

For this investigation and for the modeling of the interface, two different types of interfaces were examined. First of all, an interface with a coefficient of friction equal to 0.98 and a cohesion equal to 1.8 MPa was assumed, and the numerical results were compared with the experimental results of the beams strengthened with UHPFRC layers. The use of dowels in the experimental investigation, resulted in an improved performance of the strengthened beams with low values of slip at the interface. Consequently, in the second investigation, the connection at the interface using dowels was assumed as monolithic and this assumption was validated with the comparison of the experimental results with the numerical for a perfect connection at the interface. In Figure 5.10 a comparison between the numerical and the experimental results for a non-monolithic connection is presented.

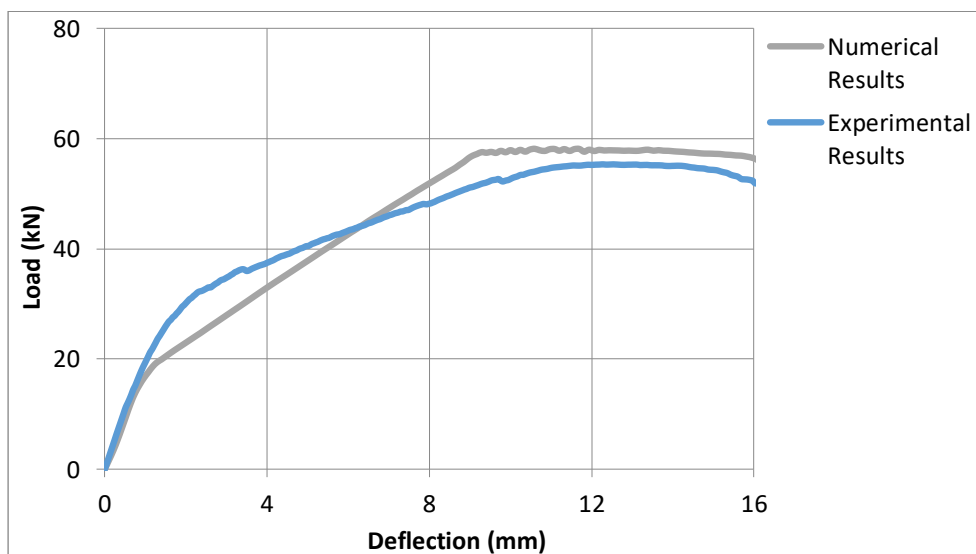
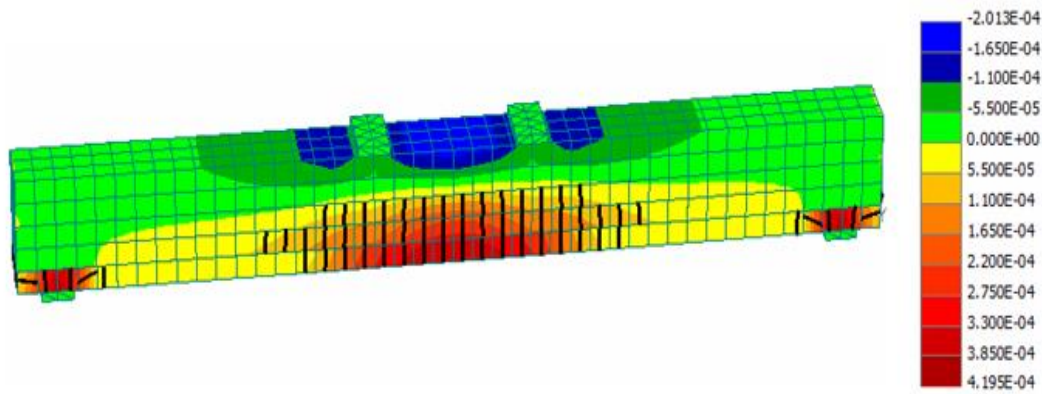
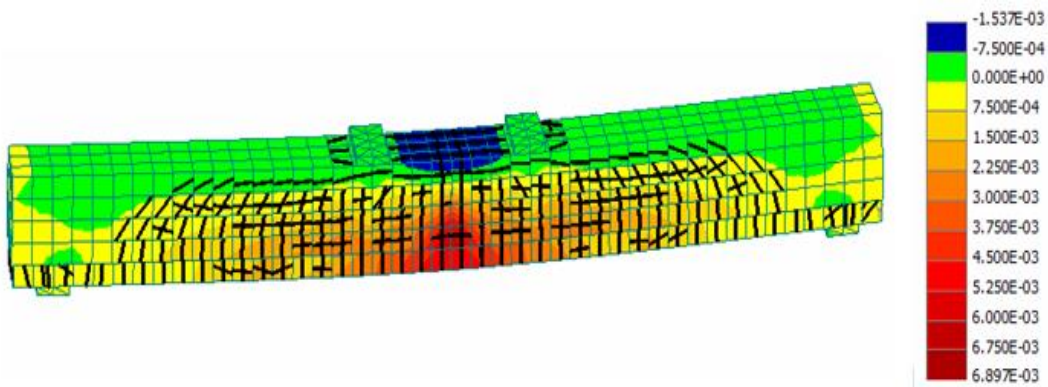


Figure 5.10 Numerical versus experimental results for the beams strengthened with UHPFRC layers for a non-monolithic connection at the interface

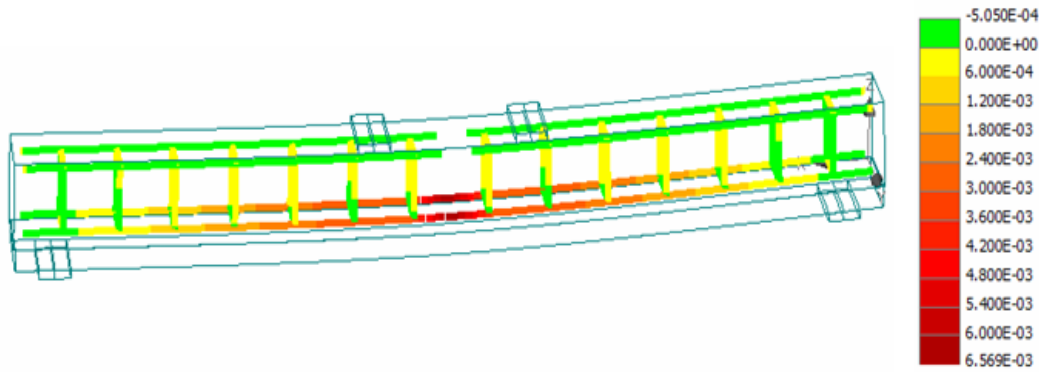
As shown in Figure 5.10, a positive correlation between the numerical and the experimental results can be observed, and similar values for the load carrying capacity of the strengthened beams were obtained (58.2 kN for the numerical investigation versus 55.3 kN for the experimental investigation). In Figure 5.11, the crack pattern and the strain distribution of the strengthened beam with an UHPFRC layer, assuming a non-monolithic connection at the interface, are presented.



(a)



(b)



(c)

Figure 5.11 Crack pattern and strain distribution of the existing RC beam strengthened with an UHPFRC layer and a non-monolithic connection at the interface: a) at the first crack load, b) at the maximum load and c) the strain distribution at the reinforcement at the maximum load

As illustrated in Figure 5.11, high values of strain can be distinguished in the middle of the span length on both the UHPFRC layer and the existing RC beam. These results are in accordance with the experimental results of the strengthened beams with layers since the damage of the beams was localized on the UHPFRC layer and in the middle of the span length, while progressively propagating on the existing RC beams.

In Figure 5.12, a comparison between the numerical results for a monolithic connection at the interface and the experimental results for the beams strengthened with UHPFRC and dowels, is presented.

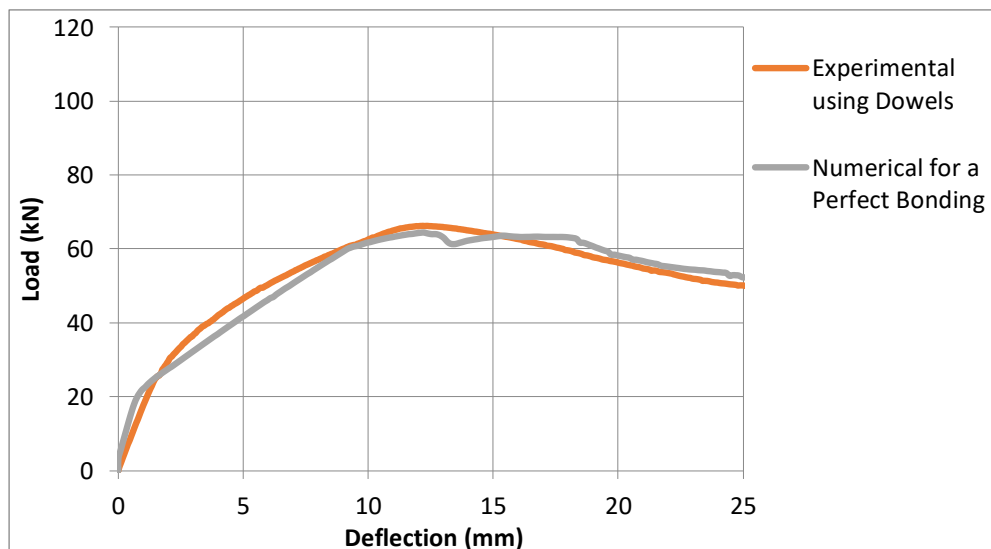
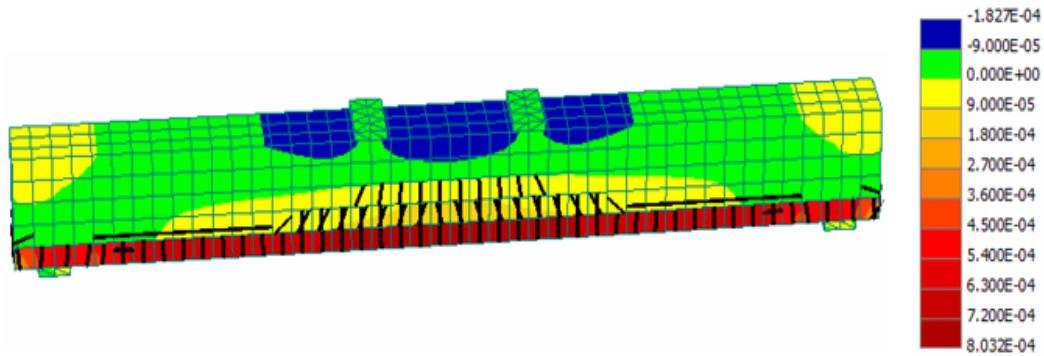
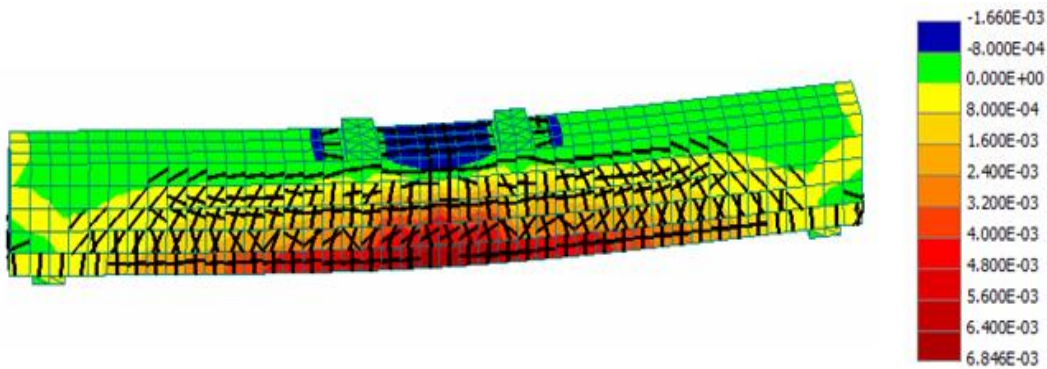


Figure 5.12 Numerical versus experimental results for the beams strengthened with UHPFRC layers assuming a monolithic connection at the interface

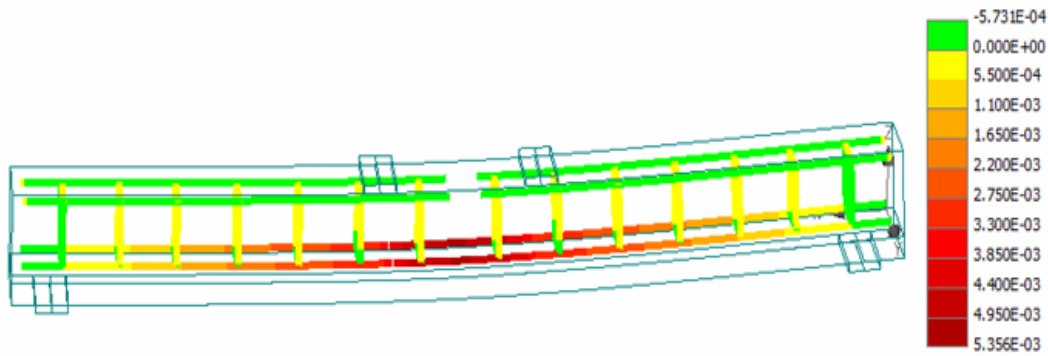
The results of Figure 5.12 indicate a perfect agreement between the numerical and the experimental results for a monolithic connection at the interface and similar values for the load carrying capacity were achieved (64.4 kN for the numerical investigation versus 66.2 kN for the experimental investigation). This agreement between the experimental and the numerical results indicates the effectiveness of the dowels as the same behavior with the monolithic beam of the numerical analysis was achieved. The crack pattern and the strain distribution during the analysis are presented in Figure 5.13.



(a)



(b)



(c)

Figure 5.13 Crack pattern and strain distribution of the strengthened beams with UHPFRC layers considering a monolithic connection at the interface at: a) the first crack load, b) the maximum load and c) the strain distribution on the reinforcement at the maximum load

The use of dowels at the interface resulted in an increase of 10% of the load carrying capacity of the strengthened beams. As illustrated in Figure 5.13, the layer was in tension almost along the whole length and high values of strain be distinguished. By contrast, as illustrated in Figure 5.11, for a non-monolithic connection at the interface, the stress and the strain were localized in the middle of the span length. From these results, it is clear that for a monolithic connection at the interface, the stress was more uniformly distributed along the length of the beam. This resulted in a higher contribution of the layer to the load carrying capacity of the beams.

5.3.3 Numerical modeling of beams strengthened with UHPFRC layers and steel bars

For the numerical modeling of the strengthened beams using UHPFRC layers and steel bars, the numerical model of the previous investigation was adopted and two steel bars with a diameter of 10 mm were added to the UHPFRC layer as a reinforcement of the layer. The geometrical model used for the analysis is presented in Figure 5.14.

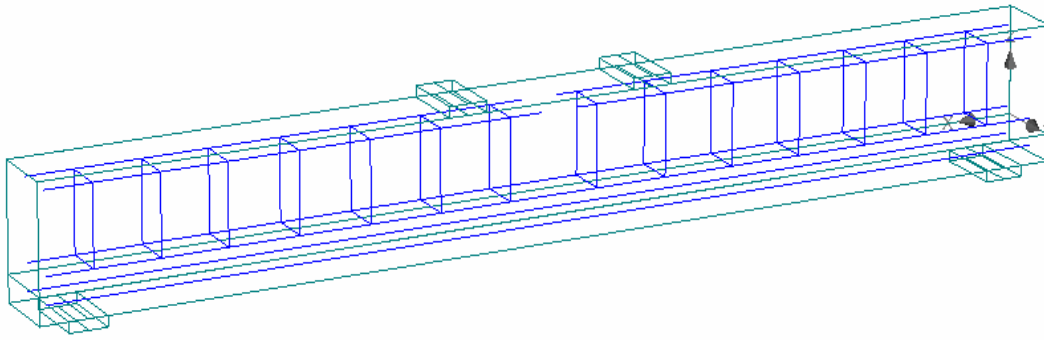


Figure 5.14 Geometrical model used for the modeling of the strengthened beams with UHPFRC layers and steel bars in ATENA

The numerical results of the beam strengthened with an UHPFRC layer and steel bars are presented in the same graph with the respective average experimental results in Figure 5.15.

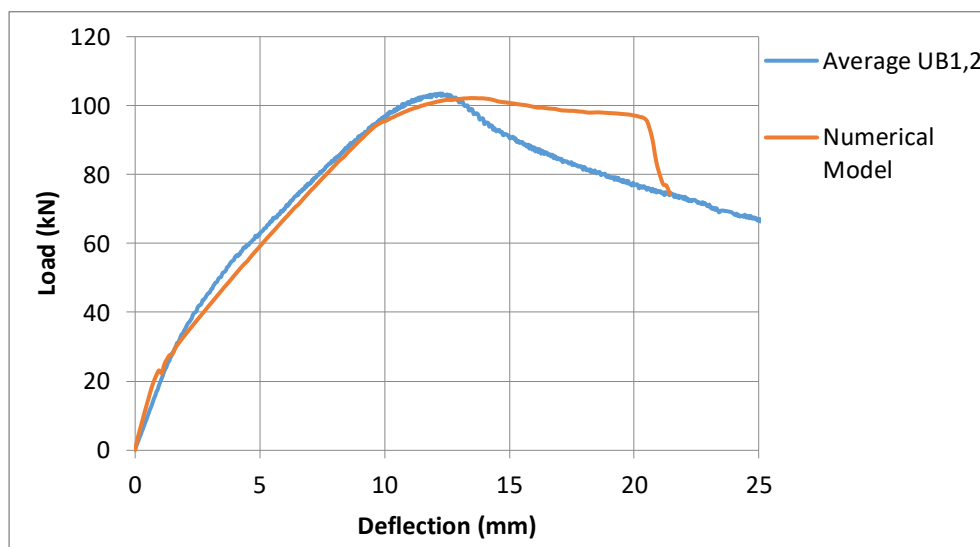


Figure 5.15 Numerical versus experimental results for the strengthened beams with UHPFRC layers and steel bars

The results of Figure 5.15 indicate a perfect agreement between the numerical and the experimental results up to the maximum load. Hence, similar values for the load carrying capacity of the strengthened beams were achieved (102.1 kN for the numerical investigation versus 103.5 kN for the experimental investigation). After this point, it can be noticed that the descending branch of the experimental curve drops more gradually. This can be attributed to the sudden failure of the compressive side of the beam of the experimental investigation once the maximum compressive strength of the compressive side had been reached. From the graph, a sudden drop of the load can be distinguished at the post-peak branch. This is related

to numerical instabilities and convergence problems at high levels of damage. The crack pattern and the strain distribution of the strengthened beam are presented in Figure 5.16.

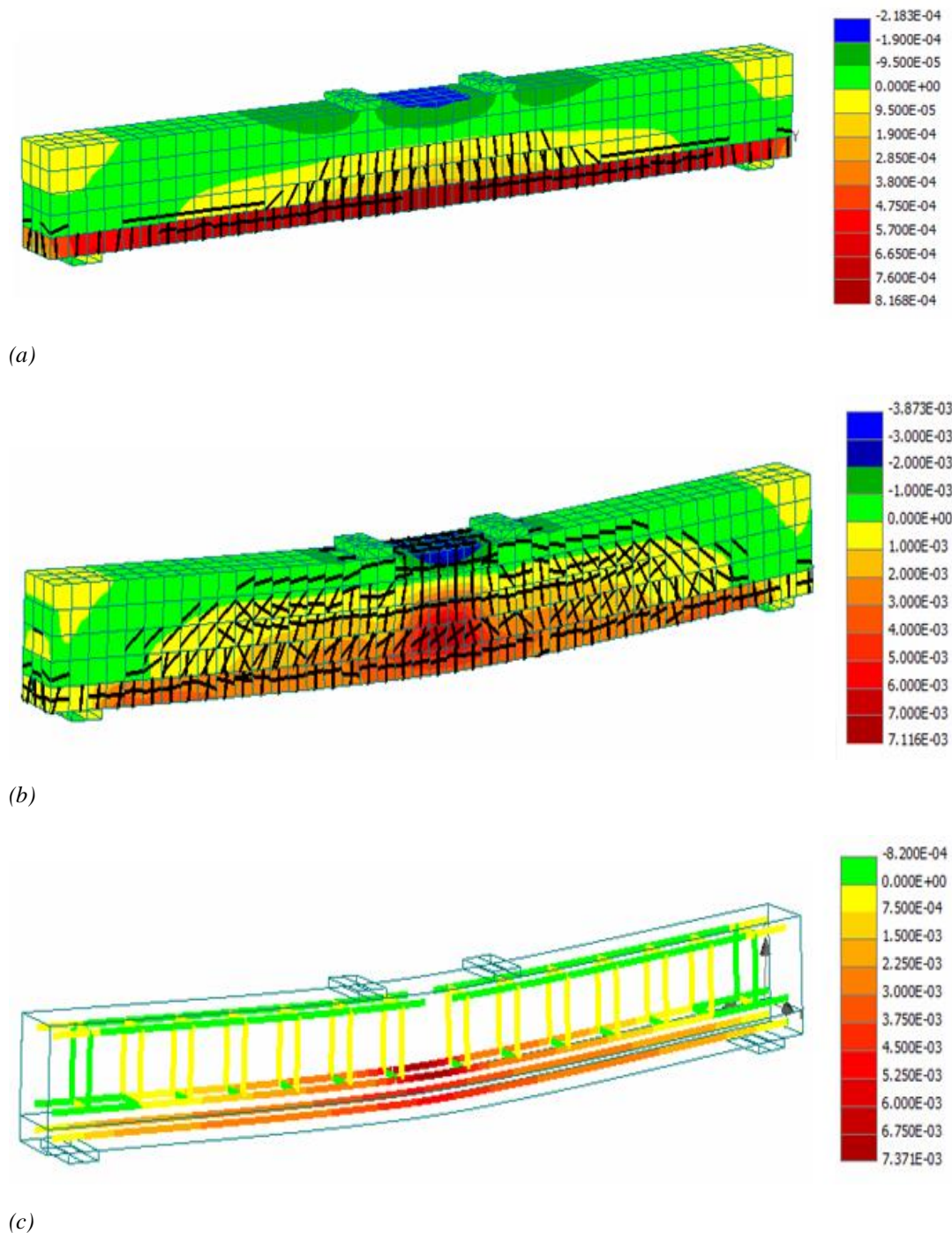


Figure 5.16 Crack pattern and strain distribution of the existing RC beam strengthened with UHPFRC layer and steel bars: a) at the first crack load, b) at the maximum load and c) the strain distribution at the reinforcement at the maximum load

The addition of steel bars at the layer supported the layer, and resulted in a high increase of the load carrying capacity of the strengthened beams. As illustrated in Figure 5.16, extremely high values of strain can be determined at the maximum load along the whole length of the

layer and at the reinforcement, which indicates the contribution of the layer to the load carrying capacity of the beam. Moreover, high values of strain and major cracks can be distinguished at the compressive side of the beam. This is consistent with the experimental results since during the experimental testing of the strengthened beams with UHPFRC layer and steel bars, the failure started once the compressive strength of the compressive side had been reached.

5.3.4 Numerical modeling of the strengthened beams with jackets on three sides

For the validation of the numerical model used for the modeling of the strengthened beams using a three-side jacket, the numerical results were compared with the respective experimental results. The existing RC beam and the geometry of the jacket of the numerical investigation were identical with the experimental investigation, as presented in Section 4.4.4. The geometrical model for the finite element analysis is presented in Figure 5.17.

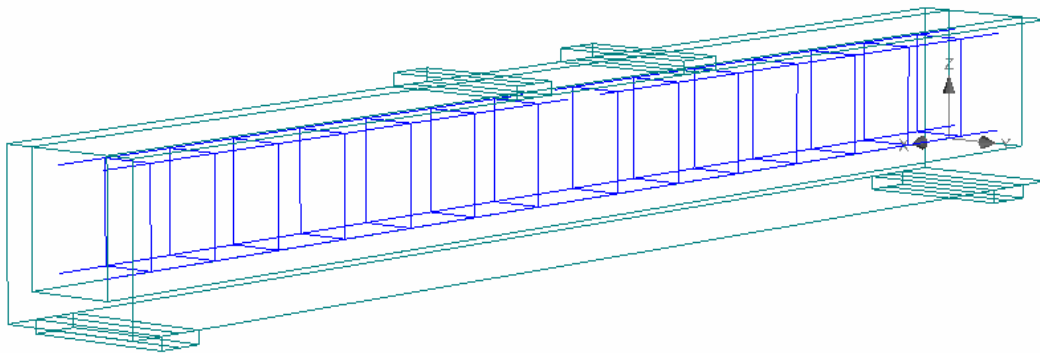


Figure 5.17 Geometrical model used for the numerical modeling of beams strengthened with three-side jackets

The numerical results of the RC beam strengthened with a three-side are presented in the same graph with the respective experimental results in Figure 5.18.

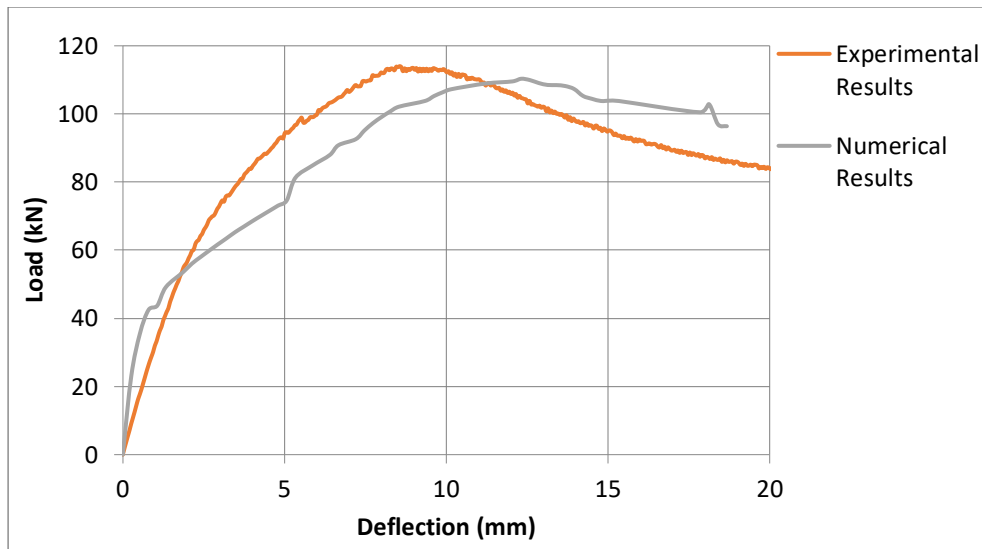
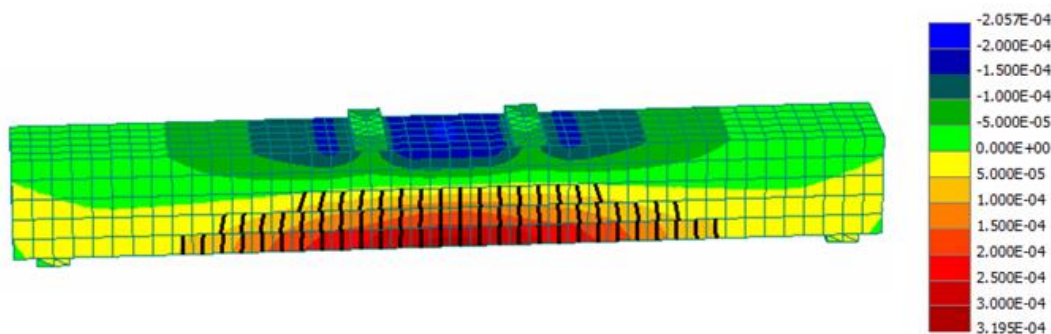
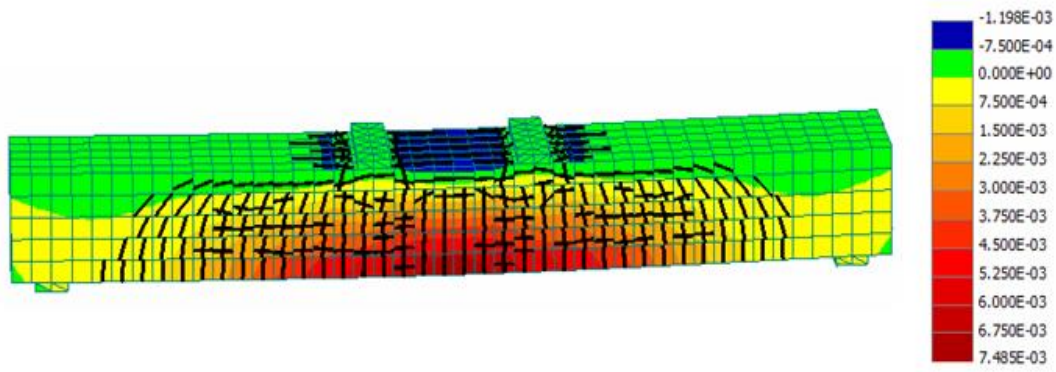


Figure 5.18 Numerical versus experimental results for the beams strengthened with three-side jackets

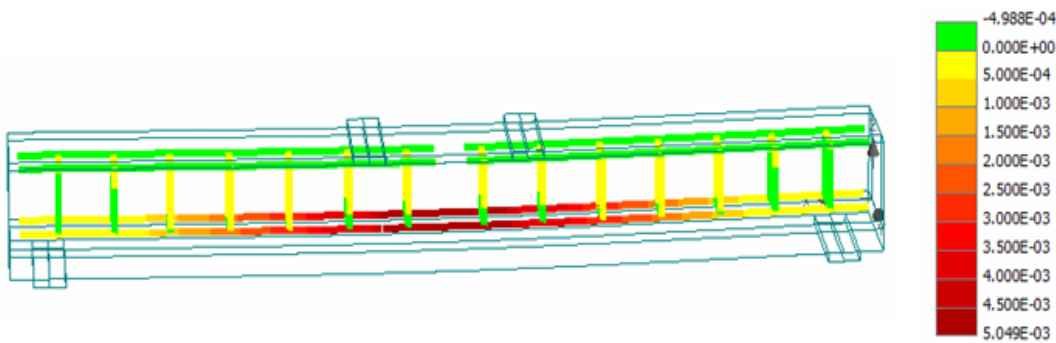
The results of Figure 5.18 indicate a positive agreement between the experimental and the numerical results for the load carrying capacity of the strengthened beams (110 kN for the numerical investigation versus 114.5 kN for the experimental investigation). However, differences in the stiffness and the post elastic state can be distinguished. For the numerical analysis the interface conditions were assumed consistent and identical for all the three sides. However, during the preparation of the interface of the strengthened beams, the roughened area was big and despite the fact that the measured roughness depth was the same for all the examined beams, it is possible that the level of preparation for the beams strengthened with three-side jackets was not identical in all the three sides. Also, local deficiencies in the UHPFRC, which can be attributed to the preparation and the application of the material, or the distribution of the fibers, cannot be taken into consideration in the software. This can also explain the differences between the numerical and the experimental investigation. The crack pattern and the strain distribution of the beam strengthened with a three-side jacket are presented in Figure 5.19.



(a)



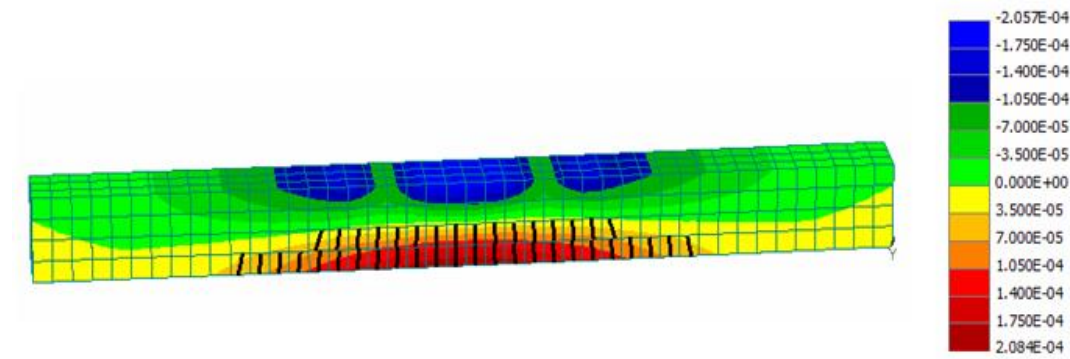
(b)



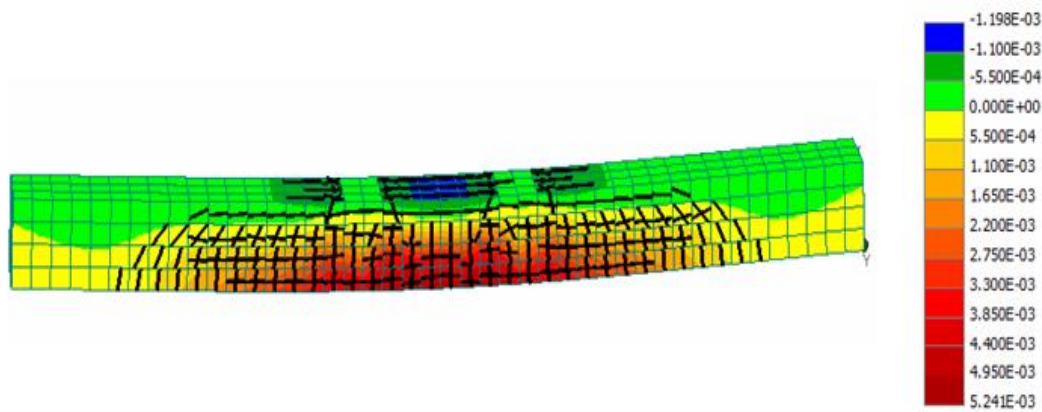
(c)

Figure 5.19 Crack pattern and strain distribution of the existing RC beam strengthened with three-side jacket: a) at the first crack load, b) at the maximum load and c) strain distribution at the reinforcement at the maximum load

As illustrated in Figure 5.19, the damage of the strengthened beam was localized in the middle of the span length at the tensile side. High values of strain on both the beam and the reinforcement can be observed in this area. This failure pattern accords with the failure of the strengthened beam of the experimental investigation. The crack pattern and the strain distribution of the existing RC beam inside the jacket is presented in Figure 5.20.



(a)



(b)

Figure 5.20 Crack pattern and strain distribution of the existing RC beam inside the jacket: a) at the first crack load and b) at the maximum load

As shown in Figure 5.20, lower values of strain on the existing beam inside the jacket can be distinguished, compared to the values of strain of the control RC beam (see Figure 5.8). This indicates the effectiveness of the jacket to support high values of load.

5.4 Sensitivities Analysis

5.4.1 The effect of layer depth on the performance of the strengthened beams

A crucial parameter for the performance of the examined technique is the depth of the layer. For the experimental investigation of the present research, a layer depth of 50 mm was adopted for the strengthening of the existing beams. The selection of the appropriate depth is related to parameters such as; the geometry of the existing elements, the desired performance of the strengthened elements, the decision to increase or not the stiffness of the strengthened elements or the total cost of the technique. In the present section, the effect of layers' depth on the performance of the strengthened elements has been investigated hynumerically.

Existing RC beams were strengthened with layers with various depths and the performance of these elements has been evaluated.

The numerical and experimental results of the previous sections indicated that the connection at the interface affects how well the strengthened members function. Therefore, two types of connections at the interface were examined in the present investigation; monolithic as well as a non-monolithic connection with a coefficient of friction equal to 0.98 and a cohesion equal to 1.8 MPa. In Figure 5.21, the numerical results for the different layer depths and a non-monolithic connection at the interface are presented.

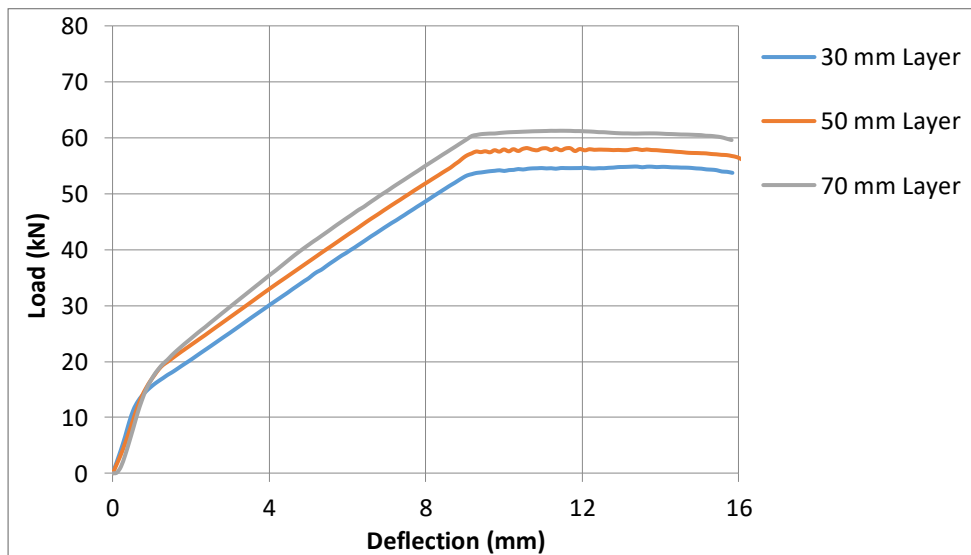


Figure 5.21 Numerical results for the load and the deflection for the different depths of layer and a non-monolithic connection at the interface

The results of Figure 5.21 indicate that the depth of the layer affects the load carrying capacity of the strengthened beams significantly. While the maximum load of the beams strengthened with a 30 mm layer was 54.9 kN, the respective values for the layer depths of 50 mm and 70 mm were found to be equal to 58.2 kN and 61.3 kN respectively. Also, for increasing depths, the stiffness of the strengthened beams also increased. Therefore, the stiffness of the beams strengthened with a 30 mm, a 50 mm and a 70 mm layer was 18.4 kN/mm, 18.5 kN/mm and 19 kN/mm respectively. From these results it can be noticed that when the depth of the layer was increased from 30 mm to 70 mm, the load carrying capacity was increased by 12 % and the stiffness was increased by 3 %. The increase of the load (%) for increasing layer depths is presented in Figure 5.22.

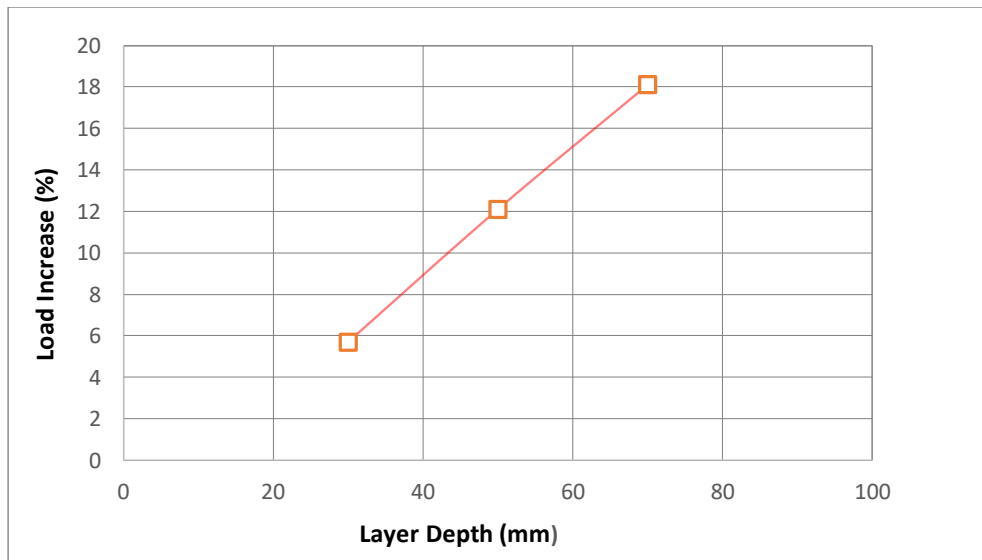
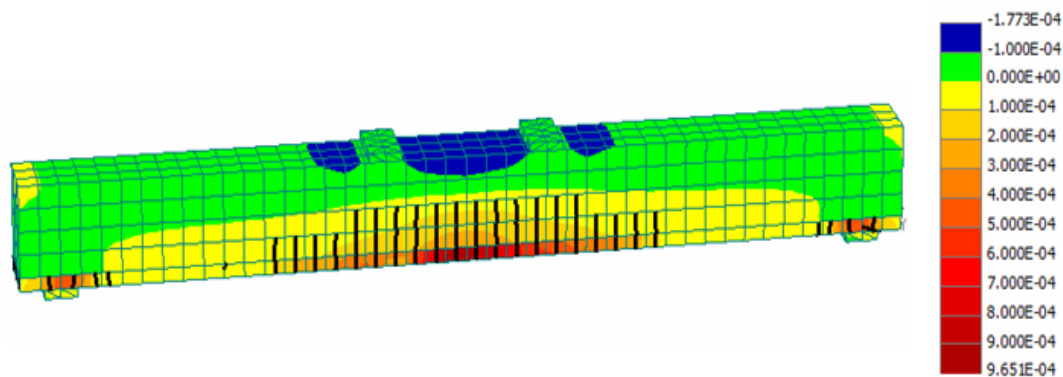


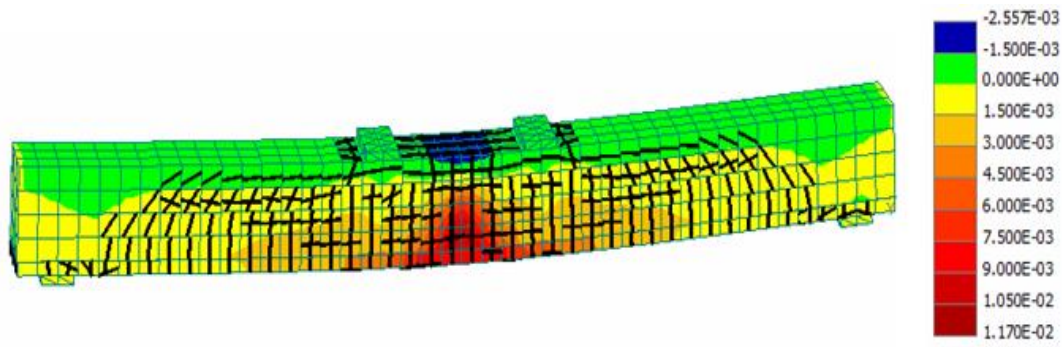
Figure 5.22 Increase of the load (%) for increasing layer depths

From Figure 5.22 a proportional increase of the load (%) for increasing layer depths can be distinguished. More specifically, when the depth of the layer was increased from 30 mm to 50 mm, the load carrying capacity was increased by 6.4%, while an increase of 6.1% was noticed when the layer depth was increased from 50 mm to 70 mm.

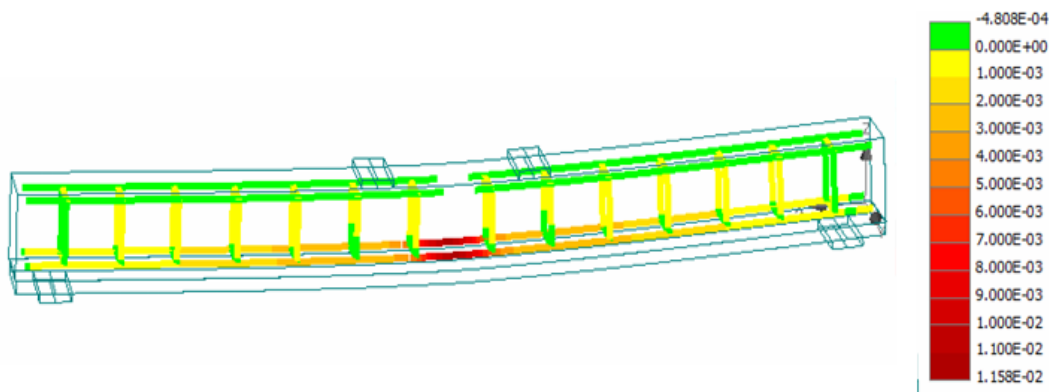
The crack pattern and the strain distribution of the strengthened beam with a 50 mm layer is presented in Figure 5.11. In Figure 5.23, the crack pattern and the strain distribution of the strengthened beam with a 30 mm layer are presented.



(a)



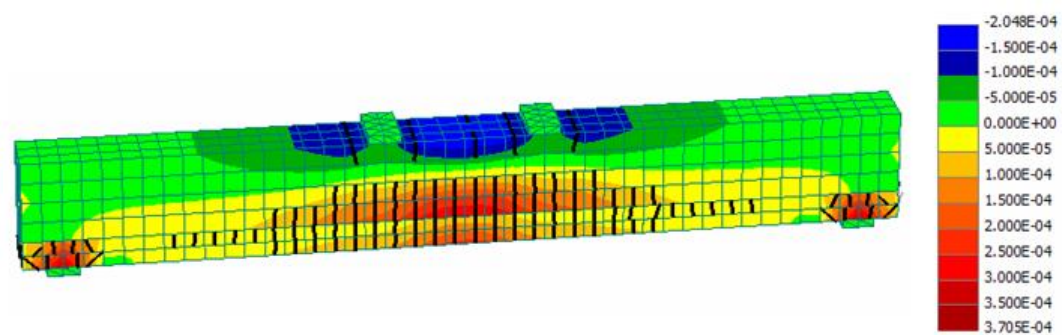
(b)



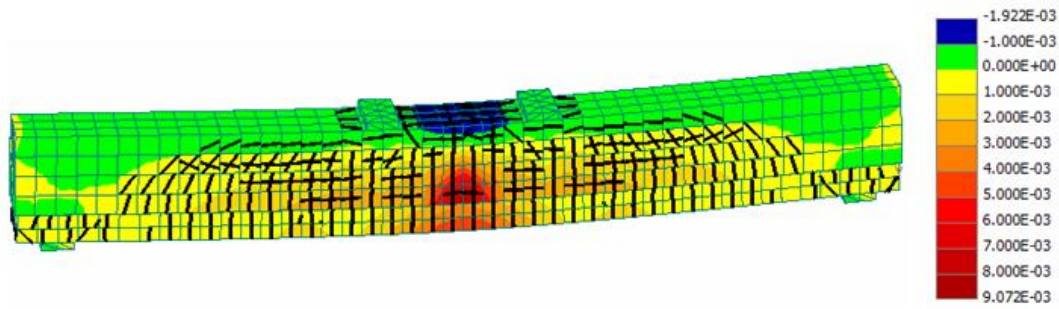
(c)

Figure 5.23 Crack pattern and strain distribution of the existing RC beam strengthened with a 30 mm layer at the tensile side for a non-monolithic connection at the interface: a) at the first crack load, b) at the maximum load and c) strain distribution at the reinforcement at the maximum load

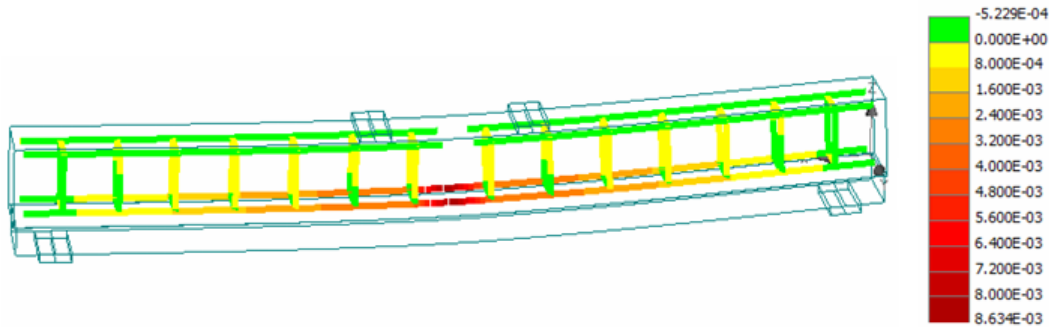
In Figure 5.24, the crack pattern and the strain distribution of the strengthened beam with a 70 mm layer are presented.



(a)



(b)



(c)

Figure 5.24 Crack pattern and strain distribution of the existing RC beam strengthened with a 70 mm layer at the tensile side for a non-monolithic connection at the interface: a) at the first crack load, b) at the maximum load and c) strain distribution at the reinforcement at the maximum load

The failure mode of the strengthened beams with different layer depths was identical and high strain concentration in the middle of the span length on both the tensile and compressive sides can be distinguished. However, for lower depths, higher deformations of the layer and strain values can be distinguished.

The same investigation was conducted for the different layer depths, considering a monolithic connection at the interface. The numerical results are presented in Figure 5.25.

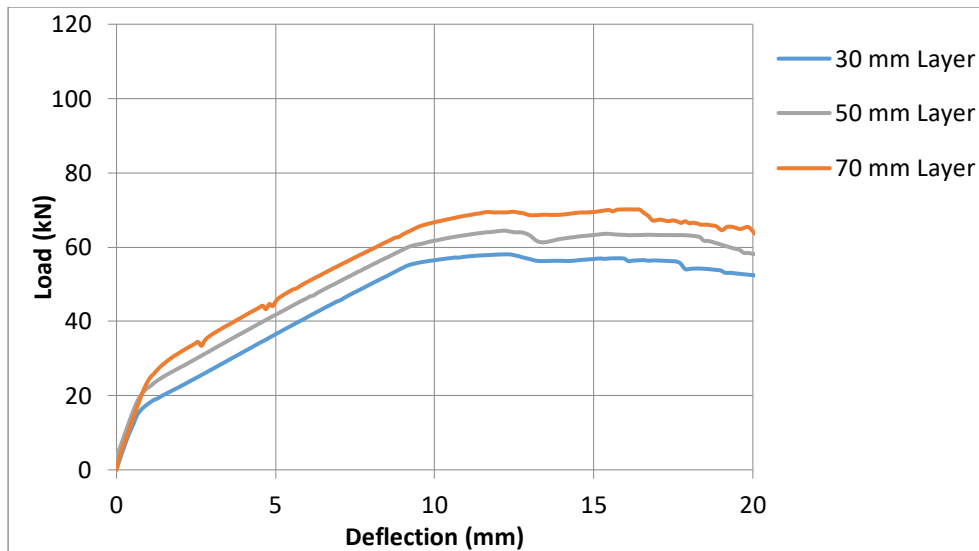


Figure 5.25 Numerical results for the load and the deflection for the different layer depths for a monolithic connection at the interface

According to Figure 5.25, the maximum load of the beams strengthened with a 30 mm layer was found to be equal to 58.1 kN, while the respective values for the beams strengthened with layers with depths of 50 mm and 70 mm, were 64.4 kN and 70.2 kN.

The increase of the load (%) for increasing layer depths is presented in Figure 5.26.

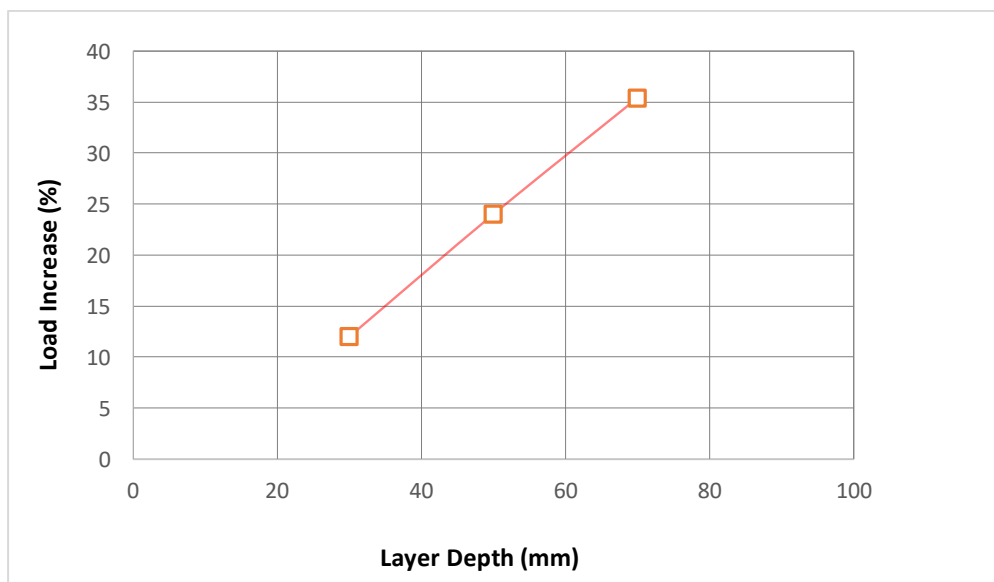


Figure 5.26 Increase of the load (%) for increasing layer depths for a monolithic connection at the interface

From Figure 5.26 a proportional increase of the load (%) for increasing layer depths can be distinguished. When the depth of the layer was increased from 30 mm to 50 mm, the load carrying capacity was increased by 12%, while an increase of 11.6% was noticed when the layer depth was increased from 50 mm to 70 mm. The stiffness, on the other hand, was also

increased for increasing depths. Therefore, the stiffness of the beams strengthened with a 30 mm, a 50 mm and a 70 mm layer was found to be equal to 22.8 kN/mm, 23.6 kN/mm and 24.4 kN/mm respectively. In Figure 5.27, the crack pattern and the strain distribution of the beam strengthened with a 30 mm layer is presented.

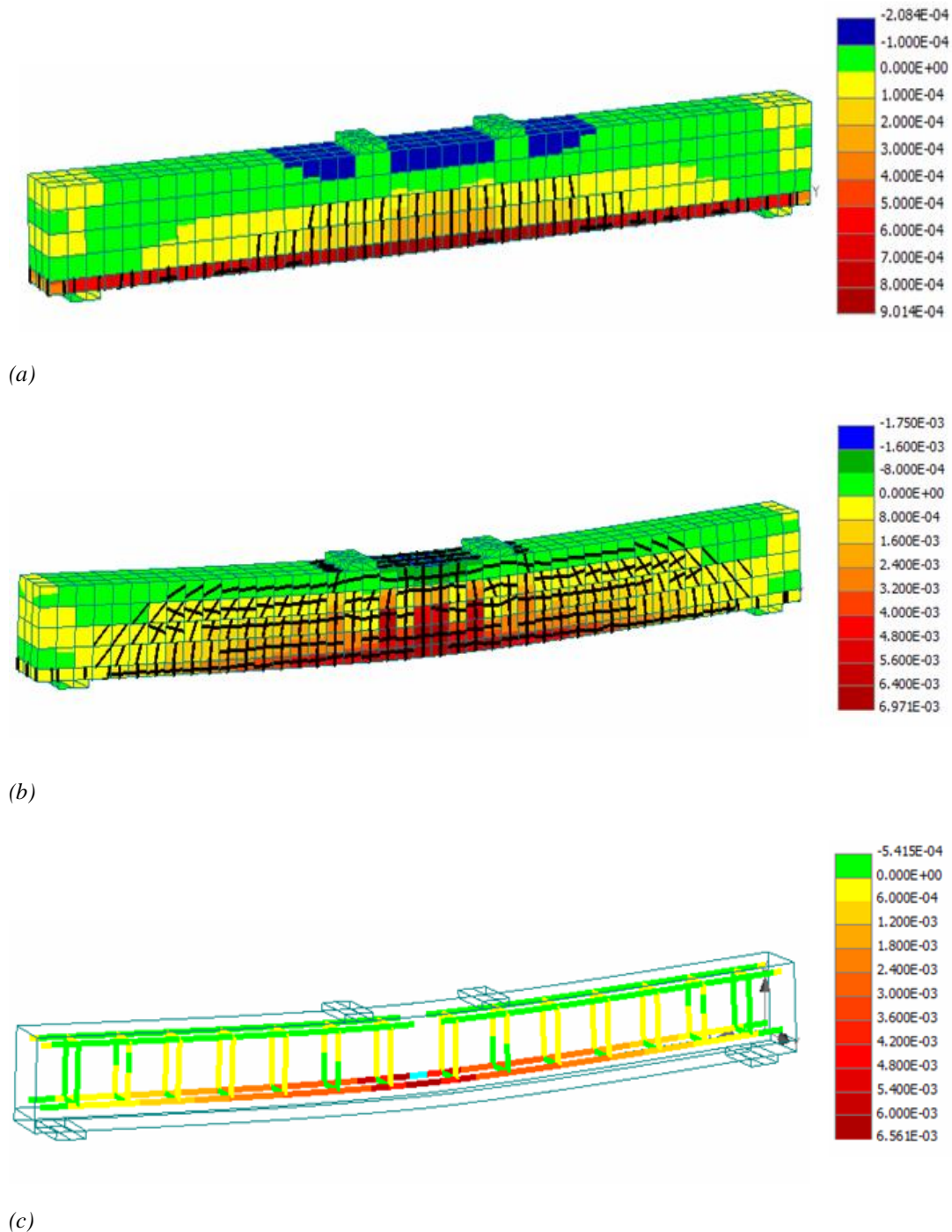


Figure 5.27 Crack pattern and strain distribution of the existing RC beam strengthened with a 30 mm layer at the tensile side and a monolithic connection at the interface: a) at the first crack load, b) at the maximum load and c) the strain distribution at the reinforcement at the maximum load

In Figure 5.28, the crack pattern and the strain distribution of the beam strengthened with a 70 mm layer is shown.

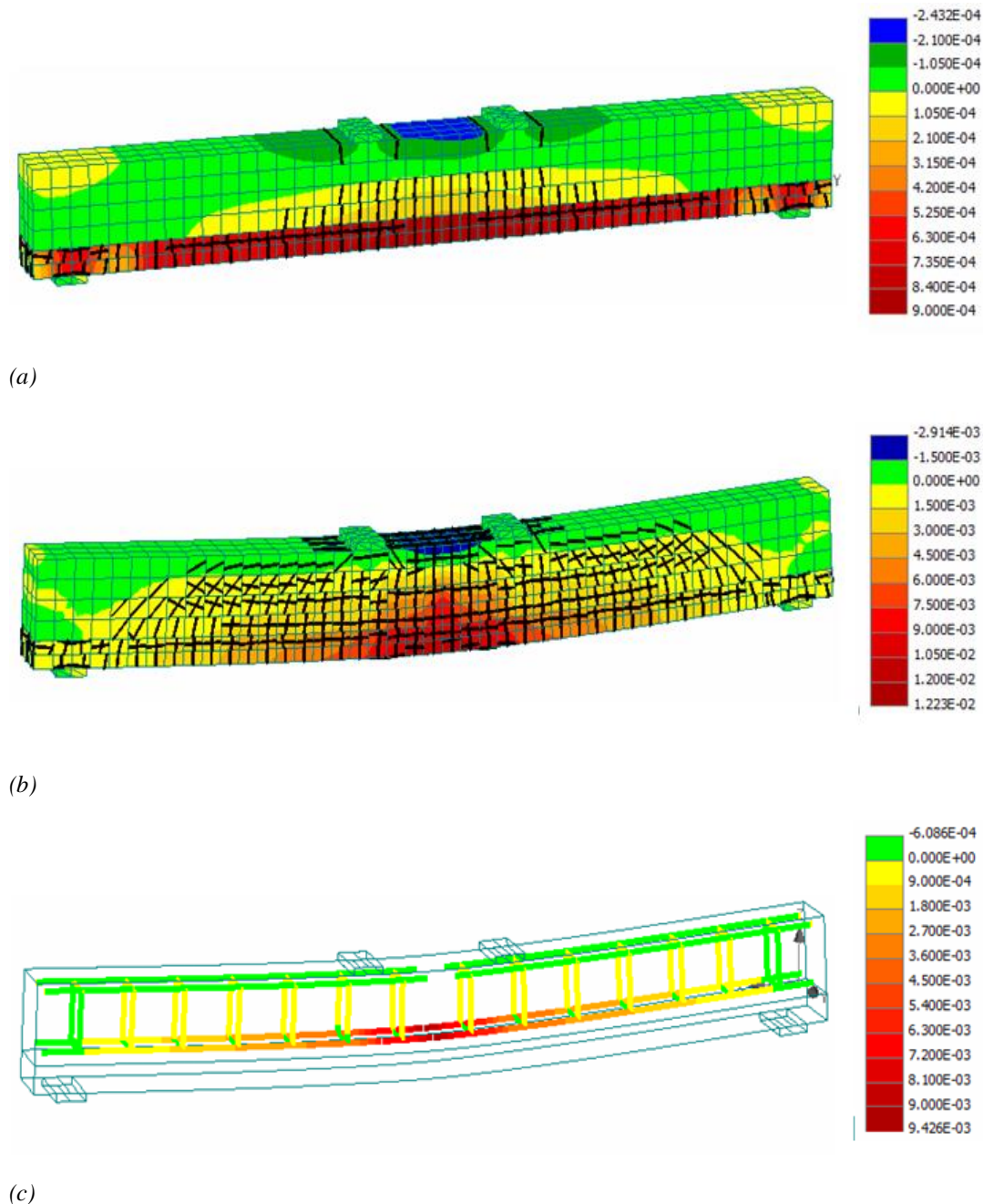


Figure 5.28 Crack pattern and strain distribution of the existing RC beam strengthened with a 70 mm layer at the tensile side and a monolithic connection at the interface: a) at the first crack load, b) at the maximum load and c) the strain distribution at the reinforcement at the maximum load

From Figures 5.27 and 5.28, a similar failure mode for the beams with the different depths can be distinguished, with high values of strain at the tensile side of the beam. However, it can be noticed that the 30 mm layer was in tension along the whole length, which indicates the deformation capacity of the thinner layer. Table 5.1 presents the numerical results for the

first crack load (f_0) and the maximum load (f_m) for the different depths of layers and the different types of interface.

Specimen	f_0 (kN)	$\Delta f_0/f_{IBnum,0}$ (%)	f_m (kN)	$\Delta f_m/f_{IBnum,m}$ (%)
Control Beam (IB_{num})	10	-	51.9	-
30 mm Layer (Non-monolithic)	12.8	28	54.9	6
30 mm Layer (Monolithic)	15.9	59	58	12
50 mm Layer (Non-monolithic)	15.3	53	58.2	12
50 mm Layer (Monolithic)	21.9	119	64.4	24
70 mm layer (Non-monolithic)	17.7	77	61.3	18
70 mm layer (Monolithic)	24.9	149	70.2	35

Table 5.1 Yield and maximum load for the different layer depths and the different types of interface

The results of Table 5.1 indicate the effectiveness of the dowels. Comparing the first crack load (f_0) and the maximum load (f_m) of the strengthened beams for the different types of interfaces (monolithic and non-monolithic), it can be noticed that the use dowels has an almost two-fold higher increase (%) on both the first crack load and the maximum load.

5.4.2 Coefficients of monolithic behavior

The results of the previous sections, indicated that the connection at the interface between the existing member and the new layer is an important parameter which affects the performance of the strengthened members. The target behavior of the strengthened members is the monolithic. However, in most cases, the performance of the strengthened members is lower compared to the performance of the monolithic members. In Figure 5.29, a typical behavior of a strengthened and a monolithic member, according to the Greek Code for Interventions (2013,) is presented.

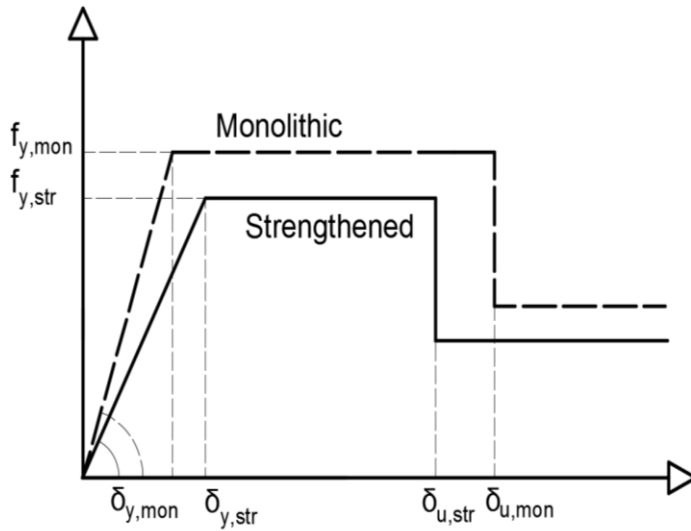


Figure 5.29 Comparison of the performance of a strengthened and a monolithic member (Greek Code of Interventions, 2013)

According to the Greek Code of Interventions (2013), the effectiveness of a strengthening technique can be evaluated with the comparison of the performance of the strengthened with the monolithic member. For this reason, coefficients of monolithic behavior can be used. For the evaluation of the performance of the strengthened members of the present research, the following coefficients have been calculated:

$$K_r = \frac{f_{y, \text{str}}}{f_{y, \text{mon}}} \quad (5.1)$$

Where $f_{y, \text{str}}$ is the resistance of the strengthened member at the yield load; $f_{y, \text{mon}}$ is the resistance of the monolithic member at the yield load.

$$K_k = \frac{K_{\text{str}}}{K_{\text{mon}}} \quad (5.2)$$

Where K_{str} is the stiffness of the strengthened member; K_{mon} is the stiffness of the monolithic member.

$$K_{\theta, y} = \frac{\delta_{y, \text{str}}}{\delta_{y, \text{mon}}} \quad (5.3)$$

Where $\delta_{y, \text{str}}$ is the deformation of the strengthened beam at the yield load; $\delta_{y, \text{mon}}$ is the deformation of the monolithic beam at the yield load.

$$K_{\theta,u} = \frac{\delta_{u, \text{str}}}{\delta_{u, \text{mon}}} \quad (5.4)$$

Where $\delta_{u, \text{str}}$ is the deformation of the strengthened beam at the maximum resistance; $\delta_{u, \text{mon}}$ is the deformation of the monolithic beam at the maximum resistance.

For the calculation of the coefficients K_k , K_r , $K_{\theta,y}$, $K_{\theta,u}$ as monolithic beam was considered the RC beam of the numerical investigation with a perfect connection at the interface (see Figure 5.12), while as strengthened beam was considered the RC beam of the numerical investigation using a coefficient of friction equal to 0.98 and a cohesion equal to 1.8 MPa. The values of the coefficients are presented in Table 5.2.

Layer Depth	K_k	K_r	$K_{\theta,y}$	$K_{\theta,u}$
30 mm	0.94	0.95	1.17	0.89
50 mm	0.69	0.9	1.19	0.87
70 mm	0.7	0.88	1.30	0.71

Table 5.2 Coefficients of monolithic behavior

The results of Table 5.2 indicate that the performance of the thinner elements is approaching the monolithic. Hereby, higher values of coefficients of monolithic behavior can be distinguished for the strengthened beam with a 30 mm layer, compared to the coefficients obtained for strengthening with 50 mm and 70 mm layer depths.

5.4.3 The effect the tensile strength of UHFRC on the performance of the strengthened beams

The properties of UHPFRC are highly dependent on the amount of steel fibers in the mixture and the subsequently on the tensile strength of the material. As presented in Section 3.6, different percentages of steel fibers in the mixture result in different properties of the material in terms of strength, ductility and fracture energy. The selection of the appropriate fiber content is related to certain parameters, such as the cost, the mechanical properties and the ease of the preparation and application of the material. For the preparation of the layers and the jackets of the experimental investigation, a fiber content of 3 % was adopted. Based on the experimental results of the direct tensile tests, the tensile strength was found to be equal

to 11.5 MPa. However, even higher values of tensile strength can be achieved. From the experimental investigation of the present thesis, a tensile strength of 12.5 MPa was achieved using 6 % steel fibers (see Section 3.6.4). For the investigation of the effect of the tensile strength of the UHPFRC on the performance of the strengthening technique, different values of tensile strength have been examined. Hence, apart from tensile strengths of 11.5 MPa and 12.5 MPa, an extremely high value of 14 MPa, which has been reported in the literature (AFGC-SETRA, 2013), was also investigated. The numerical results for this investigation are presented in Figure 5.30.

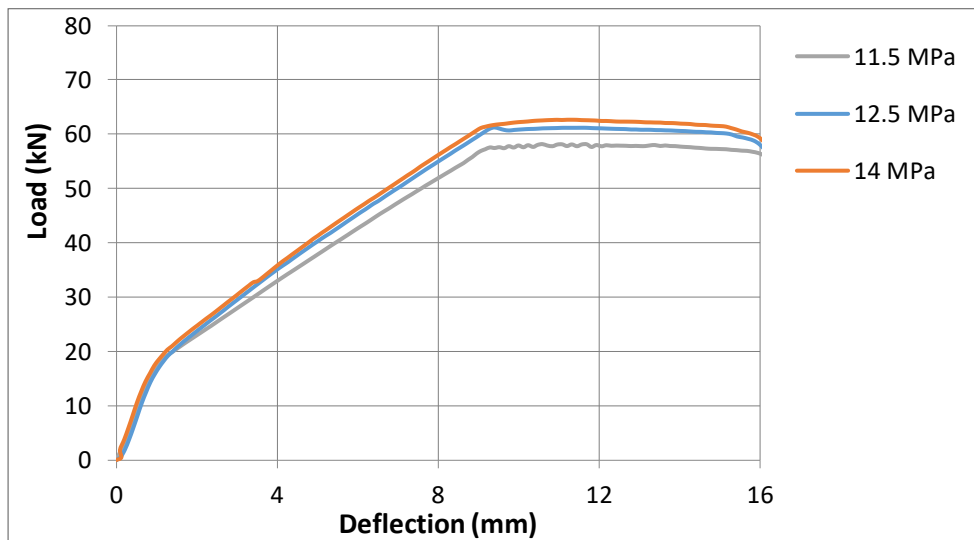


Figure 5.30 Performance of strengthened RC beams with layers with different tensile strengths

From the results of Figure 5.30, the first crack and the maximum load were identified and the results are presented in Table 5.3.

Specimen	f_0 (kN)	$\Delta f_0/f_{IBnum,0}$ (%)	f_m (kN)	$\Delta f_m/f_{IBnum,m}$ (%)
Control Beam (IB_{num})	10	-	51.9	-
Tensile Strength 11.5 MPa	15.3	53	58.2	12
Tensile Strength 12.5 MPa	17.1	71	61.2	18
Tensile Strength 14 MPa	18.5	85	62.7	21

Table 5.3 Yield and maximum load for the different tensile strengths

The results of Figure 5.30 and Table 5.3 indicate that the tensile strength of the UHPFRC layer affects the performance of the strengthened beams. Therefore, for the tensile strengths 11.5 MPa, 12.5 MPa and 14 MPa the respective first crack loads were found to be equal to 15.3 kN, 17.1 kN and 18.5 kN. The respective values for maximum loads were calculated to be 58.2 kN, 61.2 kN and 62.7 kN. Based on these results, it can be noticed that once the tensile strength increased from 11.5 MPa to 12.5 MPa, the first crack load of the strengthened beam increased by 21% and the maximum load by 8 %. However, a lower increase could be seen when the tensile strength increased from 12.5 MPa to 14 MPa, in which case, the first crack load increased by 8 % and the maximum load by 2.5 %.

5.4.4 The effect of shrinkage on the performance of the strengthened beams

Based on the measurements of shrinkage in Section 3.7, an initial shrinkage strain value of 565 microstrain was imposed on the elements of the additional layer. However, since shrinkage is highly affected by the environmental conditions and the age of the specimens, there may be variations in the shrinkage strain value. For this reason, a sensitivity analysis has been conducted for the examined strengthened beams and strain values of 200 microstrain, and without shrinkage being imposed on the layers. The numerical results of the strengthened beams for the different values of shrinkage are presented in Figure 5.31.

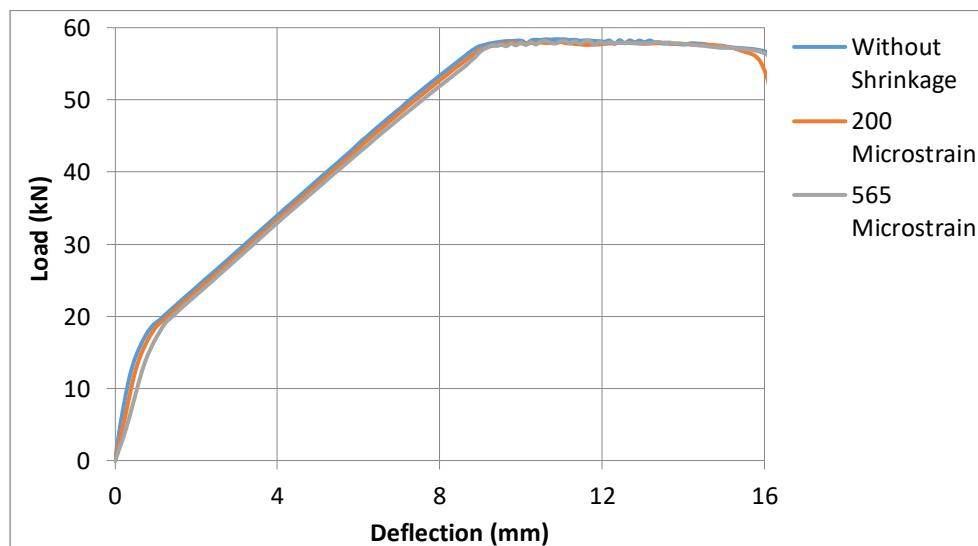


Figure 5.31 Numerical results for strengthened beams with UHPFRC layers at the tensile side for different values of shrinkage

The load carrying capacity of the strengthened beams was not significantly altered by the different values of shrinkage. However, for the increasing values of shrinkage, the stiffness of the beams was decreased. Therefore, the stiffness of the beam without shrinkage was found to be equal to 26.1 kN/mm, and the respective values for shrinkage equal to 200 microstrains and 565 microstrains were calculated to be 19.2 kN/mm and 18.5 kN/mm respectively. Shrinkage produces cracks, which affects the performance of the cementitious matrix. However, the post-cracking response of the layers is mainly related to the steel fibers and the tensile characteristics of the layer. Subsequently, the load carrying capacity of the beams was hardly affected.

5.4.5 Strengthening of RC beams using UHPFRC layers at the compressive side

For the experimental evaluation of the performance of the UHPFRC as a strengthening material, the RC beams were strengthened with layers and jackets at the tensile side of the beams. In the present section, the performance of existing RC beams for strengthening at the compressive side has been investigated numerically. For this investigation, a layer depth of 50 mm was adopted, which is identical with the layer depths of the experimental investigation. The numerical results for this investigation together with the results for the control beam are presented in the same graph in Figure 5.32.

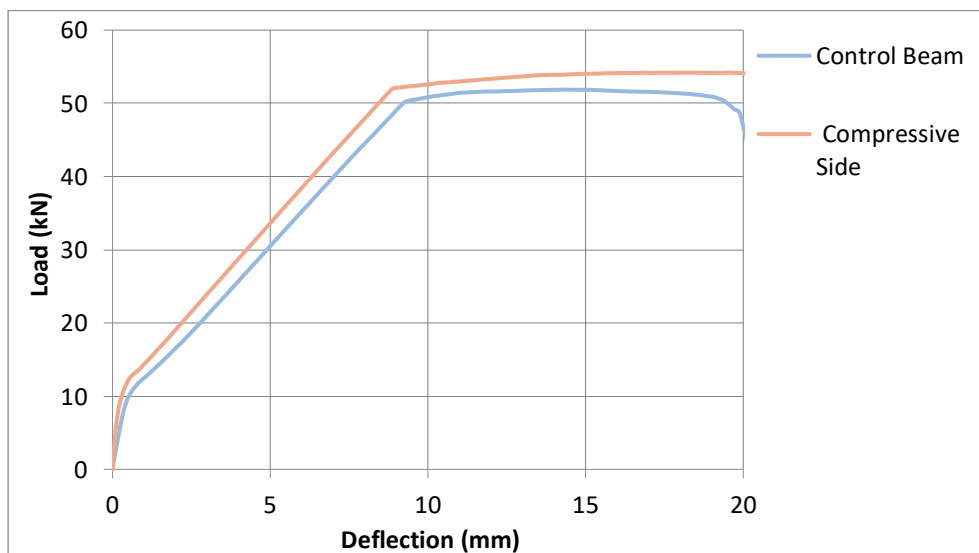


Figure 5.32 Numerical results for the existing RC beam and the beam strengthened with a layer at the compressive side

From Figure 5.32, a slight increase of the stiffness and the maximum load of the strengthened beam can be distinguished. The crack pattern and the strain distribution of the strengthened beam with a layer at the compressive side are presented in Figure 5.33.

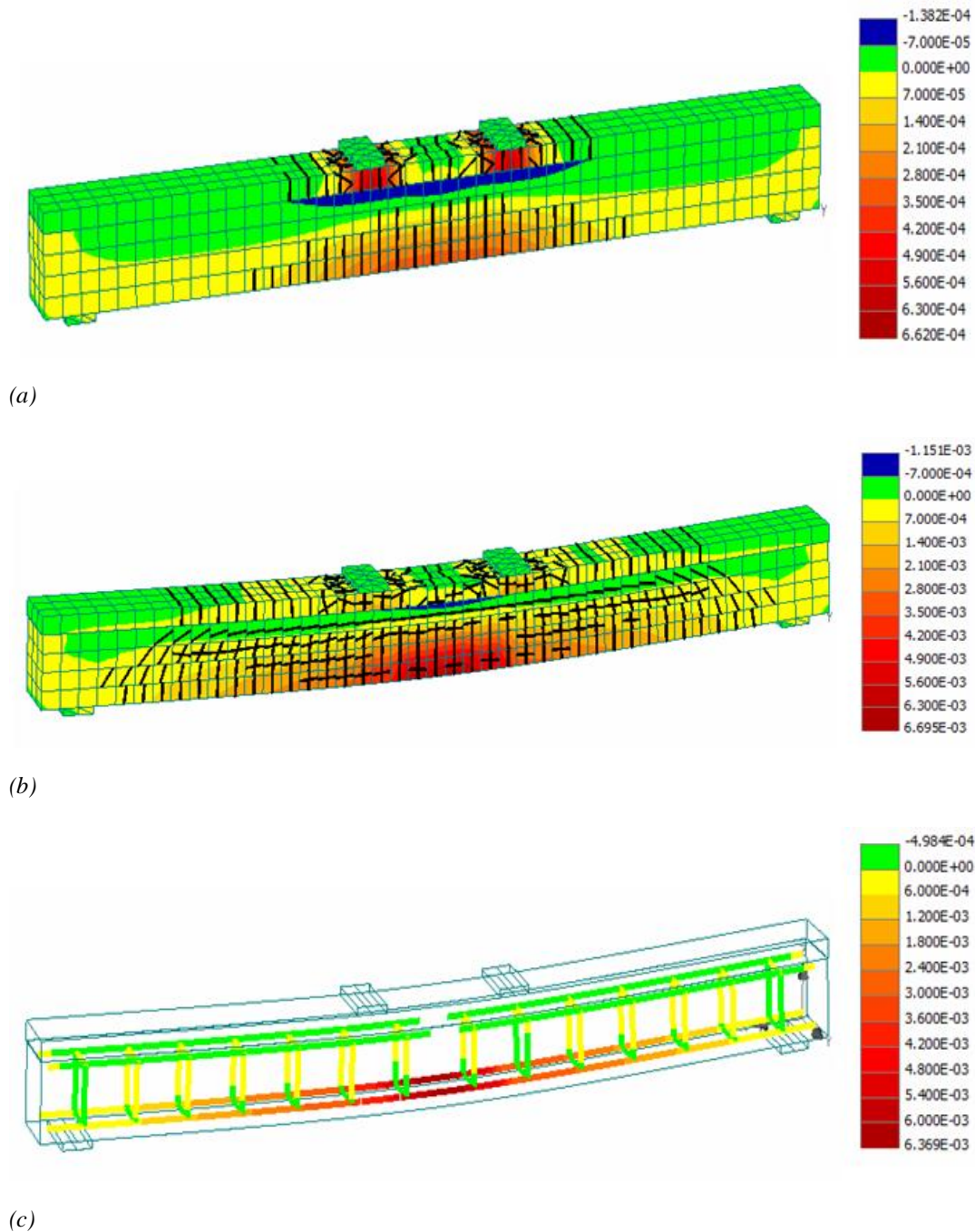


Figure 5.33 Crack pattern and strain distribution of the existing RC beam strengthened with a layer at the compressive side: a) at the first crack load, b) at the maximum load and c) the strain distribution at the reinforcement at the maximum load

As illustrated in Figure 5.33, the damage was localized in the middle of the span length and at the tensile side of the existing RC beam, an area where high strain concentrations can be distinguished. Alternatively, deformations and damages of the layer at the compressive side are hardly distinguishable.

In Table 5.4, the values for the first crack and the maximum load of the control beam and the beam strengthened with a layer at the compressive side are shown. In the same table, the respective numerical results for the beam strengthened with a layer with the same depth at tensile side are presented.

Specimen	f_0 (kN)	$\Delta f_0/f_{IBnum,0}$ (%)	f_m (kN)	$\Delta f_m/f_{IBnum,m}$ (%)
Control Beam (IB_{num})	10	-	51.9	-
Strengthening at the Compressive Side	10.5	5	54.2	5
Strengthening at the Tensile Side	15.3	53	58.2	12

Table 5.4 Numerical results for strengthening at the compressive and the tensile sides

The results of Table 5.4 show that a higher load carrying capacity of the strengthened beam was achieved for strengthening at the tensile side; in which case, a subsequently higher contribution of the layer can be distinguished. More specifically, for strengthening at the compressive side, the first crack and the maximum loads of the existing beam were increased by 5 %; moreover an increase of 53 % at the first crack load and 12 % at the maximum load were noticed for strengthening at the tensile side.

5.4.6 Strengthening of existing RC beams with different configuration of the reinforcement

The existing RC beams of the present research were reinforced using two longitudinal ribbed steel bars with a diameter of 12 mm at the tensile side of the beams. Stirrups with a diameter of 10 mm were also placed every 150 mm (see Section 4.4.1). This reinforcement represents relatively weak beams. In the present section, a different configuration of the reinforcement of the existing RC beam has been investigated. More specifically, steel bars with a diameter of 8 mm were used as a longitudinal reinforcement, while stirrups with a diameter of 8 mm

were placed in a distance of 200 mm and used as a shear reinforcement. This configuration represents weaker existing RC beams compared to the experimental investigation. The geometry and the reinforcement of the existing members are presented in Figure 5.34. The existing RC beam was strengthened with a 50 mm layer at the tensile side. The properties of the material were identical with the previous investigations (see Section 5.2).

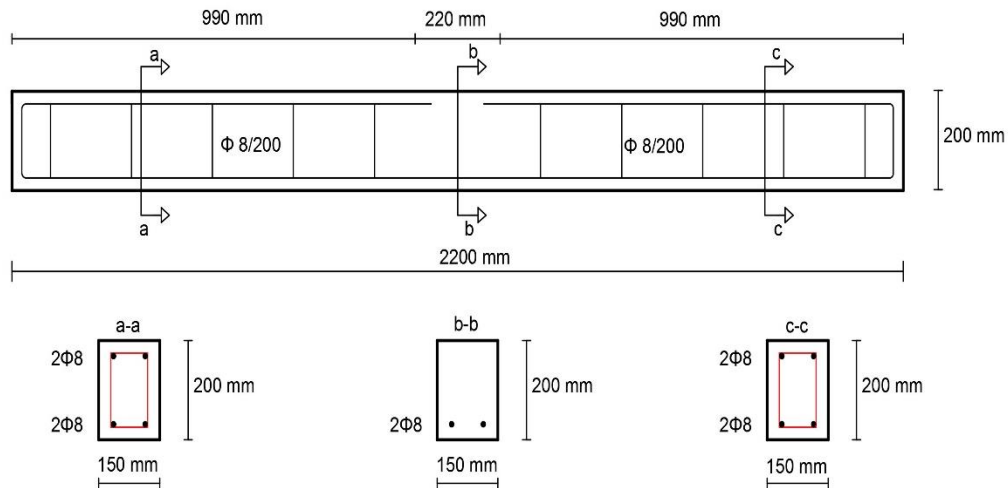


Figure 5.34 Reinforcement of the weaker existing RC beam

The load-deflection results of the existing RC beam and the strengthened beam are presented in the same graph in Figure 5.35.

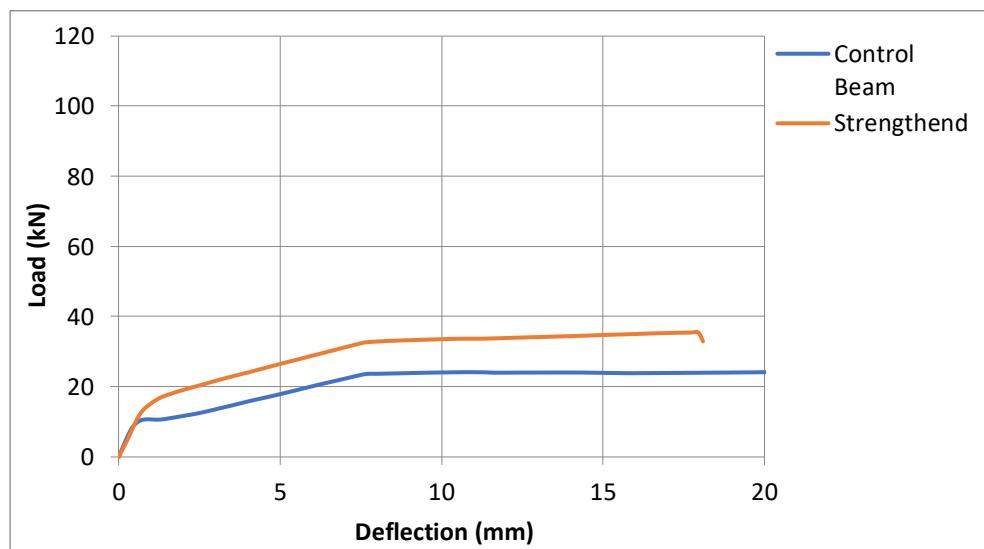


Figure 5.35 Load versus deflection results for the weaker existing RC beam and the strengthened beam

Based on Figure 5.35, the first crack and the maximum load of the control beam and the strengthened beam were identified and are presented in Table 5.5.

Specimen	f_0 (kN)	$\Delta f_0/f_{IBnum,0}$ (%)	f_m (kN)	$\Delta f_m/f_{IBnum,m}$ (%)
Control Beam (IB_{num})	8.4	-	24.7	-
Strengthened Beam	14.1	68	35.4	43

Table 5.5 Results for strengthening of a weaker RC beam

From the results of Figure 5.35 and Table 5.5, it is clear that the performance of the strengthened beams is highly affected by the amount of the reinforcement of the existing beams. Hence, an increase of 68 % at the first crack load and 43 % at the maximum load was noticed for the strengthening of a weaker existing member. For a weaker existing RC beam, the layer acts at an earlier phase until it reaches its maximum load carrying capacity. However, for a stronger existing member, the layer is activated at a later stage, and possibly not in its elastic state. It is worth mentioning that based on the numerical results using the reinforcement of the experimental investigation, the increase of the first crack and the maximum load were found to be equal to 53 % and 12 % respectively.

5.4.7 The effect of the amount of reinforcement at the UHPFRC layer

For the strengthening of RC beams using UHPFRC layers and steel bars, steel bars grade B500 C with a diameter of 10 mm were adopted as a reinforcement of the layer. The selection of the appropriate amount of reinforcement at the layer is related with parameters such as the cost of the technique, the depth of the layer and the desired performance of the strengthened elements. In the present section, the effect of the amount of reinforcement of the layer on the performance of the strengthened beams has been investigated. A sensitivity analysis has been conducted and the performance of the strengthened beams using different diameters of steel bars, has been investigated. The layers were reinforced with steel bars grade B 500C with diameters of 10 mm, 12 mm, 14 mm and 16 mm and the numerical results are presented in Figure 5.36. In the same graph the numerical results of the strengthened beam with an UHPFRC layer without steel bars are also presented.

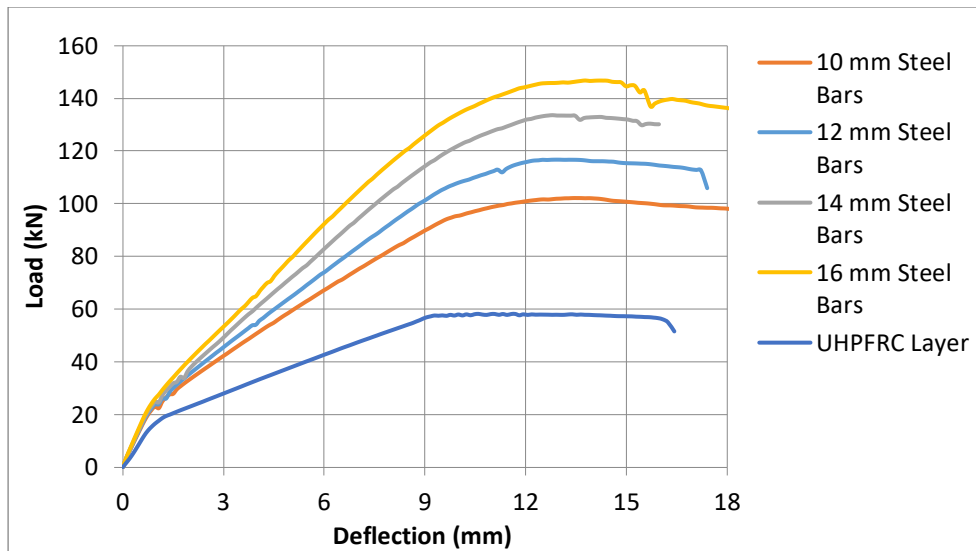


Figure 5.36 Load versus deflection results for the different diameters of steel bars of the UHPFRC layer

From Figure 5.36, the first crack and the maximum loads were identified and all the numerical results for the different diameters of steel bars are presented in Table 5.6.

Specimen	f_0 (kN)	$\Delta f_0/f_{IBnum,0}$ (%)	f_m (kN)	$\Delta f_m/f_{IBnum,m}$ (%)
Control Beam (IB_{num})	10	-	51.9	-
UHPFRC Layer	15.3	53	58.2	12
UHPFRC Layer and 10 mm Bars	23.1	131	102.1	97
UHPFRC Layer and 12 mm Bars	23.8	138	116.7	124
UHPFRC Layer and 14 mm Bars	24.8	148	133.7	158
UHPFRC Layer and 16 mm Bars	27.5	175	146.8	183

Table 5.6 Numerical results for different amounts of reinforcement of the layer

From the results above, it is apparent that the amount of reinforcement of the layer affects the performance of the strengthened beams significantly. Hence, an increase of 51% at the first crack load and 75% at the maximum load was observed with the addition of steel bars with a diameter of 10 mm to the layer. Also, an increase of 19% at the first crack load and 44% at

the maximum load was observed when the 10 mm bars were replaced by 16 mm bars. The increase of the load carrying capacity for the increasing ratio of the reinforcement ($\rho_s = A_s/bh$) is presented in Figure 5.37. As can be seen, an almost proportional increase in the load carrying capacity (%) can be distinguished when the ratio of the reinforcement is increased from 0.01 to 0.014, while a lower increase can be distinguished when the ratio is increased from 0.014 to 0.016.

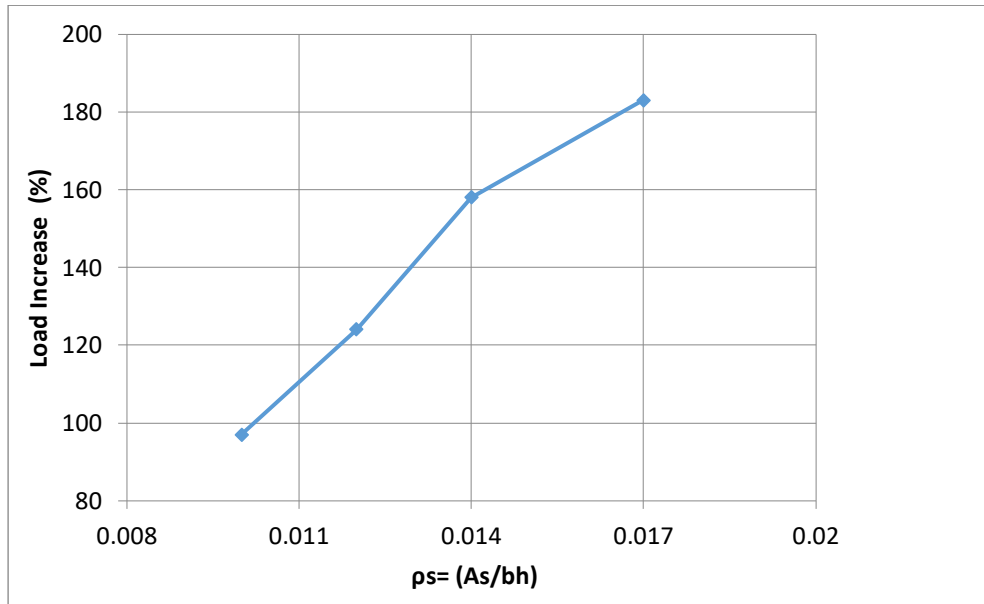


Figure 5.37 Load increase for increasing amounts of reinforcement

The stiffness of the strengthened beams, on the other hand, was also slightly altered by the different diameters of the steel bars, and the values of 28.7 kN/mm, 29.6 kN/mm, 30.5 kN/mm and 31.6 kN/mm were identified for the steel bars with diameters of 10 mm, 12 mm, 14 mm and 16 mm respectively.

5.4.8 The effect of steel grade on the performance of the strengthened beams with UHPFRC layers and steel bars

For the previous investigations, steel bars grade B500 C were used as reinforcement of the layers. This is a commonly used type of reinforcement which combines positive mechanical properties and low cost. However, different types of reinforcement with enhanced properties can be found on the market. Based on Habel et al. (2006), the performance of the strengthened members can be increased with the use of steel bars of a higher steel grade to the layer. Therefore, in the present investigation, a comparison between the performance of the strengthened beam using steel bars of a different grade is presented. More specifically, steel

bars grade B700, with yield stress at 700 MPa and a diameter of 10 mm, were used as reinforcement of the layer, and the numerical results were compared with the results obtained using steel bars grade B500 C, with the same diameter. It worth noting that the selection of the appropriate type of reinforcement is related to the desired properties of the reinforcement and also the total cost. The numerical results for the different grades are presented in Figure 5.38.

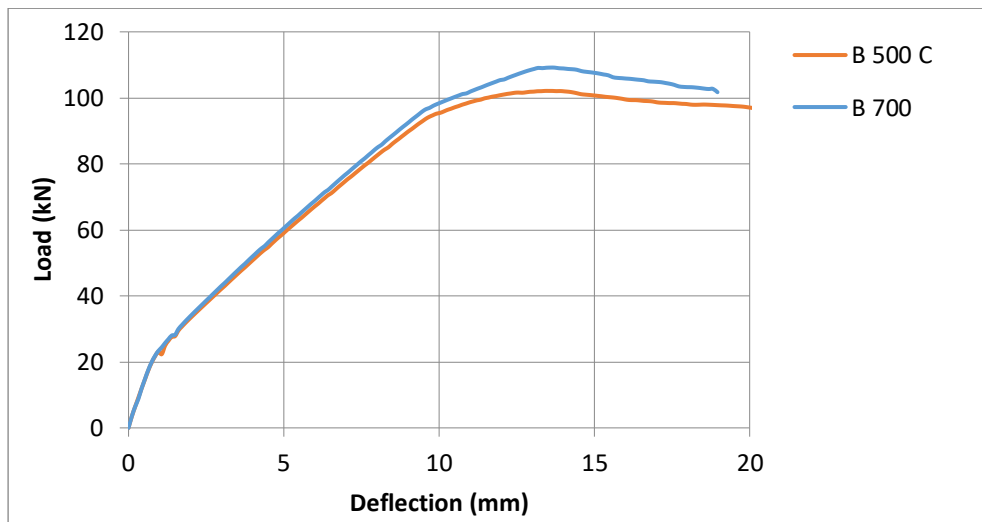


Figure 5.38 Load versus deflection results for the different steel grades

The values for the first crack and the maximum load of the strengthened beams of Figure 5.38 are presented in Table 5.7.

Specimen	f_0 (kN)	$\Delta f_0/f_{IBnum,0}$ (%)	f_m (kN)	$\Delta f_m/f_{IBnum,m}$ (%)
Control Beam (IB_{num})	10	-	51.9	-
B 500 C	23.1	131	102.1	97
B 700	24.4	144	109.2	110

Table 5.7 Numerical results for the different steel grades

The results of Figure 5.38 and Table 5.7 specify that the performance of the strengthened beams can be increased for a higher steel grade. Hence, the use of steel bars grade B700, had as a results an increase of 6 % on the first crack load and 7% on the maximum load. However, the stiffness was not significantly affected.

5.4.9 Strengthening with various layer depths and various diameters of steel bars

From the results of the previous investigations, it is evident that the depth of the layer and amount of the reinforcement of the layer are crucial parameters affecting the performance of the strengthened beams. In the present section, different alternatives for the selection of the appropriate layer depth and the amount of reinforcement are analysed, and a comparison is drawn. For this numerical investigation, three different layer depths were examined, namely 30 mm, 50 mm and 70 mm, and these layers were reinforced with steel bars with diameters of 10 mm and 16 mm. The grade of the steel bars in all these cases was B500 C. All the numerical results for the differing diameters and layer depths are shown in the same graph in Figure 5.39.

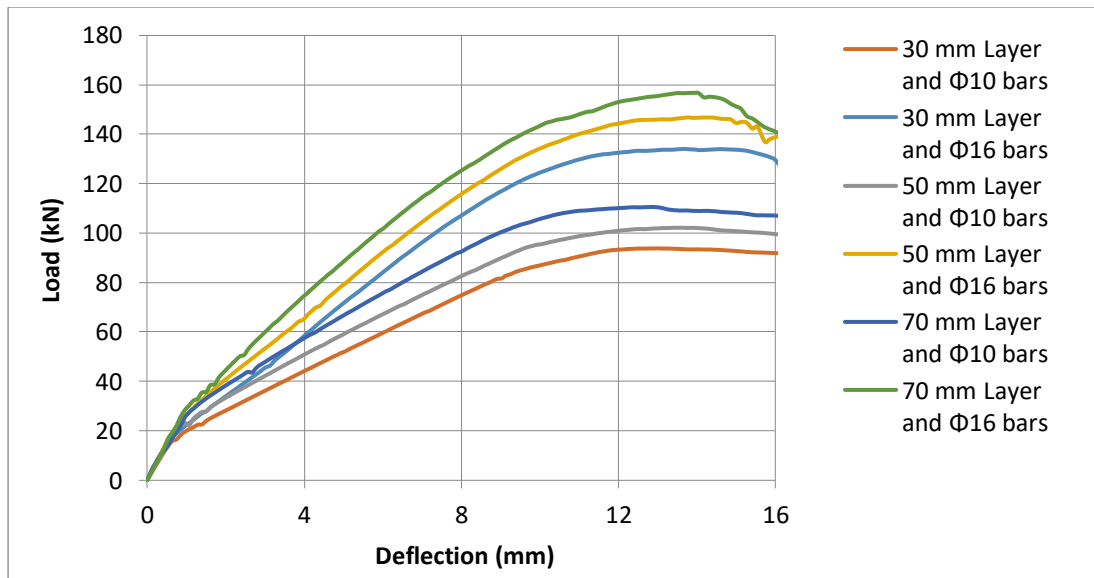


Figure 5.39 Load versus deflection results for different layer depths and different diameters of steel bars

From Figure 5.39, the first crack and the maximum load were identified and the results are presented in Table 5.8.

Specimen	f_0 (kN)	$\Delta f_0/f_{IBnum,0}$ (%)	f_m (kN)	$\Delta f_m/f_{IBnum,m}$ (%)
Control Beam (IB_{num})	10	-	51.9	-
30 mm Layer and $\Phi 10$ Bars	15.8	58	93.8	81
30 mm Layer and $\Phi 16$ Bars	20.6	106	134	158
50 mm Layer and $\Phi 10$ Bars	23.1	131	102.1	97
50 mm Layer and $\Phi 16$ Bars	26	160	146.8	183
70 mm Layer and $\Phi 10$ Bars	27.5	175	110.6	113
70 mm Layer and $\Phi 16$ Bars	30.2	202	156.7	202

Table 5.8 Numerical results for the different diameters of the steel bars and the different layer depths

The results of Figure 5.39 and Table 5.8 suggest that the amount of the reinforcement at the layer is more important than the depth of the layer. Therefore, the performance of the strengthened RC beam with a 30 mm layer and steel bars with a diameter of 16 mm seems a significant improvement compared to the performance of the UHPFRC layers with depths of 50 mm and 70 mm and the steel bars with a diameter of 10 mm. As expected, the optimum functioning was achieved for the 70 mm layer depth and steel bars with a diameter of 16 mm; in this case, the maximum load was found to be 156.7 kN and the stiffness was 30.2 kN/mm.

5.4.10 Strengthening with jackets and steel bars

The experimental results of the full-scale beam testing indicated that the strengthening with jackets on three sides of the beams is a highly effective technique, which can achieve a high load carrying capacity. This is also a technique which can be used to prevent the shear failure of the existing RC beams. The use of steel bars together with UHPFRC jackets could dramatically increase the load carrying capacity of the beams. In the present section, and in order to achieve the optimum performance of the jackets, an investigation is undertaken into

how well this technique functions using UHPFRC jackets and steel bars. Hence, in this case the existing member of the numerical investigation was strengthened with a jacket on three sides with the same dimensions as the experimental study. Additionally, two steel bars with a diameter of 10 mm and grade B500 C were placed at the tensile side of the beams, as illustrated in Figure 5.40.

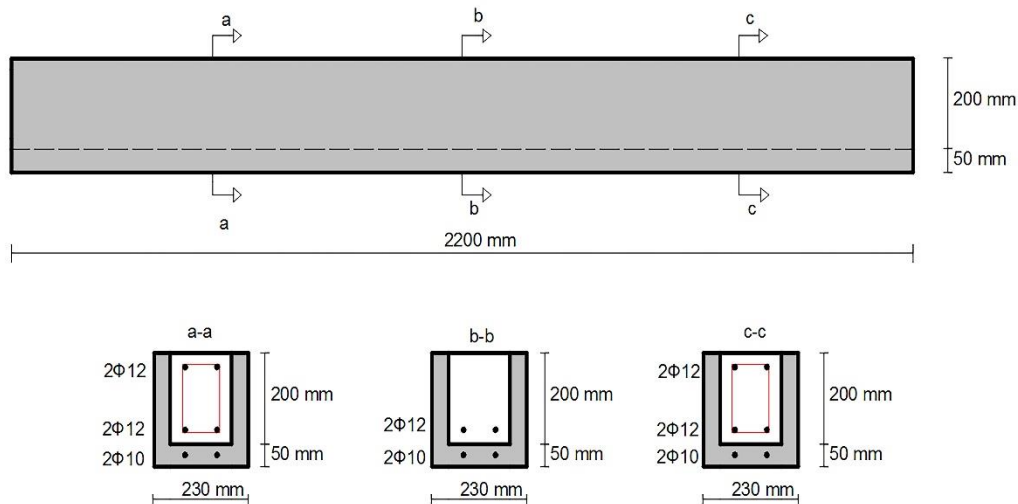


Figure 5.40 Strengthening with a three-side jacket and steel bars

The numerical results for the existing RC beam, the RC beam strengthened with a jacket and the RC beam strengthened with a jacket with steel bars are presented in the same graph in Figure 5.41.

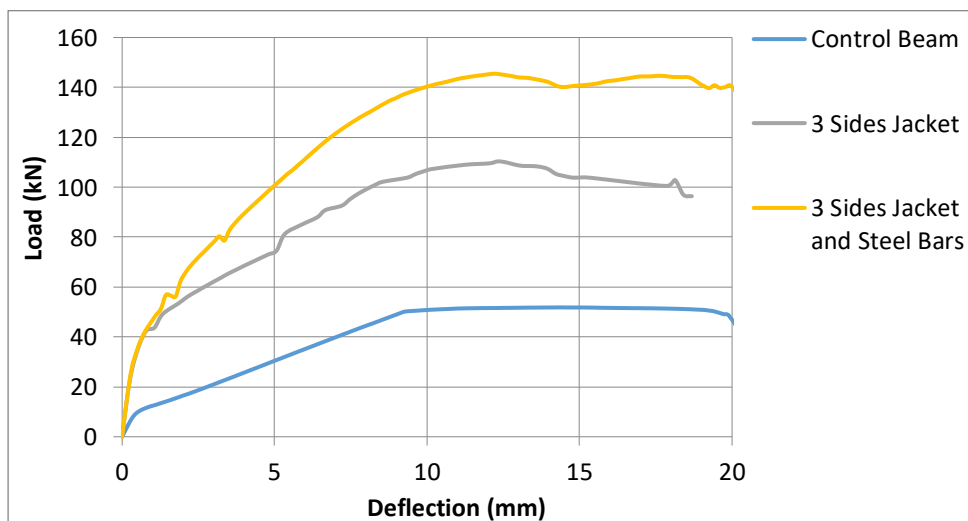


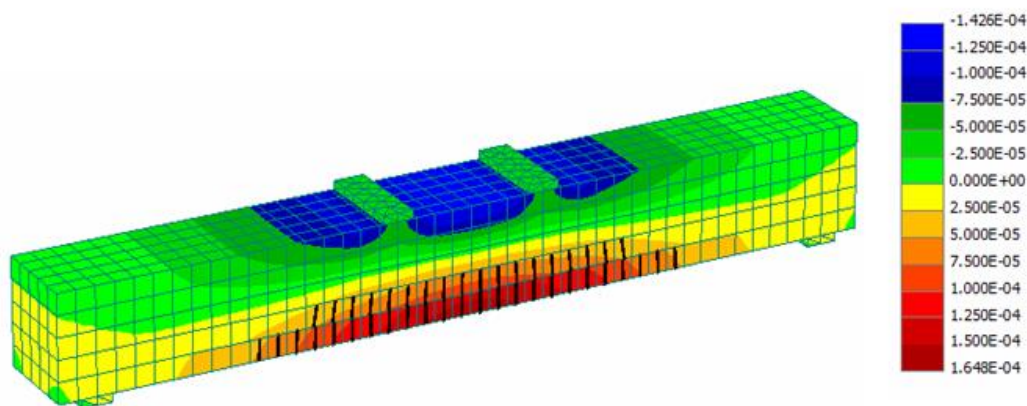
Figure 5.41 Load versus deflection results for the strengthened beams with three-side jacket and three-side jacket and steel bars

The results for the yield and the maximum load are presented in Table 5.9.

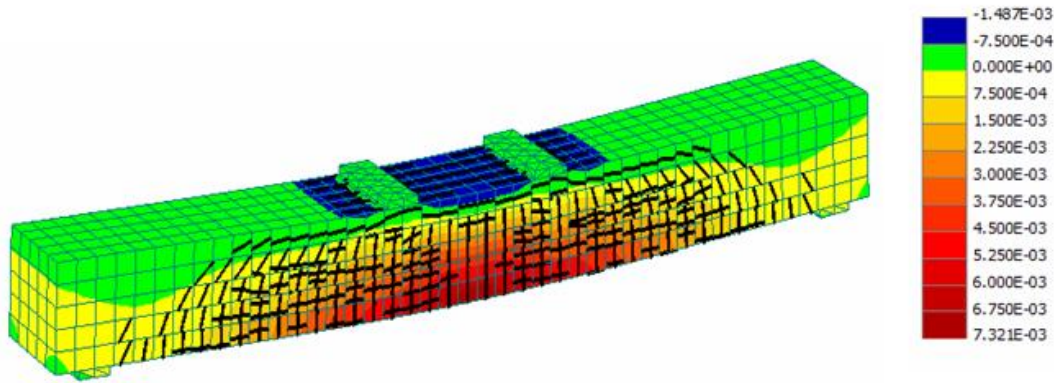
Specimen	f_0 (kN)	$\Delta f_0/f_{IBnum,0}$ (%)	f_m (kN)	$\Delta f_m/f_{IBnum,m}$ (%)
Control Beam (IB_{num})	10	-	51.9	-
Three-Side Jacket	23.1	131	110	112
Three-Side Jacket and Bars	27.3	173	145	179

Table 5.9 Numerical results for strengthening with a three-side jacket and a three-side jacket with steel bars

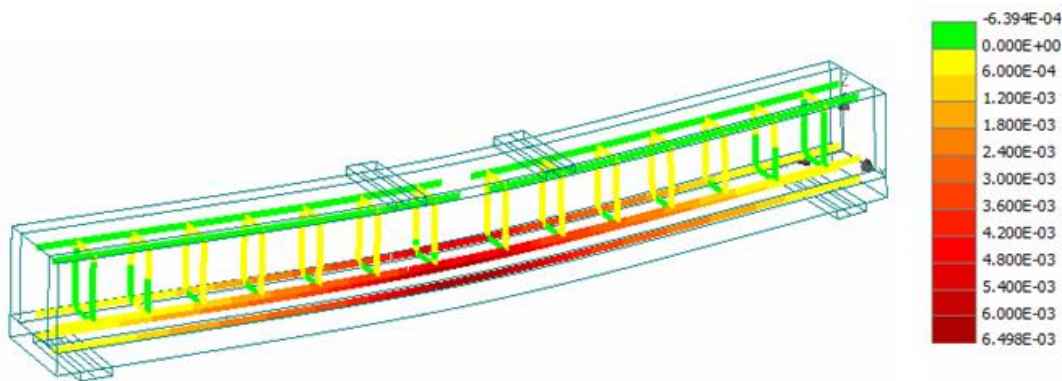
The results of Table 5.9 indicate the effectiveness of the strengthening with a jacket on three sides. Hence, with the addition of UHPFRC jacket on three sides, the first crack load increased by 131 % and the maximum load by 112 %. Further, an increase was noticed with the addition of steel bars at the tensile side of the jacket, meaning that the first crack and the maximum loads increased by 173 % and 179 % respectively. The crack development and the strain distribution are specified in Figure 5.42.



(a)



(b)



(c)

Figure 5.42 Crack pattern and strain distribution of the existing RC beam strengthened with a jacket on three sides and steel bars: a) at the first crack load, b) at the maximum load and c) the strain distribution at the reinforcement at the maximum load

As shown in Figure 5.42, the addition of steel bars produced high values of strain along the whole length of the jacket and high values of strain can also be distinguished at the reinforcement.

5.5 Conclusions

In the present chapter, crucial parameters of the examined technique have been investigated numerically. From the numerical modelling of the examined technique the following conclusions can be drawn:

- The depth of the layer affects the performance of the strengthened beams significantly. Hence, from the numerical investigation for a monolithic behavior at the interface between

the RC beam and the UHPFRC layer, it was noticed that when the depth of the layer was increased from 30 mm to 70 mm, the load carrying capacity was increased by 21 % and the stiffness by 7 %. For a non-monolithic behavior on the other hand, the load carrying capacity was increased by 12 % and the stiffness by 3 %.

- For increasing fiber content and subsequently higher tensile strength, the load carrying capacity increases. Hereby, 8% higher load carrying capacity was achieved when the tensile strength was increased from 11.5 MPa to 14 MPa.
- The shrinkage affects mainly the stiffness of the strengthened members, while the load carrying capacity is not affected significantly.
- Better performance is achieved for strengthening at the tensile side compared to the performance achieved for strengthening at the compressive side. More specifically, from the numerical analysis, it was noticed that for strengthening at the compressive side, the load carrying capacity was increased by 5%, while the respective increase for strengthening at the tensile side was 12%.
- The addition of steel bars to the layer can increase the load carrying capacity of the strengthened members significantly. Also, the amount of reinforcement of the layer is an important parameter affecting the performance of the strengthened members. Hereby, when steel bars with a diameter of 10 mm were placed at the layer, the load carrying capacity of the strengthened beam was increased by 75%. A further increase of 44% was noticed when the 10 mm steel bars were replaced by 16 mm steel bars.
- The grade of the steel bars affects the performance of the UHPFRC layer. More specifically, an increase of 7% was noticed when the steel bars B500 C were replaced by steel bars B700.
- The amount of reinforcement of the layer is an important affecting the performance of the strengthened beams significantly. Also, the numerical results indicated that the amount of the reinforcement is a more important parameter compared to the depth of the layer. Hereby, a better performance was achieved using a layer depth of 30 mm and steel bars with a diameter of a 16 mm, compared to the performance achieved using a layer depth of 70 mm and steel bars with a diameter of 10 mm.
- The addition of steel bars to the jacket can further increase the load carrying capacity of the jacket. Hence, a further increase of 32% on the load carrying capacity of the strengthened beams was noticed with the addition of two steel bars with a diameter of 10 mm at the tensile side of the jacket.

6. CONCLUSIONS AND FUTURE WORK

6.1 Conclusions

In the present chapter, the conclusions of the present research are presented. Aim of the present chapter is to summarize the findings of the present research and to clearly identify if the UHPFRC is a material which can be used for strengthening purposes, which was the main aim of the present research. Also, the present chapter, set as target to identify the research topics in which the research should now be focused.

The first part of the present research was focused on the optimization of the UHPFRC and the investigation of the properties of the material which are missing from the literature. From this investigation the following conclusions can be drawn:

- The use of high strength cement increase both the tensile and the compressive strength of the UHPFRC.
- The steel fiber content in the mixture affects the compressive strength, the tensile characteristics and the fracture energy of the UHPFRC. Therefore, different models, depending on the fiber content, are required for the modelling of the response of the material in tension.
- The big volume of fibers in the mixture (higher than 4 %), has a negative effect on the workability of the mixture.
- The heat curing accelerates the strength development and high strength in a short period can be achieved. However, heat curing for more than 12 days is not suggested, as it has not any further effect on the strength development.
- From the investigation of the flexural performance of UHPFRC prisms with various depths, it was clear that there is a 'size effect'. More specifically, it was noticed that the flexural strength is decreased as the layer depth is increased.
- From the study of the performance of UHPFRC under cyclic loading it was noticed that the modulus of elasticity is considerably reduced after the first loading cycle and then it is slightly further reduced as the number of cycles are increased. Also, another important finding from this investigation is that the monotonic response of the specimens is approaching the cyclic response.

An objective of the present research was the investigation of crucial parameters of the material which are missing from the literature such as; the effect fiber content and curing regimes on the performance of UHPFRC, the study of the “size effect” of the material and also the development of an optimum mixture design which can be adopted for strengthening purposes. From the first part of the present research, it was evident that UHPFRC is a material with unique properties and the properties of the material are highly affected by the fiber content. Therefore, apart from the mechanical properties, the fiber content changes completely the behavior of the material and different models are required for the modelling of the stress-strain behavior of the material in tension. The available models in the literature cannot accurately model the response of the material in tension. Hence, in the present research, different models, for the different fiber contents have been proposed for the modelling of the response of the material in tension. However, an important parameter which should be taken into consideration, when the fiber content is selected is the rheological properties of the material. The effective rheological properties of the material are of high importance for strengthening applications, as conventional methods for the compaction cannot be applied. Another important parameter which affects the performance of UHPFRC is the curing regimes. Thus, high mechanical properties in a short period can be achieved with heat curing. However, it should be noted that despite the fact that the optimum properties of the material are achieved for heat curing for 12 days, heat curing for 5 days has as a result very high mechanical properties, close to the optimum that the material can achieve. Hence, if the cost of the heat curing is taken into consideration, this period can be considered as the optimum period for the heat curing. An important finding of the first part of the present research was that there is a “size effect” on the flexural performance of UHPFRC. Hence, this is a parameter which should be taken into consideration when UHPFRC is designed, and the construction of thick elements should be avoided. Finally, a further objective of the present research was the study of the performance of the material under cyclic loading. From the study of the performance of UHPFRC under cyclic loading it was found that the monotonic response of the specimens was approaching the cyclic response. This assumption can be used for the computational modelling of the response of the material under cyclic loading.

The following investigation of the present research was focused on the realistic application of the UHPFRC for the strengthening of full scale beams. Aim of this investigation was to examine if the UHPFRC can be used as a strengthening material, while an objective was to examine the interface behavior between the existing RC beams and the UHPFRC layers and

if these two material can exhibit monolithic behavior. From this investigation the following conclusions can be drawn:

- The strengthening with UHPFRC layers has as a result a big increase in the stiffness of the strengthened elements. Hence, lower deformations for the imposed loads can be distinguished, while the formation of the cracks under service conditions is also delayed.
- The addition of the dowels at the interface improve the bonding between UHPFRC and concrete. Therefore, besides an increase in stiffness, produces a remarkable increase in the load carrying capacity of the beams.
- The load carrying capacity of the strengthened beams increases dramatically with the addition of steel bars to the layer.
- The optimum performance is achieved with the construction of three-side jackets.
- The bonding between UHPFRC and concrete, is effective with low values of slip at the interface. Also, from the comparison of the experimental results of the present research with available studies in the literature for strengthening with RC layers, it can be deduced that the bonding between UHPFRC and concrete is more effective with significant lower values of slip at the interface.

From the results of the second part of the present research it was evident that the strengthening with UHPFRC is a well promising technique as in all the examined cases the performance of the existing members was improved. Hence, based on the target of the strengthening technique, different strengthening configurations can be selected. More specifically, if the strengthening technique sets as target lower deformations for imposed loads and also delayed formation of the cracks under service conditions, strengthening with UHPFRC layers should be selected. If on the other hand, the strengthening technique set as target higher load carrying capacity, steel bars to the layer can be added. The construction of three-side jackets is suggested in cases that apart from big increase in the stiffness, big increase in the load carrying capacity is required, while this is a method which can be used for the shear strengthening of existing RC members. Finally, if a monolithic connection at the interface between the existing member and the new layer is required, dowel can be used. Despite the fact that the bonding between UHPFRC and concrete is superior compared to concrete to concrete interfaces, the dowels at the interface, can further improve the connection and higher load carrying capacity can be achieved.

The last part of the present research, was focused on the numerical investigation of crucial parameters of the examined technique which had not been investigated experimentally. Hence, finite element analysis was conducted and from this investigation, the following conclusions can be drawn:

- The depth of the layer affects the performance of the strengthened beams significantly.
- Higher percentages of steel fibers in the UHPFRC mixture, and subsequently higher tensile strength, has as a result higher properties of the layers and higher load carrying capacity for the strengthened beams.
- The shrinkage affects mainly the stiffness of the strengthened members, while the load carrying capacity is not affected significantly.
- Better performance is achieved for strengthening at the tensile side compared to the performance which can be achieved for strengthening at the compressive side.
- The amount of reinforcement of the layer is an important parameter affecting the performance of the strengthened members significantly.
- Improved performance can be achieved with the use of steel bars of a higher grade to the UHPFRC layer.
- The addition of steel bars to the jackets can further increase the performance of the jackets.

An objective of the present research was the optimization of the examined technique and the investigation how parameters such as: the layer depth, the fiber content, the amount of reinforcement and the steel grade of the reinforcement of the layer affect the performance examined technique. From the last part of the present research, it was clear that the most important parameter which affects the performance of the strengthened elements is the amount of the reinforcement of the layer. Also, in cases that improved performance of the strengthened elements is required, parameters such as the layer depth, the fiber content, and the steel grade of the reinforcement of the layer should be taken into consideration during the design of the technique.

6.2 Future work

From the experimental and the numerical investigation of the present research, it is clear that the application of UHPFRC for the strengthening of RC structures is a well promising technique. However, further research can be conducted on the topic of strengthening of

structures using this advanced material. For the application of the technique in earthquake prone areas, the study of strengthened members, such as beams and columns, under cyclic loading is of high importance. Hence, the response of strengthened elements with UHPFRC layers and jackets under various loading histories and reversed cyclic loading is suggested in order to investigate the structural response of the strengthened members. Also, another parameter which need to be investigated, is the effect of variable climates on the performance of the strengthening technique.

Research on the UHPFRC is also considered necessary. The development and optimization of UHPFRC using environmental friendly materials is a challenging topic. Hence, the research on UHPFRC should now be focused on the development of a material which combine both high mechanical properties and environmental protection. This can be achieved, using recycled steel fibers and also cement replacements. Also, the use of construction and demolition recycled materials as replacement of the constituents of UHPFRC, such as the aggregates, is a well promising technique, which needs further investigation.

The present research, was focused on the strengthening of RC structures using UHPFRC. However, nowadays there are also a number of masonry structures which do not have the required safety level. The unique properties of UHPFRC, together with the ease of preparation and application of the material, can be used for the strengthening of masonry structures. However, further experimental research on this topic is required.

List of References

ACI 318-14, (2014). Building Code Requirements for Structural Concrete. Farmington Hills, MI: American Concrete Institute, Print.

Association Française de Genie Civil (AFGC), (2013). Ultra High Performance Fiber Reinforced Concrete- Interim Recommendations. Bagneux, France.

Balsamo, A., Di Ludovico, M., Lignola, G., Prota, A., Manfredi, G., Cosenza, E., (2012). Composites for structural strengthening. L. Wiley Encyclopedia of Composites, 2nd Edition, John Wiley and Sons.

Bastien-Masse, M., Brühwiler, E., (2016). Experimental investigation on punching resistance of R-UHPFRC–RC composite slabs, *Materials and Structures*, 49(5), pp. 1573-1590.y

Benson, S.D.P, Karihaloo, B., (2005). CARDIFRC-Development and mechanical properties- Part III: Uniaxial tensile response and other mechanical properties. *Magazine of Concrete Research*, 57 (8), pp. 433-443.

Bournas, D.A., Triantafillou, T.C., Zygouris, K., Stavropoulos, F., (2009). Textile-reinforced mortar versus FRP Jacketing in seismic retrofitting of RC columns with continuous or Lap-spliced deformed bars. *Journal of Composites for Construction*. 13(5), pp. 360-71.

Bruhwiller, E., Denarie, E., (2008). Rehabilitation of concrete structures using Ultra-High Performance Fibre Reinforced Concrete. UHPFRC-2008: The Second International Symposium on Ultra High Performance Concrete, 5-7 March 2008, Kassel, Germany,

BS EN 1015-3:1999, (1999). Methods of test for mortar for masonry-Part 3: Determination of consistence of fresh mortar (by flow table), British Standard European Norm, BSI

BS EN 12390-3:2009, (2009). Testing hardened concrete-Part 3: Compressive strength of test specimens. British Standard European Norm, BSI.

BS EN 1992-1-1:2004, (2004). Eurocode 2: Design of Concrete Structures. General Rules for Buildings. BSI.

BS 4449:2005, (2005). Steel for the reinforcement of concrete. Weldable reinforcing steel. Bar, Coil and Decoiled product. Specification, BSI.

CEB Bulletin No. 213/214, (2013). CEB-FIP Model Code 90. International Federation for Structural Concrete, Lausanne.

- Cervenka, V., Jendele, L., Cervenka, J., (2013). ATENA Program Documentation: Part 1 Theory. Prague, Czech Republic.
- DIN 50014, (1985). Climates and their technical application: Standard Atmospheres.
- EN 1992-1-1:2004, (2004). Design of Concrete Structures-Part 1-1:General Rules and Rules for Buildings. European Norm, BSI.
- European Tyre Recycling Association., (2004). Available at: <http://www.etra-eu.org/>.
- Fardis, M., Dritsos, S., (2003). Evaluation of Earthquake Damages, Repair and Strengthening of Concrete Structures. Patra, Hellenic Open University (in Greek).
- Farhat, F., Nicolaides, D., Kanelopoulos, A., Karihaloo, B., (2007). High Performance Fibre Reinforced Cementitious Composite (CARDIFRC) - Performance and application to retrofitting. *Engineering Fracture Mechanics*, 74(1), pp. 151-167.
- Faria, R., Oliver, J., Cervera, M., (1999). A strain based plastic viscous -damage model for massive concrete structures. *International Journal of Solids and Structures*, 34 (14), pp. 1533-1558.
- Ferrara, L., Ozyurt, N., Di Prisco, M., (2011). High mechanical performance of Fiber Reinforced Cementitious Composites: the role of casting-flow induced fiber orientation. *Materials and Structures*, 44, pp. 109-128.
- Fib Bulletin No 55.,(2012). Model Code 2010. International Federation for Structural Concrete , Lausanne.
- Fib Bulletin No 43, (2008). Structural Connections for precast concrete buildings. International Federation for Structural Concrete, Lausanne.
- Greek Organization for Seismic Planning and Protection, (2013). Greek Code of Interventions. Athens, Greek Ministry for Environmental Planning and Works.
- Habel, K., Denarie, E., Bruhwiler, E., (2006). Structural response of elements combining Ultra High-Performance Fiber Reinforced Concretes and Reinforced Concrete. *Journal of Structural Engineering*, 132 (11), pp. 1793-1800.
- Hassan, A., Jones, S., Mahmud G., (2012). Experimental test methods to determine the uniaxial tensile and compressive behavior of Ultra High Performance Fibre Reinforced Concrete (UHPRFC). *Construction and Building Materials*, 37(0), pp. 874-882.

Japan Society of Civil Engineering (JSCE), (1984). Part 3-2: Method of tests for steel fiber reinforced concrete. Concrete library of JSCE.

Kang, S., Kim J., (2011). The relation between fiber orientation and tensile behavior in an Ultra High Performance Fiber Reinforced Cementitious Composites (UHPFRCC). *Cement and Concrete Research*, 41(10), pp. 1001-1014.

Kang, S., Lee, Y., Park, Y., Kim, J., (2010). Tensile fracture properties of an Ultra High Performance Fiber Reinforced Concrete (UHPFRC) with steel fiber. *Composite Structures*, 92(1), pp. 61-71.

Kesne, K., Billington, S., S. Douglas K.S., (2003). Cyclic Response of Highly Ductile Fiber-Reinforced Cement-Based Composites. *ACI Materials Journal*, 100 (5), pp. 381-390.

Lampropoulos, A., Paschalis, S., Tsioulou, O., Dritsos S., (2015). Strengthening of reinforced concrete beams using Ultra High Performance Fiber Reinforced Concrete (UHPFRC). *Engineering Structures*, 106, pp. 370-384.

Mazars, J., Pijaudier-Cabot, G., (1989). Continuum damage theory: Application to concrete. *Journal of Engineering Mechanics*, 115 (2), pp. 345-365.

Nicolaides, D., Kanellopoulos, A., Petrou, M., Savva, P., Mina, A., (2015). Development of a new Ultra High Performance Fibre Reinforced Cementitious Composite (UHPFRCC) for impact and blast protection of structures. *Construction and Building Materials*, 95, pp. 667-674.

Noshiravani, T., Bruhwiler, E., (2016). Experimental investigation on Reinforced Ultra-High Performance Fiber-Reinforced Concrete composite beams subjected to bending and shear, *ACI Structural Journal*, 110 (2), pp.251-262.

Papanicolaou, C., Triantafillou, A., (2002). Shear Transfer Capacity Along Pumice Aggregate Concrete and High-Performance Concrete Interyfaces. *Materials and Structures*, 35 (4), pp. 237-245.

Pilakoutas, K., Neocleous, K., Tlemat, H., (2004). Reuse of tyre steel fibres as concrete reinforcement. *Proceedings of the ICE- Engineering Sustainability*, 157 (3), pp. 131-138.

Portland Cement Association, (2015). Cement Consumption. Available at: <http://www.cement.org/index.asp> [Accessed 27-11-2015].

Raof, M.S., Koutas, L.N., Bournas, D.A., (2017). Textile-reinforced mortar (TRM) versus fibre-reinforced polymers (FRP) in flexural strengthening of RC beams. *Construction and Building Materials*, 151, pp. 279-291.

RILEM TC 162-TDF, (2002). Test and design methods for steel fiber reinforced concrete- Design of steel fiber reinforced concrete using the σ -w method: principles and applications. *Materials and Structures*, 35: pp. 75-81.

Saetta, A., Scotta, R., Vitaliani, R., (1999). Coupled Environmental -Mechanical damage model of RC structures. *Journal of Engineering Mechanics*, 128 (8), pp. 930-940.

Safdar, M., Matsumoto, T., Kakuma, K., (2016). Flexural behavior of reinforced concrete beams repaired with Ultra High Performance Fiber Reinforced Concrete (UHPRC), *Composite Structures*, 157, pp., 448-460.

Sahinagic-Isovic A.P.M., Markovsk, M., Cecez, M., (2012). Shrinkage strain of concrete- causes and types. *Gradevinar*, 64, pp. 727-734.

Sika Limited, (2017). Available at: <http://gbr.sika.com/> [Accessed 18-1-2017].

Sima, J., Roca, P., Molins, C., (2008). Cyclic Constitutive Model for Concrete. *Engineering Structures*, 30 (3), pp. 695-706.

Sinha, B. P., Gerstle, K.H., Tulin, L.G., (1964). Stress-Strain Relations for Concrete Under Cyclic Loading. *Journal of American Concrete Institute*, 61(2), pp. 195-211.

Technical Chamber of Greece, (2017). Available at: <http://web.tee.gr/> , [Accessed 18-8-2017].

Technical Chamber of Greece, (2004). Strengthening of structures against seismic loading, Available at: <http://lee.civil.ntua.gr/pdf/dimosiefseis/vivlia/enisxisi.pdf>, [Accessed 12-8-2017].

Tetta, Z.C., Koutas, L.N., Bournas, D.A., (2016). Shear strengthening of full-scale RC T-beams using textile-reinforced mortar and textile-based anchors, *Composites Part B*, 95, 225-239.

Tetta, Z.C. and Bournas, D.A., (2016). TRM vs FRP jacketing in shear strengthening of concrete members subjected to high temperatures. *Composites Part B*, 106, pp. 190-205.

Teychenne D.C., Franklin R.E., Erntroy H.C., Marsh B.K., (1997). Design of Normal Concrete Mixes. 2nd Edition, Building Research Establishment.

Triantafillou, A., (2004). Strengthening of Reinforced Concrete Structures using Composite Materials. 2nd Edition, Patra, (In Greek).

University of Patras, (2013). Repair and Strengthening of Structures, Available at: www.episkeves.civil.upatras.gr/index.htm [Accessed 6-2-2014].

Whitey, C., (1937). Design of Reinforced Concrete Members under Flexure or Combined Flexure and direct Compression. ACI Journal Proceedings, 8(4), pp.483-498.

Wille, K., Naaman, A., (2010). Fracture energy of UHPFRC under direct tensile loading. Proceedings of Fracture Mechanics of Concrete and Concrete Structures: Recent Advances in Fracture Mechanics of Concrete-7, 23-28 May 2010, Seoul, South Korea.

Wight, J.K., MacGregor, J.G., (2012). Reinforced Concrete Mechanics and design, Sixth Edition, ISBN-13: 9780132176521

Yoo, Y., Shin, H., Yang, J., Yoon, Y., (2013). Material and bond properties of Ultra High Performance Fiber Reinforced Concrete with micro steel fibers. Composites, Part B: Engineering, 58, (2013), pp. 122-133.

Yankelevsky, D. Z., Reinhardt, H.W., (1989). Uniaxial Behavior of Concrete in Cyclic Tension. Journal of Structural Engineering, 115(1), pp. 166-182.